



**THERMAL MODELLING
OF
DEEP BAR INDUCTION MOTOR
AT STALL**

by

MOHAMMAD REZA FEYZI

A thesis submitted in fulfilment of the requirement for the degree of

Doctor of Philosophy

in

The University of Adelaide

Department of Electrical and Electronic Engineering

Faculty of Engineering

November 1997

To:

my wife, Mohanna,

and

my sons, Arshya and Aarashi

CONTENTS

Summary	vi
Statement of originality	viii
Acknowledgment	ix
List of Author’s related publications	x
List of Principal Symbols	xi
List of abbreviations	xv
List of Tables	xvi
List of Figures	xviii
Chapter 1: Introduction	1
Chapter 2: Magnetic Field Analysis	8
1.0 Introduction	8
2.0 Field Analysis by the Finite Element Method.....	9
2.1 Formulation.....	10
2.2 Calculation of other parameters in terms of magnetic vector potential	14
3.0 Determination of Currents In An Induction Motor	14
3.1 Current displacement in the solid bars or deep bar effect.	17
3.2 Effect of space harmonics on the rotor bar currents	20

4.0	Field Analysis of Induction Motors	23
5.0	Calculation of the Terminal Parameters of the Stator and the Rotor.	25
5.1	Calculation of the stator parameters	26
5.1.1	Stator winding resistance	26
5.1.2	Stator winding inductances	26
5.2	Calculation of the rotor parameters	28
5.2.1	Calculation of r_b	30
5.2.2	Calculation of r_c	31
5.2.3	Calculation of x_b	31
5.2.4	Calculation of x_r	32
6.0	Estimation of Loss Density	32
6.1	Estimation of iron loss distribution.	33
6.2	Estimation of ohmic loss distribution	34
7.0	Magnetic Analysis of Induction Motor	34
7.1	Solution procedure	36
7.2	Application of stator and rotor currents	42
Chapter 3: Thermal Analysis		47
1.0	Terminology	47
1.1	Mechanisms of heat transfer.	48
1.2	Boundary conditions.	48
1.3	Different regimes of thermal analysis.	49
1.4	Solution Techniques	49
2.0	Conductive Heat Transfer	50
2.1	Conduction in one dimensional thermal systems	50
2.1.1	General formulation.	50
2.1.2	Determination of conductive heat transfer in one-dimensional system.	51
2.2	Conduction in multi-dimensional thermal systems	53
2.2.1	Determination of conductive heat transfer in a multi-dimensional systems	55
2.3	Lumped parameter method	55
2.4	Numerical analysis of conductive heat transfer	57
2.4.1	Finite difference method	57
2.4.2	Resistance element method	60
2.4.3	Finite Element Method.	62

3.0	Convective Heat Transfer	64
3.1	Evaluation of h_c	65
3.2	The effect of fins	69
4.0	Radiation	70
Chapter 4: Thermal Modelling of Induction Motor		71
1.0	Introduction	71
1.1	Symmetry and periodicity planes	73
2.0	Possible approaches for thermal modelling	75
2.1	Three dimensional model	75
2.1.1	Two dimensional modelling	76
3.0	History of thermal modelling of induction motor	77
4.0	Some considerations about the material properties	85
4.1	A brief comparison of copper cages and aluminium cages	87
Chapter 5: Modelling Procedure		89
1.0	Introduction	89
2.0	Magnetic analysis	90
2.1	Model generation for magnetic analysis	90
2.2	Boundary conditions for magnetic model	91
2.3	Application of loads (currents) on the magnetic model	92
2.4	Solution	94
2.4.1	Estimation of local reluctivities	96
2.4.2	Determination of equivalent circuit parameters	97
3.0	Thermal analysis	101
3.1	Model generation for the thermal analysis	101
3.1.1	Determination of material properties for conductive heat transfer	102
3.2	Applying the boundary conditions on the thermal model	108
3.3	Applying the loads on the thermal model	110
3.3.1	Calculation of rotor bar currents for 2-D model	110
3.3.2	Effect of temperature changes during the solution procedure	113

3.4	Sensitivity analysis	116
3.4.1	Sensitivity analysis of the rotor parts	116
3.4.2	Sensitivity analysis of stator parts	126
3.4.3	Sensitivity to convection film coefficients	127
Chapter 6: Simulation and Test Results		131
1.0	Introduction	131
2.0	Measurement of temperature	131
2.1	Sources of measurement errors	132
3.0	Specifications of the models	133
4.0	Verification of the results	134
4.1	Test setup for model one	135
4.2	Verification of the results for model one	136
4.3	Test setup and verification of results for model two	144
4.4	Some general comments on the results	156
5.0	Study of heat flow in the motor	156
5.1	Results from the lumped parameter model	159
5.2	Some comments on the results of current topic	162
Chapter 7: Transient Thermal Analysis During Starting		165
1.0	Introduction	165
2.0	Procedure of the modelling	166
2.1	Dynamic equivalent circuit of the motor	169
2.2	Determination of equivalent circuit parameters	170
3.0	Procedure of the preliminary tests	171
4.0	Test setup and Verifications	174
Chapter 8: Conclusion		182
Appendix A: MMF of a Distributed Windings		186

1.0	MMF of a single phase winding	186
2.0	Travelling wave MMF of a poly-phase winding	188
3.0	Equivalent windings	189
Appendix B: Measurement of Thermal Conductivity of Solids		191
1.0	Radial heat flow method	191
2.0	Hot wire method	192
Appendix C: Additional Graphs		195
Appendix D: Temperature Measurement with Thermocouples		209
1.0	Introduction	209
2.0	Thermocouple Circuits	210
2.1	General Case	210
2.2	Cold-Junction Compensation	210
2.3	Linearizing the Data	214
Bibliography		215

SUMMARY

As with all motors, the performance of an induction motor while at standstill, whether in the course of a normal starting sequence or as a result of stall, is of crucial importance to a designer. Since the motor is under full voltage, a fast temperature rise may occur in different parts of the motor before the power source is isolated, or substantial acceleration occurs. This may damage some parts of the motor, or cause a premature aging of the electric insulation in various parts of the motor, in particular the stator winding. In addition, in applications where the motor is surrounded by a potentially explosive atmosphere, an unexpected temperature rise at any point in a motor may be enough to ignite the existing mixture of gases. To avoid such phenomena, the temperature distribution in the motor should be predicted as accurately as possible to ensure reliable protection of the motor against overheating in critical points. This work is an attempt to improve the accuracy of prediction of transient temperature distribution in an induction motor, with particular attention to the modelling of deep-bar cage motors.

The accuracy of thermal models is strongly dependant on that of the initial data. This data includes both geometry-related parameters and the relevant material properties. Furthermore, an accurate picture of the distribution of the thermal loads in the motor is crucial to the final results.

The distribution of the loads in the thermal model is extracted from a two-dimensional magnetic analysis employing a harmonic finite element method. This procedure enables inclusion of the deep-bar effect in the rotor bars and consequently an accurate estimation of the distribution of losses in these areas. The effect of the non-linearity of the iron core is included in the magnetic analysis using the “effective reluctivity” and “simultaneous static and harmonic analysis” methods.

Although a three dimensional thermal model of the complete motor is ideally required, a reduced system including only half of one slot pitch is proposed as the main model. This is supplemented by a two-dimensional model to study the peripheral variation of temperature in the motor.

The proposed method is applied to two induction motors, 15kW and 250kW, used as models one and two respectively. The analysis results were verified by direct locked rotor tests on the motors. Two individual locked rotor tests with different voltages were performed on each model and the variation of temperature with time at 17 points on model one and 20 points on model two was recorded for this purpose. Finally, a transient analysis on the motor during start up was carried out where, a dynamic equivalent circuit is proposed for induction motors and a method to determine the parameters of this circuit is suggested. The validity of this analysis is checked against the test results on the 15kW motor only.

STATEMENT OF ORIGINALITY

This work contains no material which has been accepted for the award of any other degree or diploma in any university or other tertiary institution and, for the best of my knowledge and belief, contains no material previously published or written by another person, except where due reference has been made in the text.

I give consent to this copy of my thesis, when deposited in the University Library, being available for loan and photocopying.

Mohammad Reza Feyzi

LIST OF PRINCIPAL SYMBOLS

Symbol	Description
A	Area of surface, area of convection surface, m^2
\dot{A}	The magnetic vector potential (in z direction), Wb/m
\dot{A}_0	The mean value of \dot{A} over the cross sectional area, Wb/m
A_{sslot}	The apparent area of stator slots.
\dot{B}	The magnetic flux density, Wb/m^2
B_{peak}	Peak value of local flux density, Wb/m^2
$B_{x,i}$	The peak value of x component of the imaginary part, Wb/m^2
$B_{x,r}$	The peak value of x component of the real part, Wb/m^2
$B_{y,i}$	The peak value of y component of the imaginary part, Wb/m^2
$B_{y,r}$	The peak value of y component of the real part, Wb/m^2
\dot{D}	The electric flux density, C/m^2
\dot{E}	The electric field strength, V/m
\mathcal{F}	Functional
\dot{H}	The magnetic field strength, A/m
I_{nb}	Total rms value of current in rotor bar number n
\hat{I}_1 and \hat{I}_2	Amplitudes of stator and rotor currents calculated from the equivalent circuit
$\hat{I}_{b,rotor}$	Amplitude of the bar current in the rotor cage;
$\hat{I}_{b,stator}$	Amplitude of the bar current in the equivalent stator cage winding;
I_v	rms value of v th harmonic bar current
I_μ	rms value of μ th harmonic bar current
J	Current density, A/m^2

- J_0 The average or low frequency current density in the bar, A/m^2
- $|J_{z,e}(x,y)|$. . . Current density in the element in position (x,y)
- K_{acc} Acceleration factor
- L_0 Inductance of the gap above the bar (if there is any gap)
- L_{mean} the mean length of turns in the stator winding,
- L axial length of the cylinder, the significant (or characteristic) length (Ch3)
- N_1 The number of turns per pole in the primary winding (stator)
- P_a The apparent power per killo gram, VA/Kg
- R_{ij} Thermal resistance between nodes i and j .
- S_2 The number of slots in the secondary (rotor)
- T_w Wall temperature, $^{\circ}C$
- T_{∞} Bulk temperature of the fluid, $^{\circ}C$
- T Temperature, $^{\circ}C$
- T_i, T_j Temperature at nodes i and j respectively;
- T_i Inside surface temperature
- T_o Outside surface temperature
- V Velocity of the fluid;
- a The cross sectional area of each individual stator conductors, m^2
- a_{mean} The mean area of the end ring, m^2
- c Specific heat, $J/(Kg \cdot ^{\circ}C)$
- da_e Area of the element
- $dW_i(x,y)$. . . Local iron losses
- f Frequency, Hz
- g Number of slots per pole; also, acceleration of gravity, N/Kg
- g' Number of slots per pole and per phase
- h_c Convective heat transfer coefficient, $W/(m^2 \cdot ^{\circ}C)$

- i_1 to i_n The current flowing through segments 1 to segment n
- j Imaginary unit equal to $\sqrt{-1}$
- k_{w1} Winding factor of the primary winding
- k_r Thermal conductivity of the wall in the radial direction, $W / (m \cdot ^\circ C)$
- k_x Thermal conductivity of the element in x direction, $W / (m \cdot ^\circ C)$
- l_{mean} The mean length of each end ring, m
- l_1 to l_n Inductance of individual segment disregarding any mutual inductances
- m The number of conductors in parallel in the stator winding.
- m Number of parallel paths in the winding,
- q Number of phases; also, heat flux, W
- q The transferred heat in x direction, W
- q''' The loss density in the stator slot area, or heat generation, W/m^3
- q_i The heat delivered to node i by heat generation;
- q_r Heat transfer in the radial direction
- r_1 to r_n Resistance of individual segments
- r_c The per phase equivalent resistance representing the iron losses.
- $r_{2,eq}$ The equivalent rotor resistance including the end-ring effect, Ω
- r_1 The per phase resistance of stator winding,
- r'_2 The per phase resistance of the rotor winding transferred to stator side,
- $r_{b,eq}$ Equivalent resistance of a bar in a cage rotor allowing end-ring effects,
- r_b Resistance of a bar alone,
- r_c Resistance of one ring segment between two adjacent bars,
- r_i Inside radius
- r_o Outside radius
- t Time, *seconds*
- x_1 The per phase leakage reactance of stator winding, Ω

- x'_2 The per phase leakage of the rotor winding transferred to stator side, Ω
- $x_{b, eq}$ Equivalent reactance of a bar in a cage rotor allowing end-ring effects, Ω
- x_b Reactance of a bar alone, Ω
- x_c Reactance of one ring segment between two adjacent bars, Ω
- x_m The per phase mutual inductance between rotor and stator windings, Ω
- $x_{2, eq}$ The equivalent rotor reactance including the end-ring effects, Ω
- α Thermal diffusivity of the material (CH3)
- α_v phase angle related to harmonics v and μ respectively
- α_μ phase angle related to harmonics v and μ respectively
- μ Viscosity of the fluid.
- v Harmonic pole-pair numbers
- μ Harmonic pole-pair numbers
- v Reluctivity, m/H
- v_{app} Applied Reluctivity, m/H
- ρ Volume charge density, C/m^3 ; also, density of any solid, Kg/m^3
- ρ_c Density of iron (core), Kg/m^3
- σ Spread of phase group in electrical radians; electric conductivity, mho/m
- τ Time, *seconds*
- τ_c Time constant, *seconds*
- ω The angular frequency, *rad/seconds*

LIST OF ABBREVIATIONS

Abbreviation	Definition
FEM	Finite Element Method
LPM	Lumped Parameter Method
TC	Thermo Couple
TEFC	Totally Enclosed Fan Cooled

LIST OF TABLES

Table 2-1	The variation of current and squared current in the rotor bars.	22
Table 3-1	The Values of Nodal Resistances for Cartesian and Cylindrical Coordinate Systems	61
Table 3-2	Empirical values of constants to be used in (3-42) for horizontal cylinders.	68
Table 4-1	A comparison between the conditions for the transient and steady state analysis of induction motor	73
Table 4-2	A statistical survey of the field of papers in ICEM's	78
Table 4-3	Search results in FirstSearch database on 7 August 1997	78
Table 4-4	Some thermal properties of Aluminium at 20 °C	85
Table 4-5	The percentage of each material in the compositions of aluminium used in cast rotor cages	86
Table 4-6	Some thermal properties of Iron and steel (max. C =1.5%) at 20 °C	86
Table 5-1	Thermal properties of different materials used in model one	108
Table 5-2	Thermal properties of different materials used in model two	109
Table 5-3	The contribution of each harmonic in the losses of a rotor bar in different positions.	111
Table 5-4	The variation of thermal conductivity and the thermal coefficient of electric resistivity for some main parts in an induction motor [33].	114
Table 5-5	Summarised results for the copper/lamination thermal contact resistance	119

Table 5-6	Variation of the hot point temperature in different components as percentage of the hot point temperature at normal conditions at the same part individually	127
Table 5-7	Variation of the hot point temperature at $t = 26$ seconds within different components when the convection coefficient of the given boundary is changed.	129
Table 5-8	The convected heat from different boundaries of the motor at $t = 26$ seconds	130
Table 6-1	Specification of the models	133
Table 6-2	Specifications of Walker's [73] model	152
Table D-1	NIST Polynomial Coefficients	214

LIST OF FIGURES

Fig. 1-1	Minimum values of the time t_E of the motors in relation to the starting current ratio, I_A/I_N	4
Fig. 1-2	Demonstration of the measurement of time t_E	5
Fig. 2-1	Equivalent circuit of an induction motor	15
Fig. 2-2	The general form of equivalent circuit including the effect of space harmonics	18
Fig. 2-3	A rotor bar embedded in a slot and its preliminary equivalent circuit	19
Fig. 2-4	The equivalent circuit of a rotor bar	20
Fig. 2-5	Per-unit distribution of current density in a solid rotor bar.	20
Fig. 2-6	Two dimensional magnetic circuit of a typical four pole induction motor.	24
Fig. 2-7	Distribution of current in a cage rotor.	29
Fig. 2-8	Flow chart of the magnetic analysis by effective reluctivity method	35
Fig. 2-9	The procedure of a non-linear harmonic analysis by using the effective reluctivity method	37
Fig. 2-10	Variation of permeability and reluctivity of iron core as functions of flux density	39
Fig. 2-11	Variation of gradient of the reluctivity of iron core	40
Fig. 2-12	The procedure of the new method using a simultaneous non-linear static and a harmonic analyses	43
Fig. 3-1	A typical thermal system showing different possible boundary conditions	48
Fig. 3-2	Two samples of the elementary one dimensional thermal systems	51

Fig. 3-3	The elementary one dimensional thermal system including a three layer wall.	52
Fig. 3-4	Volume elements for three dimensional heat conduction analysis in the Cartesian coordinate system	54
Fig. 3-5	A typical presentation of lumped parameter equivalent circuit.	56
Fig. 3-6	A typical meshing for the finite difference solution method.	57
Fig. 3-7	Equivalent circuit of a general conduction node.	60
Fig. 3-8	Volume elements for three dimensional heat conduction analysis	61
Fig. 3-9	Sketch illustrating one dimensional rectangular fins.	69
Fig. 5-1	Meshing layout for one pole of Model 1 and the details of the selected area	91
Fig. 5-2	Demonstration of the applied boundary conditions,	92
Fig. 5-3	Winding layout for phase “A”.	94
Fig. 5-4	Distribution of field mmf when the actual currents are applied on the stator winding only	95
Fig. 5-5	Open circuit test results.	99
Fig. 5-6	Results from OC and SC test results.	100
Fig. 5-7	Meshed volumes of the 3-dimensional thermal model for Model 1.	103
Fig. 5-8	The meshed view of the modelled parts of the stator winding and the rotor cage.	104
Fig. 5-9	Williams’ [74] test results about the conductivity of laminated iron	107
Fig. 5-10	Demonstration of contribution of some harmonics in the heat generation	112
Fig. 5-11	Distribution of current density along the depth of the rotor bar in different temperatures	113
Fig. 5-12	The actual procedure of thermal analysis	115
Fig. 5-13	The geometry of model both for magnetic and thermal analysis	117
Fig. 5-14	Temperature distribution in the bar after 0.2, 0.4, 0.6, 0.8 and 1.0 sec.	118
Fig. 5-15	Effect of the conductivity of slot liner on the aluminium bar heating	121
Fig. 5-16	Effect of the conductivity of slot liner on the copper bar heating.	122
Fig. 5-17	Variation of total losses in the aluminium bar as a function of time.	124
Fig. 5-18	Comparison of the temperature distribution in the bar	125

Fig. 5-19	The distribution of current density and its deviation from a uniform conductivity distribution in the bar	126
Fig. 5-20	The variation of convected heat as percentage of total power loss in the motor from	128
Fig. 6-1	Profile of the equivalent slot pitch of models one and two.	134
Fig. 6-2	Location of thermocouples on the rotor	136
Fig. 6-3	The location of the TC's on the rotor and stator windings etc.	138
Fig. 6-4	Variation of temperature along the radial axis of rotor bar with time and location, full voltage (419 volts)	139
Fig. 6-5	Variation of temperature along the axial direction of the rotor, full voltage (419 volts)	141
Fig. 6-6	Variation of temperature along the peripheral direction of the rotor with time and location, full voltage (419 volts).	143
Fig. 6-7	Comparison of simulation results from the 3-D model with the test results at different locations in the stator, full voltage (419 volts)	145
Fig. 6-8	Location of thermocouples on the rotor parts of model two.	146
Fig. 6-9	Variation of temperature at the axial location on the rotor (model2)	147
Fig. 6-10	Variation of temperature at the rotor end-ring (model2).	149
Fig. 6-11	Vector demonstration of the heat flow within the rotor end-ring at selected times as indicated	150
Fig. 6-12	Variation of temperature at the peripheral and radial locations on the rotor	151
Fig. 6-13	Variation of temperature at the test points on the stator core (model2)	153
Fig. 6-14	Variation of temperature at the test points on the stator winding (model2)	154
Fig. 6-15	Distribution of temperature at t = 26 sec. in the modelled parts (model 2)	155
Fig. 6-16	The thermal equivalent circuit of a stalled induction motor.	157
Fig. 6-17	The variation of thermal flux through different parts in the motor.	160
Fig. 6-18	The variation of average temperature in different nodes on the rotor and stator	161
Fig. 6-19	Variation of the effective thermal resistances	162
Fig. 6-20	The ratios of the maximum temperature to the average temperature within components	163

Fig. 7-1	The equivalent circuit of an induction motor	168
Fig. 7-2	Test results from the test on the cage-less motor	173
Fig. 7-3	Variation of rotor resistance and inductance with frequency	175
Fig. 7-4	Motor currents in different conditions and the associated error	176
Fig. 7-5	Measurement results from the run-up test.	177
Fig. 7-6	Variation of temperature along the indicated paths in the rotor cage	179
Fig. 7-7	The measurement results and comparison with the analysis results at the indicated points	180
Fig. A-1	MMF of a uniformly distributed phase winding and one distributed in limited number of slots	186
Fig. B-1	Schematic diagram of a radial thermal conductivity measurement apparatus	192
Fig. B-2	Schematic diagram of a hot-wire thermal conductivity test	193
Fig. C-1	Distribution of field mmf when the stator winding only is sinusoidally excited.	196
Fig. C-2	Distribution of field mmf when the rotor bars only are sinusoidally excited.	197
Fig. C-3	Distribution of field mmf when both of the rotor cage and stator winding are sinusoidally excited.	198
Fig. C-4	Distribution of the real component of magnetic flux density in the air-gap	199
Fig. C-5	The distribution of the real component of current density at the rotor bars of the 2-D model.	200
Fig. C-6	The distribution of the real component of flux density in the 2-D model.	201
Fig. C-7	Distribution of heat generation in a rotor bar as a function of its relative spatial position to the stator mmf.	202
Fig. C-8	Distribution of heat generation in a rotor bar as a function of its relative spatial position to the stator mmf.	203
Fig. C-9	Distribution of heat generation in a rotor bar as a function of its relative spatial position to the stator mmf.	204
Fig. C-10	Variation of temperature along the radial axis of rotor with time and location, reduced voltage (289 volts).	205
Fig. C-11	Simulation and test results with reduced voltage (289 volts).	206

Fig. C-12	Simulation and test results with reduced voltage (289 volts)	207
Fig. C-13	Simulation and test results with reduced voltage (289 volts)	208
Fig. D-1	Schematic diagram of a J-Type Thermocouple	210
Fig. D-2	Compensation of cold junction error by using a reference temperature. . . .	211
Fig. D-3	Illustration of thermocouple law of Intermediate Metals	212
Fig. D-4	Compensation of cold junction error by using the thermocouple law of intermediate metals	212



CHAPTER ONE

INTRODUCTION

Nowadays, the substantial role of the induction motor is evident in driving the wheels of industry, and it is by far the most common type because of its major advantages.

The invention of this type of motors dates back to more than a century, and its capabilities have been extensively improved during this long period. The main part of the analytical groundwork for the machine design was completed before 1930. However, prior to the appearance of the computer in the world of electric machines in 1950's, no sophisticated design was possible. Therefore, designers had to compromise the accuracy of their work to the effort they would spend on a single design. In addition, many evaluating prototypes were manufactured prior to the mass production of a newly designed motor. Otherwise, no motor could find its way beyond the designer's desk.

Before the advent of cast aluminium rotors in 1925 [35], the rotor cages of induction motors were assembled by individual copper or copper alloy conductor bars in the slots brazed or welded to the end-ring of similar material at either end of the rotor. This is still a common practice with very large motors, generally larger than 2500kW [19], or in some special cases. Casting rotors allows filling the conductor bar slots with aluminium, binding the entire assembly together and producing the end-ring and cooling fan vanes in a single economical process. The resultant assembly, compared to the similar assembly of copper cage and fan, is more robust and less noisy. In addition, since the rotor bars fill the slots completely, a cast rotor should maintain its balance indefinitely whereas a welded or brazed cage may lose its balance in time since the conductors do not fill the slots completely.

Lack of any electrical contact between the stationary and the rotating parts in a cage motor is the outstanding feature of this motor, in particular among the large machines. This eliminates any need for brushes and slip rings or commutator and not only reduces the final specific cost and at the same time specific volume of the machine but makes it more robust. Consequently, this type of motor needs less maintenance than a DC or synchronous motor for a given application. Induction motors are manufactured in a wide range of power, from few watts to several mega-watts, to be used in a variety of applications, from a coffee grinder to a huge cement mill.

Normally, a reasonably high resistance of rotor circuit results in a higher starting torque but lower efficiency of the induction motor. To take advantage of high starting torque and at the same time high efficiency, in a wound rotor induction motor, the rotor resistance is kept at the minimum; then, an external resistor is added into the rotor circuit during the starting. A similar result can be achieved by taking advantage of the deep bar effect (see page 17) in a cage rotor.

In order to maximise the utility factor in a plant, most of apparatus, including the induction motors, should be operated as near to their full load as possible. On the other hand, temperature rise is the main factor to limit the output power of an electric machine. Therefore, a good knowledge of the distribution of temperature in a motor is necessary to maximise its utility factor. In addition, it may save a considerable amount of dollars via a optimum usage of materials. Otherwise, the uncertainties in the estimation of temperature rise in certain parts should be overcome by using some extra materials and/or a material with higher grade than the desired. In some circumstances, it is overcome by de-rating of the motor to a lower power which results in a higher specific cost of the product.

The winding temperature directly influences the selection of insulation class for both the winding conductors and the slot liners. In addition, the characteristics of the insulation is temperature dependant and an Arrhenius relationship shows that the insulation life is halved for every 8°C to 10°C increase in the operating temperature [30]. Therefore, an optimum selection of insulation class directly involves a correct temperature prediction in different parts of the motor. In brief, the success of any design hinges on an advance knowledge of the most likely temperature rise in critical points of the machine.

Unfortunately, there are still many unknown and/or uncertain factors for the optimum design of an induction motor. Thermal properties of some parts in the motor are perhaps the dimmest spots in this process. As an example, while there is still a wide scatter in the determination of convection film coefficient for a simple smooth isothermal cylindrical surface horizontally mounted in the air¹, the same coefficient for the irregular external surface of the motor, surrounded by the fins, terminal box, end-caps, and mounting is the key factor in the determination of temperature distribution in the motor at steady state!

In addition to the design capabilities which may minimize the final cost/kW of any type of motor for the manufacturer, an appropriate selection of the motor for any specific application has a vital role in the optimization of the cost for the consumer. Each environment desires its specific requirements to meet safety issues or any other policies. Therefore, the motors are manufactured with a variety of designs to suit in different applications. For example, in a refinery or a chemical plant, where the environment is potentially in a high risk of fire, any source of heat or spark should be isolated from the possibly existing flammable gases in the area. This prescribes usage of so called “totally enclosed fan cooled” (TEFC) induction motors. Needless to say that the specific cost of such motor is much higher than that of a simpler design which meets the requirement to be installed in a well ventilated room to operate a lift.

Today, TEFC induction motors are widely used in many industrial plants. However, the feature of this design limits the heat flow from different boundaries into the surroundings and consequently the output power for a certain frame reduces significantly. Although this problem is partially overcome by improving the class of the insulation, the temperature rise is still a crucial factor in the rating and consequently, on the \$/kW of this type of induction motors. The rapid growth in the capabilities of sophisticated design and also the techniques of mass production on the one hand and the increase in the number of the world wide competitor manufacturers on the other hand provides a challenging environment for this product.

1. From different methods, and using different constants proposed in Holman [33] for a solved example, the values of this coefficient are 1.00 P.U., 1.35 P.U., 1.52 P.U. and 1.71 P.U assuming the minimum value as the base. Some of the equations are given on section 3.1 on page 65.

Over the years, several problems have been detected in using induction motors and accordingly, suitable remedies were found and some standard requirements were defined for each application to cover both the technical and safety issues. Therefore, in addition to the economic side of the problem, any product should comply with the standard requirements for any proposed plant in each country. As an example, according to Australian standard 2380.6 [70] in relation to the “Electrical Equipments for Explosive Areas”, any induction motor which is used in such environments should undergo a blocked rotor test to ensure the temperature in any point in the motor does not exceed a permissible pre-defined level within a minimum time of t_E . The time interval t_E is a function of I_S/I_N , the ratio of starting current to the rated current, as shown in Fig. 1-1. In order to determine t_E the motor is loaded

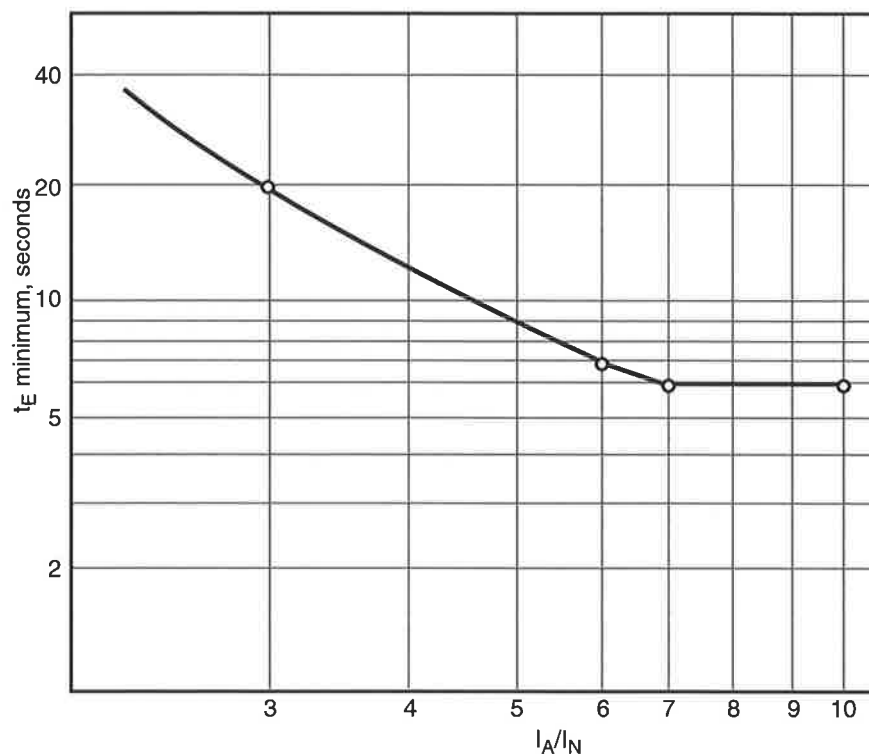


Fig. 1-1 Minimum values of the time t_E of the motors in relation to the starting current ratio, I_A/I_N

with its rated power for a period in which all parts of the motor reach thermal steady state conditions. Then it is stalled under the rated voltage and t_E is checked as demonstrated in Fig. 1-2. In this figure, t_1 is a time interval in which the temperature at all points in the motor under rated load reaches steady state and t_2 is the time interval under stalled conditions in

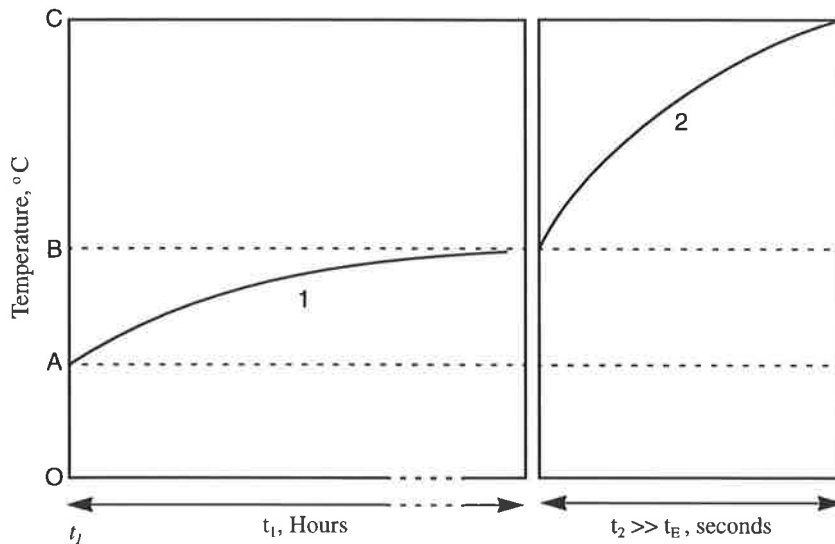


Fig. 1-2 Demonstration of the measurement of time t_E :

A = highest permissible ambient temperature,

B = limiting temperature (determined by the class of the insulation),

C = The hot point temperature,

1 = temperature rise during the rated service

2 = temperature rise during the stalled motor test

which the hot point temperature reaches the maximum permissible level. In order to fulfil the standard requirements t_2 should not be shorter than t_E .

Terms “stall” and “blocked rotor” are frequently used in this thesis and because of many similarities in their conditions they may be confused with each other. Theoretically, a motor “stalls” while it is running under normal voltage because the load torque exceeds its pull out torque. A “blocked rotor” test implies that the motor is blocked initially and then a voltage, which is not necessarily the rated voltage, is applied. In this thesis, unless expressed explicitly, the blocked rotor is also assumed to be under the full voltage.

The steady state equivalent circuit proposed by Steinmetz [71] is still being used by designers and analysts. However, the parameters of this circuit can be determined with a higher accuracy now. This allows a more accurate prediction of rotor and stator currents at steady state conditions. There are also some well developed transient models based on coupled circuit theory which are used to predict electrical transients and are useful in evaluating instantaneous torque variation in response to defined perturbations in the terminal conditions. When thermal performance is to be determined, however, the use of these

transient models is rarely necessary due to the characteristic thermal time constants in a motor which are orders of magnitude longer than their electrical counterparts.

Thus in most design work the classic equivalent circuit is usually used to estimate the behaviour of the motor at any speed, and also for the purpose of transient analysis during the start up. Because of the variation of rotor resistance and the iron losses with speed, the accuracy of this equivalent circuit may not be enough to predict the motor behaviour in this transient regime; the error becomes significant in the case of deep bar cage motors. This is discussed in detail in chapter 7 and it is shown that the error in the predicted rotor current varies from 2.5% to more than 60% when the speed varies from zero to the synchronous speed (see Fig. 7-4b on page 176).

The prediction of motor temperature is based on the evaluation of loss distribution in the motor from the electric and the magnetic analyses of the motor. Therefore, any error in any of these parts propagates into the thermal analysis as a squared law. Today, the temperature distribution in a motor at steady state may be predicted with a reasonable accuracy. This provides a reliable protection of the motor against overheating as a result of overloading, abnormal ambient temperature, and so on while motor is running. However, the personal experience of the author during a 20-year involvement in this type of machine has shown that, except for the overloading, a major part of thermal failures in the motor occurs when the motor is under any of the following abnormal operating conditions:

- (a) The motor fails to start (stall before speeding up);
- (b) The motor stalls as a result of overloading (stall while running under normal conditions);
- (c) Motor is started under such a condition that the starting time is long (e.g. under a high inertia load).

The baseline of all of the above cases is a standstill condition. Therefore, in this work, the most effort is dedicated to investigate the temperature distribution in the motor when the motor is energized under blocked rotor conditions. Nevertheless, the purpose of this work is not just simply determination of the temperatures but rather, to find the region of the highest loss and to estimate the components of heat flow in the motor.

Most of the published works are based on some experimental results on the motor under simulation which is applicable only to an existing motor. One of the outstanding points of the present work is its capability to generate the model without such requirements. Having enough information about the physical dimensions of a motor along with the appropriate properties of the constructional materials in hand, the proposed method enables estimation of the picture of temperature distribution in the motor. All of the above information may be gathered from the design data sheets.

Organisation of this thesis. The nature of present work requires the study of two different disciplines, magnetic and thermal fields, in a single induction motor. Although the results of the disciplines are closely interlinked, nevertheless, to avoid any confusion on the one hand, and allowing for wider investigation on each field on the other hand, it was decided to separate the discussion on each field as long as the consistency of the study permitted. Consequently, the main parts of the literature review on the magnetic analysis and the thermal analysis were also separated and located individually in the relevant chapters.

Chapter two deals with possible approaches on the magnetic analysis. Chapter three is dedicated to the study on possible methods of thermal analysis where the advantages and disadvantages of each method along with their limitations are also discussed. Chapter four is also related to the thermal analysis. In this chapter the first milestones of the thermal analysis are implanted and possible approaches for the thermal modelling are discussed. The following chapters are mainly oriented toward the application of the proposed method to the study on two TEFC induction motors used as models one and two in this project.

The procedures of construction of magnetic and thermal models are widely discussed in chapter five. The features of the two dimensional magnetic model and the relevant analysis results are also reported in this chapter. The analysis and test results on both models at stall conditions are located in chapter 6.

Despite the concentration of this thesis on standstill conditions, a transient analysis of an accelerating motor is also carried out and relevant material is located in chapter seven.

* * * * *

CHAPTER TWO

MAGNETIC FIELD ANALYSIS

Contents: Field Analysis by the Finite Element Methods, Determination of Currents in an Induction Motor, Field Analysis of Induction Motors, Calculation of the Terminal Parameters of the Stator and the Rotor, Estimation of Loss Density, Magnetic Analysis Of Induction Motor

1.0 INTRODUCTION

Electromagnetic fields are governed by the Maxwell's equations as follows:

$$\nabla \times \dot{E} = -\frac{\partial \dot{B}}{\partial t} \quad (2-1)$$

$$\nabla \times \dot{H} = J + \frac{\partial \dot{D}}{\partial t} \quad (2-2)$$

$$\nabla \cdot \dot{D} = \rho \quad (2-3)$$

$$\nabla \cdot \dot{B} = 0 \quad (2-4)$$

where:

\dot{E} = The electric field strength, (V/m)

\dot{B} = The magnetic flux density, Wb/m²

t = time, seconds

\dot{H} = The magnetic field strength, A/m

J = Current density, A/m²

\vec{D} = The electric flux density, C/m^2

ρ = Volume charge density, C/m^3

Since analytical solutions of these equations are limited to a simple geometry of the field and its boundaries, and also limited to linear magnetic characteristics, numerical methods, mainly the finite element method, have found great favour with engineers and designers [67]. Today, it is probably the most powerful tool to handle field problems with complex geometry and/or non-linear material properties.

Wislow [85] was one of the first who employed the finite element method to solve electromagnetic problems and within a short time its application in electromagnetics expanded dramatically. By this method, any complex geometry of the problem is discretized into finite numbers of simply shaped elements with linear local reluctivities, so that the electromagnetic equations can be constructed for each of them individually; then they are solved simultaneously. The non-linearity of the saturable materials can be included by iteration in linearised equations [66].

2.0 Field Analysis by the Finite Element Method

In many instances, a considerable simplification arises both conceptually and in computation if the fields are represented by potential functions. Then, a well-known principle of minimum potential energy, namely that “the potential distribution in the field must be such as to minimise the stored energy”, is employed to find the most probable potential distribution in the interest region. The solution starts with the construction of the governing equations. Then, an energy function is sought so that minimising of that function satisfies the governing equations. This is the technique which is used in the finite element method.

Minimising of the energy function determines the coefficients and thereby implicitly determines an approximation of the potential distributions. Having the potential distribution, other parameters can be calculated. In order to consider different aspects of the problem, different solution strategies have been developed.

When all of the excitation currents and also the magnetic material properties of the magnetic circuit are time independent, the solution is referred as *static analysis* [36,37]. It may be a linear or non-linear analysis depending on the B-H characteristics of the magnetic circuit

medium. In a more complicated case, when the excitation currents and/or magnetic properties of the field medium are time-varying, then a *time stepping analysis* (or a set of successive transient analyses) is carried out [53].

2.1 Formulation

Since the main object in this project is the analysis of an induction motor, the formulation is directed to cover this purpose rather than a general discussion. An induction motor is a three dimensional object and therefore it should be analysed through a three dimensional model. However, for many reasons, it will be treated as a two-dimensional magnetic circuit. The reasons for this simplification will be discussed later.

In two-dimensional models, using the magnetic vector potential allows implementation of a unique form of governing equation for both the conducting areas and non-conducting areas. The areas which are subject to eddy currents, e.g. rotor bars, are called conducting areas while the iron-core area, air-gap and stator winding areas are treated as non-conducting areas. In the terminology of finite element magnetic analysis, a non-conducting area is not necessarily an electrical insulator, but it means no eddy current is taken into account in that area.

The magnetic vector potential for a two dimensional model is defined as:

$$\nabla \times \dot{B} = \dot{A} \quad (2-5)$$

where,

\dot{A} = The magnetic vector potential, Wb/m

\dot{B} = The magnetic flux density, Wb/m^2

However, to uniquely define a vector in a region, both the curl and the divergence of the vector should be specified. In the two dimensional field, \dot{A} has only a component in z direction, \dot{A}_z , so that:

$$\frac{\partial \dot{A}_z}{\partial z} = 0 \quad (2-6)$$

As a result for all of the field domain:

$$\nabla \cdot \dot{A} = 0 \quad (2-7)$$

So, the magnetic vector potential is uniquely defined. From now on, unless mentioned explicitly, the z component of this vector, \dot{A}_z , will be simply represented by \dot{A} .

Including the magnetic vector potential defined by (2-5) and (2-7) in Maxwell's equations (2-1) to (2-4) results in the general integro-differential equation of the two dimensional field, in terms of magnetic potential, \dot{A} :

$$\frac{\partial}{\partial x} \left(\nu \cdot \frac{\partial \dot{A}}{\partial x} \right) + \frac{\partial}{\partial y} \left(\nu \cdot \frac{\partial \dot{A}}{\partial y} \right) = -j + \sigma \frac{\partial \dot{A}}{\partial t} \quad (2-8)$$

where,

\dot{A} = The magnetic vector potential, Wb/m

j = The current density in the bar area, A/m^2

ν = reluctivity, m/H

σ = The electric conductivity, S/m

In general, except for very simple geometry of the model and boundaries, and also linear material properties, this equation can not be solved analytically to yield explicit values for the field parameters. Therefore, the field parameters should be evaluated by numerical techniques such as the finite element method.

Numerical methods are usually lengthy jobs on the computer. Therefore, features of the specific problems should be exploited whenever possible to simplify the formulation without sacrificing the accuracy of the solution.

In a general case, when the excitation currents and/or magnetic properties of the field medium are time-varying, then a *time stepping technique* (or a set of successive transient analyses) is carried out [53]. In this method, the solution time is divided into (usually) equal time intervals and during each time interval, the parameters are assumed to be invariant. The initial conditions for each time step are extracted from the previous step. If the magnetic

characteristics of the field medium are non-linear, a much longer solution time is expected since any individual time step should be iterated to find the most accurate solution.

In (2-8), the term $\sigma \frac{\partial \dot{A}}{\partial t}$ represents the eddy current induced in the conducting areas of the field due to the time-varying magnetic flux. When all of the excitation currents and also the magnetic material properties of the magnetic circuit are time independent, the solution is referred as *static analysis* [66]. In a static analysis, \dot{A} is also independent of time. Then, from (2-8) for a time invariant magnetic field:

$$\frac{\partial}{\partial x} \left(\mathbf{v} \cdot \frac{\partial \dot{A}}{\partial x} \right) + \frac{\partial}{\partial y} \left(\mathbf{v} \cdot \frac{\partial \dot{A}}{\partial y} \right) = -j \quad (2-9)$$

Depending on the magnetic characteristics of the field media, a static analysis may be linear or non-linear. The non-linearity of the solution is handled by iteration which considerably increases the computing time.

In a linear magnetic circuit, fed from sinusoidally time-varying excitation currents, all of the time varying parameters, including \dot{A} , vary sinusoidally with time at the steady state conditions¹. This fact simplifies the governing equation significantly so that (2-8) can be written as:

$$\frac{\partial}{\partial x} \left(\mathbf{v} \cdot \frac{\partial \dot{A}}{\partial x} \right) + \frac{\partial}{\partial y} \left(\mathbf{v} \cdot \frac{\partial \dot{A}}{\partial y} \right) = -J_0 + j\omega\sigma (\dot{A} - \dot{A}_0) \quad (2-10)$$

The new parameters in this equation are:

J_0 = The average or low frequency current density in the bar, A/m^2

\dot{A}_0 = The mean value of \dot{A} over the cross sectional area, Wb/m

ω = The angular frequency, rad/sec

j = imaginary unit equal to $\sqrt{-1}$

1. This should not be confused with the spatial distribution of the field which is related to the winding layout.

This type of spatial solution is called *harmonic analysis* method [40]. In this method complex variables are used to represent voltages, currents and field parameters so that the governing equations can be resolved into their real and imaginary components to be solved. Eddy currents induced in the conducting parts of a magnetic circuit due to the time-varying magnetic fields, redistribute the current patterns and modify the field. The outstanding feature of harmonic analysis its capability to consider this effect, so called *skin effect* or *deep bar effect* (see page 17). On the other hand, it is limited to a linear magnetic circuit with sinusoidally time-varying excitation currents. This method will be discussed in more detail later in this chapter.

In actual electromechanical or electromagnetic devices, which employ ferromagnetic materials in their magnetic circuits, the characteristics of iron are not linear. As a result, even when they are fed from sinusoidal voltage sources, the magnetic field parameters vary non-sinusoidally with time. Therefore, a time stepping finite element method [53] should be implemented to solve the associated field problems. In this method, the coefficients of the system equations are time dependent and they should be solved iteratively. As a result, this solution method occupies a large memory in the computer and uses a long computing time.

The application of the concept of effective reluctivity [45] converts the essentially non-linear magnetic circuit into a linear system for analysis so that both the magnetic field and the current density in the control region vary sinusoidally with time. This assumption allows the use of the harmonic analysis strategy [55]. In this feature, each non-linear element is replaced by a similar shape of element except its reluctivity, ν , is locally linear with the magnetic flux density, B . In fact, ν is the local effective reluctivity of the element and it is defined as a function of the local value of B . Loumi [45] compared the output results from the application of this method to the analysis results from the time stepping analysis of the same model and showed that the definitions of ν_{eff} , extracted by:

$$\nu_{eff} = \frac{1}{T} \int_0^T \nu(t) dt \quad (2-11)$$

provides the best agreement between two methods. However, because the values of magnetic flux density are not known before the solution, an iterating process is still necessary to find

the most accurate values of the locally linear reluctivities. Other limitations of this method along with an alternative method are given in section 7.1 on page 36.

2.2 Calculation of other parameters in terms of magnetic vector potential

Having the $\dot{A}(x, y)$ evaluated in the field of interest, the values of B_x and B_y can be calculated as follows:

$$B_x = \frac{\partial \dot{A}}{\partial y} \quad (2-12)$$

and

$$B_y = -\frac{\partial \dot{A}}{\partial x} \quad (2-13)$$

The current density in the conducting areas, such as the area of solid rotor bars in a cage rotor, is the combination of applied current and the induced eddy current in it. In a harmonic analysis, it is calculated from:

$$\dot{J} = -J_0 + j\omega\sigma (\dot{A} - \dot{A}_0) \quad (2-14)$$

The current density in the areas which are not subject to eddy currents remains equal to the externally applied level.

The inductances are calculated by looking at the stored energy in the region of interest and can be estimated from:

$$W = \frac{1}{2} \cdot Re \left(\int_S \dot{A} \cdot \dot{J}^* \cdot ds \right) \quad (2-15)$$

where, \dot{J}^* is the complex conjugate of the current density phasor, \dot{J}

3.0 DETERMINATION OF CURRENTS IN AN INDUCTION MOTOR

To carry out the magnetic analysis of an induction motor, the currents in the rotor and stator windings should be known. Usually the classic equivalent circuit of the motor is used to find

the values of the currents. In case the equivalent circuit parameters are not available, they should be measured, calculated or estimated by any available method. A method to estimate a set of equivalent circuit parameters before the motor is manufactured is discussed later in this chapter.

The classic equivalent circuit of the induction motor is shown in Fig. 2-1. In this figure, the

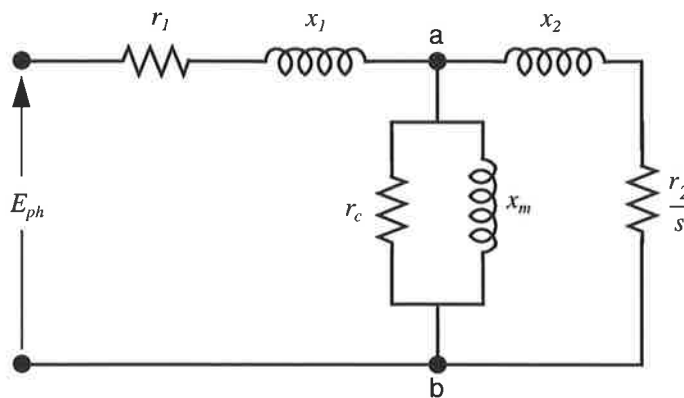


Fig. 2-1 Equivalent circuit of an induction motor

stator is represented by its ohmic resistance r_1 and leakage reactance x_1 . The rotor cage (or winding) is transferred to the primary and it is also represented by its equivalent ohmic resistance r'_2 and equivalent leakage reactance, x'_2 . Despite the restrictions of this circuit as explained in section 2.1 on page 169 (chapter 7), it is usually used for any status of the motor, including standstill, to estimate the fundamental components of rotor and stator currents.

In Fig. 2-1,

r_1 = the per phase resistance of stator winding,

x_1 = the per phase leakage reactance of stator winding,

r'_2 = the per phase resistance of the rotor winding transferred to stator side,

x'_2 = the per phase leakage of the rotor winding transferred to stator side,

x_m = the per phase mutual inductance between rotor and stator windings,

r_c = the per phase equivalent resistance representing the iron losses.

r'_2 and x'_2 are calculated as follows:

$$r'_2 = \frac{4(N_1 k_{w1})^2 q}{S_2} \cdot r_{2,eq} \quad (2-16)$$

$$x'_2 = \frac{4(N_1 k_{w1})^2 q}{S_2} x_{2,eq} \quad (2-17)$$

where:

N_1 = The number of turn per pole in the primary winding (stator)

k_{w1} = Winding factor of the primary winding

q = The number of phases

S_2 = The number of slots in the secondary (rotor)

$r_{2,eq}$ = The equivalent rotor resistance including the end-ring effect

$x_{2,eq}$ = The equivalent rotor reactance including the end-ring effect

All of the circuit parameters may be predicted from the geometry of the core laminations and the design data of the motor. A more accurate method for calculation of $r_{2,eq}$ and $x_{2,eq}$, taking the deep bar effect into account is described in following sections in this chapter. In Fig. 2-1, the magnetization current i_m is represented by the current in x_m . Also, the per phase iron losses, W_i , are equal to the losses in r_c . Since both i_m and W_i are non-linear functions of the applied voltage, then any set of values for equivalent circuit are valid only for a certain phase voltage.

A major problem associated with using the equivalent circuit at standstill is the effect of saturation on the values of x_1 and x'_2 . Although the non-linear feature of the magnetic circuit limits any major increase in the mean flux density, the flux path at both stator and rotor slot bridges may saturate as a result of high short circuit currents flowing in the windings. Therefore, x_1 and x'_2 do not remain linear any more. Since, in a two pole machine, the reactance of end windings dominates the stator reactance, the inclusion of saturation may affect the calculated stator current by not more than 5% while this figure may rise to more than 25% for a higher number of poles [73]. In an idealised machine the stator and rotor currents establish sinusoidally distributed mmf's in the air-gap when they are

excited individually or together. However, in an actual three phase induction motor, the distribution of stator mmf is not an actual sinusoidal. As a result, a set of $1 \pm 6n$ order harmonics are produced in the air-gap and consequently, additional reactances and resistances appear in the equivalent circuit to take the harmonic effects into account [1]. Fig. 2-2 shows the general form of equivalent circuit for a polyphase induction motor including the effect of space harmonics. In this figure, each block is similar to the basic equivalent circuit of the motor (for the fundamental harmonic) representing the reaction of the motor for any particular harmonic.

3.1 Current displacement in the solid bars or deep bar effect

The eddy currents in conducting areas cause the displacement of current in the area and consequently modify the magnetic field. This is more severe in the solid bars of the cage rotors, where the conductivity and the applied current are high. As a result, the distribution of current density in the rotor bars varies as a function of the geometry of the bar as well as frequency. This increases the effective resistance of the rotor and alters the motor characteristics. In addition, this effect along with the rotor bar temperature introduces a speed and temperature dependant short circuit current for the induction motor during a locked rotor test, or when a running motor stalls. Therefore, an accurate evaluation of motor current, taking these effects into account, may be used to improve[46] the reliability of the protection system.

To demonstrate why and how the current density in the bar varies with the frequency, a simply shaped rectangular bar embedded in a rectangular open slot in an iron core is examined. In Fig. 2-3a, the bar is divided into n equal segments, where n is large enough so that the current density in each segment can be assumed to be uniform. The segments are inter-connected in parallel via the end-rings at the connection area of each bar and the end-rings at either side. An equivalent circuit like Fig. 2-3b can be immediately constructed for the segments. In this circuit, the resistances of all of the segments are equal. However, the linkage flux of any segment is a function of the radial location (vertical direction in this figure) of the segment in the slot, increasing as the segment moves toward the bottom of the slot. As a result, the inductances of segments decrease monotonically for the segments 1 to n . If an alternating current i_{bar} is applied to the bar, the parallel paths will share the current

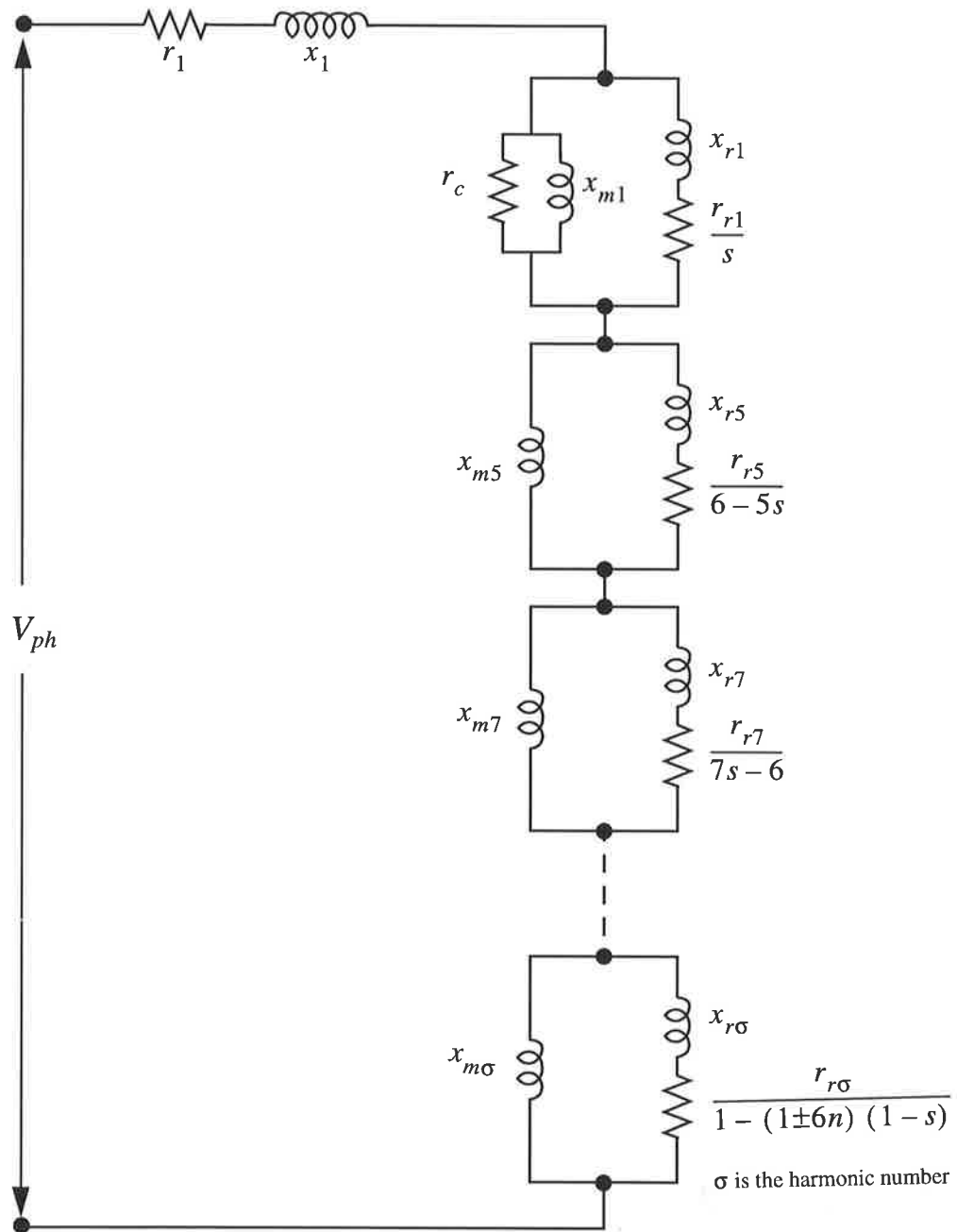


Fig. 2-2 The general form of equivalent circuit including the effect of space harmonics

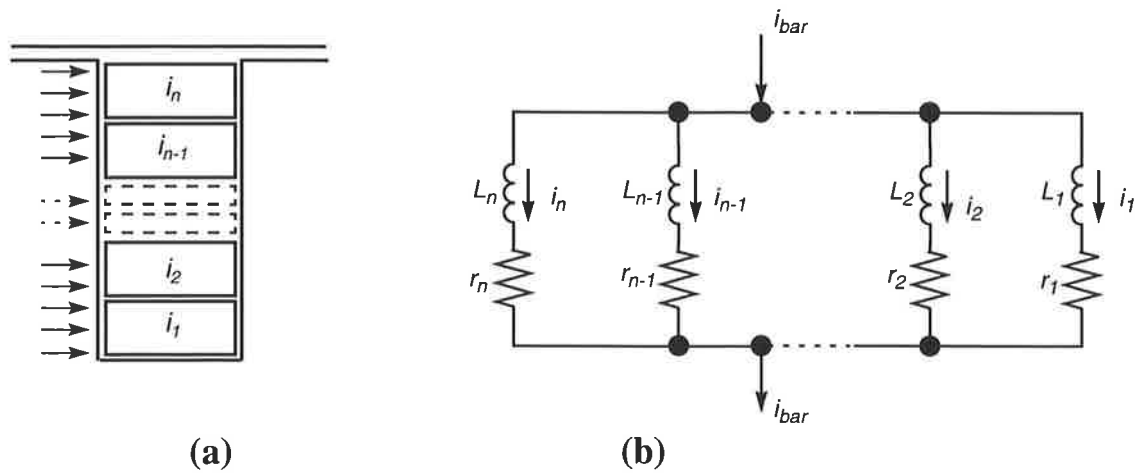


Fig. 2-3 (a) A rotor bar embedded in a slot (b) The preliminary equivalent circuit

unequally as a function of their location as well as the frequency. A steady state uniform current distribution in the bar may be expected only at zero frequency.

In this treatment, the reluctivity of the iron parts has been assumed to be negligible, however, there is no limitation for the shape of the slots in general. In addition, the size of the segments need not be equal. The inductance of individual segments in Fig. 2-3b includes both self-inductance of the segment and its mutual inductances with other segments. With some manipulations, the general form of the equivalent circuit can be simplified to have non-coupled inductances as shown in Fig. 2-4. In this figure:

L_0 = Inductance of the gap above the bar (if there is any gap)

l_1 to l_n = Inductance of individual segment disregarding any mutual inductances

r_1 to r_n = Resistance of individual segments

i_1 to i_n = The current flowing through segments 1 to segment n

A and B represent the bar terminals where they are connected to the end-rings in at each end.

This equivalent circuit is known as the “transmission line equivalent circuit of a rotor bar” because of its similarity to that of a transmission line. Details of the extraction of this circuit from the initial form of Fig. 2-3a along with its evaluation for three different slot profiles are published in a separate paper [24].

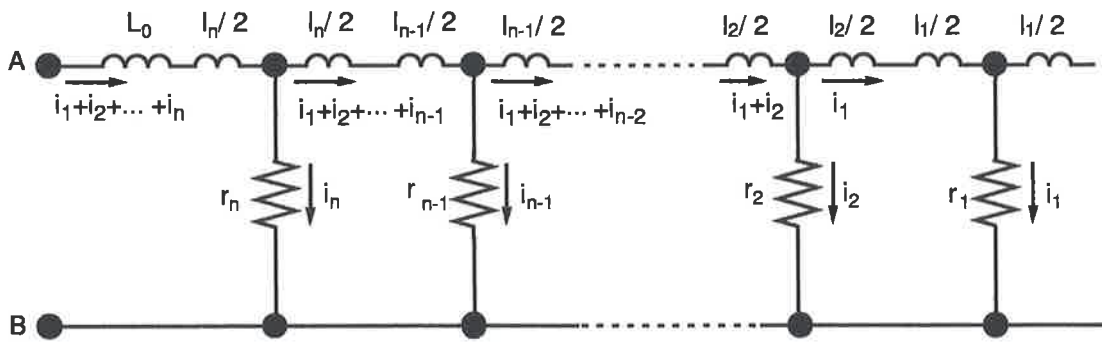


Fig. 2-4 The equivalent circuit of a rotor bar

The distribution of current density in a general form of rotor bar, can be calculated either from the finite element method using (2-14) or via a transmission line equivalent circuit [24,44]. The distribution of current density in a typical rotor bar is shown in Fig. 2-5.

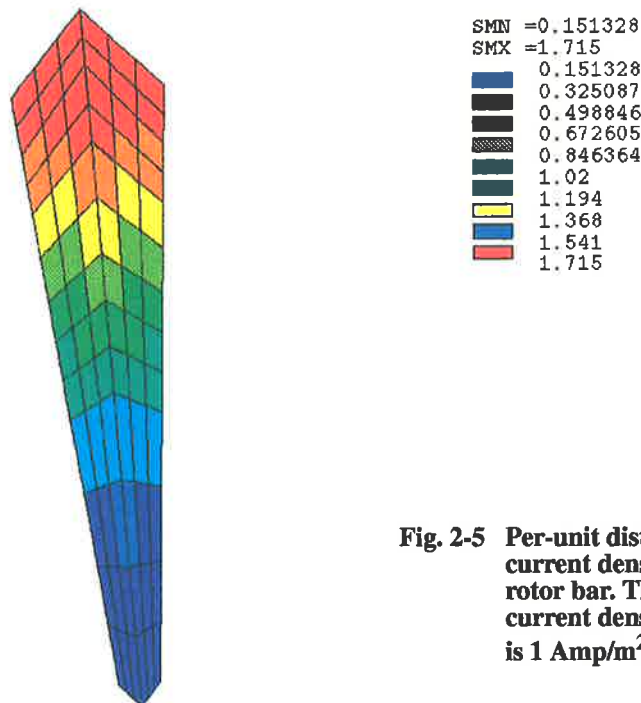


Fig. 2-5 Per-unit distribution of current density in a solid rotor bar. The applied current density on the bar is 1 Amp/m².

3.2 Effect of space harmonics on the rotor bar currents

The harmonic content of stator mmf is a function of the number of stator slots per pole as well as the winding parameters. In normal operating conditions, all of the rotor bars are equally influenced by the stator mmf; as a result all of the bars would have the same ohmic

losses. However, when the motor is at standstill, the rotor bars are fixed in certain positions so that each bar is affected by the local variation of the stator mmf. Consequently, the total rms current in a locked-rotor varies from bar to bar as a function of its mechanical position. This was first described by Oberretl [50] in 1980. He attributed this variation to the stator mmf harmonics and the effect of permeance harmonics. More recent papers by Williamson [78] justified it as an interaction between any pair of harmonic currents in each individual rotor bar.

In practice, any individual harmonic of the spatial magnetic field produces a set of sinusoidally distributed currents in the rotor bars with appropriate numbers of poles. Therefore, the total instantaneous current flowing in a particular rotor bar, which is the n th bar in a cage of N_b bars, can be written as [78]:

$$i_{nb}(t) = \sum_v I_v \cos\left(s_v \omega t - \frac{2\pi n v}{N_b} - \alpha_v\right) \quad (2-18)$$

while, the square of the current in the same, created by the interaction between any pair of the existing harmonics would be calculated as:

$$i_{nb}^2(t) = \sum_{\mu} \sum_v I_{\mu} I_v \cos\left(s_{\mu} \omega t - \frac{2\pi n \mu}{N_b} - \alpha_{\mu}\right) \cdot \cos\left(s_v \omega t - \frac{2\pi n v}{N_b} - \alpha_v\right) \quad (2-19)$$

The time average of $i_{nb}^2(t)$ at standstill, where $s_{\mu} = s_v = 1$ becomes:

$$I_{nb}^2 = \sum_{\mu} \sum_v I_{\mu} I_v \cos\left(\frac{2\pi n}{N_b} (v - \mu) + (\alpha_v - \alpha_{\mu})\right) \quad (2-20)$$

In (2-18) to (2-20):

I_{nb} = total rms value of current in rotor bar number n ,

I_{μ} = rms value of μ th harmonic bar current,

I_v = rms value of v th harmonic bar current,

v and μ = harmonic pole-pair numbers,

α_v and α_{μ} = phase angle related to harmonics v and μ respectively,

s_v and s_{μ} = slip related to harmonics v and μ respectively.

As can be found from (2-19), the rms value of the currents in any rotor bar varies as a function of its mechanical position and motor speed. The variation of the rms bar currents becomes maximum at standstill, equal to I_{nb} in (2-20).

In an irregular motor, such as pole changing motors where the even distribution of the stator winding is compromised to accommodate the pole changing facilities, the harmonic content of the stator mmf is very high. As a result, a wide variation in the rotor bar current is expected [73, 78]. However, it was shown that [84] the variation margin may reduce to $\pm 10\%$ in a standard single speed motor.

Table 2-1 shows the variation of currents and their phase angles in the rotor bars of a 15kW induction motor (used as model one in this project), extracted from (2-18), when bar number one is located at zero position. In this table, the actual phase angles of the bar currents along with the expected phase angles in a harmonic free field distribution, when only the fundamental harmonic is present, is also tabulated. The squared values of currents, I_{nb}^2 , in Table 2-1 are calculated from (2-20) for the same conditions. In this table, it is assumed that the peak value of total air-gap mmf induces a current with an amplitude of 1PU in each rotor bar. More details about the effect of spatial harmonic are described in section 3.3.1 in chapter 5.

Table 2-1 The variation of current and squared current in the rotor bars.

Bar number	I_{nb}^2 P. U.	Rotor bar current			
		$ I_{bar} $ P. U.	Phase Angle [Degrees]	Expected Phase Angle [Degrees]	Difference [Degrees]
1	1.0683	1.1120	0	0	0
2	0.8524	0.8971	24.7806	25.7143	0.9337
3	0.8215	0.8619	52.1555	51.4286	-0.7269
4	0.9436	0.9936	76.0255	77.1429	1.1174
5	0.9436	0.9936	103.9745	102.8571	-1.1174
6	0.8215	0.8619	127.8445	128.5714	0.7269
7	0.8524	0.8971	155.2194	154.2857	-0.9337
8	1.0683	1.1120	180.0000	180.0000	0

In this work, like some other researchers [81,82], the magnetic analysis will be carried out with applying just the fundamental harmonic loading of the rotor bars and the distribution of iron losses and also current distribution in each bar will be extracted for this conditions.

However, the effect of non-equal losses in the rotor bars will be included in the thermal analysis. Some other points in the loading of the rotor is discussed in section 7.2 in this chapter.

4.0 FIELD ANALYSIS OF INDUCTION MOTORS

The magnetic circuit of an induction motor is too complicated to be analysed by simple and explicit methods without with a gross simplification which may lead to erroneous results. This arises from its complex geometry and non-linear magnetic materials in its magnetic circuit. The problem is more severe at standstill since the rotor and stator currents are several times larger than their normal level; this forces some parts of the magnetic circuit to be highly saturated. Therefore, when an induction motor at standstill is supplied by a set of sinusoidal voltages as usual, neither the currents nor the flux density in the field will vary sinusoidally with time. In addition, the distribution of current in individual bars are differently affected according to the saturating level of the adjacent teeth.

In practice, variation of the electric and magnetic parameters in the axial direction is quite small. This allows a two dimensional modelling of the magnetic circuit where a significant simplification can be achieved. However, the effects of skewing in the rotor slots, the end turns of the stator winding and also the effect of end rings in the rotor cage (or the rotor end turns in a wound rotor), may not be accurately included in such model. On the other hand, this simplification allows a finer meshing of the finite element model where a more accurate solution may be achieved along with considerable saving in the computer resources. In brief, at present, despite a vast improvement in computing facilities and tools, full three-dimensional magnetic modelling of induction motors, except for special purposes [76], is uneconomic; two-dimensional models can still be improved to access higher accuracy [59]. In this case, the axial length of the motor is assumed to be infinity and only a radial cross section of the motor, as a representative of unit length of the motor, is modelled. The skewing effects of the rotor bars, and also the effects of the end windings, are taken into account by the aid of some classic and/or empirical formulas.

Usually, a two dimensional finite element analysis allows modelling of 2 poles of a motor with any number of poles. In case the number of rotor slots is not a multiple of pole pairs number, the rotor can be substituted by a modified equivalent rotor with a suitable number of

slots (see appendix A for more details). This saves considerable computing facilities and time, in particular when the number of pole-pairs is large¹. By taking advantage of peripheral periodic boundaries in the motor, the size of the model can be still reduced to only one pole, or even a smaller fraction of the motor.

One pole pitch from a four-pole induction motor is shown in Fig. 2-6. If only the

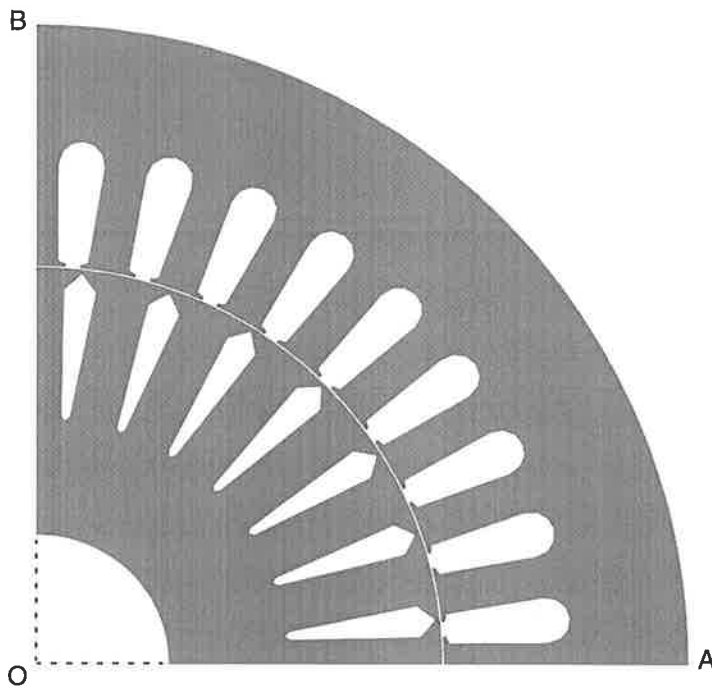


Fig. 2-6 Two dimensional magnetic circuit of a typical four pole induction motor

fundamental component of the magnetic field is considered, the magnetic potential in any point on the boundary OA in this figure is related to that of boundary OB as:

$$\dot{A}_{OA}(r, 0) = -\dot{A}_{OB}\left(r, \frac{\pi}{2}\right) \quad (2-21)$$

where the angle is measured in mechanical radians. Therefore, by applying the constraint condition of equation (2-21) on the corresponding nodes in the above boundaries, only one pole pitch of the motor can be analysed as representative of the entire motor. However, the results should be modified to include the effect of higher order space harmonics. The meshing layout for one pole from a 15kW four-pole induction motor (used as model one) is shown in Fig. 5-1.

1. According to Dymond [19] the increase in the computation time for the construction of a full 2-D model does not significantly add to the cost.

Williamson and Robinson [59, 82] applied a more limited periodicity on the calculation. They used a hybrid model including only one rotor slot pitch along with one stator phase band. Although this technique minimises the size of the model, the real parts and the imaginary parts of the equations however are not separable which adds to the calculation time. In addition, it does not allow inclusion of the effect of some of the space harmonics. For example, if a 60° phase belt is modelled, the counterpart of (2-21) for this boundary becomes:

$$\dot{A}_{OA}(r, \theta) = \dot{A}_{OB}\left(r, \theta + \frac{\pi}{3}\right) \quad (2-22)$$

In (2-22), angles are measured in electrical radians. This requirement contradicts with that of harmonics of order $6n - 1$ since they require a -60° periodicity on the same boundaries.

5.0 CALCULATION OF THE TERMINAL PARAMETERS OF THE STATOR AND THE ROTOR

The terminal parameters of the stator and the rotor are the per phase resistances and reactances of the stator and rotor respectively, including the effects of end-winding in the stator and the end-rings in the rotor cage. Each slot pitch of the rotor cage may be referred as an individual phase in the cage. Different components of the leakage reactances in a motor are as following [1]:

- (a) the primary slot reactance;
- (b) the secondary slot reactance;
- (c) the zigzag leakage reactance;
- (d) the reactance due to skew;
- (e) the belt-leakage reactance;
- (f) the coil end leakage reactance;
- (g) the incremental reactance;
- (h) The peripheral leakage reactance.

The component (g) is produced at full speed due to re-distribution of the rotor bar current; and is absent at standstill. Some classical and/or empirical formulas are available to calculate each component. However, by implementing the finite element method, the total magnitude of the reactance will be calculated by looking at the stored energy in the magnetic field. To

find the reactance of the stator and the rotor separately, each winding is excited individually and the reactances are extracted by post-processing on the results.

5.1 Calculation of the stator parameters

Stator parameters include the winding resistance and different components of reactance as calculated below.

5.1.1 Stator winding resistance

The current density in the cross section of a multi-turn stator winding can be assumed to be uniform. Therefore, having the physical properties of the conductor, along with the total length of the phase winding and the configuration of internal phase band connections, the per phase resistance for any pre-assumed temperature can be calculated from:

$$R_1 = \frac{N_{ph} L_{mean}}{\sigma m a} \quad (2-23)$$

where:

L_{mean} = the mean length of turns in the stator winding,

m = number of parallel paths in the winding,

a = cross sectional area of each individual conductor.

In practice, having the core geometry, the mean length of turns in the winding can be estimated for any designed winding layout.

5.1.2 Stator winding inductances

The stator leakage inductance is calculated from the difference between the total inductance of the stator, L_{tot} , and the inductance due to the fundamental flux density distribution in the air-gap, L_m , as in (2-24).

$$L_{1, leak} = L_{tot} - L_m \quad (2-24)$$

After the magnetic field is solved by only stator loading, the total energy in the field is calculated by (2-15). L_{tot} is related to the total energy by:

$$W_{tot} = q \cdot \left(\frac{1}{2} L_{tot} \cdot I_{ph}^2 \right) \quad (2-25)$$

where q and I_{ph} are the number of phases and the phase current respectively. Combining (2-15) and (2-25) for a three phase motor:

$$L_{tot} = \frac{1}{3I_{ph}^2} \cdot Re \left(\int_S \dot{A} \cdot \dot{J}^* \cdot ds \right) \quad (2-26)$$

In the case of the stator winding, \dot{J} is uniform in any individual slot area and it is obtained from:

$$j = \frac{\text{Total current in the slot}}{\text{Total area occupied by the winding}} \quad (2-27)$$

From the classic equivalent circuit of induction motor, Fig. 2-1:

$$\omega L_m I_{ph} = E_{ph} \quad (2-28)$$

where E_{ph} is the emf in the winding induced by the fundamental component of air-gap flux density, B_p , as in:

$$E_{ph} = \frac{(N_{ph} k_w) B_p \omega l d}{p} \quad (2-29)$$

From (2-28) and (2-29):

$$L_m = \frac{(N_{ph} k_w) l d}{p} \cdot \frac{B_p}{I_{ph}} \quad (2-30)$$

After the solution of the magnetic field, the components of the air-gap flux density are calculated from (2-12) and (2-13). Then, B_p is extracted by Fourier integration. Because of the nature of the two-dimensional modelling, both L_{tot} and L_m are calculated disregarding

the effect of the end winding. Therefore, it should be estimated separately and combined with $L_{1, leak}$ in (2-24) to give the total leakage reactance.

The general “diamond-shaped” pattern of stator end windings, together with the varying configurations of the end-rings of cage rotors, generates a complex leakage flux pattern in both ends of the motor. Normally, the field is too complex to be analysed implicitly unless some simplification is done.

Alger [1], assumed that all of the end leakage flux lines flow in the radial direction at the ends of the iron core. As a result, removal of the iron core and joining of two end-planes of the core, does not alter the flux pattern in the end winding regions. On this basis, he calculated the total end winding leakage inductance of the motor as:

$$x_e = \frac{7fqN_{ph}^2 \sqrt{D_1 D_2}}{p^2 \cdot 10^6} (pu_{sp} - 0.3) \quad \Omega/phase \quad (2-31)$$

In (2-31), D_1 and D_2 are the effective diameters of the stator and rotor end windings and pu_{sp} is the per-unit short pitching of the stator winding.

The rotor and the stator windings share the above inductance equally.

5.2 Calculation of the rotor parameters

A typical rotor slot along with the rotor end-rings is shown in Fig. 2-7. It can be considered to be a series of full pitch turns formed by pairs of conductor bars apart by a pole-pitch, joined together in a closed loop by the end conductors. If only the fundamental flux distribution exists in the air-gap, the induced emf's in the bars can be assumed to be sinusoidal. Fig. 2-7-b shows how the end rings carry the summation of the bar currents. Therefore, it affects the effective resistance of individual turns and alters the waveform of the currents. In general, this effect is small [65] and the currents in the bars, and consequently in the end-rings, can be assumed to retain sinusoidal distribution.

The currents in the successive rotor bars are out of phase by δ as:

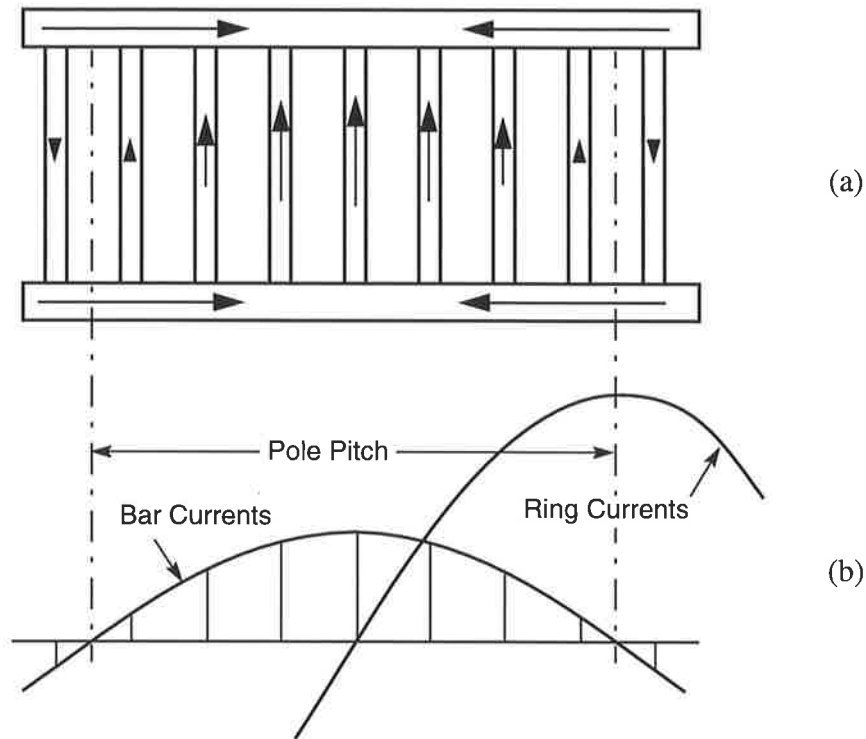


Fig. 2-7 Distribution of current in a cage rotor.

$$\delta = \frac{2\pi p}{S_2} \quad (2-32)$$

In (2-32), S_2 is the number of rotor slots. Calculations show [72] that the total resistance and reactance of a cage rotor per slot pitch are:

$$r_{b,eq} = r_b + \frac{r_c}{2 \left(\sin \frac{\delta}{2} \right)^2} \quad (2-33)$$

$$x_{b,eq} = x_b + \frac{x_c}{2 \left(\sin \frac{\delta}{2} \right)^2} \quad (2-34)$$

where:

$r_{b,eq}$ = equivalent resistance of a bar in a cage rotor allowing end-ring effects,

$x_{b, eq}$ = equivalent reactance of a bar in a cage rotor allowing end-ring effects,

r_b = resistance of a bar alone,

x_b = reactance of a bar alone,

r_c = resistance of one ring segment between two adjacent bars,

x_c = reactance of one ring segment between two adjacent bars,

Therefore, the calculation of rotor parameters can be split into the individual calculation/estimation of bar and end-ring parameters.

5.2.1 Calculation of r_b

Because the current displacement in the rotor bars is a function of frequency, calculation of the rotor resistance is less straightforward compared to the case of stator.

The effective resistance of a rotor bar is defined as:

$$R_{effective} = \frac{\text{Total ohmic losses in the bar}}{(\text{Total rms current in the bar})^2} \quad (2-35)$$

The ohmic losses per unit length of the bar is calculated from:

$$P_{ohmic} = \int_A \frac{J_z^2(x, y)}{\sigma} da \quad (2-36)$$

where, $J_z(x, y)$ is the distribution of current density in the rotor bar. This parameter can be calculated either by construction of the transmission line equivalent circuit of the bar or by implementation of finite element method (see section 3.1 on page 17). Because the magnetic field will be solved by the finite element method, and the field parameters will be available for the slot area as a matter of the course, the finite element method will therefore be used to estimate the inductance and the effective resistance of the bar.

In a two-dimensional finite element model, the ohmic loss density per unit axial length in the conducting area can be calculated from:

$$dP_{ohmic} = \frac{|J_{z,e}(x,y)|^2}{\sigma} da_e \quad (2-37)$$

where,

$|J_{z,e}(x,y)|$ = current density in the element in position (x,y)

da_e = area of the element.

$|J_{z,e}(x,y)|$ in any element can be obtained from (2-14). The counterpart of (2-35) in a finite element formulation results in:

$$R_{eff,bar} = \frac{1}{\sigma(I_{bar})^2} \sum_1^n |J_{z,e}(x,y)|^2 \cdot \Delta a_{e,i} \quad (2-38)$$

In (2-38), $\Delta a_{e,i}$ is the area of element number i and n is the total number of elements in the bar area.

5.2.2 Calculation of r_c

The current density in the end-rings is assumed to be uniform. This can be attributed to the negligible variation of the magnetic reluctance along different paths of the end-ring leakage flux. As a result, the total resistance of the end rings per slot pitch is:

$$r_c = 2 \cdot \frac{l_{mean}}{\sigma \cdot t \cdot a_{mean} \cdot Z_r} \quad (2-39)$$

where,

l_{mean} = The mean length of any end ring

a_{mean} = The mean area of end ring

5.2.3 Calculation of x_b

Similar to the rotor resistance, the rotor bar inductance can be calculated either by construction of a transmission line equivalent circuit or the finite element method. Again, because all of the field parameters are already present after field analysis, the finite element method is employed for this purpose.

Like the case of the stator, the leakage inductance of the rotor bar is estimated by looking at the stored energy in the magnetic field when all of the bars are excited with their normal current distribution as follows:

$$L_{b, leak} = L_{b, tot} - L_{b, m} \quad (2-40)$$

and

$$W_{tot} = Z_r \left(\frac{1}{2} L_{b, tot} \cdot I_b^2 \right) \quad (2-41)$$

Combining (2-40) and (2-41):

$$x_{b, tot} = \frac{\omega}{Z_r \cdot I_b^2} \cdot \int_S (\dot{A} \cdot j^*) ds \quad (2-42)$$

$L_{b, m}$ is obtained from:

$$\begin{aligned} \omega L_{b, m} \cdot I_b &= E_b \\ &= \frac{\omega B_p l d}{p} \end{aligned} \quad (2-43)$$

then,

$$x_{b, m} = \frac{\omega l d}{p} \cdot \frac{B_p}{I_b} \quad (2-44)$$

5.2.4 Calculation of x_r

As mentioned in section 5.1.2 (page 26), rotor and stator share the end-winding reactance of (2-31) equally.

6.0 ESTIMATION OF LOSS DENSITY

Losses in an induction motor are distributed almost all over the body. Only two components of general losses in an induction motor are present at stand-still; iron losses and ohmic losses. Unfortunately, there is still no explicit method for the estimation of iron losses distribution all over the core; therefore, it should be extracted analytically. The problem becomes more

complicated in the non-sinusoidal magnetic fields as described by Zhu [86]. Gilbert [28] proposed a practical method to determine the pattern of the distribution of iron losses in a previously constructed motor by using the thermal response of the motor to a unit function applied load. His method is involved in the measurement of the time variation of temperature at some specific points in the motor.

6.1 Estimation of iron loss distribution

Iron losses are non-linear functions of frequency and the local amplitude of the magnetic flux density, B_{peak} . In a two-dimensional model they can be described by:

$$dW_i(x, y) = f(B_{peak}(x, y), f) \quad (2-45)$$

where:

$dW_i(x, y)$ = local iron losses

$B_{peak}(x, y)$ = peak value of local flux density

f = frequency

In a harmonic field analysis, the parameters are calculated as a set of x and y components of their real and imaginary parts. Therefore, $B_{peak}(x, y)$ can be obtained from:

$$B_{peak}(x, y) = \sqrt{B_{x,r}^2 + B_{y,r}^2 + B_{x,i}^2 + B_{y,i}^2} \quad (2-46)$$

In (2-46):

$B_{x,r}$ = The peak value of x component of real part

$B_{y,r}$ = The peak value of y component of real part

$B_{x,i}$ = The peak value of x component of imaginary part

$B_{y,i}$ = The peak value of y component of imaginary part

All of the mentioned components of B are calculated from (2-12) and (2-13) individually.

6.2 Estimation of ohmic loss distribution

In stator winding area. The ohmic losses in the stator slot areas and the end ring cross section can be assumed to be individually uniform. The loss density in all areas of the stator slots occupied by stator windings is calculated by:

$$q'''_{sslot} = \frac{\left(\frac{2qN_{ph}}{Z_s} \cdot \frac{I_{ph}^2}{m^2} \cdot \frac{1}{\sigma a} \right)}{A_{sslot}} \quad (2-47)$$

In (2-47), N_{ph} and I_{ph} are the number of series turns per phase and the phase current respectively. Other parameters in (2-47) are as follows:

- q''' = the loss density in the stator slot area, [W/m^3]
- q = the number of phases
- σ = the conductivity of stator winding
- a = the cross sectional area of stator conductors
- m = the number of conductors in parallel in the stator winding.
- A_{sslot} = the apparent area of stator slots.

The average loss density in the stator end ring area is extracted from (2-47) by looking at the winding layout and the apparent cross section of the end windings.

In rotor cage. The ohmic losses in the rotor bar area are calculated from (2-36). The ohmic loss density in the rotor end ring areas is assumed to be uniform and is calculated by looking at the ratio of the bar resistance and the equivalent resistance of the end rings in (2-33).

7.0 MAGNETIC ANALYSIS OF INDUCTION MOTOR

Since the effect of current displacement in the rotor bars is very significant in deep bar cage rotors, a harmonic finite element analysis is preferred in this project. The procedure of the magnetic field analysis is shown as a flow-chart in Fig. 2-8. As can be seen, a set of the stator and rotor currents are required to initialise the analysis. Therefore, if the equivalent circuit parameters of the motor are known, then only block one, a non-linear solution of the field, should be executed. Otherwise, the parameters should be estimated by iteration. The details

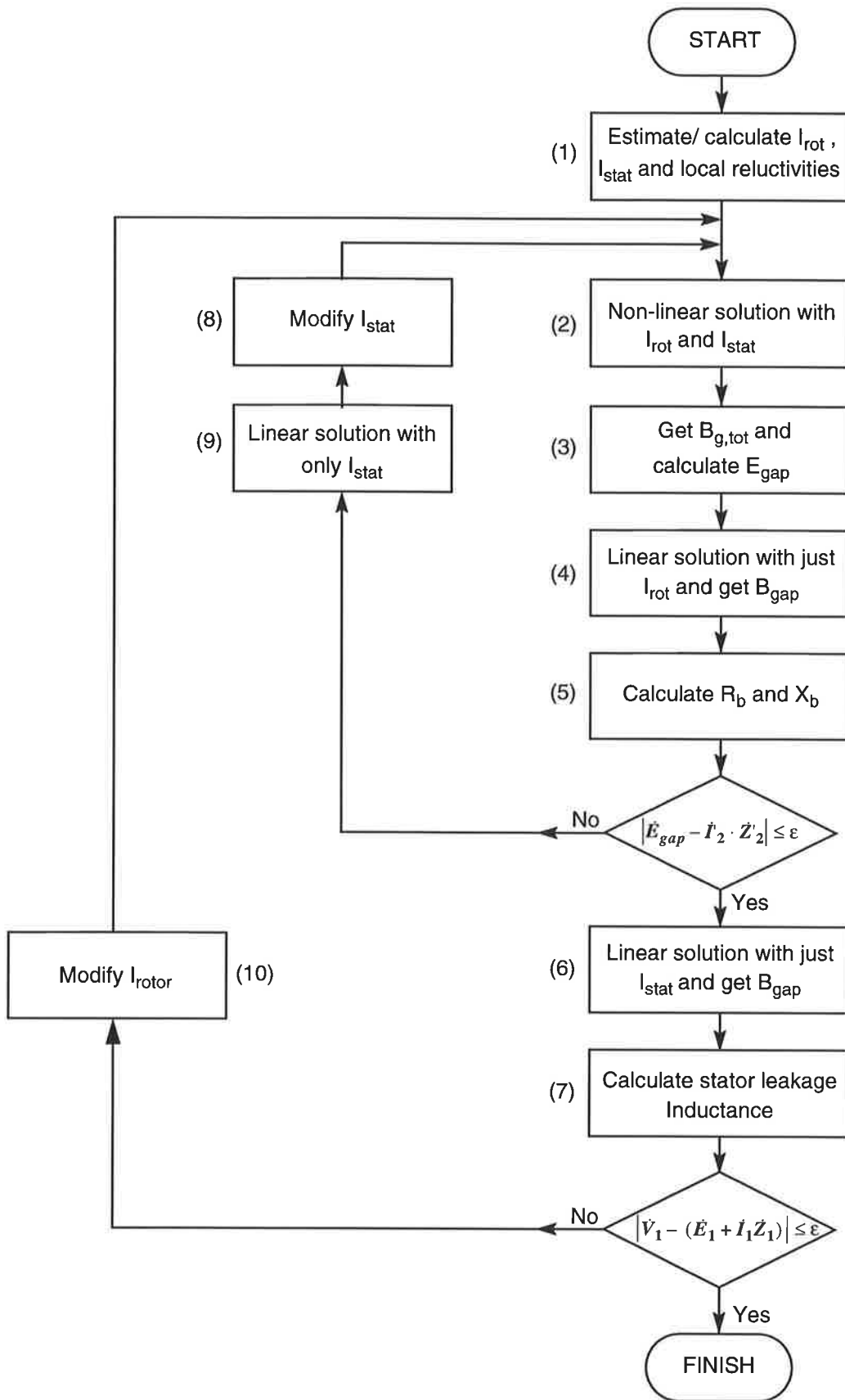


Fig. 2-8 Flow chart of the magnetic analysis by effective reluctivity method

of block (2) in Fig. 2-8 are shown in Fig. 2-9. In this figure, K_{acc} is the acceleration factor which is defined later in (2-51).

7.1 Solution procedure

The iteration starts with a set of estimated values of local reluctivities to be applied as the initial data. Then the appropriate values of currents are applied to the model and a non-linear solution is carried out (see Fig. 2-8). To check the accuracy of the estimation, the reluctivities of the elements are frozen at their last values in the non-linear solution and a linear solution is carried out while only the rotor currents are present in the model. As a criterion of convergence, the generated emf, calculated via the air-gap flux density, is compared to the voltage drop in the rotor impedance which is calculated in the last linear solution. In case the solution does not converge in the first iteration, all of the equivalent circuit parameters are updated and the process is repeated.

The $B_p(H)$ and also $VA(B_p)$ characteristics of the iron core are provided by the supplier of the iron core. There are two possible methods to obtain the $v(B_p)$ characteristics. The first choice would be the direct application of (2-11) on the $B_p(H)$ characteristics which was not used in this project. The second method of definition for $v(B_p)$ characteristics, which was successfully employed by Williamson and Robinson [80, 82], is extracted from the $P_a(B_p)$ characteristics of iron at $f = 50$ Hz and by using the equation:

$$P_a = \frac{\pi f B_p H_p}{\rho_c} \quad VA/Kg \quad (2-48)$$

where

$$\rho_c = \text{Density of iron, } Kg/m^3$$

$$P_a = \text{The apparent power per kilogram, } VA/Kg .$$

Since:

$$v = \frac{H_p}{B_p} \quad (2-49)$$

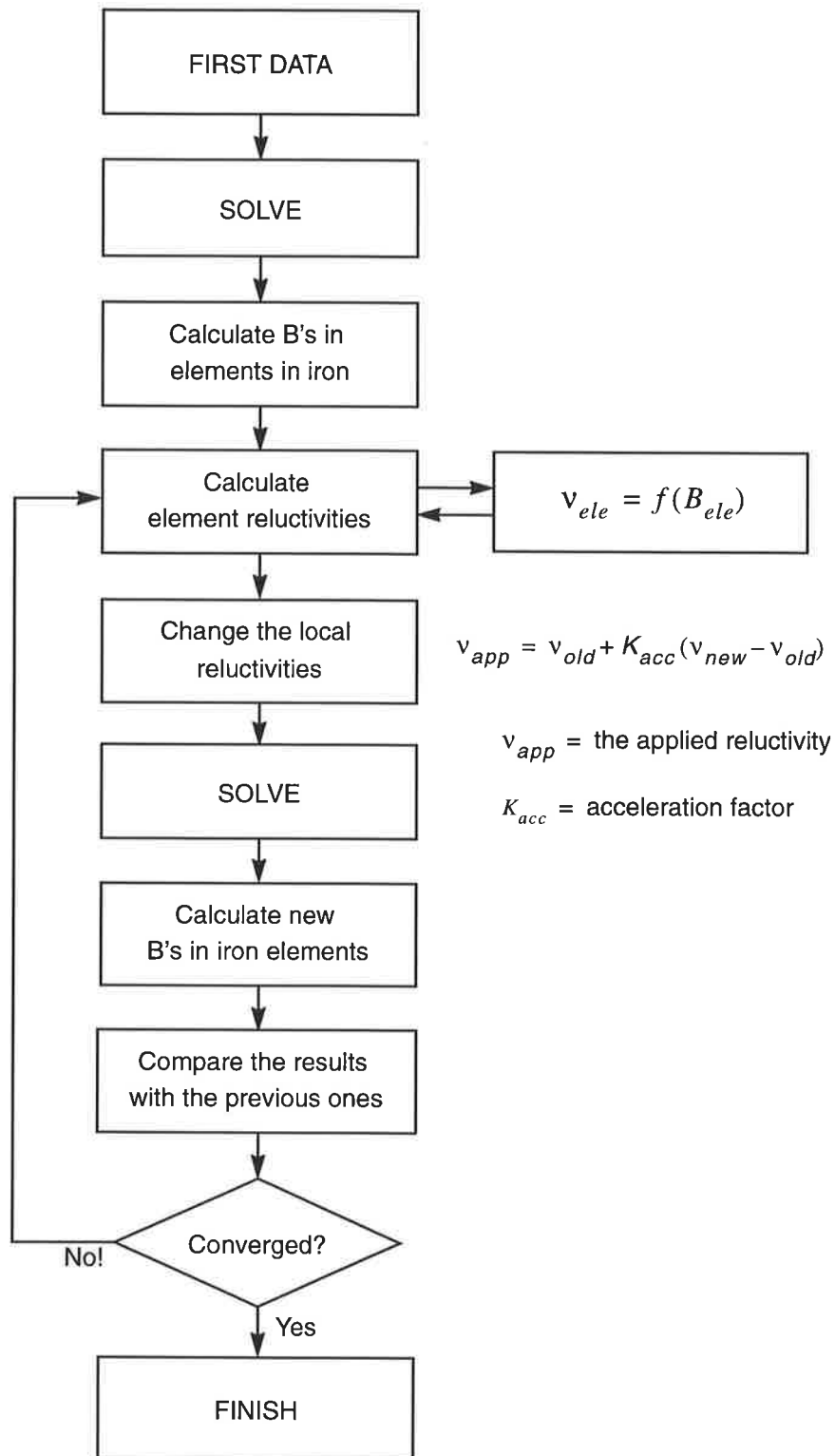


Fig. 2-9 The procedure of a non-linear harmonic analysis by using the effective reluctivity method

Then, having the $P_a(B_p)$, $v(B_p)$ can be extracted from (2-48) and (2-49) as:

$$v(B_p) = \frac{\rho_c}{\pi f} \cdot \frac{P_a}{B_p^2} \quad (2-50)$$

A successful Newton-Raphson iteration method depends on a well behaved $v(B_p)$ characteristic of the magnetic materials. Otherwise, the solution either may not converge or take significantly longer time (as a result of more iterations) to reach the specific error. Well behaved characteristics have a positive gradient of reluctivity against B_p ; in other words, is monotonically increasing with B_p . Having enough data points on the $v(B_p)$ characteristics, extracted from (2-50), cubic curve fitting is used to provide the desired characteristics. Fig. 2-10 and Fig. 2-11 show different forms of the extracted magnetic characteristics.

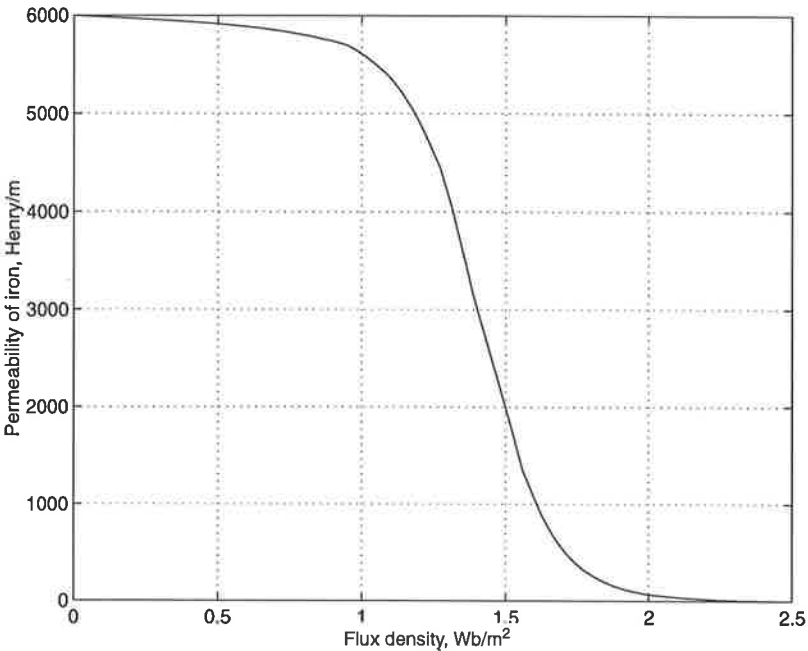
The effective reluctivity method was successfully used by some authors [52, 59, 80] in the magnetic analysis of the induction motors at normally running conditions. The main problem with this technique appears in the analysis of a motor at stall, when the excitation currents are high enough to extremely saturate the magnetic field. In this case, any high flux density at any element increases its local reluctivity to a value of equal, or very close to that of air during the interpolation. Consequently, the next iteration results in a poor flux density at the same element. So, the solution proceeds with a wide fluctuation in the estimation of reluctivities/flux densities at each element during any two consecutive iterations. This not only adds the number of iteration dramatically, in many cases the solution does not converge at all. Sometimes, application of an *acceleration factor* (or *weighting factor* [52]), limits the amplitude of oscillation to reach a converged (or earlier converged) solution. The *acceleration factor* is defined as:

$$K_{acc} = \frac{v_{app} - v_{old}}{v_{new} - v_{old}} \quad (2-51)$$

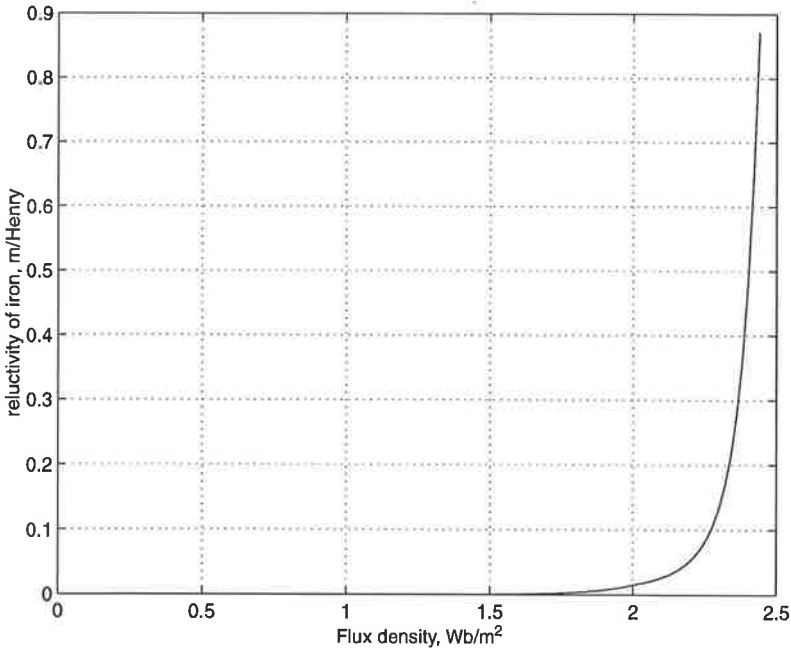
where:

K_{acc} = acceleration factor

v_{app} = applied reluctivity

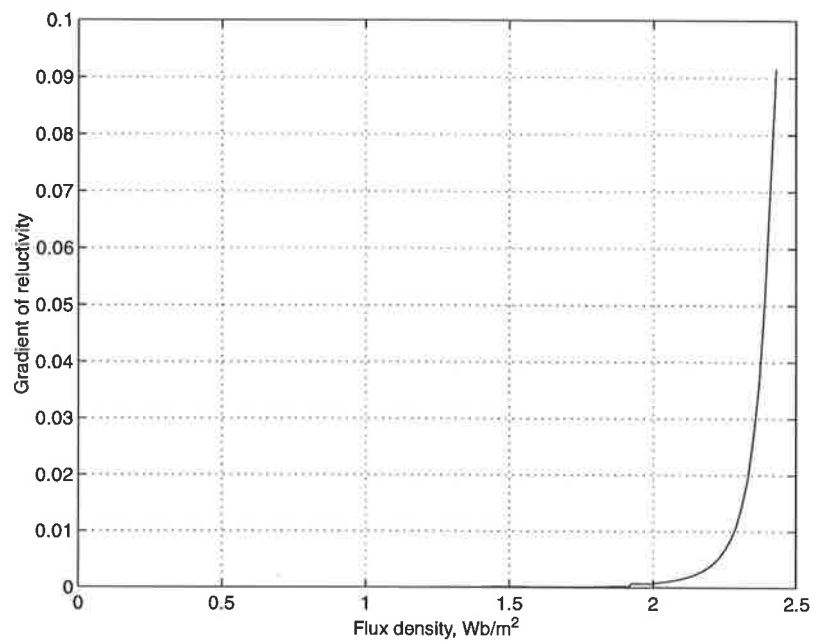


(a)

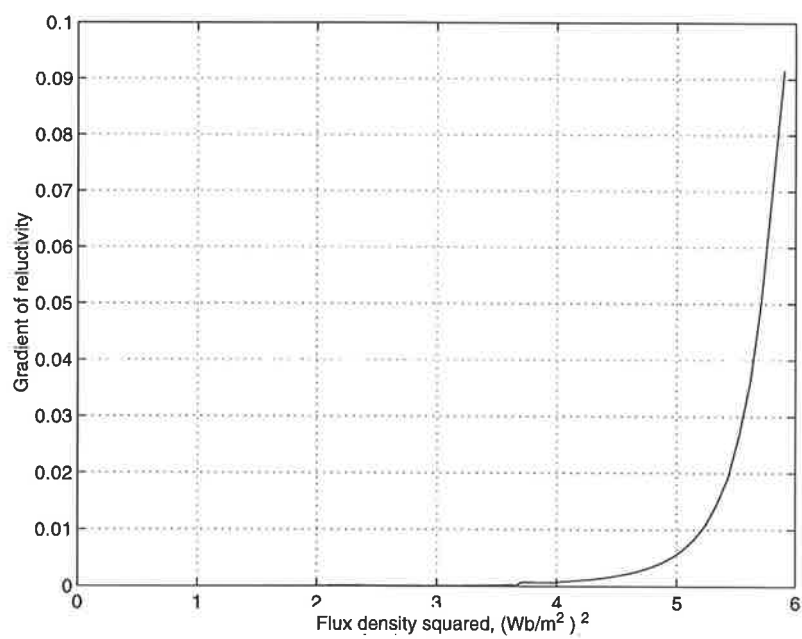


(b)

Fig. 2-10 Variation of permeability and relativity of iron core as functions of flux density.



(a)



(b)

Fig. 2-11 Variation of gradient of the relativity of iron core as a function of (a): flux density, (b) flux density squared.

v_{old} = the previous reluctivity

v_{new} = the interpolated reluctivity according to the new B_p

Alternatively, in order to pilot the solution toward convergence, the load may be applied in some equal (or unequal) sub-steps. In this case, the total procedure shown in Fig. 2-8 is started with a certain fraction the actual currents at the first sub-step with a pre-assumed estimated values of local reluctivities and a solution is carried out. Then the calculated set of element reluctivities from a converged solution for this sub-step is used as the initial values for the next sub-step with increased applied currents. This process is continued adequate times to achieve the solution when the full currents are applied on the windings.

In both cases, using acceleration factor or subdividing the solution into sub-steps, there is still some risk of deviation from the actual solution even in successfully converged solutions. This may happen as a result of several changes in the local reluctivities of the magnetic circuit after any successful iteration; this is similar to some changes in the model in any step.

Some other disadvantages of the effective reluctivity method may be concluded as follows:

- (a) The permeability of each element is related to its peak flux density in a time cycle whence there is a tendency for overestimation of the magnetic saturation [53],
- (b) The $B-H$ characteristics of iron are usually supplied by the manufacturers with a certain accuracy; so, the extraction of a new $v_{eff}(B_{peak})$ characteristic from the existing $B-H$ characteristics may be associated with a new component of error,
- (c) The new set of the elemental effective reluctivities for the next iteration are extracted from $v_{eff}(B_{peak})$ characteristic by interpolation. Therefore, the values of B_{peak} should be calculated in each iteration. Since the system equations are solved in terms of magnetic potentials, the calculation of B_{peak} as an intermediate parameter at each step adds significantly to the computation time.

The lengthiness and also the mentioned problems in using the effective reluctivity method encouraged the author to find an alternative method to shorten the computation time where a combination of normal harmonic analysis and non-linear static analysis was successfully

employed as an alternative method to solve a non-linear magnetic circuit with sinusoidally time-varying excitation currents. The new method also weakens the risk of false solution as a result of substituted local reluctivities. However, it became available for the magnetic analysis of model 2 only.

The procedure of this method is shown in Fig. 2-9. The distribution of the current density is estimated from a preliminary harmonic analysis of the model with an estimated permeability of iron parts. Then a non-linear static analysis is performed with the distributed current density, extracted from the previous harmonic analysis. The local flux densities are interpolated in $v(B_p)$ to calculate the local reluctivities. Then, they are used in the main harmonic analysis of the model. It is the author's experience that the new method converges in far less iteration steps and saves a large amount of computing facilities. The details of this method is published in a separate paper [22].

7.2 Application of stator and rotor currents

In an actual motor or its equivalent circuit, the application of voltage on the terminals of the armature winding automatically establishes the actual distribution of currents in different windings of the motor. However, in a finite element model the winding areas on the rotor one hand and the similar area on the stator on the other hand are not inter-connected virtually. Needless to say there is no actual or virtual magnetic linkage between the stator and rotor windings. Therefore, the distribution of current in the stator and rotor slot areas should be calculated/estimated separately. The winding configuration and the relative position of the stator and the rotor (for a locked rotor) should be taken into account in this calculation.

Excitation of a three phase winding sets up a whole series of space harmonics of order $6a \pm 1$ where a is a positive integer (see appendix A). These harmonics are opposed by the space harmonics generated by the rotor cage in much the same way as the fundamental. Therefore, the reaction of the rotor cage to space harmonics should be predicted and applied on the rotor bars in addition to the fundamental current distribution. To determine the current distribution in the rotor cage an idealized case of the problem is primarily examined.

Let the rotor winding be a conducting surface which is overlaid on the rotor core. Also, the air-gap is short enough to minimise the leakage flux in the air-gap. In this case, the rotor

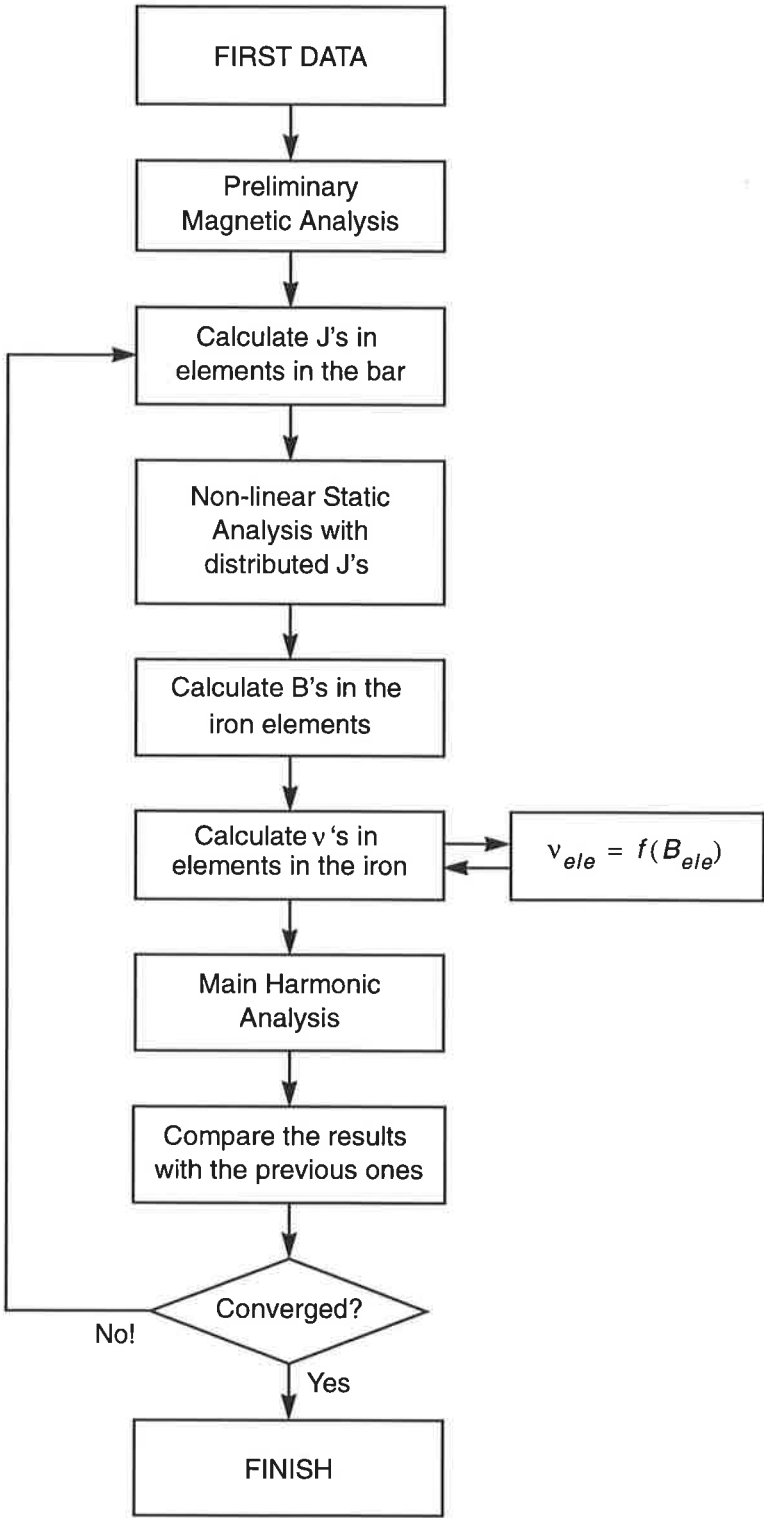


Fig. 2-12 The procedure of the new method using a simultaneous non-linear static and a harmonic analyses

winding reacts as a short circuited secondary for all of existing harmonics in the air-gap, created by the stator excitation. A squirrel cage shaped current map will appear on the conducting surface which has its sides exactly opposite to any stator slot opening and carrying the same current as in the stator slot opposite to it but in the reverse direction. A motor with a large number of rotor slots per pole may simulate the same reaction as an ideal cage at any time without imposing extra harmonics in the air-gap.

In practice, this number is usually large enough regarding only the fundamental harmonic. However, the rotor reaction is unable to counterbalance the higher order harmonic including the slot harmonics. A good knowledge of the constructional components of the current in each rotor bar allows accurate loading of the rotor in a finite element model but it obviously involves extra analytical work. Any of the following approximations may be employed in a finite element simulation:

1. Replace the rotor with an equivalent cage [79] having the same number of slots as the stator. Then apply the actual distribution of the stator and rotor current, on each winding. This allows accurate implementation of rotor reaction. However, the calculation of the stator and rotor leakage reactances will be inaccurate since the magnetic circuit of the machine has to be modified. Also, it may alter the deep bar effect.
2. As before but instead of replacing the rotor cage, the rotor current is distributed on the nodes at the surface of the rotor as a current sheet. This will represent a fictitious conducting surface over the rotor core as an ideal rotor cage, and allows a similar treatment as the equivalent cage. Although the geometry of the magnetic circuit of the motor is not changed, but:
 - a. The actual position of the rotor currents are displaced,
 - b. The deep bar effect may not be included,
 - c. The modification effect of the rotor currents on the saturation level in the stator teeth [79], is ignored,
 - d. The leakage inductance of the rotor can not be calculated accurately.

This method was used by Robinson [59] with some modifications. He compensated total stator current distribution by a set of currents on the rotor surface opposite to the

stator slot openings to act as an ideal cage. Then the predicted magnetizing current was applied as a sinusoidally distributed current sheet on the rotor surface.

3. Ignore the space harmonics and apply sinusoidally distributed currents in the stator and rotor slots individually, each establishing the fundamental mmf distribution of the appropriate winding. If the per pole number of rotor and stator slots are large enough for the fundamental harmonic, this will not introduce extra space harmonics in the air gap. The deep bar effect can be included accurately and the leakage reactance involved in the fundamental harmonic only will be calculated for each winding.
4. The rotor and stator currents are applied as sinusoidally distributed current sheets on the surface of the stator and rotor on either side of the air-gap. However, in a finite element model, the current should still be distributed on a limited number of nodes even if the number of nodes is usually large enough to emulate a continuous current sheet. Virtually, this is equivalent to the previous method except the stator and rotor currents are moved from the inside of the slots to the surface of the corresponding parts; also, they are distributed as in virtual cages with a large number of bars. Therefore, the deep bar effect should be ignored and also the stator and rotor leakage reactances can not be evaluated accurately.
5. Alternatively, a combination of 2 and 3 can be employed. The actual current distribution is applied on the stator slots while the rotor carries a sinusoidally distributed current to produce its fundamental mmf in the air gap. A set of current segments, are also spread on the nodes opposite to stator slots, to counteract all of the space harmonics except for the fundamental. This may result in a more accurate calculation of stator leakage reactance while the deep bar effect will be also included with a good accuracy. Still some error may appear in the evaluation of rotor leakage reactance.

Normally, the stator winding is so distributed in the slots to minimize the amplitude of higher spatial harmonics. Furthermore, higher order harmonics are more strongly opposed by the rotor reaction as the order of harmonic increases [59]. To optimize the solution, it was decided to employ option 3. This resulted in fairly accurate results with a acceptable size of database file and computation time. A combination of the classical equivalent circuit and the finite element model is used to evaluate the stator and rotor currents for the fundamental harmonic distribution. As with many other researchers [55, 59, 78], the leakage reactances

are assumed to be produced by this harmonic only. In brief, it is implicitly assumed that the rotor mmf completely cancels all mmf's in the air-gap except for the fundamental component. This gives rise to second and third order errors in calculation [1], which is far less than the permissible error margins for the thermal analysis.

Results of some more study about the above options are described in section 2.3 in chapter 5.

* * * * *

CHAPTER THREE

THERMAL ANALYSIS

Contents: Mechanisms of Heat Transfer, Boundary Conditions, Different Regimes of Thermal Analysis, Solution Techniques, Conductive Heat Transfer, Convective Heat Transfer, Radiation.

1.0 TERMINOLOGY

Heat is the thermal state of energy. It is measured in Joules.

Heat transfer analysis refers to the branch of science that seeks to predict the energy transfer between any two points as a result of temperature difference.

A **thermal model** is a mathematical emulation of a physical system through which the rate of heat transfer and the distribution of temperature in the real system can be estimated/predicted. A thermal model can be broken into three main parts:

- (a) **Thermal system or body:** Thermal system or body is the object or objects within or between which heat transfer occurs,
- (b) **Thermal sources:** Whatever injects thermal energy into the system, are treated as thermal sources of the model. It is usually called measured in Watts per unit volume and may include the delivered heat to the body via convection, radiation or direct heat generation in the body,
- (c) **The surroundings:** The region outside the thermal system is called the surroundings.

1.1 Mechanisms of heat transfer

Heat transfer occurs in three modes:

Conduction: Conduction is the internal energy exchange from one body in perfect contact with another body, or from one part of a body to another part, without any relative motion between the origin and destination, due to a temperature difference.

Convection: Convection is defined as the heat transfer between the surface of an object and its surrounding fluid, by the motion of the fluid, when they are at different temperatures.

Radiation: Radiation is the communicated thermal energy between two systems in the absence of any medium.

1.2 Boundary conditions

In general, the boundaries of a thermal system may include any combination of the following conditions as shown in Fig. 3-1:

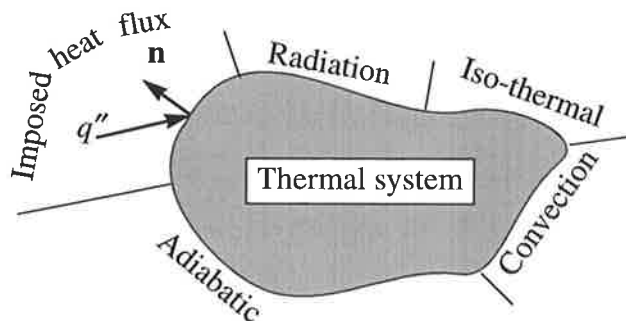


Fig. 3-1 A typical thermal system showing different possible boundary conditions

Convection (as defined in section 1.1);

Radiation (as defined in section 1.1);

Imposed heat flux, which imposes a certain value of heat flux through the boundary as:

$$q'' \cdot n = \text{constant} \quad (3-1)$$

where, q'' is the heat flux in W/m^2 and n is the unit vector, outward normal to the surface.

Adiabatic (isolated) is a common boundary which is a special case of imposed heat flux with the value of zero. Therefore, for any isolated boundary:

$$q'' \cdot n = 0 \quad (3-2)$$

Iso-thermal or Dirichlet boundary conditions (imposed temperature) refers to a boundary with a constant temperature, $T(x, y, z)$, or:

$$T(x, y, z) = \text{constant} \quad (3-3)$$

1.3 Different regimes of thermal analysis

Steady state analysis in which no change in the stored energy occurs;

Transient analysis through which the time history of the temperature variation at any point (node) of interest can be extracted.

1.4 Solution Techniques

One solution technique is the **analytical method**, through which an explicit solution for the governing equations can be achieved. However, in most practical thermal problems the geometry and the boundaries are too complicated to be solved analytically.

The **lumped parameter method (or lumped-heat-capacity system)**, is a simple technique that assumes homogeneous material properties and a uniform temperature distribution in a certain component. It is only valid if the internal thermal resistance of any component is much smaller than its external resistance (see section 2.3).

Alternatively, any of the **Numerical methods** as follows may be implemented:

- (a) **Finite difference method**, which approximates a continuous temperature gradient with differential increments in the temperature and space coordinates,
- (b) **Resistance element method**, in which the body is discretized into a finite number of elements and each is substituted with one or a group of lumped thermal resistor(s),

- (c) **Finite element method**, where the body is discretized into a finite number of elements and the temperatures in the associated nodes are estimated looking at the heat balance in the system.

2.0 CONDUCTIVE HEAT TRANSFER

A general thermal system may include different modes of heat transfer mechanisms to be analysed in a steady state or transient regimes. In this section, some aspects of conductive heat transfer are overviewed.

2.1 Conduction in one dimensional thermal systems

In a one dimensional thermal system, heat transfer occurs only along one of the coordinates. With certain loading and boundary conditions, it may also be a plain wall, a cylinder or a sphere in Cartesian, cylindrical or spherical coordinate systems respectively.

2.1.1 General formulation

The heat flow through a large plain wall is calculated from:

$$q = -k_x A \frac{\partial T}{\partial x} \quad (3-4)$$

where,

q = the transferred heat in x direction, W

k_x = thermal conductivity of the element in x direction, $W/m \cdot ^\circ C$

A = area of surface, m^2

T = Temperature, $^\circ C$

In a steady state regime, T varies only with x . Therefore, the heat transfer and temperature distribution can be simply calculated by integrating (3-4) along x . However, if the temperature of the solid is changing with time, or there are any heat sources or heat sinks in the body, the analysis is more complex. This case, for a plane wall element of thickness dx , as shown in Fig. 3-2-a. The heat balance law for this element implies that:

$$\left(\begin{array}{l} \text{Energy conducted into the} \\ \text{left face + heat generated} \\ \text{in the element} \end{array} \right) = \left(\begin{array}{l} \text{Energy conducted out} \\ \text{from right face + increase} \\ \text{in the internal energy} \end{array} \right) \quad (3-5)$$

This leads to a more general form of Fourier's law of heat conduction as:

$$\frac{\partial}{\partial x} \left(k_x \cdot \frac{\partial T}{\partial x} \right) + q''' = \rho c \frac{\partial T}{\partial \tau} \quad (3-6)$$

where,

q''' = Heat generation, W/m^3

ρ = Density, Kg/m^3

c = Specific heat, $Joul/Kg \cdot ^\circ C$

τ = Time, seconds

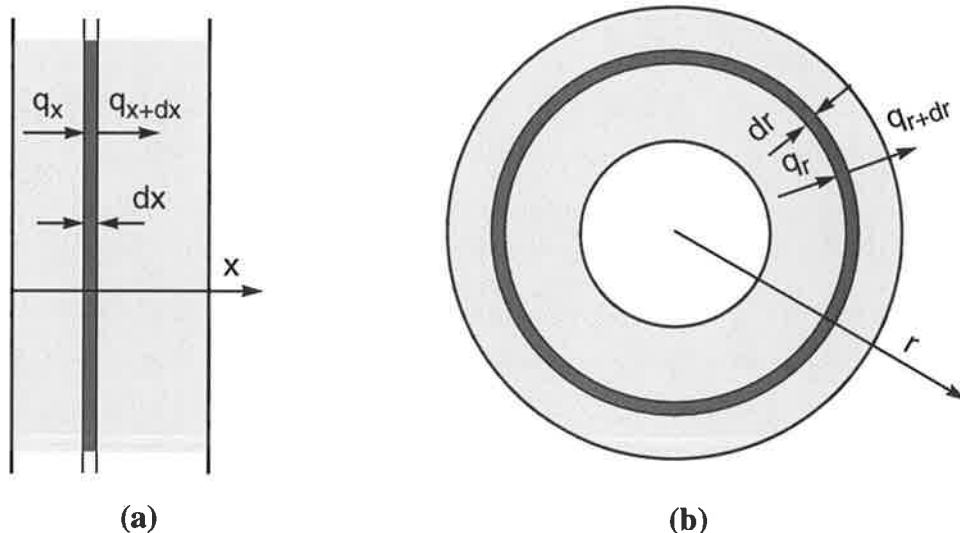


Fig. 3-2 Two samples of the elementary one dimensional thermal systems

2.1.2 Determination of conductive heat transfer in one-dimensional system

The heat transfer through a plain wall at steady state is considered as a one dimensional thermal system. From (3-4) if k is constant along Δx , the heat transfer through a wall of thickness Δx is calculated as:

$$q = -\frac{k_x A}{\Delta x} \cdot (T_2 - T_1) \quad (3-7)$$

or:

$$q = -\frac{\Delta T}{R_{th}} \quad (3-8)$$

In (3-8), R_{th} is called as the “thermal resistance” of the wall which is defined as:

$$R_{th} = \frac{\Delta x}{kA} \quad (3-9)$$

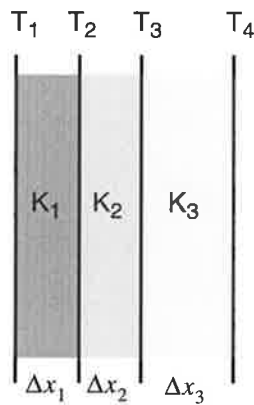


Fig. 3-3 The elementary one dimensional thermal system including a three layer wall

If more than one material is present as layers of thickness $\Delta x_1, \Delta x_2, \dots$, the thermal resistances of the layers are connected in series. For example, in Fig. 3-3, it can be shown that:

$$q = \frac{T_1 - T_4}{\frac{\Delta x_1}{k_1 A} + \frac{\Delta x_2}{k_2 A} + \frac{\Delta x_3}{k_3 A}} \quad (3-10)$$

Therefore, the total thermal resistance, $R_{th, tot}$, is:

$$R_{th, tot} = \frac{\Delta x_1}{k_1 A} + \frac{\Delta x_2}{k_2 A} + \frac{\Delta x_3}{k_3 A} \quad (3-11)$$

Taking advantage of a cylindrical co-ordinate system, the heat transfer through the wall of a long cylindrical body, as shown in Fig. 3-2-b, can be similarly calculated from:

$$q_r = \frac{2\pi k_r \cdot L (T_i - T_o)}{\ln (r_o/r_i)} \quad (3-12)$$

where,

q_r = heat transfer in the radial direction

k_r = thermal conductivity of the wall in the radial direction

L = axial length of the cylinder

T_i = inside surface temperature

T_o = outside surface temperature

r_i = inside radius

r_o = outside radius

In this model, the thermal resistance of the cylindrical wall is expressed as:

$$R_{th} = \frac{\ln (r_o/r_i)}{2\pi k_r \cdot L} \quad (3-13)$$

2.2 Conduction in multi-dimensional thermal systems

In a more than one dimensional thermal system, the energy balance equation is constructed for a unit volume. The counterpart of (3-5) for a three dimensional thermal element, as shown in Fig. 3-4, in cartesian coordinates yields:

$$q_x + q_y + q_z + q''' = q_{x+dx} + q_{y+dy} + q_{z+dz} + \frac{\partial E}{\partial \tau} \quad (3-14)$$

E is the internal energy of the element.

By substituting q_{x+dx} , q_{y+dy} and q_{z+dz} with the first two terms of the relevant Taylor-series expansion, the general form of (3-14) may be extracted as:

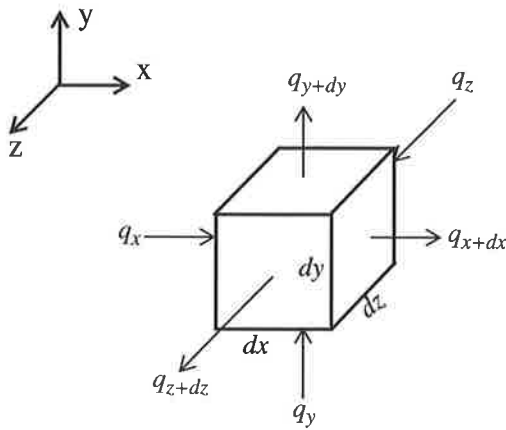


Fig. 3-4 Volume elements for three dimensional heat conduction analysis in the Cartesian coordinate system.

$$\frac{\partial}{\partial x} \left(k_x \cdot \frac{\partial T}{\partial x} \right) + \frac{\partial}{\partial y} \left(k_y \cdot \frac{\partial T}{\partial y} \right) + \frac{\partial}{\partial z} \left(k_z \cdot \frac{\partial T}{\partial z} \right) + q''' = \rho c \frac{\partial T}{\partial \tau} \quad (3-15)$$

In (3-15), k_x , k_y and k_z are the thermal conductivities of the element in x , y and z directions respectively.

In practical problems, the dimensions of individual elements can be selected small enough so that k_x , k_y and k_z can be assumed to be invariant within any individual element whence (3-15) can be simplified as:

$$k_x \cdot \frac{\partial^2 T}{\partial x^2} + k_y \cdot \frac{\partial^2 T}{\partial y^2} + k_z \cdot \frac{\partial^2 T}{\partial z^2} + q''' = \rho c \frac{\partial T}{\partial \tau} \quad (3-16)$$

Finally, in a thermally isotropic region, $k_x = k_y = k_z = k$ and (3-16) becomes:

$$\frac{\partial^2 T}{\partial x^2} + \frac{\partial^2 T}{\partial y^2} + \frac{\partial^2 T}{\partial z^2} + \frac{q'''}{k} = \frac{\rho c}{k} \cdot \frac{1}{\alpha} \cdot \frac{\partial T}{\partial \tau} \quad (3-17)$$

In (3-17):

$$\alpha = \frac{k}{\rho c} \quad (3-18)$$

and it is called as the “thermal diffusivity” of the material. The larger the value of α , the faster heat will diffuse through the material.

Similar equations can be extracted in other coordinate systems.

2.2.1 Determination of conductive heat transfer in a multi-dimensional systems

The temperature distribution in a two or three dimensional system can be achieved by solving the general governing equation of (3-15), (3-16) or (3-17). However, except for the models of very simple geometry and simple boundary conditions, this equation can not be solved analytically, or, the solution involves in such a complex series that numerical evaluation becomes exceedingly difficult.

An alternative simple technique for multi-dimensional systems is a lumped parameter method which is limited to special models as described in the next topic. When the analytical method and the lumped parameter method fail to solve the problem, the numerical methods, such as finite element method, resistance element method or finite difference technique are very useful. The introduction of these techniques has made it possible to predict accurate localised temperature distributions in very complex geometries. However, despite the presence of these powerful techniques, their success is still contingent upon the availability of reliable information on the loss density distribution, thermal data and characteristics of the composite materials used in the construction of the induction motor.

2.3 Lumped parameter method

The lumped parameter method, or lumped-heat capacity system is an alternative technique of solution for multi-dimensional thermal systems, in which the distribution of temperature and material properties are assumed to be uniform in the entire body. Therefore, the internal resistance of the model should be much smaller than its external resistance. This means that the physical dimensions of the model associated with the thermal conductivity of the material should be small enough to meet this assumption. A good thermal conductor with convection boundaries, e.g. cooling of a small hot steel ball in air or water, can be approximated by this method. However, such a system is still idealized since a temperature gradient should exist in the body if heat is to be conducted.

In implementing the lumped parameter method, the entire body is presented as a thermal node (see Fig. 3-5) from which the thermal capacity of the body is connected to the ground.

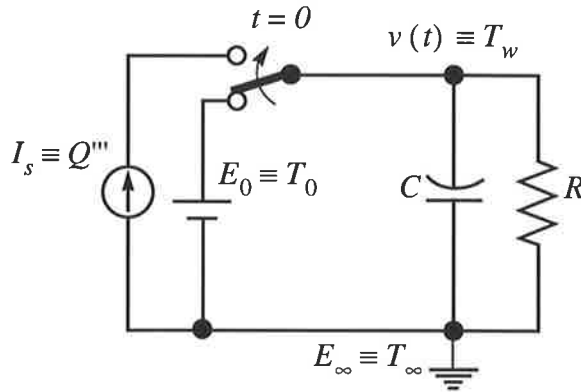


Fig. 3-5 A typical presentation of lumped parameter equivalent circuit

$v(t) \equiv T_{wall}$, Temperature at the entire body

$E_{\infty} \equiv T_{\infty}$, Bulk temperature

$E_0 \equiv T_0$, Establishes the initial temperature

$Q''' = \sum_V q''' \cdot \Delta V$, Total heat generation in the entire body

$R \equiv R_{th} = 1 / (hA)$

$C \equiv C_{th} = \rho c V$

$E_{\infty} \equiv T_{\infty}$

Thermal sources and the thermal resistance of the convective boundaries are substituted by a current source and a resistor respectively and are connected in parallel with the capacitor. The voltage source simulates the initial temperature of the body while the current source is equivalent to the total heat generation within the body regardless how it is distributed. Therefore, the current through R is equivalent to the heat flowing out from the body. Solution for the electric circuit of Fig. 3-5 yields:

$$\begin{aligned} v(t) &= (E_0 - I_s R) e^{-t/\tau_c} + R I_s \\ &= E_0 e^{-t/\tau_c} + R I_s (1 - e^{-t/\tau_c}) \end{aligned} \quad (3-19)$$

where, τ_c is the time constant of the circuit.

In terms of thermal parameters, (3-19) can be re-written as:

$$T - T_{\infty} = (T_0 - T_{\infty}) e^{-t/\tau_c} + R_{th} Q''' (1 - e^{-(hA/\rho c V) t}) \quad (3-20)$$

where, V and Q''' are the volume and the total heat generation in the entire body respectively.

If the thermal system includes materials with non-uniform properties and/or if the heat sources are distributed non-uniformly in the body, as in an induction motor, each part of the system should be simulated individually and then interconnected to construct the final thermal model [11, 47]. Even though the accuracy of solution can be improved by this technique, there are still many uncertainties in the way they are connected. The choice of subdivision of machine into elementary components is usually a compromise between the simplicity of the model and the accuracy of the results [11]. This is more complicated for a non-steady analysis. Some other limitations of this method are discussed in section 3.0 in chapter 4.

2.4 Numerical analysis of conductive heat transfer

To carry out a numerical analysis, the model is usually discretized into a number of elements and it is solved either by a finite difference or resistance element method.

2.4.1 Finite difference method

A two dimensional thermally uniform body as shown in Fig. 3-6 is considered to

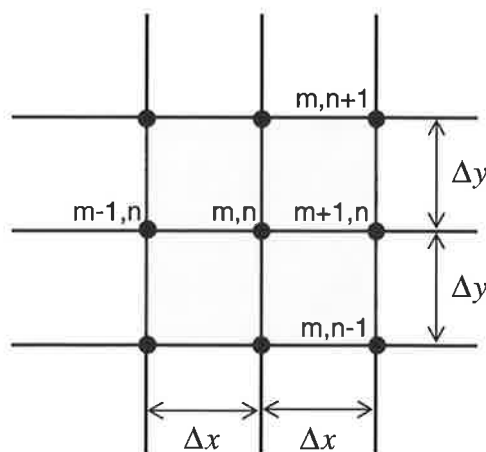


Fig. 3-6 A typical meshing for the finite difference solution method

demonstrate the application of finite difference method. The body is to be divided into equal increments in both x and y directions individually. The numbering policy of the nodes is shown in the figure. Re-writing (3-17) for this model under steady state conditions results in:

$$\frac{\partial^2 T}{\partial x^2} + \frac{\partial^2 T}{\partial y^2} + \frac{q'''}{k} = 0 \quad (3-21)$$

Finite differences are used to approximate continuous temperature gradients with differential increments in the temperature and space coordinates. The temperature gradients along x and y directions are:

$$\left. \frac{\partial T}{\partial x} \right]_{\left(m+\frac{1}{2}\right),n} \approx \frac{T_{(m+1),n} - T_{m,n}}{\Delta x}$$

$$\left. \frac{\partial T}{\partial x} \right]_{\left(m-\frac{1}{2}\right),n} \approx \frac{T_{m,n} - T_{(m-1),n}}{\Delta x}$$

$$\left. \frac{\partial T}{\partial y} \right]_{m,\left(n+\frac{1}{2}\right)} \approx \frac{T_{m,(n+1)} - T_{m,n}}{\Delta y}$$

$$\left. \frac{\partial T}{\partial y} \right]_{m,\left(n-\frac{1}{2}\right)} \approx \frac{T_{m,n} - T_{m,(n-1)}}{\Delta y}$$

$$\left. \frac{\partial^2 T}{\partial x^2} \right]_{m,n} = \frac{\left. \frac{\partial T}{\partial x} \right]_{\left(m+\frac{1}{2}\right),n} - \left. \frac{\partial T}{\partial x} \right]_{\left(m-\frac{1}{2}\right),n}}{\Delta x} = \frac{T_{(m+1),n} + T_{(m-1),n} - 2T_{m,n}}{(\Delta x)^2} \quad (3-22)$$

$$\left. \frac{\partial^2 T}{\partial y^2} \right]_{m,n} = \frac{\left. \frac{\partial T}{\partial y} \right]_{m,\left(n+\frac{1}{2}\right)} - \left. \frac{\partial T}{\partial y} \right]_{m,\left(n-\frac{1}{2}\right)}}{\Delta y} = \frac{T_{m,(n+1)} + T_{m,(n-1)} - 2T_{m,n}}{(\Delta y)^2} \quad (3-23)$$

Substituting (3-22) and (3-23) in (3-21), the finite difference approximation for node m,n becomes:

$$\frac{T_{(m+1),n} + T_{(m-1),n} - 2T_{m,n}}{(\Delta x)^2} + \frac{T_{m,(n+1)} + T_{m,(n-1)} - 2T_{m,n}}{(\Delta y)^2} + \frac{q'''}{k} = 0 \quad (3-24)$$

For a set of square grids with $\Delta x = \Delta y$, (3-24) is simplified as

$$T_{(m+1),n} + T_{(m-1),n} + T_{m,(n+1)} + T_{m,(n-1)} + \frac{q''' \cdot (\Delta x)^2}{k} - 4T_{m,n} = 0 \quad (3-25)$$

Equation (3-25) can be extracted for all of the nodes in the meshed medium. Then, they should be solved simultaneously. For a thermal field with a total node number of n , the system of equations is:

$$\begin{aligned}
 (a_{11}T_1 + a_{12}T_2 + \dots + a_{1n}T_n = C_1) \\
 (a_{21}T_1 + a_{22}T_2 + \dots + a_{2n}T_n = C_2) \\
 \dots\dots\dots \\
 \dots\dots\dots \\
 (a_{n1}T_1 + a_{n2}T_2 + \dots + a_{nn}T_n = C_n)
 \end{aligned}
 \tag{3-26}$$

where T_1, T_2, \dots, T_n are the nodal temperatures, a 's and C 's are constants. In a matrix notation:

$$[A] \cdot [T] = [C] \tag{3-27}$$

and

$$[T] = [A]^{-1} \cdot [C] \tag{3-28}$$

In (3-27) and (3-28):

$$[A] = \begin{bmatrix} a_{11} & a_{12} & \dots & a_{1n} \\ a_{21} & a_{22} & \dots & a_{2n} \\ \dots & \dots & \dots & \dots \\ a_{n1} & a_{n2} & \dots & a_{nn} \end{bmatrix}$$

$$[T] = [T_1 \ T_2 \ \dots \ T_{nn}]^T$$

$$[C] = [C_1 \ C_2 \ \dots \ C_{nn}]^T$$

In general (but not always), finer meshing produces more accurate equations but on the other hand, a larger database with a longer computing time results. In practical problems, because of uncertainties in boundaries, an increase in the number of nodes does not necessarily lead to a higher accuracy. It is not uncommon to have an approximation as large as $\pm 15\%$ to $\pm 20\%$ in

the film convection coefficients¹ [33]. Therefore, the optimum sizes of meshes should be investigated to gain the best accuracy without using extra computing facilities.

2.4.2 Resistance element method

When a numerical analysis is to be performed which takes into account the material property variations in different directions, the resistance element formulation is conceptually and practically preferred.

Like the finite difference method, the heat transfer region is discretized into a finite number of elements and then the concept of resistance elements is used for writing the heat transfer equations between any pair of adjacent nodes. Designating the node of interest with the subscript i and adjoining nodes with subscript j , the general situation of node i can be shown as Fig. 3-7.

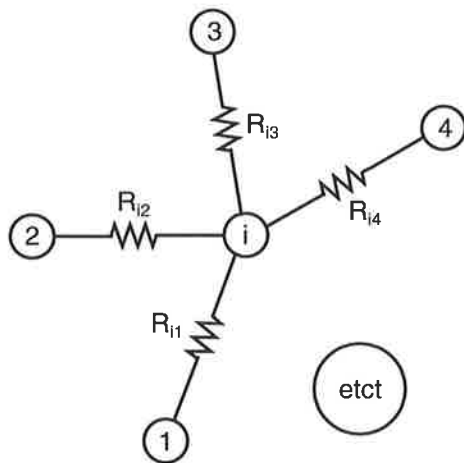


Fig. 3-7 Equivalent circuit of a general conduction node

In a steady state condition, the net heat input to node i must be zero. Then:

$$q_i + \sum_j \frac{T_j - T_i}{R_{ij}} = 0 \quad (3-29)$$

where,

q_i = the heat delivered to node i by heat generation;

1. This coefficient is defined later in this chapter

T_i, T_j = temperature at nodes i and j respectively;

R_{ij} = thermal resistance between nodes i and j .

The outstanding feature of this method is its capability to handle the analysis of complicated three-dimensional shapes in which volume elements are usually employed to simulate the internal nodal resistances in the system. The volume elements for Cartesian and cylindrical coordinate systems are shown in Fig. 3-8 and the values of internal nodal resistors for each

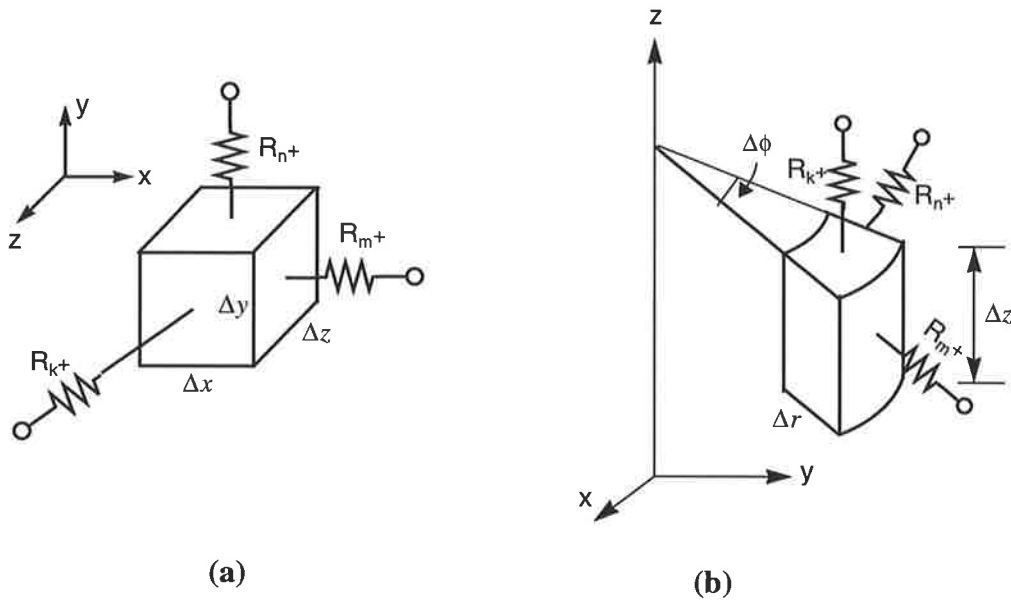


Fig. 3-8 Volume elements for three dimensional heat conduction analysis (a) Cartesian coordinate system (b) Cylindrical coordinate system.

system are given in Table 3-1.

Table 3-1 The Values of Nodal Resistances for Cartesian and Cylindrical Coordinate Systems

	Cartesian	Cylindrical
Nomenclature for increments	x, m y, n z, k	r, m φ, n z, k
Volume element ΔV	$\Delta x \cdot \Delta y \cdot \Delta z$	$r_m \cdot \Delta r \cdot \Delta \phi \cdot \Delta z$
R_{m+}	$\frac{\Delta x}{\Delta y \cdot \Delta z \cdot k}$	$\frac{\Delta r}{(r_m + \Delta r/2) \cdot \Delta \phi \cdot \Delta z \cdot k}$
R_{m-}	$\frac{\Delta x}{\Delta y \cdot \Delta z \cdot k}$	$\frac{\Delta r}{(r_m - \Delta r/2) \cdot \Delta \phi \cdot \Delta z \cdot k}$
R_{n+}	$\frac{\Delta y}{\Delta x \cdot \Delta z \cdot k}$	$\frac{r_m \cdot \Delta \phi}{\Delta r \cdot \Delta z \cdot k}$

Table 3-1 The Values of Nodal Resistances for Cartesian and Cylindrical Coordinate Systems

	Cartesian	Cylindrical
Nomenclature for increments	x, m y, n z, k	r, m φ, n z, k
Volume element ΔV	$\Delta x \cdot \Delta y \cdot \Delta z$	$r_m \cdot \Delta r \cdot \Delta \phi \cdot \Delta z$
R_{n-}	$\frac{\Delta y}{\Delta x \cdot \Delta z \cdot k}$	$\frac{r_m \cdot \Delta \phi}{\Delta r \cdot \Delta z \cdot k}$
R_{k+}	$\frac{\Delta z}{\Delta x \cdot \Delta y \cdot k}$	$\frac{\Delta z}{r_m \cdot \Delta \phi \cdot \Delta r \cdot k}$
R_{k-}	$\frac{\Delta z}{\Delta x \cdot \Delta y \cdot k}$	$\frac{\Delta z}{r_m \cdot \Delta \phi \cdot \Delta r \cdot k}$

For a transient analysis, the solution is carried out in successive time steps. The heat balance equation at any time step for Fig. 3-7 can be written as:

$$\boxed{\text{Net heat delivered into node } i} = \boxed{\text{Increase in the internal energy}} \quad (3-30)$$

Therefore, in the p 'th time step, the time interval between T^p to T^{p+1} , the application of (3-30) yields:

$$q_i + \sum_j \frac{T_j^p - T_i^p}{R_{ij}} = C_i \cdot \frac{T_i^{p+1} - T_i^p}{\Delta \tau} \quad (3-31)$$

Finally, the temperature at node i at the end of this time step is calculated as a function of the nodal temperatures at the previous time step:

$$T_i^{p+1} = \left(q_i + \sum_j \frac{T_j^p}{R_{ij}} \right) \frac{\Delta \tau}{C_i} + \left(1 - \frac{\Delta \tau}{C_i} \sum_j \frac{1}{R_{ij}} \right) T_i^p \quad (3-32)$$

2.4.3 Finite Element Method

The previous methods fail to analyse a thermal system, or become very tedious when:

1. The geometry of the model and/or boundaries are too complicated;
2. The thermal properties of the constructional materials are not equal in different directions,

3. The thermal properties of the constructional materials, and/or the distribution of thermal loads are time variant;

A good implementation of the finite element method can easily cope with any of the aforementioned problems and the temperature distribution and any other thermal parameters within the model can be calculated with any required resolution. In this project, the finite element technique is used to solve the conduction problem in the induction motor in transient condition. The implementation of this technique may be summarised in the following steps [6]:

1. Formulate the governing transient heat conduction equations;
2. Deduce the energy functional for this equation;
3. Write the minimization equations by differentiating the functional with respect to each of the element nodal temperatures;
4. Specify interpolation polynomial (shape functions) for the elements so that the minimization equation can be directly integrated;
5. Solve the set of algebraic linear equations at each time step.

Considering the geometry of the motor, the cylindrical-polar form of (3-16) is used as follows:

$$\frac{1}{r} \frac{\partial}{\partial r} \left(k_r \cdot r \cdot \frac{\partial T}{\partial r} \right) + \frac{k_\theta}{r^2} \cdot \frac{\partial^2 T}{\partial \theta^2} + k_z \cdot \frac{\partial^2 T}{\partial z^2} + q''' = \rho c \frac{\partial T}{\partial \tau} \quad (3-33)$$

where, r , θ , and z are the co-ordinates of the cylindrical-polar system and k_r , k_θ , and k_z are the thermal conductivities of the elements in corresponding directions.

The functional for the above parabolic partial differential equation is so chosen that the Euler equation of the functional is same as (3-33) itself. This is necessary and sufficient condition for minimization of the functional to give a true solution of the partial differential equation.

Referring to the Euler equation:

$$\frac{1}{r} \frac{\partial}{\partial r} \left(r \cdot \frac{\partial \mathcal{F}}{\partial T_r} \right) + \frac{\partial}{\partial \theta} \cdot \left(\frac{\partial \mathcal{F}}{\partial T_\theta} \right) + \frac{\partial}{\partial z} \cdot \left(\frac{\partial \mathcal{F}}{\partial T_z} \right) - \frac{\partial \mathcal{F}}{\partial T} = 0 \quad (3-34)$$

where:

\mathcal{F} = Functional

T_r , T_θ , and $T_z = \frac{\partial T}{\partial r}$, $\frac{\partial T}{\partial \theta}$, and $\frac{\partial T}{\partial z}$ respectively

Then the functional form for (3-33) may be deduced as:

$$\mathcal{F} = \int_V \left(\frac{k_r}{2} \cdot \left(\frac{\partial T}{\partial r} \right)^2 + \frac{k_\theta}{2r^2} \left(\frac{\partial T}{\partial \theta} \right)^2 + \frac{k_z}{2} \left(\frac{\partial T}{\partial z} \right)^2 - Tq''' \right) dV + \int_V \frac{\rho c}{2\Delta\tau} (T^2 - 2T \cdot T_0) dV \quad (3-35)$$

In this equation, $\Delta\tau$ is the length of each time step, T_0 is the initial temperature at the time step and V is the volume.

The solution is involved in the minimization of (3-35), where the initial conditions and also the boundary conditions in the model are needed. The procedure results in a system of simultaneous equations. Any algebraic procedure, such as Gaussian elimination method or Newton-Raphson technique may be used to find the nodal temperatures as the first set of results. Any other thermal parameters, like heat flow or temperature gradient are usually extracted from the nodal solution (nodal temperatures).

3.0 CONVECTIVE HEAT TRANSFER

The convective heat transfer between a solid and a fluid in contact with it is evaluated by means of the following equation:

$$q = A\bar{h}_c (T_w - T_\infty) \quad (3-36)$$

where:

q = heat flux [W]

\bar{h}_c = convective heat transfer coefficient [$W/m^2 \cdot ^\circ C$]

A = Area of convecting surface [m^2]

T_w = wall temperature [°C]

T_∞ = bulk temperature of the fluid [°C]

The convection equation in this form seems to be very simple. However, the simplicity is misleading because it employs the \bar{h} rather than a law of heat transfer by convection. The actual value of the convective heat transfer coefficient is a complicated function of the fluid flow, the thermal properties of the fluid medium and the geometry of the solid. It is also a function of the wall temperature and also the location where the fluid temperature T_∞ is measured.

In practice heat transfer between a solid and a fluid takes place by a combination of conduction and mass transport. Heat is conducted from a hot wall on a solid to the particles of fluid on the neighbourhood of the wall and increases the internal energy of the fluid. Then it is transferred by motion of the fluid particles. The reverse of this action happens when the solid is in at lower temperature than the surrounding fluid.

The convection is classified as “natural convection” when the motion is the result of any temperature variation in the fluid. Natural cooling of a small transformer is an example of natural convection. Otherwise, when the motion is caused by any external energy source, as in a fan-cooled rotating machine, the convection is called “forced convection”.

3.1 Evaluation of \bar{h}_c

A pure mathematical method or so called dimensional analysis techniques may be employed in order to evaluate the convective heat transfer coefficient.

A **pure mathematical method** requires the simultaneous solution of the equations describing the fluid motion and the transfer of energy in the moving fluid. This requirement however limits the scope of exact mathematical analysis to laminar flow conditions. In a laminar flow, the fluid moves in layers, each fluid particle following a smooth and continuous path. They march along well defined lines one behind the other and maintain their order even when they turn a corner or pass an obstacle. Otherwise it is a turbulent flow.

Dimensional analysis¹ method combined with experiments is an alternative method which is more applicable in practical problems. In this technique, the well known Buckingham π -theorem [38] is employed to define four correlated dimension-less parameters as follows:

(a) *Nusselt number*, \overline{NU} , which is defined as:

$$\overline{NU} = \frac{\bar{h}_c L}{k_f} \quad (3-37)$$

where:

\bar{h}_c = the average convection coefficient,

L = the significant (or characteristic) length²,

k_f = the thermal conductivity of the fluid.

It can be shown that \overline{NU} interprets the ratio of temperature gradient in the fluid immediately in contact with the surface of the solid to a reference temperature gradient $(T_w - T_\infty) / L$.

Having the \overline{NU} measured or calculated, \bar{h}_c can be easily calculated from (3-37).

(b) *Reynold's number*, Re , which is a criterion to assess if a flow is laminar or turbulent.

It is defined as:

$$Re = \frac{VL\rho}{\mu} \quad (3-38)$$

where:

V = velocity of the fluid;

L = the significant (or characteristic) length;

ρ = density of the fluid;

-
1. With the aid of dimensional analysis, the results of one series of tests may be applied to a variety of other problems. Also, by taking advantage of the "principle of similarity" (or so called "model law"), one may use a set of measured/calculated parameters for one model in another model with different physical dimensions but having specific conditions to meet the principle of similarity [38].
 2. The characteristic length depends on the geometry and the positioning of the surface. For a horizontal cylinder it is equal to the diameter of the cylinder.

μ = dynamic viscosity of the fluid.

(c) *Grashof number* which is defined as:

$$Gr_L = \frac{g\beta(T_w - T_\infty)L^3}{\nu^2} \quad (3-39)$$

and can be interpreted as the ratio of the buoyancy force to the viscous forces in the free convection. It has a role of similar to that played with *Reynold's number* in a forced convection. When the buoyancy is the only driving force, the fluid velocity may entirely determined by the quantities contained in the Grashof number. In (3-39), the new parameters are:

β = the volume coefficient of expansion, for ideal gases, $\beta = 1/T$

g = the acceleration of gravity in $[N/(kg)]$

ν = the kinematic viscosity of the fluid

(d) *Prandtl number*, Pr is the ratio of two molecular transport properties, the kinetic velocity μ/ρ which takes into account the velocity distribution, and the thermal diffusivity $k/(\rho c)$, which is a measure of temperature profile. Therefore:

$$\begin{aligned} Pr &= \frac{\mu/\rho}{k_f/(\rho c_p)} \\ &= \frac{c_p \cdot \mu}{k_f} \end{aligned} \quad (3-40)$$

c_p is the specific heat of fluid at constant pressure.

Three dimensionless parameters of \overline{NU} , Re , Pr are generally related by:

$$\overline{NU} = \Phi(Re) \cdot \Psi(Pr) \quad (3-41)$$

Another correlation among the dimensionless parameters which has been found empirically for some specific circumstances subject to free convection is:

$$\overline{NU}_f = C(Gr_f \cdot Pr_f)^m \quad (3-42)$$

where the subscript f indicates that the dimensionless parameters are evaluated at the film temperature of:

$$T_f = \frac{T_\infty + T_w}{2} \quad (3-43)$$

The empirical values of $Re_f \cdot Pr_f$, C and m for a horizontal cylinder are given in Table 3-2 [33]. Also, the \overline{NU} can be extracted from another empirical expression for use over a wide

Table 3-2 Empirical values of constants to be used in (3-42) for horizontal cylinders.

$Re_f Pr_f$	C	m
10^{-10} to 10^{-2}	0.675	0.058
10^{-2} to 10^2	1.02	0.148
10^2 to 10^4	0.850	0.188
10^4 to 10^7	0.480	1/4
10^7 to 10^{12}	0.125	1/3

range of $10^{-5} < Gr \cdot Pr < 10^{12}$ as:

$$\overline{NU}^{1/2} = 0.60 + 0.387 \left(\frac{Gr \cdot Pr}{(1 + (0.559/Pr)^{9/16})^{16/9}} \right)^{1/6} \quad (3-44)$$

In brief, having the physical properties of the surrounding air, β , T_∞ , ν , c_p , μ and k_f , for any horizontally mounted induction motor of external equivalent diameter of L and a body temperature of T_w , Gr and Pr may be calculated from (3-39) and (3-40) respectively. Then, if $Gr \cdot Pr$ falls between 10^{-5} and 10^{12} , which is usually the case¹ in normal situations, \overline{NU} is calculated from (3-44) and then \bar{h}_c can be easily calculated from (3-37).

It is noteworthy that, most of the empirical formulas are involved in some error and a wide scatter may be expected on the calculated values for the same parameter from different applicable formulas.

1. Otherwise, other empirical formulas are available in many references such as [33] and [38].

3.2 The effect of fins

Fins increase the convected heat from a certain body, mainly in a free convection, by eventually increasing the effective surface. However, since all of the surface is not at the temperature of the base body, the convected heat is less than expected. This is considered by definition of fin efficiency as follows:

$$\eta_f = \frac{\text{actual heat transfer}}{\text{heat which would be transferred if entire fin area were at the base temperature}} \quad (3-45)$$

In other words, the coefficient h_c in an area with fins should be replaced by $(\eta_f \cdot h_c)$ where the entire area of the fins is assumed to be at the base temperature and subject to convection.

For rectangular fins [33], as shown in Fig. 3-9, when the heat transfer from the top of fins is

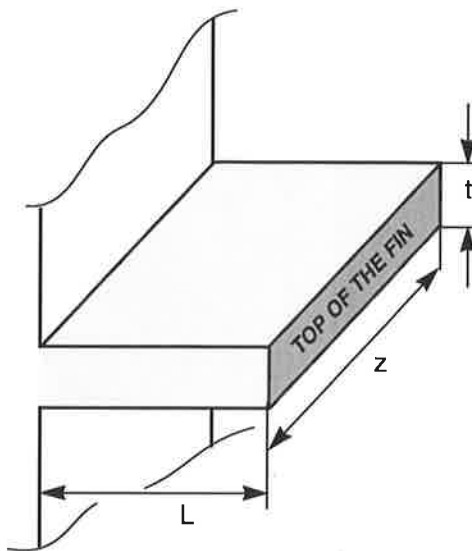


Fig. 3-9 Sketch illustrating one dimensional rectangular fins.

not considerable, η_f is calculated as:

$$\eta_f = \frac{\tanh mL}{mL} \quad (3-46)$$

In (3-46):

$$mL = \sqrt{\frac{h(2z + 2t)}{kzt}} L \quad (3-47)$$

and t , z and L are parameters related to the dimensions of the fins as shown in Fig. 3-9.

In many cases, as in induction motors, $t \ll z$ and the fin efficiency may be simplified as:

$$\eta_f = \frac{\tanh \sqrt{\frac{2h}{kt}} L}{\sqrt{\frac{2h}{kt}} L} \quad (3-48)$$

It is shown that the efficiency of triangular fins, which are normally used in induction motors, are slightly higher than the rectangular ones [33]. Therefore, (3-48) may be used to apply the effect of fins in the convected heat from the outer surface of an induction motor.

4.0 RADIATION

The net radiant exchange between two surfaces, i and j with temperatures of T_i and T_j respectively, is proportional to the difference in the absolute temperatures to the fourth power as:

$$Q_i = \sigma A_i \varepsilon_i F_{ij} (T_i^4 - T_j^4) \quad (3-49)$$

where:

Q_i = Heat transfer rate from surface i ,

σ = Stefan-Boltzman constant,

A_i = Area of surface i ,

ε_i = Effective emissivity of surface i ,

F_{ij} = View factor from surface i to surface j .

Since the actual temperatures in different external surfaces of the induction motors associated with the other constants in (3-49) are not significantly above ambient, the radiated heat from an induction motor will be ignored.

* * * * *

CHAPTER FOUR

THERMAL MODELLING OF INDUCTION MOTOR

Contents: Symmetry and periodicity planes, Possible approaches for thermal modelling, History of thermal modelling of induction motor, Some considerations about the material properties.

1.0 INTRODUCTION

Referring to the definition of a thermal model in the previous chapter, in an induction motor, all parts of the motor, including iron core, stator winding, rotor cage and any other component in the motor are the body of the thermal model. Having comprehensive information about the geometry of the motor and the thermal properties of the constructional materials in the motor, the thermal model can be generated. However, the geometry of an induction motor is usually so complex that the generation of an accurate thermal model is hardly possible, or it may take enormous computing resources and effort. In addition, the variety of materials with different thermal properties in the model adds to the complexity of the work. Furthermore, different parts with non-similar materials such as iron, copper, aluminium and air with non-uniform temperature distributions are thermally inter-linked so that the motor should be modelled with distributed parameters. The distribution effect becomes more severe in deep bar cage motors where the rotor bars have a large interface area with the iron core. In particular, during the first few seconds of starting or when the motor is stalled for any reason, the thermal loads are extremely large. Hence, the unevenly distributed losses in each individual rotor bar creates a non-uniform distribution of temperature unique to each rotor slot pitch.

In practice, depending on the permissible margins of error, some approximations may be applied. Usually, the accuracy of the modelling is compromised with the availability of

computer facilities and the programmer's effort. It is also limited by the accuracy of the available data about the material properties, dimensions, boundary conditions etc.

In a physical induction motor, heat transfer occurs in three dimensions: axial, radial and tangential. Ideally, it should be represented by an appropriate three dimensional model. However, building a full 3-D thermal model is both complicated and needs large computing facilities. In addition, it involves an enormously large data base as well so that one may have to compromise with larger element sizes which eventually reduces the accuracy of the analysis.

Taking any existing special condition into account allows the model to be simplified and/or reduced in size and/or the number of dimensions without significantly losing the accuracy of the solution. Any combination of the special conditions allows further simplification. The following features may be considered as special conditions in the thermal analysis of an induction motor:

1. Steady state solution of a running motor is studied, rather than the transient conditions of the locked motor under full voltage;
2. One or more symmetry and/or periodicity planes (to be defined later) can be detected in the thermal system;
3. Heat transfer is negligible in one or two directions, and/or from some boundaries.

In steady state analysis of a running motor, forced coolant and the high conductivity of constructional materials establishes an almost uniform temperature distribution in any individual part of the motor, e.g. rotor bars, the embedded parts of the stator winding, stator end winding etc. In such conditions the motor can be represented by a multinode lumped parameter [14,43] or a finite element model.

On the other hand, in a short interval transient analysis of a stalled motor the convected heat into the surrounding becomes negligible [78,87] while the internal thermal communication within each individual component and also among different components is substantial. Although some authors [68,78] ignore the heat transfer from the rotor bars into the surrounding iron core within the first few seconds of stall, it is shown that this may introduce an error of up to 45% within the first 1 seconds after stall on the heating of a die-casted

aluminium cage and some less error on the copper bars of an assembled copper cage [23] (also see section 3.4.1.1 on page 117). During another study in chapter 5 (section 3.4.3 on page 127), it is shown that convected heat from the motor body into the surroundings is quite negligible within the early seconds of the transient analysis of the stationary motor.

Some main features of an ordinary steady state analysis of a running motor¹ are compared to that of a short time transient analysis of a blocked rotor motor under rated voltage in Table 4-1.

Table 4-1 A comparison between the conditions for the transient and steady state analysis of induction motor

Condition	Transient, stalled under full voltage	Steady state, running
Total ohmic losses	Several times the rated power	a small fraction of the rated power
Effect of stator mmf harmonics	Rotor ohmic losses are un-equally distributed among the rotor bars	Losses in all rotor bars individually are equal
Distribution of Rotor bar losses in any bar area individually	Non-uniform	Almost uniform
Total Iron losses	Very small compared to the ohmic losses	Comparable with the ohmic losses
Distribution of total losses	Concentrated in the rotor and stator slots and their end ring/winding areas	Almost distributed in all parts of the motor
Temperature gradient	Very high, mainly in the slot areas	Generally very low*, some larger in the interface areas between any two different materials including outer surfaces
Type of heat transfer	Mainly Conduction	Conduction and convection

* This is as a result of forced coolant in the motor which provides a fairly uniform distribution of temperature in iron, copper and aluminium parts.

Taking advantage of any possible symmetry plane(s) in the model allows the system to be represented by a certain fraction of the entire body. Ignoring the variation of the rms values of current in individual rotor bars, a greater number of symmetry planes may be detected in a transient analysis.

1.1 Symmetry and periodicity planes

In addition to their specific features, symmetry planes are eventually adiabatic boundaries as defined in (3-2). Periodicity planes are another type of boundary condition in which a set of

1. Steady state analysis may be carried out on a motor at stall but it is practically unrealistic under full voltage.

constraint conditions is applied on the boundary to express the required periodicity on the modelled part of the system, similar to (2-21) and (2-22) for the case of a magnetic field.

Both symmetry planes and periodicity planes may be recognized by looking at the physical geometry of the model, the properties of constructional materials, and the distribution of loads in the model. Consequently, the thermal features and also the magnetic and electrical characteristics of the model influence in the finding of such planes.

The electric time constants of the electric circuit at standstill are usually short enough to be neglected in comparison to that of the thermal system. Consequently, even for the transient thermal analysis, the steady state results from electric and magnetic solutions can be used to estimate the distribution of the ohmic and iron loss density in the model. However, the data should be updated from time to time as they may vary with temperature.

The ohmic loss density in the rotor slot pitches on the one hand and in the stator slot pitches on the other hand are locally tangentially periodic in each individual part, rotor¹ and stator. The same local periodicity may be detected for the iron loss density if the radial magnetic reluctance along the peripheral direction in the magnetic circuit is assumed to be uniform. In fact, if the effect of slot openings do not introduce significant variation in the peripheral reluctance of the air-gap, all similar points on different slot pitches at the rotor and at the stator experience the same time variation of flux density individually. Therefore, one may expect a similar variation of iron losses in all slot pitches of the rotor and that of stator individually.

From the view point of thermal modelling, except for the shaft layout of an induction motor at stall, the geometry of both rotor and stator, including their appropriate windings, is symmetric about the central radial plane. Therefore, no heat flow is expected across this plane and therefore, the temperature gradient on this plane is zero.

Depending on the number of slots on the rotor and stator, some peripheral periodicity planes can be detected. If the number of rotor and stator slots per pole are whole numbers, only one pole pitch of the motor may be selected as the representative of entire system.

1. As described in chapter 2, the spacial higher order harmonics of stator mmf violate this condition to some extent. This effect for thermal model is discussed in chapter 5.

The air-gap in induction motors is usually short so that any possible motion of air in this region is negligible in a stationary motor. Consequently, no thermal communication is expected between rotor and stator surfaces via convection through the air-gap [56]. In addition, since the thermal conductivity of air is much less than that of its adjacent parts [11, 21], the distribution of the temperature on each of the rotor and stator surfaces may be assumed to be uniform individually. This fact raises a new periodicity allowing further reduction in the size of the model; and therefore only half of the stator slot pitch along with half of the rotor slot pitch, each including only half of the axial length of the motor, may be sufficient to represent the entire motor via a hybrid model.

In practice, the ohmic losses in individual rotor bars are slightly affected by the interaction between any pair of different space harmonics [78], being maximum at standstill. As a result, although the total losses in the cage remains unchanged, the ohmic losses in each bar vary as a function of spatial location (and speed). Therefore, in order to predict the most critical situation in the rotor, the rotor bar with the largest ohmic loss should be examined when a single-bar model is due to be constructed. The effect of unequal losses in the bars may be studied on a supplementary two dimensional model if necessary, representing a cross section of the motor as described in chapter 6

2.0 POSSIBLE APPROACHES FOR THERMAL MODELLING

The methods which have been used by the author to investigate the thermal behaviour of induction motors can be classified into two major approaches, Lumped Parameter Method (LPM) and Finite Element Method (FEM). Each have their use, and the choice of method is normally governed by the data and computing resources available. The major specifications of LPM were explained in chapter three (see section 2.3 on page 55). The basic theory of the finite element method was also explained in the same chapter (see section 2.4.3 on page 62). Since this technique is used as the main solution tool in this project, more features of this method, in particular when implemented as two or three dimensional model, are investigated in this chapter.

2.1 Three dimensional model

Unlike the magnetic (and electric) fields of the motor, in which the variation of the parameters is negligible along the axial direction, significant variation of thermal parameters

are expected in a thermal model along all of the three directions, radial, tangential, and axial. Therefore, construction of a three dimensional model is inevitable. However, for the sake of optimization, the smallest realistic fraction of the motor is presented considering the symmetry and periodicity planes.

As described in the previous section, a hybrid model including the fraction of:

$$\frac{\text{axial length}}{2} \times \left(\frac{\text{rotor slot pitch}}{2} + \frac{\text{stator slot pitch}}{2} \right) \quad (4-1)$$

from the motor may present all of the motor properties in both steady state and transient conditions. However, the rotor and stator slot pitches are not equal in general; so, in order to preserve the continuity of the model, the heat flow and/or the average temperature in the air-gap should be used as the interface between the two parts of the model. This assumption ignores the heat flow into the end-caps from both parts of the model. Otherwise, the two parts of the model should be linked by using more complicated, multi-parameter interface variables. It is shown in chapter 5 that the convected heat from all parts of the motor during the short transient analysis is not significant.

Solution of the hybrid model with one or more interface parameters involves an iteration method for each of the parameters which is a lengthy and time consuming process. Employing the idea of equivalent rotor [77], the two parts of the model may be combined to generate an equivalent model. The actual rotor is replaced with a rotor with the same number of slots as the stator allowing the model to be modified as:

$$\frac{\text{axial length}}{2} \times \frac{\text{equivalent slot pitch}}{2} \quad (4-2)$$

A major advantage of this model is its ability to cope with modelling of any induction motor with any number of poles, slots in the rotor and stator, and with any shape of laminations.

2.1.1 Two dimensional modelling

Depending on the physical properties and loading conditions of the model, the heat transfer in the axial or peripheral direction may be ignored. If the heat transfer is negligible in any direction, a uniform temperature is assumed in that direction whence the number of dimensions in the model may be reduced to two. A cross-sectional two dimensional model

can be constructed when the heat transfer along the axial direction is ignored. When the peripheral component of heat transfer is ignored [11], the motor can be represented as an axisymmetric two dimensional model [17,56]. In an actual motor, the main tangential heat transfer may occur in the interface of slot walls in the core and the slot contents both in the rotor and the stator.

Cross sectional two dimensional modelling. This method has been used by some authors [32, 60, 78] in both steady state and transient analysis of induction motors. The effect of end windings and the end rings can not be included accurately. This is probably the main disadvantage of this modelling. The error becomes significant in the transient analysis where a large temperature variation is expected along the axial direction. Details of implementation of this method is explained in section 3.1 in chapter 5.

Axisymmetric modelling. In this method some approximations on both the material properties and distribution of the loads is inevitable. In fact, the character of this model demands a cylindrical geometry for any individual part in the model, including the stator and rotor teeth and windings. However, in an actual motor, the teeth and the embedded parts of the winding in the rotor and similar parts in the stator share the same cylindrical space in the model individually. Therefore, some equivalent components should be defined to represent the effect of the combination of the teeth (iron) and the windings in the stator (copper) and the rotor (copper or aluminium) individually. In addition, a suitable scheme should be specified for application of the ohmic and iron losses in each area.

3.0 HISTORY OF THERMAL MODELLING OF INDUCTION MOTOR

Thermal modelling of an induction motor is a wide area which accommodates any study on the temperature and heat transfer related problems in the induction motors. Some examples on this issue are the thermal protection of induction motor [87], study on the thermal stress in the rotor bars [26, 29], temperature distribution in an inverter fed motor [14] and study on the influence of any second order parameter on the motor heating.

A short and statistical review on the number of induction motor related papers show that there has been less attention into the thermal modelling of induction motors compared to any other analysis fields of this type of electric machines. Probably, this is because majority of the electrical engineers are less interested in the heat transfer related problems compared to

their main fields of study, or they do not classify this subject within the field of electrical engineering. Therefore, there is an intermittent work in this area. As an example, the number of thermal analysis related articles in the proceedings of five successive “IEE International Electrical Machine and Drive” Conferences from 1989 to 1997 are shown in Table 4-2. As

Table 4-2 A statistical survey of the field of papers in ICEM’s

Year	Total induction motor related papers	Thermal analysis related papers
1989	15	0
1991	9	2
1993	28	1
1995	26	2
1997	not available yet	not available yet

another example, the number of records with some relevant keywords were searched in the “FirstSearch” database in the field of science and engineering. This database covers the scientific and technical journals and conference proceedings in physics, electrical engineering and electronics, computing and control, and information technology from January 1969 to the present. The results of this search, performed on 7 August 1997 are tabulated in Table 4-3. Still, the majority of the published works are studied the motor under

Table 4-3 Search results in FirstSearch database on 7 August 1997

Key words used	Number of records found
induction motor+*	7739
analysis induction motor+	786
thermal induction motor+	73
temperature induction motor+	54
heating induction motor+	30
thermal analysis induction motor+	16
heating cage rotor+	4

* The sign “+” at the end of word acts as a wild character in the search, allowing to find all words starting with motor.

steady state conditions using different approaches.

Thermal systems have distributed parameters [87] and therefore any attempt for a pure analytical solution of the associated thermal field must be based on unrealistic

simplifications. In order to investigate the effect of peripheral variation of rotor bar currents in an induction motor, Williamson and Lloyd [78] carried out an analytical simulation on a copper bar cage rotor at standstill. They studied the thermal field of a rectangular bar, assuming a uniform distribution of electric conductivity throughout the bar and also ignored the heat flow through the bar/core interface during the early seconds after start up. The analysis results were verified by measurement. A peripheral variation of 39°C to 95°C was recorded in the cage of an open-slot, 3mm air-gap, 425kW stalled induction motor within the first 30 seconds.

Construction of a lumped parameter model is also based on some simplifications. In a LPM the thermal system is divided into a number of components and each component is represented by a thermal node. The nodes are inter-connected via fixed thermal resistances. In general, LPM suffers from the following problems:

1. The temperature distribution is assumed to be uniform within any component, being equal to the temperature at the assigned node;
2. The thermal resistance between any pair of adjacent components is assumed to be constant with time.
3. The physical location of the nodes in the motor for the purpose of temperature measurement may not be clear particularly in models with few nodes,
4. In the models with a larger number of nodes, the geometry of some components must be significantly simplified. e.g. assumption of many components as cylindrical shells and the stator teeth as a collection of cylindrical segments connected thermally in parallel [47], or entire rotor segment including the core and bar parts, as single nodes [43] etc.

On the other hand, it is usually simple to implement and needs minor computing resources. In addition, it yields a simple insight to the internal heat flow between the components of any complex geometry.

Depending on the application of the model, the number of thermal nodes (excluding the reference node, normally the ambient temperature) in a LPM can be as few as two [14, 21] which yields rough values of temperature in the rotor and stator individually. In an improved

LPM, Mellor and et al. [47] divided the motor into 10 components and represented each component with one, two or three-node equivalent circuits so that a 20-node equivalent circuit was obtained for the motor by interconnection of individual components. This model was successfully used in the steady state and semi-steady state analysis of some induction motors.

In many cases, in particular in steady state analysis, at least one measurement is needed for the evaluation of thermal resistances prior to the model generation [11,14,42,47]. Namburi [49] used the steady state temperature rise in the motor as an indicator of power loss. This method gives more accurate results than that via direct measurement of the input and output powers. In his work, Namburi fitted the transient test results at five points in the motor on a set of lumped parameter based equations. Then he proposed a virtual lumped parameter method for the same motor to predict the temperature rise under a given load. Therefore, while this approach is obviously case dependant, the prediction of temperature is possible at the test points only.

Consideration of the aforementioned problems implies that although a LPM may be suitable for steady state analysis, its results can not be accurate enough in a transient analysis unless the number of nodes is large. In this case, the sizes of components may be small enough to assume a uniform temperature distribution within each component.

The rapid initial heating of the stator copper causes different time constants on the stator part of the model [14], in particular between the copper and the core. This gives rise to a significant difference between the maximum and the average values of temperature in the stator where, for design or protection purposes, the maximum temperature within any component (the hot point temperature) is more important than the average value within it. In his tests, Kylander [42] measured a wide steady state temperature variation of 20°C , (110°C to 130°C), along the axial length of a 15kW induction motor when running under 67% of rated load.

According to Zochol [87], the distribution of temperature throughout a motor is not as important as its value at certain critical points; assuming the air-gap as a good barrier between rotor and stator, he proposed a LPM including a combination of two uncoupled LPM's, a two-node model for the stator and a single node model for the rotor, and employed it in the evaluation of the temperature in some critical points within the motor both at the

steady state and the transient analysis. In a recent work, Kylander [43] generated a 107-node LPM for both steady state and transient analysis of small cage induction motors. Ignoring the peripheral temperature variation in general¹, he divided the motor axially into a number of shell elements while each element of individual components, such as rotor bars, stator teeth etc. was treated to have a peripherally uniform temperature. In addition to some other simplifications, all of the thermal contact resistances except for the one at the interface of the stator winding and stator core were ignored in Kylander's [43] work. Although it was a successful attempt, the simplicity of the method was sacrificed to improve the accuracy and capabilities of the modelling. The resolution and complexity of the method in fact approaches that used in the finite element method.

Elton's [21] work was based on a comprehensive interactive electrical, thermal and mechanical modelling. He extracted the distribution of current and the ohmic losses in the rotor bar from a ladder equivalent circuit for the deep bar rotor. The thermal model included two individual lumped parameter thermal models for the stator and rotor, assuming the air gap as a substantial barrier to heat transfer between the two main parts of motor. The swing equation of induction motor also was employed to represent the mechanical behaviour of the motor. He extracted the total losses for a 18000hp induction motor from the manufacturer's data to estimate the average temperature in each member rather than the temperature distribution in the motor body.

To improve the accuracy of the application of thermal loads on the lumped parameter method, Bousbaine [13] proposed the time-temperature method to identify the distribution of iron losses in the stator core. His method is involved the measurement of temperature at as many as possible points in the stator core. He installed 60 thermo-couples (TC's) in the stator core of a 4kW 4-pole induction motor, 20 TC's on each plane of three. Although it may improve the accuracy, the loading effect of the TC's may introduce a new source of error.

The so called "thermal network" method is used by some authors using the same basis as the lumped parameter method. Some basic theory of this method was described in section 2.4.2 in chapter 3 (page 60). When the network is constructed for the purpose of steady state analysis only, the capacitors to represent the thermal capacity of different parts are absent in

1. Only the temperature difference between stator coil sides and the stator teeth was taken into account.

the model. Using this method, Gryglewicz [31] studied the distribution of temperature within an induction motor with radial and axial cooling ducts and verified the results with direct measurement of temperature in some points within the motor including the cooling air. In another work, Cannistra [17] compared the outcome of his thermal network equivalent circuit with that of an axisymmetric finite element analysis while he applied the rotor losses at the top of rotor teeth. In addition, the reciprocal influence of heat fluxes between the rotor and stator was ignored in Cannistra's work assuming proper ventilation. In a relatively comprehensive network equivalent circuit, Gerlando [27] studied the thermal behaviour of a 2-pole, 3kW induction motor. He also included the effect of the reduction of heat exchange between the ribs and cooling air accepting: (i) the air flow reduces along the ribs, (ii) the temperature of the coolant air increases along the ribs.

In no circumstances can the accuracy of the results be better than that of input data. Yet, some sources of error arise during the computer simulation and/or the test. In the lumped parameter method, the distribution of loss density, mainly in models with a small number of nodes, is quite dissimilar to that in the actual motor which decreases the accuracy of the final results. For more sophisticated analyses of the motor, more complicated methods such as numerical techniques are employed.

Among the numerical methods FEM has been in more favour with electrical machine related analysts because of its capabilities. As explained earlier in this chapter, depending on the features of the model and the expected accuracy of the results, a two or three dimensional model may be constructed for an induction motor.

In his work, Bousbaine [12] ignored the axial heat transfer in a 15kW induction motor and constructed a cross-sectional 2D model in order to correlate the measured/calculated loss density distribution resulting from: (i) a normal three dimensional FE analysis by Sarker [63], (ii) a lumped parameter method by Mellor [47] and (iii) a temperature time method by Bousbaine [13]. The results showed a fairly good agreement in the stator parts but very large disagreement appeared in the rotor parts. He concluded that the uncertain temperature measurements on the running rotor parts were responsible for this error.

Ignoring the peripheral variation of temperature, Rajagopal performed a semi-transient analysis on two TEFC induction motors, 3.7 kW and 5.7kW to find the variation of

temperature in different parts when the motor is started and reaches to steady state conditions electrically and mechanically. He also used equivalent uniform thermal conductivities in the model to include the effect of the insulations and the copper in the stator.

During an investigation into the material for rotor bars, Dymond [19] split the motors into three groups, less than 250hp, 250hp to less than 2500hp and 2500hp or over. As long as the thermal capacity during stall conditions is adequate, and/or where the economics of mass production suggests, the use of cast aluminium rotor windings is preferred. From the view point of temperature rise, most units in the first group are generally stator limited. Casting of the rotor winding in the motors of the second group may be still more economical considering the quantity of mass production but the governing factor at stall conditions is the rotor thermal capacity. Machines of power 2500 hp or more are almost always manufactured using fabricated rotor cage construction as briefly described in chapter one.

Walker [73] used four open slot motors of 30, 425, 1306 and 2200 kW as his models and assumed that the highest temperature in a stalled condition, even for the 30kW motor, would occur in the cage bars and the end-rings as they are the regions with the highest loss density in the motor. His work was based on the thermal analysis of one periodicity part from a copper cage induction motor with simple cross section of bars including rectangular, L shaped or T shaped bars. To save computer resources, he preferred to break the model into four smaller parts. The rotor bar was modelled as a combination of 3-D geometry but with one dimensional thermal conduction along the bar and a 2-D model to carry out the temperature distribution in the bar cross section. He applied an adiabatic boundary in the interface areas between the bar and the slot walls to justify the single dimensional analysis along the bar although some heat transfer from the bar to iron was traced within the 2-D analysis. It is shown in section 3.4.1.2 on page 119 that the large interface area between the rotor bar and core provides a good medium for thermal communication between these parts, even in a copper cage.

Griffith & et al. carried out a comprehensive study on the thermal response of the rotor cage and studied the behaviour of the cage under different conditions, including acceleration, full load running and locked rotor. They represented the die-casted aluminium cage of a 600kW induction motor as a half slot pitch 3-D finite element model and extracted the distribution of

temperature within it. They demonstrated that a temperature difference, as large as 80 °K may occur between the top and the bottom parts of the bar within the first 25 seconds of stall.

In another attempt, Guenov [32] employed Schwar's method to reduce the governing 3-dimensional steady state heat transfer equation of:

$$k_x \cdot \frac{\partial^2 T}{\partial x^2} + k_y \cdot \frac{\partial^2 T}{\partial y^2} + k_z \cdot \frac{\partial^2 T}{\partial z^2} + q''' = 0 \quad (4-3)$$

into two simultaneous 2-dimensional equations like:

$$k_x \cdot \frac{\partial^2 T}{\partial x^2} + k_y \cdot \frac{\partial^2 T}{\partial y^2} + q''' = 0 \quad (4-4)$$

$$k_y \cdot \frac{\partial^2 T}{\partial y^2} + k_z \cdot \frac{\partial^2 T}{\partial z^2} + q''' = 0$$

where additional conditions were needed to satisfy other requirements.

In a recent work, Chan [18] carried out a study on the heating process of a rotor bar during start-up. Assuming equal heat generation and heat flow within each rotor slot pitch, he selected one rotor slot pitch as the domain of his transient heat flow study. From the generated 3-D finite element model Chan [18] showed that the temperature at the top parts of the bar may rise to a high level of 150° within 20 seconds, cooling to 50° within the next 30 seconds. He attributed this large drop in the temperature to a significant fall in the current at the top parts of the bar soon after starting, while a sensitivity analysis showed that the thermal conductivity and capacity of the bar and also iron core contributes significantly to damping the temperature gradient in an aluminium bar (see section 3.4.1 on page 116).

To the best knowledge of the author, as yet there are no published works on the three dimensional transient finite element thermal analysis for the entire induction motor. Therefore, in this project the full motor is studied and the relevant side effects are examined.

4.0 SOME CONSIDERATIONS ABOUT THE MATERIAL PROPERTIES

The validity of a thermal model relies strongly on the accuracy of the thermal constants of the materials in the thermal system. In many circumstances physical constants of pure materials or any particular alloyed materials are available in the manufacturer's manual, data tables or handbooks. However, in some cases a minor change in the ratios of impurity introduces a major change in the thermal properties of the material. Therefore, any uncertainty in the composition of the material may result in a significant analysis error.

Aluminium is used as the main material of cast rotor cages but pure aluminium is not suitable for die casting. In practice, to improve some physical properties of aluminium, including castability, it is alloyed with a certain percentages of copper, iron, silicon, titanium and/or vanadium depending on the desired properties. For example, in the small cages, the percentage of silicon is usually more than that in large cages in order to cope with die casting problems. Table 4-4 shows the variation of thermal constants of aluminium for some impurities. In this table, ρ , c_p , k and α are the density, specific heat, thermal conductivity and thermal diffusivity of aluminium. The composition of some alloys used in the cast

Table 4-4 Some thermal properties of Aluminium at 20 °C

Percentage of each metal	ρ , kg/m ³	c_p , kJ/kg°C	k , W/m°C	α , m ² /s ($\times 10^5$)
Pure: 100% Al	2,707	0.896	204	8.418
Al-Cu (Duralumin): 94-96% Al, 3-5% Cu, trace Mg	2,787	0.883	164	6.676
Al-Si (Silumin, copper bearing): 86.5% Al, 1% Cu.	2,659	0.867	137	5.933
Al-Si (Alusil): 78-80% Al, 20-22% Si.	2,627	0.854	161	7.172
Al-Mg-Si: 97% Al, 1% Mg, 1% Si, 1% Mn.	2,707	0.892	177	7.311

rotors are given in Table 4-5 as a percentages by weight [13]. Except where the range is given, the percentages are the maximum values. aluminium is the remainder.

The thermal conductivity of the iron core is also very sensitive to different types of impurities. As can be seen in Table 4-6, a slight impurity of carbon as small as 0.5% causes a significant fall in the thermal conductivity of iron as large as 19.1%.

Table 4-5 The percentage of each material in the compositions of aluminium used in cast rotor cages

Alcan composition Designation	Copper	Iron	Magnesium	Manganese	Nickel	Silicon	Titanium	Zinc	Other element	
									Each	Total
40020	0.10	0.50-0.8	-	-	-	0.28-0.48	-	-	0.03	0.10
42230	0.1-1.5	0.14-0.25	0.50-0.6	0.05	-	4.5-5.5	0.20	0.05	0.05	0.15
43020	0.10	0.6	0.05	0.10	-	4.5-6.0	0.20	0.10	0.05	0.15
44225	3.0-4.0	0.7-1.1	0.10	0.10	0.10	7.5-9.5	-	0.10	*	0.20
46050	0.10	0.7-1.1	0.07	0.10	0.10	11.0-13.0	-	0.10	*	0.20

* Tin, 0.1 Maximum

Table 4-6 Some thermal properties of Iron and steel (max. C =1.5%) at 20 °C

Percentage of each metal	ρ , kg/m ³	c_p , kJ/kg °C	k , W/m°C	α , m ² /s (x10 ⁵)
Pure iron	7,897	0.452	73	2.034
Wrough iron: C = 0.5%	7,849	0.460	59	1.626
Carbon steel: C = 0.5%	7,833	0.465	54	1.474
Carbon steel: C = 1.0%	7,801	0.473	43	1.172
Carbon steel: C = 1.5%	7,753	0.473	36	0.970

The thermal conductivity of laminated iron in the direction normal to lamination planes is significantly different from that in parallel to the laminating direction [58] and it varies as a function of some parameters such as:

- The pressure under which the laminations are clamped;
- the thickness of individual lamination sheets;
- the type and thickness of inter-lamination insulators;
- surface finish of laminations, i.e. whether hot or cold produced;

It is also significantly affected by the quality of punching. A poor quality of punching leaves some burres of unpredictable thickness at the edges of the cutting lines. This not only raises the effect of eddy currents, but alters the thermal conductivity of the iron packet along the axial direction. Therefore, the wide scatter in the values of thermal conductivities of sheet steel laminations in the existing literature [58] is not unexpected.

A similar problem exists in a group of stranded conductors as in the stator winding so that the thermal conductivity along the conductors is significantly larger than that across the

conductors. The ratio of the equivalent conductivities along the axial direction and across the strands is mainly a function of:

- (a) Diameter of individual conductors,
- (b) Thermal conductivity of the filling material (such as lacquer),
- (c) Filling factor of the slot.

Since the ratio of net copper area to the apparent winding area in the end winding is different from the slot filling factor, the effective thermal conductivity in this area should be evaluated separately. The application of the aforementioned considerations is explained in section 3.1.1 on page 102.

The electric conductivity of solid aluminium (or copper) in the rotor cage plays a leading role in the redistribution of current in the rotor bars. Fortunately, according to the existing data tables [35], the electric conductivity of aluminium does not change considerably when the percentages of the impurities vary within the normal limits.

4.1 A brief comparison of copper cages and aluminium cages

Since most of thermal and electrical properties of a cast aluminium and a fabricated copper cage are different, a clear and logical comparison between them is impracticable. There are still many other parameters, such as reliability, price for mass production, durability and so on which should be taken into account in an actual assessment of each technique. In this section, they are compared by looking at the thermal and electrical behaviour of each material when used as the cage.

The electric conductivity of aluminium is about 60% that of copper. Thus an induction motor with assembled copper cage may have a better on load efficiency but with less starting torque than that of an aluminium cage of the same size.

On the other hand, the density of aluminium is about 30% of copper. Therefore, the weight of an aluminium conductor is half that of an electrically equivalent copper conductor. Also, the aluminium cage experiences less stress from centrifugal forces; it has less starting inertia; and produces less vibration while running.

The thermal capacity of an aluminium cage is slightly more than that of an electrically equivalent copper cage. This results in less temperature rise in a motor at stall during the same period.

* * * * *

CHAPTER FIVE

MODELLING PROCEDURE

Contents: Model Generation for Magnetic Analysis, Boundary Conditions for Magnetic Model, Application of Loads (currents) on the Magnetic Model, Determination of Equivalent Circuit Parameters, Model Generation for the Thermal Analysis, Boundary Conditions on the Thermal Model, Applying the Loads on the Thermal Model, Sensitivity Analysis, Sensitivity Analysis of the Rotor Parts, Sensitivity Analysis of Stator Parts, Sensitivity to Convection Film Coefficients.

1.0 INTRODUCTION

In this chapter, the general procedure of the model generation along with some concerns about the modelling are addressed. First the procedure of the magnetic modelling is described and then it is repeated for the thermal part. In the mean time, the effect of stator mmf spacial harmonics and also the results of sensitivity analysis for some parameters are discussed.

In general, depending on the specification of any model, a certain fraction of the motor could be selected as a representative of the total body. By taking advantage of periodicity planes, one pole pitch of the motor is modelled to carry out the magnetic analysis. However, for a transient thermal analysis, more periodicity planes were detected. Therefore, only one slot pitch of the motor is used to construct a 3 dimensional thermal model.

Note: This chapter is dedicated to discuss the general modelling procedure for both models and all of the discussion, unless expressed explicitly, equally applies on both models. Therefore, for the sake of simplicity and space saving, and in particular avoiding repeated materials, all of the discussion is referred to model one, a 15kW TEFC motor; also, the given figures are also related to this model to keep the consistency of the figures.

The units of temperature in all graphs and illustrations in chapter and the rest of this thesis is degrees Celsius, ' ($^{\circ}C$) .

2.0 MAGNETIC ANALYSIS

Magnetic analysis of the model includes four main stages:

- (a) Model generation,
- (b) Applying the boundary conditions,
- (c) Applying the loads,
- (d) Solution.

2.1 Model generation for magnetic analysis

Since the numbers of stator slots and also rotor slots per pole are whole numbers, selection of one pole pitch of the motor to construct a 2-D model was a straight forward process. Otherwise, the rotor should have been substituted by an equivalent rotor [79].

All parts of the model are meshed mainly with rectangular second order plane elements. The element sizes are selected considering the local complexity of the field, finer meshing in the air-gap and slots areas, and some coarser ones in the middle parts of the rotor core as well as the stator yoke. With an optimum variation of element sizes in the model, the smallest size of database along with the shortest computing time can be achieved without sacrificing the accuracy of solution. Unfortunately, there is still no well defined criterion for this optimization; therefore, the choice of the most suitable element sizes in each part of the model is guided by experience and preliminary results. The air-gap is meshed with square elements each occupying one electrical degree of the air-gap so that the magnetic field parameters in the air-gap are averaged in any one electrical degree.

Fig. 5-1 shows the overall meshing of the model along with the details of the meshing for a selected area.

The rotor bar elements are treated as conducting areas to allow inclusion of the skin effect. Normally, the area of any single conductor in the stranded stator winding is too small to be considered as subject to eddy currents. Also, the eddy currents induced in the laminated iron core can hardly modify the magnetic field established by the currents in the stator and rotor windings. Therefore, the stator winding and the iron core areas are treated as non-conducting

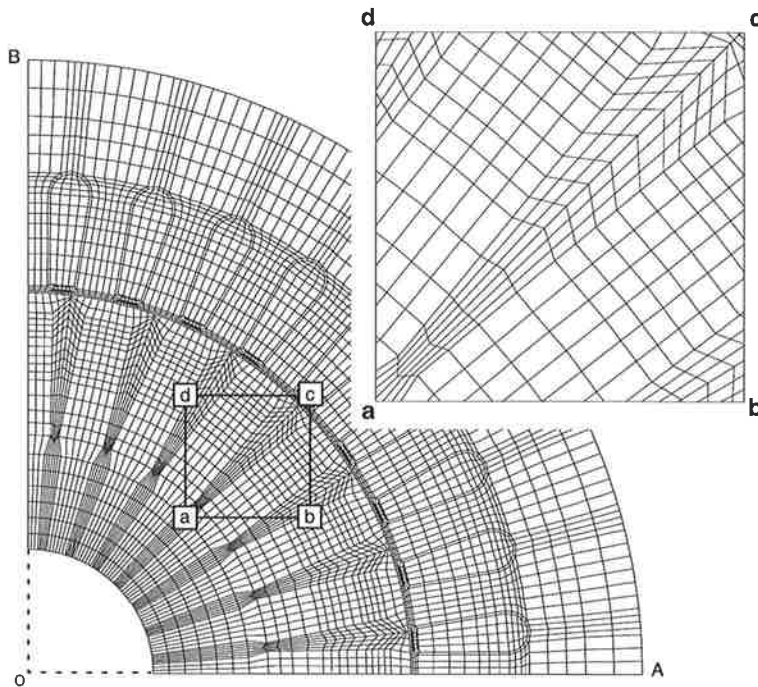


Fig. 5-1 Meshing layout for one pole of Model 1 and the details of the selected area

areas in the finite element model. Although the effect of eddy currents in the iron core are ignored in the magnetic analysis but the distribution of eddy current and hysteresis losses in this component is evaluated separately and is included in the thermal analysis.

2.2 Boundary conditions for magnetic model

To carry out the magnetic field analysis, the boundary conditions for the model should be well defined. The magnetic permeability of iron, mainly in the outer parts of the stator core, where the iron is not magnetically saturated, is much higher than that of air. Therefore, it is assumed that the flux lines are closed within the iron rather than leaking out. This means the external surface of the stator can be treated as a magnetic equi-potential surface. This boundary condition is applied on the model by imposing:

$$\dot{A}_z = 0 \quad (5-1)$$

on all nodes at the external surface of the stator core. In addition, since the skin depth on the solid shaft is very low at frequencies over 10 Hz [59], in practice no flux line penetrates into the shaft at standstill, where the frequency is much higher than 10 Hz. Therefore, the same boundary condition as the external surface of the stator core, (5-1), is applied on the inner surface of the rotor core. The skin depth is defined as:

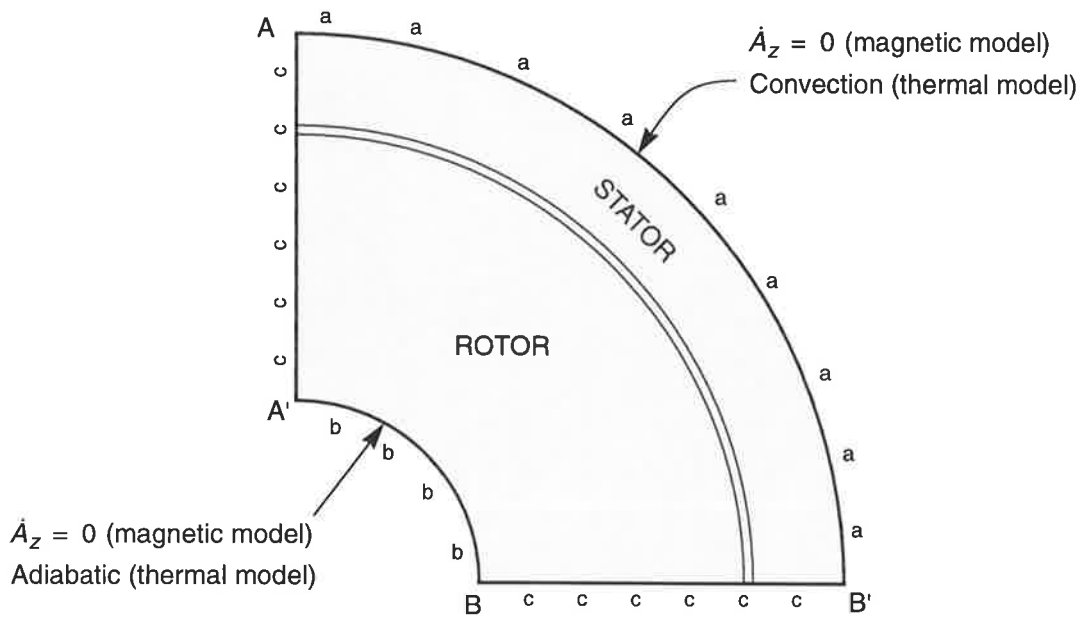


Fig. 5-2 Demonstration of the applied boundary conditions,
a and b:Equi-potential boundaries in magnetic model
a and b:Convection and adiabatic boundaries in thermal model
c: Constraint boundaries in both models.

$$d_{sk} = \sqrt{\frac{2}{\omega\mu\sigma}} \quad (5-2)$$

in which d_{sk} is the “skin depth”. Fig. 5-2 shows different applied magnetic boundaries on model 1 (and model 2). To impose a π -electric radian peripheral periodicity on the radial surfaces of the model, AA' and BB' in Fig. 5-2, a constraint boundary condition of:

$$\dot{A}(r, 0) = -\dot{A}\left(r, \frac{\pi}{2}\right) \quad (5-3)$$

is applied on the nodes at these boundaries. In this equation, $\dot{A}(r, \theta)$ is the mechanical coordinates of any node in the cylindrical coordinate system.

2.3 Application of loads (currents) on the magnetic model

The currents may be applied on the finite element model in some different ways as described in section 7.2 on page 42. In this analysis, option 3 in which only the fundamental harmonic of stator and rotor mmf's are considered, was found to be optimal. The rotor and stator

currents are applied on the areas of rotor and stator slots individually as two sets of sinusoidally distributed current density loads.

This means the stator winding is substituted by an equivalent cage (see appendix A); the amplitude of the currents is the same in all slots but they are equally time phase shifted in successive slots. It is noteworthy that the stator winding areas are still treated as non-conducting areas since they are not subject to eddy current (see section 2.1 on page 10). The amplitude of the rotor and stator bar currents are calculated from:

$$\hat{I}_{b,rot} = \frac{3k_{w1}N_{ph}}{S_2/2} \cdot \hat{I}_2 \quad (5-4)$$

$$\hat{I}_{b,stator} = \frac{3k_{w1}N_{ph}}{S_1/2} \cdot \hat{I}_1 \quad (5-5)$$

respectively where:

$\hat{I}_{b,rotor}$ = Amplitude of the bar current in the rotor cage;

$\hat{I}_{b,stator}$ = Amplitude of the bar current in the equivalent stator cage winding;

\hat{I}_1 and \hat{I}_2 = Amplitudes of stator and rotor currents calculated from the equivalent circuit.

The phase angles between I_1 and I_2 should be modified as a function of the slot pitch angle on each member of the motor to provide the actual spatial phase shift between the stator and rotor mmf's in the finite element model.

Fig. 5-3 shows the stator winding diagram for phase A of model one. The stator has a double layer, 1-7, 1-9, 1-11 concentric winding. The Fourier analysis results for the distribution of mmf in the air-gap, when the actual currents are applied on the stator winding only, is shown in Fig. 5-4. Fig. 5-4a shows only the higher order harmonics in the air-gap while they are compared to the fundamental component in Fig. 5-4b. In order to evaluate the accuracy of the analysis, all of the extracted components are added and are compared to the actual distribution of the mmf in Fig. 5-4c. In this figure, the fundamental component of the mmf is

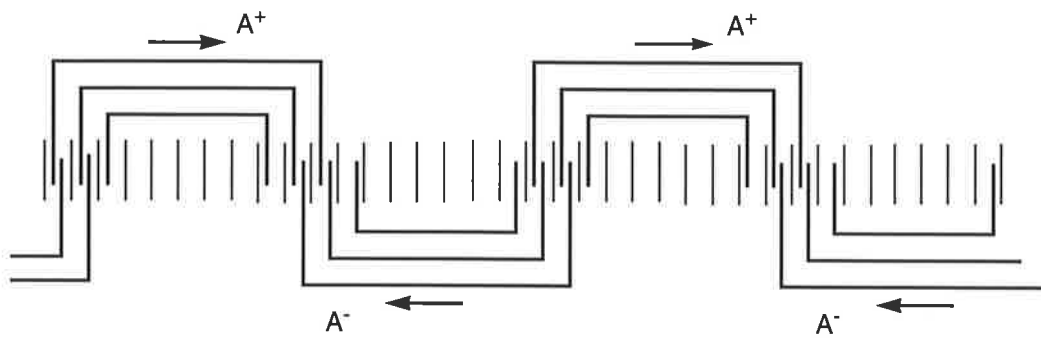


Fig. 5-3 Winding layout for phase “A”

also shown as a criterion for comparison. Similar comparison have been carried out for the following excitation and the results are shown in Fig. C-1 to Fig. C-3 in Appendix-E:

- (a) When only the stator winding is excited with sinusoidally distributed currents (Fig. C-1);
- (b) When only the rotor winding is excited with sinusoidally distributed currents (Fig. C-2);
- (c) When both the stator and rotor windings are excited with sets of sinusoidally distributed currents (Fig. C-3);

As can be seen, the amplitude of individual higher order harmonics resulting from the stator excitation only are almost zero while they are about 0.1% to 0.4% of the fundamental component when the rotor bars (only) are excited. This may be attributed to the per pole number of rotor slots, 7, which gives rise to the amplitude of these orders of harmonic. The distribution of the real component of the actual flux density in the air-gap and its harmonics are also shown in Fig. C-4. The methods of the solution to achieve the flux density is explained in the following section.

2.4 Solution

In order to take saturation effect into account, the “effective reluctance method”, as described in section 7.1 on page 36, is used (for this model only). The procedure of the solution is shown in Fig. 2-8 in the same chapter. As can be seen in Fig. 2-8, a set of initial values is needed in order to initiate the solution. The number of iterations in the solution process is

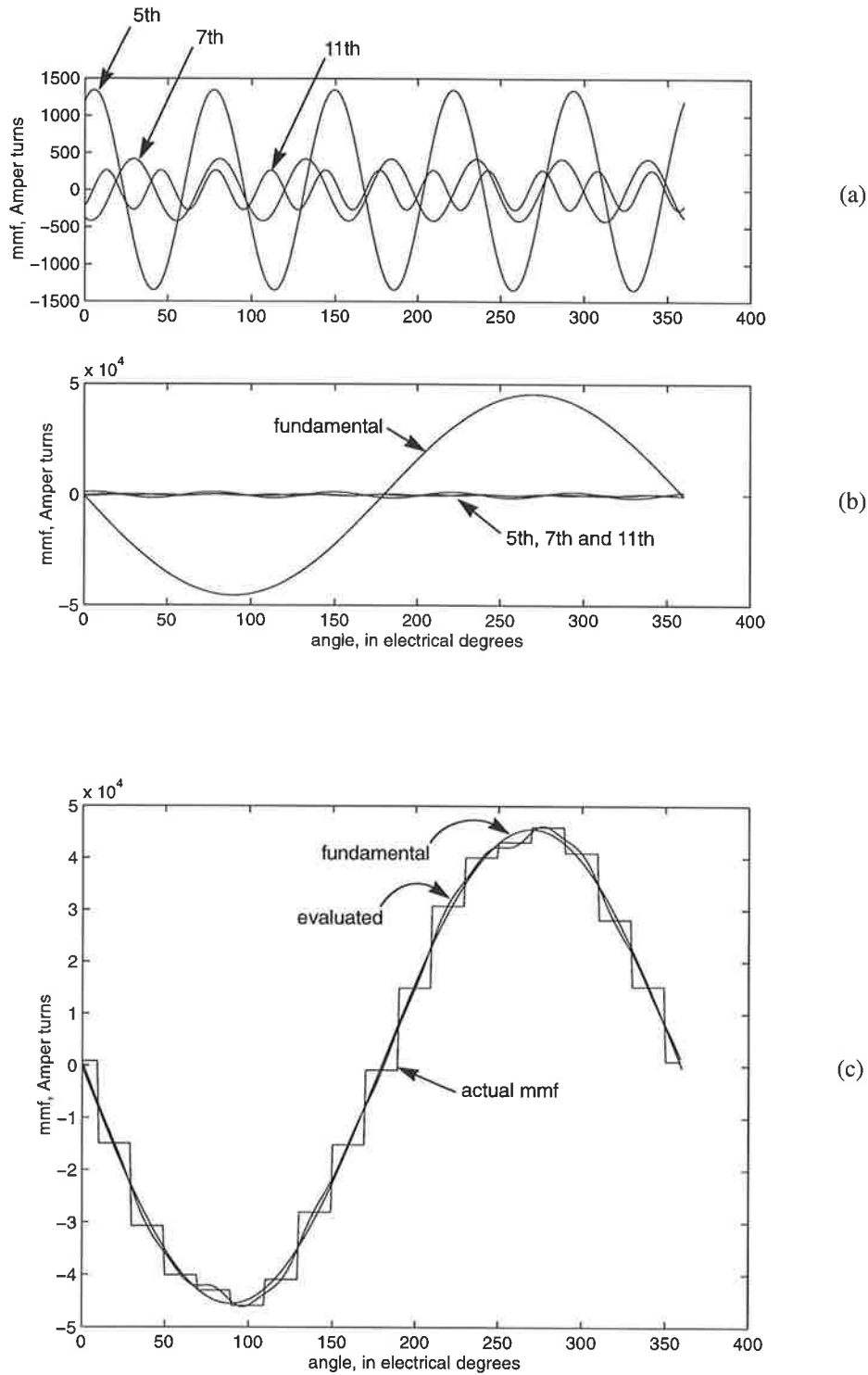


Fig. 5-4 Distribution of field mmf when the actual currents are applied on the stator winding only:

- a:** Distribution of 5th, 7th and 11th space harmonics,
- b:** Distribution of 5th, 7th and 11th space harmonics along with the fundamental harmonic,
- c:** Actual field mmf along with the fundamental and the evaluated mmf distribution

strongly dependant on the accuracy of these values. In particular, since the magnetic circuit of the motor at stall is extremely saturated in some parts, a wide variation in the local reluctivities within the magnetic circuit is not unexpected. Therefore, regarding the CPU time, a good estimation of initial values becomes more critical in this solution. The distribution of the real component of current density in the bars and also the flux density in the 2-dimensional model, when the motor was supplied by the rated voltage, are shown in Fig. C-5 and Fig. C-6 respectively.

2.4.1 Estimation of local reluctivities

Because of the wide variation of reluctivities in the model, loaded with locked rotor currents, any attempt to a random estimation of reluctivities failed. In other words, although the relevant magnetic characteristics ($\nu(B)$ and $\nu^2(B)$) were carefully smoothed, the amplitude of oscillation of the ν at the elements was not damping down in successive iterations. Therefore it was decided to perform a static FE analysis on the model with a set of dc currents in the rotor and stator slots, each equal to the real component of the current phasors at that stage. Then the resultant flux density distribution was used to estimate the initial values for the local reluctivities for the same loading¹.

The non-linear solution stage (block 2 in Fig. 2-8, detailed in Fig. 2-9) was iterated 9 times before the convergence was achieved; this is only one iteration for the inner loop in Fig. 2-8. A variable acceleration factor (see section 7.1 on page 36) was used and the stator and rotor currents were applied in 3 sub-steps in order to minimise the amplitude of oscillation of local reluctivities. The CPU time may be extremely long if the values of initial currents are not close enough to the actual values in the motor. This case is not expected for the analysis of the motor when it is operating with the rated load current.

Since the motors were available, it was preferred to find the accurate currents to be applied on the models for the sake of time saving. Although determination of the accurate values for the voltage dependant equivalent circuit parameters was not a straight forward procedure (see the next section) it was still preferred because it allowed finding the motor currents for any values of applied voltage.

1. This initiated a novel method (see Fig. 2-9) which became available for the solution of model 2.

2.4.2 Determination of equivalent circuit parameters

Although the results of a normal locked rotor and no-load tests may be accurate enough for many engineering purposes, they suffer from the following sources of error in general:

- (a) The waveform of the stator current is assumed to be sinusoidal although it is distorted as a result of non-linearity in the magnetic circuit. This introduces some measurement errors, mainly in the measurement of current,
- (b) The resistance of the rotor is extracted from the results of blocked rotor while it is different when the motor is running (deep bar effect [1]),
- (c) The value of X_m , is extracted from the no-load test with the expected operating voltage, assuming a constant sinusoidal voltage of $E_m = \text{test voltage}$ is present in the motor during its normal operation. In practice, E_m is different from the applied voltage and varies with load as a result of voltage drop across Z_1 . In particular, it is no longer sinusoidal because of large non-sinusoidal voltage drop on Z_1 . The effect becomes severe for large stator currents, e.g. in a motor at stall or when running with large slip. In this case, the values of X_1 and X_2 are not constant as the magnetic circuit undergoes saturation.

In the standard locked rotor and no load tests, the motor is fed from a sinusoidal voltage source and the rms values of the voltage and current as well as the average value of associated power are measured by appropriate metering instruments. Even by using an accurate rms ammeter, the harmonic content of current will also be included in the measurement results. This causes some error in the determination of equivalent circuit parameters¹. Any distortion in the waveform of voltage will result in additional error since the measurement of voltage and power will not be valid any more.

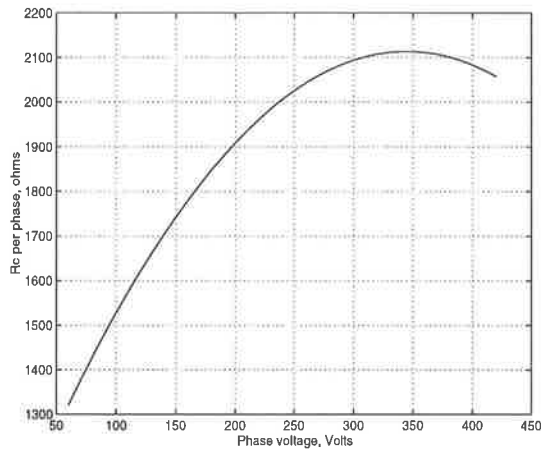
In a motor at stall, or operating with large slip, the large non-sinusoidal magnetization current may over-ride the load component of the stator current; resulting in a severely

1. This error is different from measurement error. In other words, it would occur even if the measuring instruments were ideal.

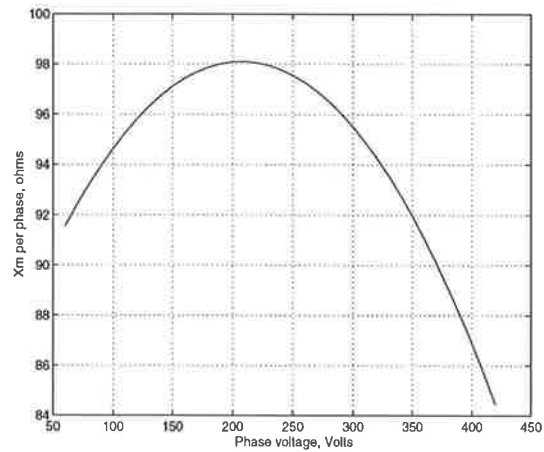
distorted stator current. Boglietti [10] showed that the equivalent circuit parameters of an induction motor, considering only the fundamental components of voltage and current, are the same when the motor is fed from a sinusoidal source or an inverter with a square or PWM waveform. In order to construct an equivalent circuit for the fundamental harmonic, the associated components of the current, voltage and power should be measured. Considering the above notes, in particular 'c', indicates that the standard procedure for the measurement of the equivalent circuit parameters will not be valid for the case of this study. Consequently, a modified method of test is used as describe below. In addition, since the results at some different voltages including the rated voltage are needed here, comprehensive tests were performed on both motors for this purpose. The available voltage source in the laboratory was found to be a flattened top sinusoid which gave rise to the harmonic content of the waveforms of current, voltage and power.

In order to measure the fundamental component (or any specific harmonic) of current, voltage and the associated power, the usage of filters is not recommended since they involve some new sources of error, such as phase shift error. Boglietti [10] employed a full digital power analyser PM3000 which allowed measurement of first harmonics of the parameter under measurement. In this project a recording device was used to save the time variation of current and voltage. A R340 Tectronics™ storage oscilloscope with a R232 interface was used to transfer the data into a PC. The voltage was applied via a 1000:100 voltage transformer. In order to minimise the waveform and also phase shift errors for the current, a hall-effect current transducer was preferred. During the light running test, the shaft speed was held at the synchronous speed by a mechanically coupled synchronous motor and a DC motor for models one and two respectively. This was crucial mainly at no-load tests under low voltages.

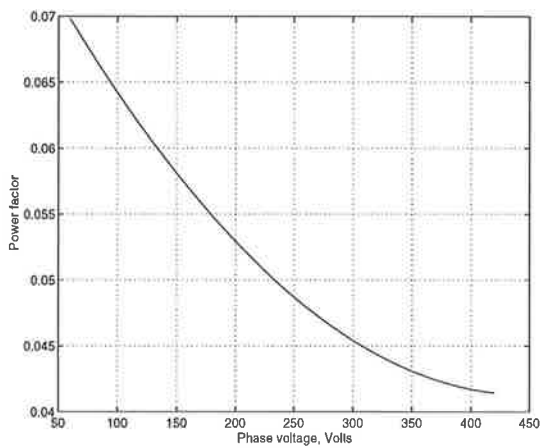
The test results for both locked rotor and no-load tests were recorded for a wide variation of applied voltage. The data were taken with a rate of 20000 samples/sec. and were processed to find the fundamental components of current and voltage from which the average value of power was extracted for each test point. Figures 5-5 and 5-6 show the results of these tests, including the values of the equivalent circuit parameters of the motor at stall within a wide range of voltage. Fig. 5-5 shows the variation of R_c and X_m as functions of the voltage, extracted from the OC test. Fig. 5-6a and Fig. 5-6b are resulted from the SC test only while,



(a)



(b)



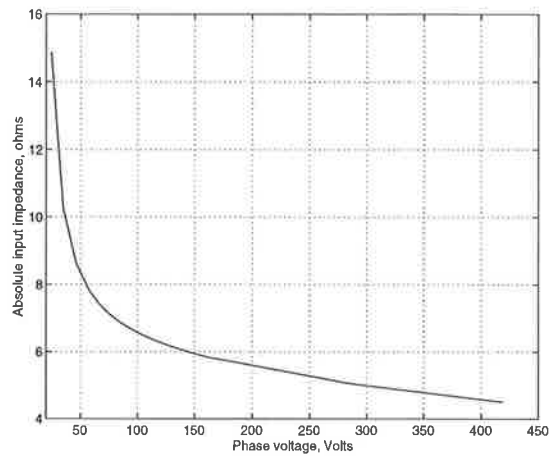
(c)

Fig. 5-5 Open circuit test results:
a: Variation of R_c with phase voltage;
b: Variation of X_m with phase voltage;
c: Variation of power factor with voltage.

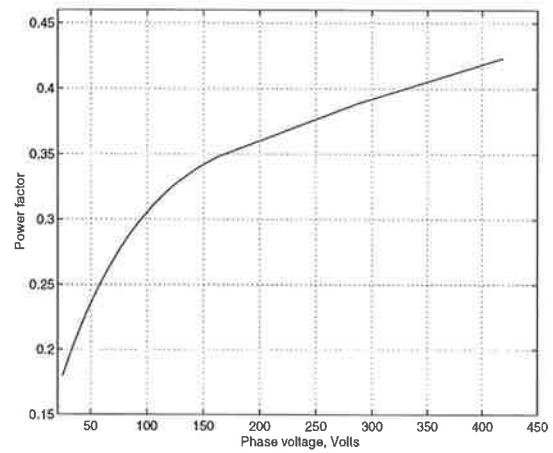
Fig. 5-6c and Fig. 5-6d are extracted from the combination of both tests, taking into account the effect of no-load branch on the SC results.¹ The corresponding set of SC test for any input voltage in the OC test is extracted on the basis of following assumptions in order to construct the equivalent circuit for any value of applied voltage:

1. The resistance of stator is known (by direct measurement as in the standard test);
2. The leakage reactance of the primary and the secondary windings are equal (as in the standard test);

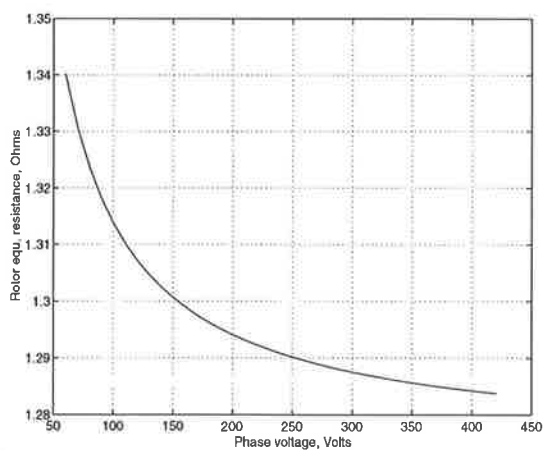
1. Each S.C. test was carried out for a short time only and the motor was left un-energised for a long time prior the following test to ensure the temperature in different parts of the motor remain within limited margins.



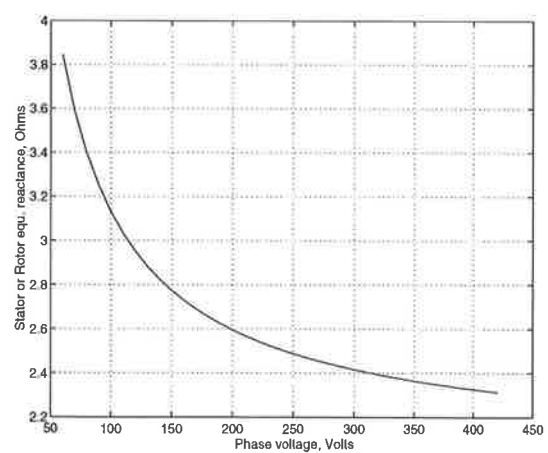
(a)



(b)



(c)



(d)

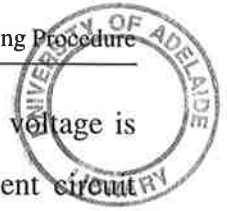
Fig. 5-6 Results from OC and SC test results:

a: Variation of SC input impedance with phase voltage;

b: Variation of SC power factor with phase voltage;

c: Variation of rotor resistance with SC input voltage;

d: Variation of rotor or stator reactance with SC input voltage



3. An OC test is considered to be corresponding to a SC test if the OC test voltage is equal to E_m in the SC test. This will take the variation of the equivalent circuit parameters with voltage and current into account.

3.0 THERMAL ANALYSIS

As the magnetic analysis, this analysis also includes the same stages as:

- (a) Model generation
- (b) Applying the boundary conditions
- (c) Applying the loads
- (d) Solution

3.1 Model generation for the thermal analysis

As described in section 2.0 in chapter 4, the entire thermal system of the induction motor is represented by a three dimensional model including a half of equivalent slot pitch and having a half of the axial length of the motor. In addition, a supplementary cross sectional two dimensional model is generated to investigate the effect of the variation of current in different rotor bars.

Three-dimensional model. The stator winding is divided into three parts as follows:

- Part 1. The embedded part of stranded stator winding in the stator slots;
- Part 2. The straight part of the extension of Part1 outside of the slot but before joining to the first bend of the inner phase belt;
- Part 3. The rest of the end winding;

Parts one to three are substituted by equivalent uniform solids, named as SBAR1, SBAR2 and SRING respectively with appropriate properties individually. The cross sectional area of SBAR1 and SBAR2 are similar to the whole winding area in the slot while SRING is a cylindrical shell with a larger cross sectional area which is extracted from the winding layout.

The rotor cage is also divided into two parts, the bar (RBAR) and the ring (RRING), considering their different thermal behaviours in the model.

All parts of the models are meshed with first order 3-dimensional 8-node solid elements. The complex parts of the boundaries might be meshed with higher order elements [62] to improve the accuracy of the results in the expense of significantly longer CPU time. However, an investigation showed no considerable improvement in the transient analysis results when higher order elements were used. In another preliminary analysis, it was found that the temperature gradient along the axial direction is much less than that in the radial direction. This allows a relatively coarser meshing along the axial direction. The other sizes of the solid elements are adopted to be similar to the two dimensional magnetic model meshing of the same model. In other words, the core and its contents in the 3-D model seems to be generated by dragging the 2-D magnetic element areas along the axial length. This allows an easier and in particular, more accurate transferring the thermal loads (loss density) from the magnetic model into the corresponding thermal model. Fig. 5-7 shows a general view of the 3-dimensional thermal model for model one. The stator winding and the rotor cage are shown in some more details in Fig. 5-8.

Two-dimensional model. Only one pole-pitch of the motor is selected to represent the entire motor. All parts of this model are meshed with 4-node plane elements with the same shapes and sizes as that of the magnetic model. The back iron areas are also meshed with similar elements. Therefore, the meshed 2-D thermal model for model one also appears same as the magnetic model as shown in Fig. 5-1, if the back iron areas are not shown.

3.1.1 Determination of material properties for conductive heat transfer

The conduction related properties of the constituent materials in a thermal model are:

- (a) Thermal conductivity, k_x, k_y, k_z ;
- (b) The specific heat capacity, c ;
- (c) Density, d .

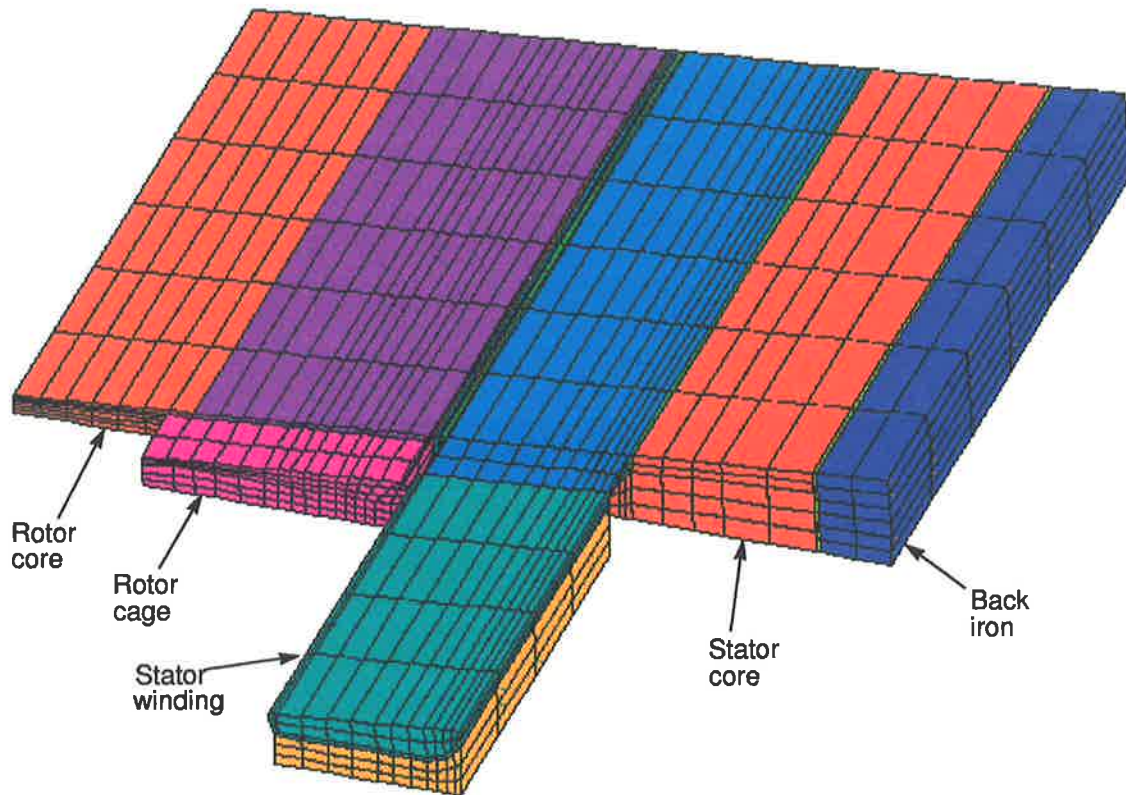


Fig. 5-7 Meshed volumes of the 3-dimensional thermal model for Model 1

Taking all of aforementioned properties into account, 8 and 9 different materials, including the equivalent ones, can be detected within entire bodies of models 1 and 2 as shown in Tables 5-1 and 5-2 respectively.

In order to include the effect of laminations in the iron core and also the effect of stranding in the stator winding, as explained in section 4.0 on page 85, the elements in these volumes are attributed as having orthotropic thermal conductivities along different directions as k_x , k_y and k_z . k_x and k_y are used to demonstrate the thermal conductivity along x and y direction across the motor where k_z denotes the same along the axial direction of the motor.

The conductivity of stranded copper winding is dominant along the wires. Therefore, k_z in parts one and two and also k_y in part three of the stator winding are the dominant

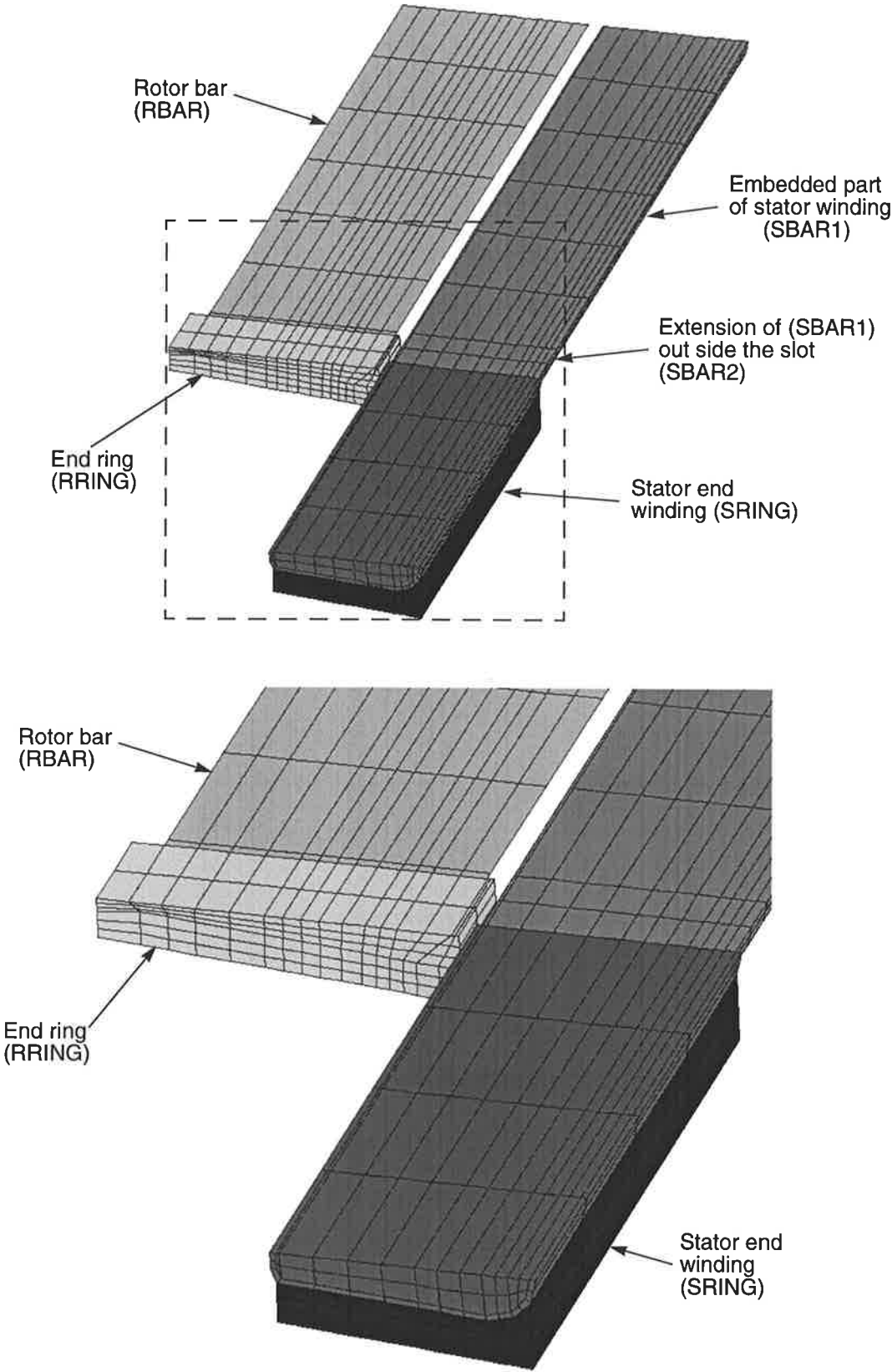


Fig. 5-8 a: The meshed view of the modelled parts of the stator winding and the rotor cage, b: The zoomed view of the shown part in 'a'

components of thermal conductivity in each part. The small arc of the slot pitch on the stator end winding is assumed to be a straight line in this evaluation. Parts one to three on the stator winding refers to SBAR1, SBAR2 and SRING in Fig. 5-8.

The effect of the pure areas of copper and lacquer in the slot should be taken into account in the evaluation of the properties of the equivalent material used for SBAR1. Let:

k_{laq} = Conductivity of laquer

ρ_{laq} = Density of laquer

c_{laq} = Specific heat of laquer

a_{laq} = Net area occupied by laquer

k_{cop} = Conductivity of copper

ρ_{cop} = Density of copper

c_{cop} = Specific heat of copper

a_{cop} = Net area occupied by copper

a_{slot} = slot area in the model occupied by stator winding

Then the equivalent values of k , ρ and c are calculated as:

$$k_{eq} = \frac{(k_{cop} \cdot a_{cop} + k_{laq} \cdot a_{laq})}{a_{slot}} \quad (5-6)$$

$$\rho_{eq} = \frac{\rho_{cop} \cdot c_{cop} \cdot a_{cop} + \rho_{laq} \cdot c_{laq} \cdot a_{laq}}{a_{slot}} \quad (5-7)$$

$$c_{eq} = 1 \quad (5-8)$$

In (5-6), k_{eq} is the dominant component of the thermal conductivity in each part. Equations (5-7) and (5-8) provide an equivalent thermal capacity in the model as in the actual motor.

The ratio of the a_{cop}/a_{laq} in SBAR2 is almost the same as it in SBAR1. Therefore, the same properties will be applied for SBAR2.

The gross cross sectional area, a_{gross} , in the end winding is usually larger than $(a_{cop} + a_{laq})$ because of less restriction in the end windings. The difference is assumed to be filled by air as $a_{air} = a_{gross} - (a_{cop} + a_{laq})$. Therefore, the properties of SRING is estimated from:

$$k_{eq} = \frac{(k_{cop} \cdot a_{cop} + k_{laq} \cdot a_{laq} + k_{air} \cdot a_{air})}{a_{gross}} \quad (5-9)$$

$$\rho_{eq} = \frac{\rho_{cop} \cdot c_{cop} \cdot a_{cop} + \rho_{laq} \cdot c_{laq} \cdot a_{laq} + \rho_{air} \cdot c_{air} \cdot a_{air}}{a_{gross}} \quad (5-10)$$

$$c_{eq} = 1 \quad (5-11)$$

The equivalent conductivity *across* the strands are strongly dependant on the filling factor of the slot and the shape of the conductors. Also, because of the inter-layer insulation in the slot, the radial component of this parameter is smaller than the peripheral component. Roger [60] obtained the mean equivalent conductivity of stranded copper conductors by averaging the conductivity of a group of round conductors in various random positions.

A similar process is carried out to include the effect of laminations in the iron core. Because of the inter-lamination insulation, the thermal conductivity of iron along the radial direction is slightly less than for pure core material. This is corrected by substituting an equivalent value calculated from:

$$k_{eq, radial} = k_{fe} \cdot k_{stack} + k_{insul} (1 - k_{stack}) \quad (5-12)$$

A typical values for the thermal conductivity of inter-lamination enamel, used by Williams [74], is $0.86 \text{ W/m} \cdot \text{°K}$ which introduces a 5% reduction in the radial thermal conductivity of a normal core packet with a stacking factor of $k_{stack} = 0.95$.

In contrast, the axial conductivity experiences a significant reduction as a result of laminating. Williams' [74] test results showed that the overall conductivity of a stack of laminations, normal to the plane of laminations is more influenced by the thermal contact resistance than the conductivity of the material of the laminations. The dominant part of this

resistance is formed by the fluid (usually air) trapped between the adjacent laminations. In addition, it is more sensitive to the change of the conductivity of the fluid than the change in the clamping pressure. Fig. 5-9 shows Williams' [74] test results (along with their

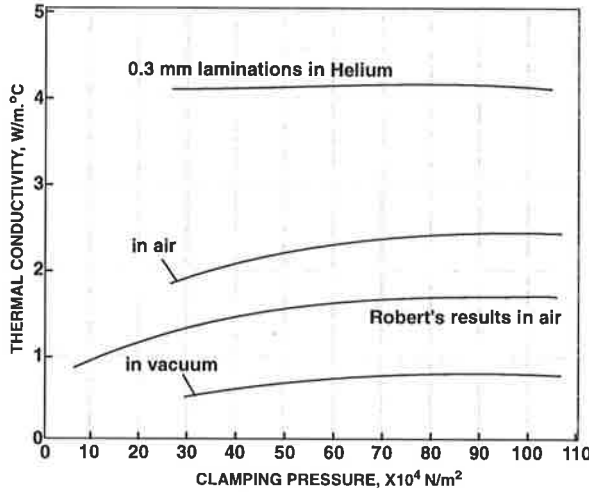


Fig. 5-9 Williams' [74] test results about the conductivity of laminated iron

comparison to Roberts's [58] results for air). As expected, the sensitivity approaches to zero for large values of clamping pressure.

Modification of Williams's [74] results for 0.3-mm laminations in an environment of air, into 0.5-mm laminations in the same environment results in a value of $3.33 \text{ W/m} \cdot ^\circ\text{C}$ for the conditions of this work. Considering the sensitivity of the results to a change in this parameter (see Table 5-7), the accuracy of this estimation can be acceptable for the purpose of this study.

The equivalent density and also specific heat in the laminated iron core are calculated from (5-13) and (5-14) respectively.

$$\rho_{eq} = \rho_{fe} \cdot c_{fe} \cdot k_{stack} + \rho_{insul} \cdot c_{insul} \cdot (1 - k_{stack}) \quad (5-13)$$

$$c_{eq} = 1 \quad (5-14)$$

The conductivity of the slot liners is uncertain although it is important in the determination of temperature in the stator winding parts. There is a wide scatter in the results of reported work for this parameter. While it was assumed to be zero in some works for a rectangular slot [78], a large value of $0.26 \text{ W/m} \cdot ^\circ\text{C}$ was assigned for the same parameter in Hwang's work for

the same slot profile [34]. In a recent work, Kylander [43] showed that the thermal resistance of the slot liner in his 15kW test model is equivalent to that of a 0.3 mm layer of air with the conductivity of $0.03 \text{ W/m}^\circ\text{C}$. He supplied the stator winding of this motor with a DC current in which all other parts in the motor remain lossless. Considering the geometry of the each model individually, the values of the thermal conductivities for this material were extracted from Kylander's work.

Tables 5-1 and 5-2 show the values of the material properties which are used in models one and two respectively. The references for some extracted parameters are not repeated in Table 5-2, since they are similar for both models.

Table 5-1 Thermal properties of different materials used in model one

Material	Thermal Conductivity $\text{W}/(\text{m} \cdot ^\circ\text{C})$			Specific Heat $\text{J}/(\text{kg} \cdot ^\circ\text{C})$	Density kg/m^3	Used in
	k_x	k_y	k_z	c	d	
Iron	54	54	0.98*	486	7750	RC and SC
Aluminium	204	204	204	896	2707	RBAR, RRING
Copper1	0.45**	0.45 ⁽ⁱⁱⁱ⁾	186.4 ⁽ⁱⁱⁱ⁾	1 ⁽ⁱⁱⁱ⁾	2462575.2 ⁽ⁱⁱⁱ⁾	SBAR1
Copper2	0.45 ⁽ⁱⁱ⁾	0.45 ⁽ⁱⁱ⁾	186.4 ⁽ⁱⁱⁱ⁾	1 ⁽ⁱⁱⁱ⁾	2462575.2 ⁽ⁱⁱⁱ⁾	SBAR2
Copper3	0.35 ⁽ⁱⁱ⁾	84.5 ^(iv)	0.35	1 ^(iv)	1287324.4 ^(iv)	SRING
Copper (pure)	386	386	386	383.1	8954	Not used directly
Lacquer ^(v)	0.19	0.19	0.19	1300	1200	Not used directly
Slot liner	0.06 ⁽ⁱ⁾	0.06 ⁽ⁱ⁾	0.06 ⁽ⁱ⁾	800	2000	Stator slots
Air	0.03	0.03	0.03	1009	0.9980	Air-gap

(i) From Kylander's [52] work

(ii) From Roger's work[60] with some modifications.

(iii) Equivalent values from (5-6) to (5-8).

(iv) Equivalent values from (5-9) to (5-11).

(v) From supplier's data sheet.

3.2 Applying the boundary conditions on the thermal model

The following boundary conditions are applied on each of the 3-D model:

- Convection boundaries on the outer surface of the motor, exposed to the surroundings.
- Convection boundaries on the surface of stator and rotor end winding exposed to end-cap.

(c) Adiabatic boundaries on the remaining parts.

Table 5-2 Thermal properties of different materials used in model two

Material	Thermal Conductivity $W/(m \cdot ^\circ C)$			Specific Heat $J/(kg \cdot ^\circ C)$	Density kg/m^3	Used in component
	k_x	k_y	k_z	c	d	
Iron (laminated)	54	54	0.98	486	7750	iron core
Copper1	0.40	0.40	189.6	1	2478408	SBAR1
Copper2	0.40	0.40	189.6	1	2478408	SBAR2
Copper3	0.3	79.8	0.3	1	1855660.72	SRING
Copper4 (pure)	386	386	386	383.1	8954	RBAR
Copper5	386	386	386	383.1	8954.0	RRING1
Copper6	276.3	276.3	276.3	1	2744731.9	RRING2
Lacquer	0.19	0.19	0.19	1300	1200	not used directly
Slot liner	0.06	0.06	0.06	800	2000	stator slots
Air	0.03	0.03	0.03	1009	0.9980	Air-gap

It is evident that the geometry of the convection boundaries is too complex to find an explicit analytical/empirical formula to calculate any accurate values of convection film coefficients, \bar{h} , for them. Furthermore, in a running motor, the end-cap is an enclosed cavity with a non-laminar air flow which adds the complexity of the problem. During a study on the temperature fields in ribbed frames, Kotrba [41] developed a formula to predict the steady state thermal properties of simple rectangular fins on outer surface of induction motors without taking the effect of the terminal box and other irregularities into account. Fortunately, in a motor at stall, even a wide variation of \bar{h} 's on these boundaries does not considerably affect the distribution of temperature within the body. This was confirmed by a set of sensitivity analyses (see Table 5-8). Therefore, some approximation in the evaluation of this parameter may be acceptable.

In this project, the outer surface of the motor is assumed as a horizontal cylinder in order to find the value of \bar{h} . The value of \bar{h} for a horizontal cylinder was calculated by using (3-39), (3-40), (3-44) and (3-37) respectively. Then the result was modified by using (3-48) in order to take the effect of fins into account. Since the outer surface of the frame is assumed to be a smooth cylindrical area in the model, the modification was applied on the value of calculated \bar{h} rather than the area of the exposed surface in the implementation of (3-48). Note that,

unlike the case of this study, the results of a steady state analysis are highly sensitive to the convection coefficient of this area. Most steady state LPM's need at least one direct measurement to determine this parameter [12, 14, 43, 47].

The stator end-winding and the rotor end-ring are also modelled as a smooth cylinders individually. The effect of extra outer surface areas is taken into account by modification of the film coefficients.

In addition to the above boundaries where relevant, a constraint condition is also applied on the appropriate nodes on the 2-D model to impose the effect of the periodicity. The counterpart of (5-3) on page 92 for this model is:

$$T(r, 0) = T\left(r, \frac{\pi}{2}\right) \quad (5-15)$$

where, $T(r, 0)$ and $T(r, \pi/2)$ are the temperatures on corresponding nodes on boundaries AA' and BB' in Fig. 5-2 and the angles are measured in mechanical radians.

3.3 Applying the loads on the thermal model

The thermal loads on the motor are extracted from the results of the magnetic analysis. The iron losses are calculated from (2-45) and the ohmic losses in the rotor bar areas and stator winding area are carried out by employing (2-47) and (2-36) respectively. However, as explained in section 3.2 on page 20, the total rms current in different bars of the rotor may vary as a result of stator mmf harmonics. In addition, since the physical properties of some materials in the model may vary with temperature, theoretically, they should be updated prior to starting any time step [6]. In practice, some properties are less sensitive to temperature so that they need not be updated at all, or they may be updated from time to time within the solution time depending on the local temperature rise. These problems are discussed in the following sections.

3.3.1 Calculation of rotor bar currents for 2-D model

The theory of stator spatial mmf harmonics was explained in section 3.2 on page 20. In this section, the effect of these harmonics is investigated on the distribution of heat generation on model 1. In order to explore the contribution of any individual harmonic on the ohmic losses,

a set of simulations were carried out and the per-unit ohmic losses in the rotor bars were calculated as a function of their angular positions; the peak value of rotor bar current is assumed as the base for PU calculation of current. The losses are calculated in a 1PU resistance on an arbitrary basis. Table 5-3 shows the results of this calculations in brief. A

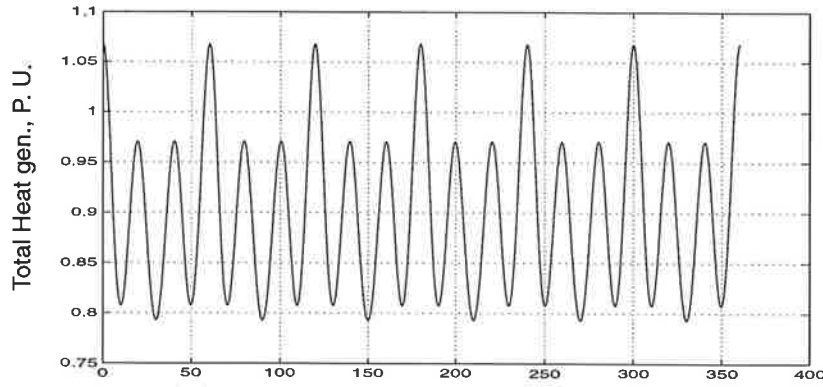
Table 5-3 The contribution of each harmonic in the losses of a rotor bar in different positions

Rotor bar no.		RB1	RB2	RB3	RB4	RB5	RB5	RB6	RB7
Angle (elet. deg.)		0	12.8571	25.7143	38.5714	51.4286	64.2857	77.1429	90.0000
Contribution of different harmonics	1st	0.8934	0.8934	0.8934	0.8934	0.8934	0.8934	0.8934	0.8934
	5th	0.0272	0.0067	-0.0230	-0.0157	0.0173	0.0246	-0.0051	-0.0257
	7th	0.0085	0.0017	-0.0072	-0.0051	0.0051	0.0076	-0.0020	-0.0079
	11th	0.0054	-0.0047	0.0031	-0.0012	-0.0011	0.0034	-0.0047	0.0050
	13th	0.0107	-0.0092	0.0063	-0.0020	-0.0024	0.0066	-0.0088	0.0099
	17th	0.0586	-0.0302	-0.0076	0.0496	-0.0450	0.0156	0.0342	-0.0483
	19th	0.0549	-0.0266	-0.0108	0.0449	-0.0392	0.0107	0.0313	-0.0408
	23rd	0.0067	0.0033	-0.0013	-0.0055	-0.0048	-0.0013	0.0039	0.0050
	25th	0.0027	0.0013	-0.0004	-0.0022	-0.0019	-0.0006	0.0015	0.0020
SUM		1.0683	0.8358	0.8524	0.9563	0.8215	0.9601	0.9436	0.7928

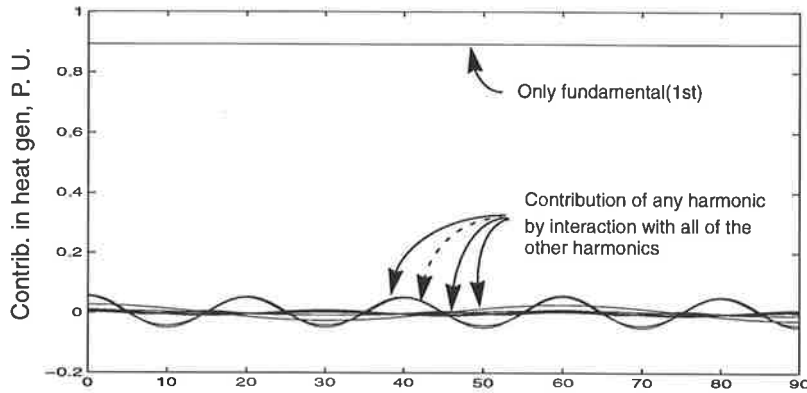
more comprehensive demonstration of this effect can be seen in Fig. 5-10. Fig. 5-10a shows the variation of entire heat generation in a rotor bar as a function of its relative mechanical position to the stator mmf when the higher order harmonics of 5, 7, ...25 are taken into account. Similar figures but taking some less harmonic orders are given in Fig. C-7 to Fig. C-9 in appendix C.

In Fig. 5-10b the contribution of the fundamental harmonic only is shown as a reference to be compared with the contribution of other harmonics. Figures 5-10c and 5-10d show the contribution of higher harmonics in detail. The calculations show that the interaction between any harmonic with the fundamental harmonic produces the main contribution of that harmonic in the heat generation, as could be expected. This fact can be seen as the dominant harmonic in the figures.

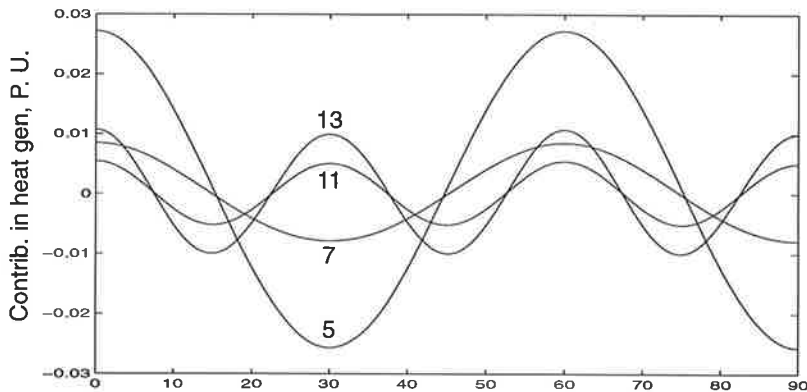
Since only one slot pitch of the motor is considered in the three dimensional model, the bar with the maximum loss is selected for modelling. However, the effect of non-equally distributed losses in the bars are investigated in a two dimensional model.



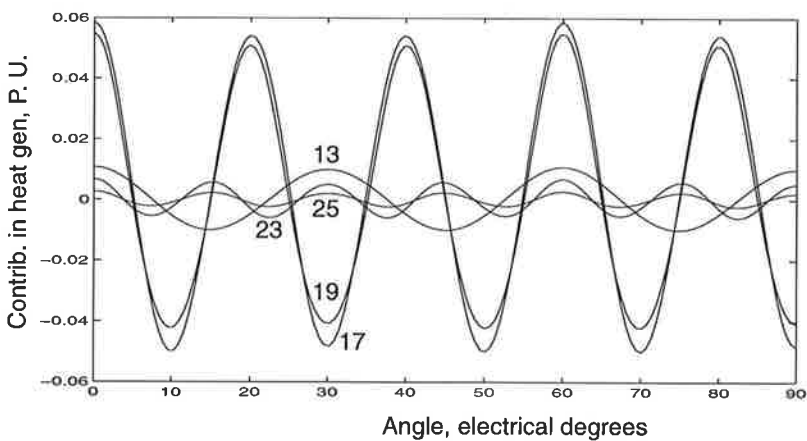
a: Total heat generation by taking the 1st to 25th harmonics into account.



b: Contribution of each harmonic in the heat generation as described.



c: Contribution of 5th to 13th harmonic in the heat generation as described.



d: Contribution of 13th to 25th harmonic in the heat generation as described.

Fig. 5-10 Demonstration of contribution of some harmonics in the heat generation.

3.3.2 Effect of temperature changes during the solution procedure

Since the magnetic reluctivity of iron and also the electric and thermal properties of many parts in the motor are theoretically temperature dependant, some parameter modifications may be necessary during the solution. At the same time, the stator and rotor currents also vary as a result of temperature rise in the windings.

The variation in the temperature in the rotor bar not only alters the rotor resistance (R'_2 in Fig. 2-1) but it modifies the current distribution in the rotor bars and consequently affects both the total losses and the distribution of thermal loads. Fig. 5-11 shows the distribution of

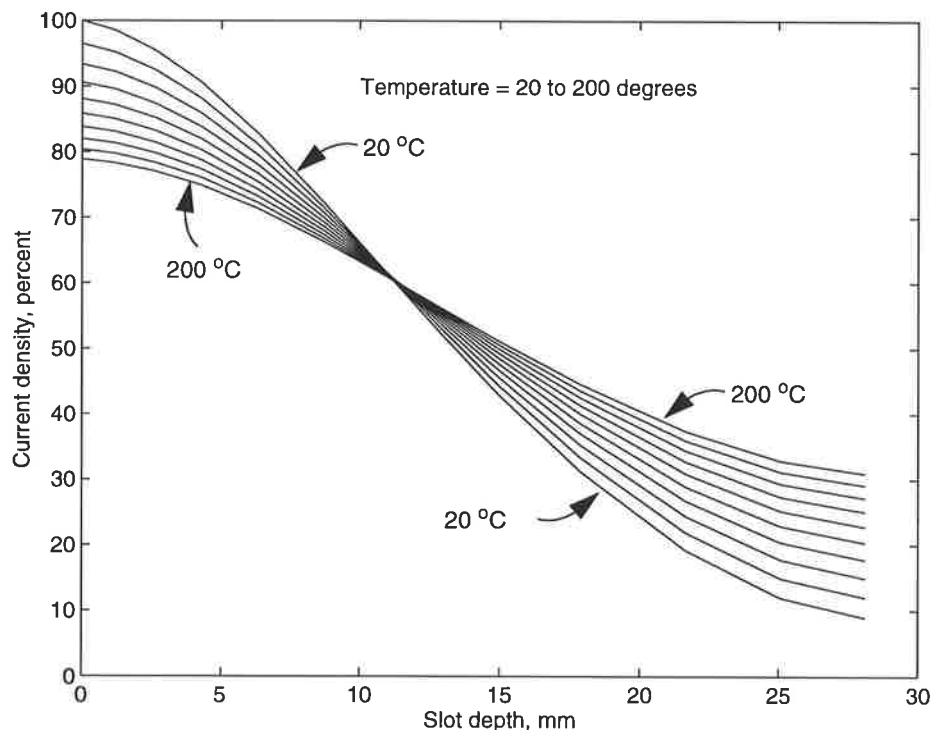


Fig. 5-11 Distribution of current density along the depth of the rotor bar in different temperatures

current density along the radial axis of a rotor bar as a function of bar temperature in model one. This figure is extracted while the bar temperature is assumed to be uniform at any pre-assumed value. However, this is unrealistic in an actual motor unless at steady state conditions. The non-uniform current distribution in the bar establishes a non-uniform temperature rise rate in the bar, high at the top and lower at the bottom parts. Accordingly, the local electrical resistivity within the bar area varies with local temperatures. In order to

include these effects in the solution, a procedure as shown in Fig. 5-12 should be implemented to carry out an actual thermal analysis. At the end of each time step the local temperatures in the rotor and stator winding elements are extracted. The average temperature in the stator winding is used to re-estimate R_1 in the equivalent circuit of Fig. 2-1 on page 15 from:

$$R_1(t) = R_1(0) (1 + \alpha t) \quad (5-16)$$

Also, the elemental conductivities in the rotor bar along with the equivalent circuit parameters should be updated prior to any magnetic solution. In practice, variation of thermal parameters between any two short time steps is very small associated to the accuracy of the available physical data. Therefore, in order to shorten the solution time, the variations may be checked in each time step and applied if they are larger than a pre-determined resolution. Still a rather long solution time is expected if the non-linear magnetic analysis is due to be executed several times for different conditions of the motor within the thermal solution steps. Some thermal properties of the major constructional materials in the models are listed in Table 5-4.

Table 5-4 The variation of thermal conductivity and the thermal coefficient of electric resistivity for some main parts in an induction motor [33].

Material	Thermal Conductivity, $W / (m \cdot ^\circ K)$				Thermal coefficient of resistivity at 20°
	0°	20°	100°	200°	
Pure copper	386	386	379	374	0.00397
Pure Aluminium	202	204	206	215	0.00406
Pure iron	73	73	67	62	not needed
Air	0.0241	0.0262	0.0317	0.0386	not needed

The variation of the bulk temperature in the end-cap area alters the convected heat from the end windings both on the rotor and the stator into the endcap. The average temperature in this area may be estimated by looking at the total increase in the internal energy of the air in this enclosed cavity. However, it was found that for a motor at standstill and during the early transient time, this effect is negligible (see Fig. 5-20). The effect of temperature on the thermal properties of the model are investigated in the following sections as a set of sensitivity analyses.

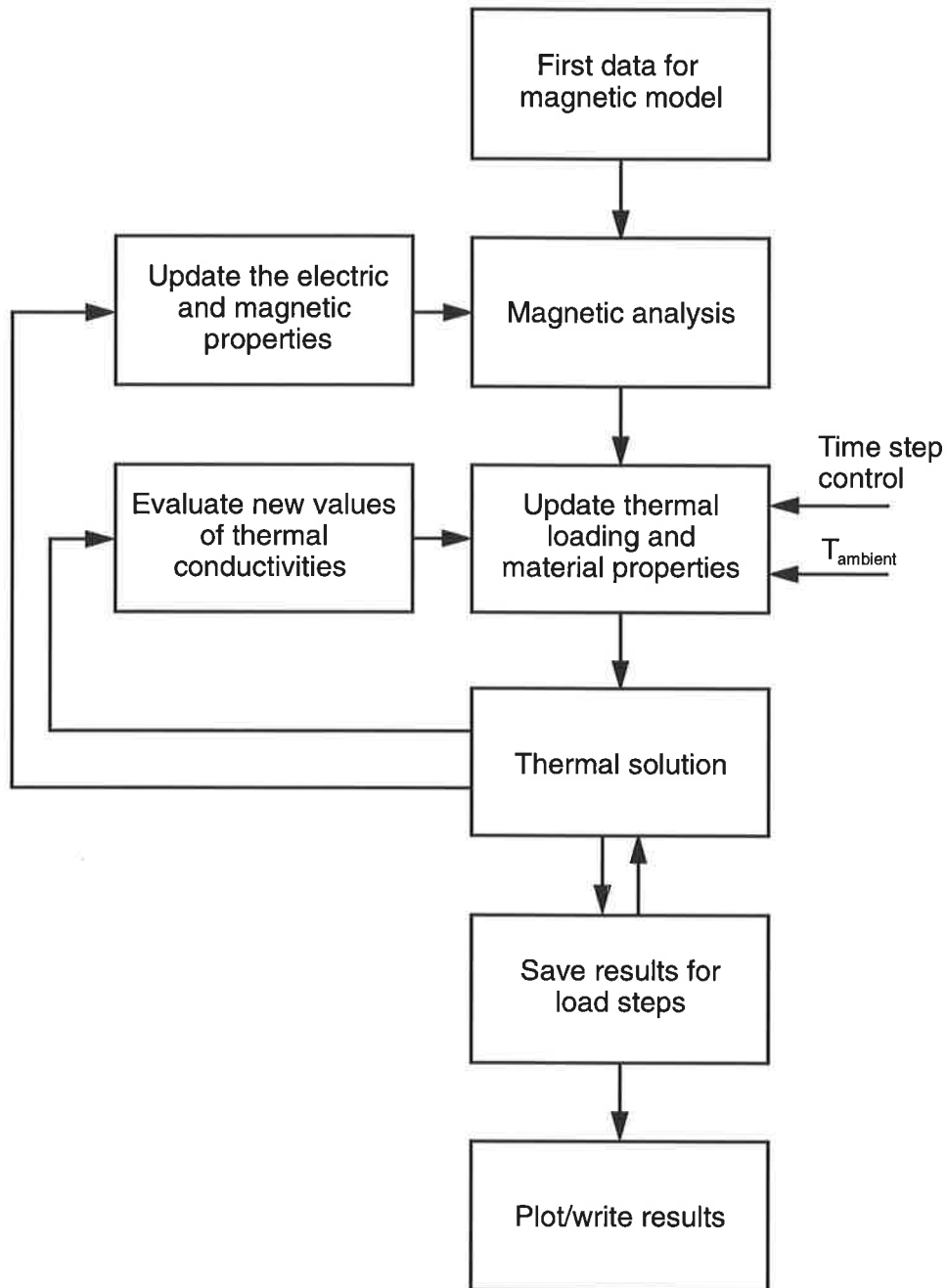


Fig. 5-12 The actual procedure of thermal analysis

3.4 Sensitivity analysis

Despite the long history of thermal modelling of induction motors, there is still no accurate formula to estimate the thermal conductivity of some composite parts in the machine. The same problem exists in the prediction of the convection coefficients in the boundaries. Furthermore, the thermal resistance at the interface areas, which plays an important role in the temperature distribution in the motor, adds uncertainties in the prediction of temperature distribution. The main parameters in this category are:

- (a) The thermal conductivity of stranded stator winding across the conductors,
- (b) The axial thermal conductivity of laminated iron,
- (c) The thermal conductivity of stator slot liner because an unknown amount of air pockets are usually trapped in either side of the liner,

In order to explore the influence of the accuracy of the estimated values for these parameters and also some other parameters on the accuracy of the final results, a set of sensitivity analyses is carried.

Temperature is a quality which governs the motor rating for different loading disciplines. Therefore, the thermal response of an IM can be good criterion to assess the sensitivity of different parts of the motor to the variation of any parameter and/or material property. From the outcome of such analysis, one may find the required accuracy for the initial data to achieve a certain accuracy in the final results. This may save enormous amount of unnecessary computing effort and time.

Since the features of the problems in the rotor and stator are different to some extent, these analyses for the two members of the motor are carried out separately.

3.4.1 Sensitivity analysis of the rotor parts

The rotor bars in a cage rotor are nearly in direct thermal contact with the iron core; therefore, the heating process of this part becomes more complicated and widely different from that of a wound rotor or the stator and it has prompted some special works on this area [18, 30, 78]. In order to investigate the effect of various parameters, including the variation of some thermal properties with temperature, a simple rectangular bar embedded in the iron

core, as shown in 5-13 is assumed as representative of a rotor bar. Although the geometry of

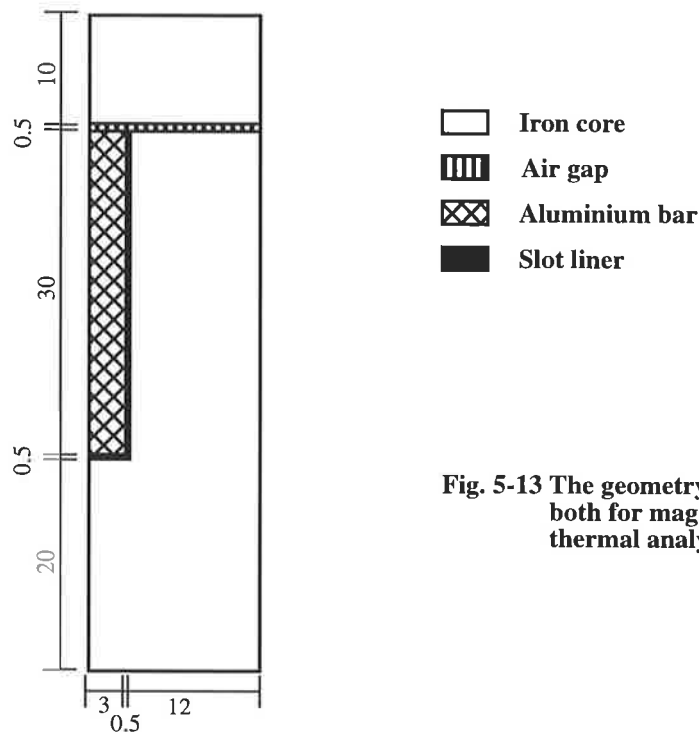


Fig. 5-13 The geometry of model both for magnetic and thermal analysis

this model is very far from the case of actual models in this project, it is noteworthy to mention that some heating related key parameters can be extracted from this simple geometry. In fact, this shape provides a uniform thermal conductivity along the radial and tangential directions of the slot and isolates the effect of any distortion in the temperature distribution as a result of any internal and/or external heat transfer within the model with unevenly distributed thermal resistance and capacitance along the bar.

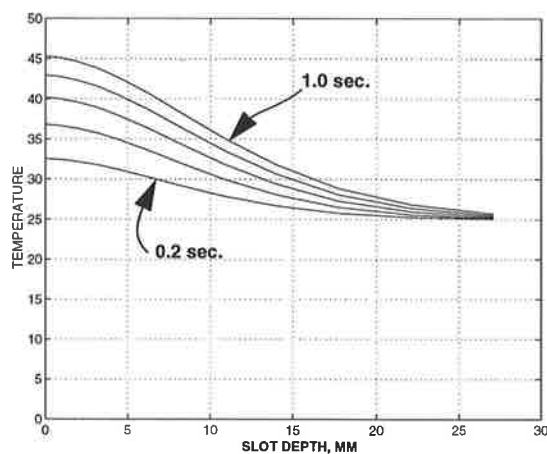
It has been conclusively shown that the heat transfer from the bar to the iron rotor core is of crucial significance in limiting temperature rise from the instant of switch-on and that conduction within the bar aids considerably in damping the differential temperature rise from the top to the bottom of the slot, again within a relatively short time after energising.

3.4.1.1 Effect of the conductivity of the aluminium bar and the slot/bar interface thermal resistance

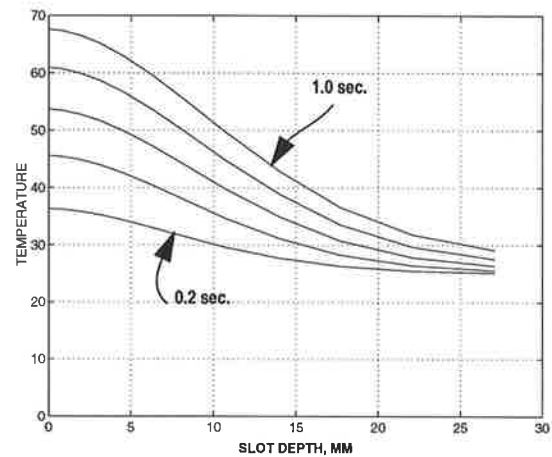
In order to demonstrate the effect of conducted heat from the bar into the iron core and also the internally conducted heat within the bar, the following analyses are carried out on an aluminium bar:

1. The thermal conductivities of aluminium and the thermal contact interface at the bar/slot interface are non-zero (normal conditions);
2. The thermal contact resistance is infinite while aluminium is a thermal conductor;
3. Both the thermal conductivity of aluminium and that of the thermal contact interface are zero.

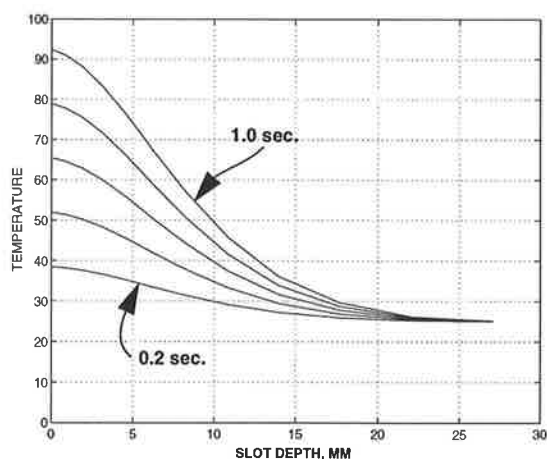
Figures 5-14a to 5-14c show the analysis results for these cases respectively. If case 1 is



(a)



(b)



(c)

Fig. 5-14 Temperature distribution in the bar after 0.2, 0.4, 0.6, 0.8 and 1.0 sec. when

- a:** Aluminium and the slot liner are conductors,
- b:** Aluminium is conductor but the slot liner is insulator,
- c:** Both aluminium and the slot liner are insulators.

chosen as the base, Fig. 5-14b indicates an over estimation as large as 10% to 45% may occur

within 0.2 sec. to 1 sec. if the conduction into iron is ignored. The error increases rapidly as the time prolongs. Comparing Fig. 5-14c to Fig. 5-14a and Fig. 5-14b also shows the rapid reaction of the conducting aluminium conductor in damping the radial temperature gradient within the bar while the thermal loading is unchanged during the analysis.

3.4.1.2 Effect of the thermal contact resistance on the heating process

The thermal resistance in the bar/slot. interface in a die-casted aluminium cage is not clear but in a well done die-casting it is expected to be considerably less than that of a copper bar. The thermal resistance of the copper bar/slot interface is a function of slot clearance. Walker [73] classified this resistance by the slot clearance as shown in Table 5-5. In normal circumstances, the use of rectangular bar allows small slot clearances. This study shows that even with artificially large clearance, the conducted heat flow into the iron has a significant effect on the bar temperature.

Table 5-5 Summarised results for the copper/lamination thermal contact resistance.

Slot clearance, W_{cl} , ($\times 10^{-3}$) meters	Thermal Resistance of Unit Area A (K/W)
<0.1	$6.6W_{cl}/A$
0.1-0.5	$33.3W_{cl}/A$
>0.5	$40.0W_{cl}/A$

In order to study this effect, a liner of 0.5mm thickness, equivalent to a 1mm clearance, is put between the bar and the iron core¹. In this study, the thermal conductivity of the 0.5mm layer material is varied between zero to 100% of that of the iron core in steps. Then a set of thermal analyses is carried out for each step applying the same thermal loading extracted from a magnetic analysis. In Fig. 5-15a, the distribution of temperature in the aluminium bar, after 2seconds, for different values of contact element conductivities are compared. Figures 5-15b to 5-15d show the temperature distribution in the same bar after 4, 6 and 10 seconds respectively.

1. Obviously, this is an abnormally large clearance; it is selected just for the sake of having reasonable element sizes in this region. Therefore, it will remain unchanged but equivalent conductivities will be used.

A set of similar analyses is carried out for a copper bar, with an equivalent clearance of 0.15mm, and having a thermal contact resistance of infinity (adiabatic boundary) to $33.3 (W_{cl}/A)$, according to Table 5-5. This means the equivalent conductivity of the existing 0.5 mm thick slot insulator should be varied between zero to 2.0 in this analysis. The resultant temperature distribution for $k_{sl} = 0, 0.4, 1.0$ and 2.0 are given in Fig. 5-16. In this figure, the total current in the copper bar is the same as used in the aluminium bar, producing a total ohmic loss of 3912.5 W in the bar.

As can be seen in figures 5-15 and 5-16, even for the first 2 seconds of stall, the conducted heat into the iron core is high enough to limit the temperature rise in the bar area significantly. In the case of the aluminium bar, the effect becomes considerable only when the thermal contact resistance approached zero. This may be attributed to the existence of a high temperature gradient in the interface boundary, forcing a significant amount of heat from the hot bar area toward the cool and high capacity thermal ocean of the iron core.

Some similar results are achieved in the copper bar. Assuming an adiabatic boundary for a copper bar with a normal clearance of 0.15 mm, introduces an error of 19% to 114% in the estimation of temperature at the top of the slot within 2 seconds and 10 seconds respectively.

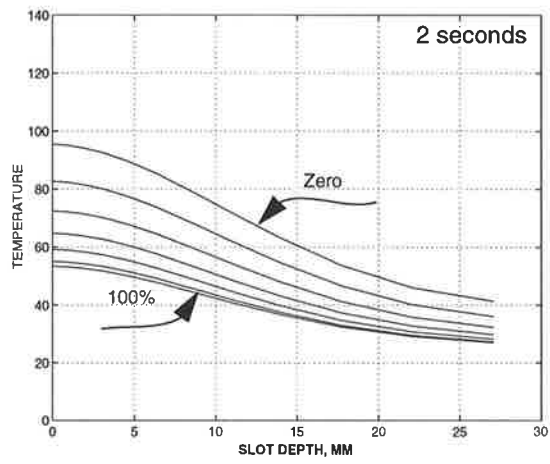
3.4.1.3 The effect of temperature dependant electric conductivity of aluminium

The non-uniform distribution of thermal resistance around the rotor bar leads to a non-uniform distribution of temperature in the bar before steady state conditions are established. In deep bar cages, the uneven distribution of current, consequently the ohmic losses (acting as the thermal loads) give rise to this problem so that in some cases the temperature difference between the top parts of the bar and the bottom parts in a single rotor slot may reach high values of 80° [30] to 100° [18] within a short transient time.

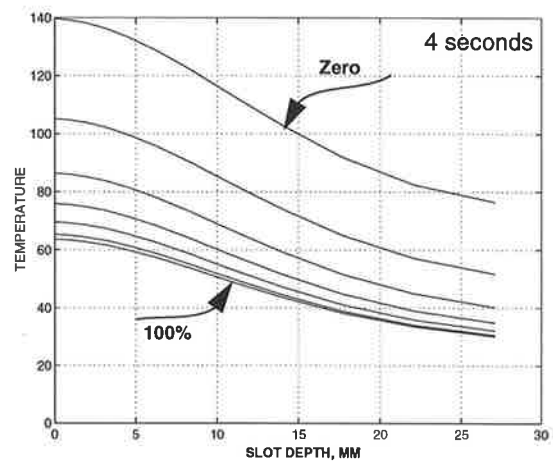
On the other hand, the electric conductivity of conductors reduces with temperature as:

$$\frac{\sigma_t}{\sigma_0} = \frac{T + 1/\alpha}{T_0 + 1/\alpha} \quad (5-17)$$

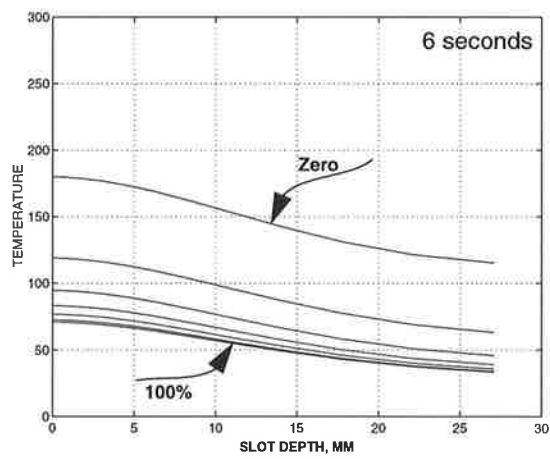
where σ_t and σ_0 are the electric conductivity of the conductor at T and T_0 degrees



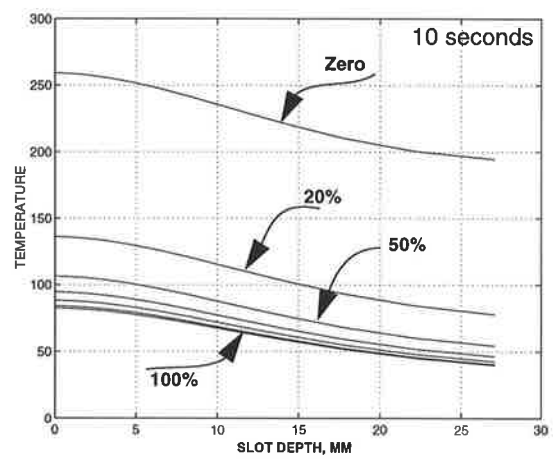
(a)



(b)



(c)



(d)

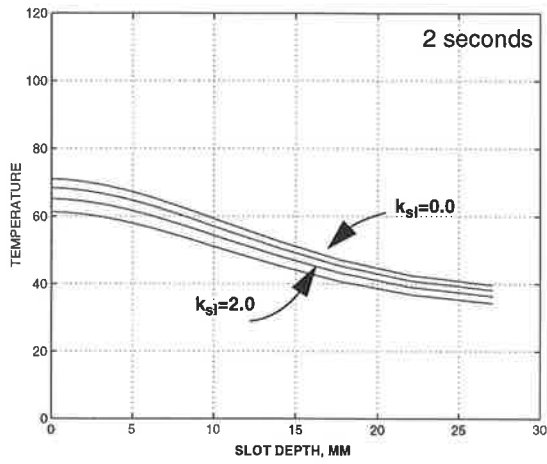
Fig. 5-15 Effect of the conductivity of slot liner on the aluminium bar heating when the conductivity of slot liner is 0, 2, 5, 10, 20, 50 and 100% of that of iron core:

a: After 2 seconds;

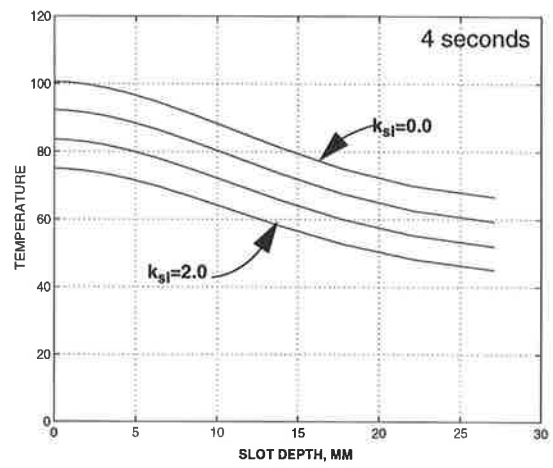
b: after 4 seconds;

c: After 6 seconds;

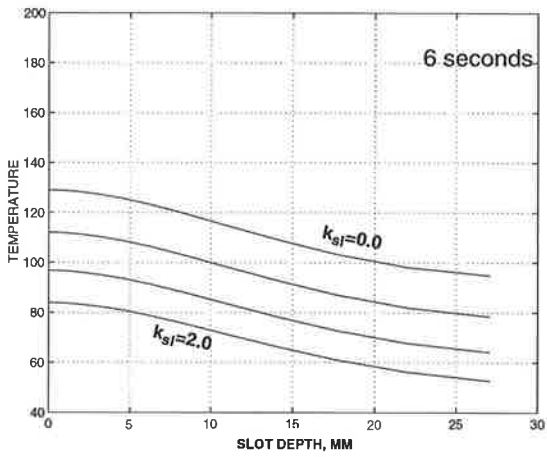
d: After 10 seconds



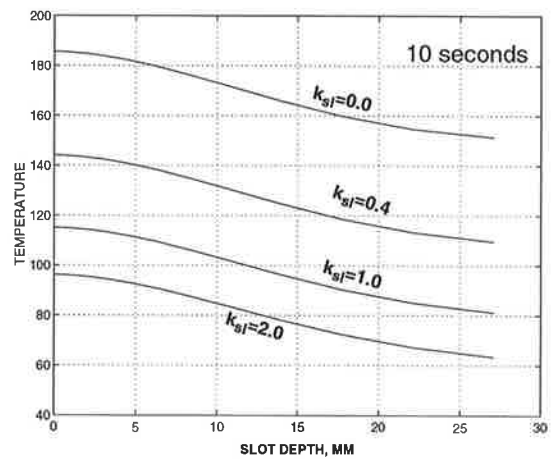
(a)



(b)



(c)



(d)

Fig. 5-16 Effect of the conductivity of slot liner on the copper bar heating for $k_{sl} = 0.0, 0.4, 1.0$ and 2.0

- a: After 2 seconds;**
- b: after 4 seconds;**
- c: After 6 seconds;**
- d: After 10 seconds.**

respectively, and α is the temperature coefficient of the conductor at T_0 degrees.

As can be seen from (2-8), skin effect is a function of σ , and consequently a function of the temperature; so a temperature-variant current distribution map would be expected in the bar during the transient analysis. Furthermore, assuming a fixed total current in the bar, results in a time-variant distribution of ohmic loss and also total ohmic loss in the bar which can be extracted from (2-36) as:

$$q''' = \frac{|J_t(x, y)|^2}{\sigma} \quad (5-18)$$

In order to clarify the effect of the local variation of σ , two sets of analyses are carried out on an aluminium bar as follows:

1. The electric conductivity of aluminium, σ , and the related current density distribution are frozen for a certain temperature and the variation of temperature along the bar is calculated in the bar as a function of time.
2. A set of consequent magnetic and thermal analyses are executed for each individual time step. The temperature pattern is extracted at the end of each time step and is used to update the local σ and current distribution in the bar by a magnetic analysis (see Fig. 5-12).

The results of two analyses are given in figures 5-18a and 5-18b. In order to apply a reasonable amount of thermal load in Fig. 5-18a, the distribution of thermal loading is extracted from a magnetic analysis, when σ is assigned to a temperature of 50° which produces a total power loss of 4484.9 W taking the skin effect into account; for the thermal analysis the ambient temperature is still assumed to be 25° . However, in Fig. 5-18b, the bar is assumed to be at the ambient temperature initially for both magnetic and thermal calculations, and the heating process is followed as described by Fig. 5-12. Except for the first magnetic analysis, the bar has a temperature dependant non-uniform conductivity, resulting in a time variant thermal loading and also a total power loss in the bar. The variation of total losses in the bar as a function of time is shown in Fig. 5-17. Even though a reasonably good agreement can be recognised between figures 5-18a and 5-18b, a comparison between these may be invalid since neither input power nor the electric

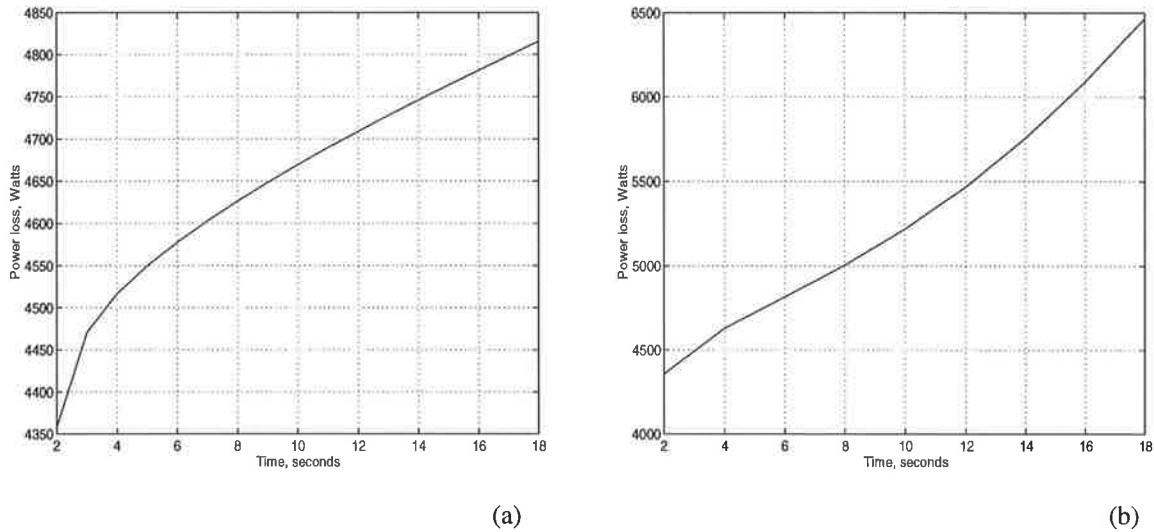


Fig. 5-17 Variation of total losses in the aluminium bar as a function of time:
a: for the case of Fig. 5-18b, b: for the case of Fig. 5-18d

conductivity of the bar is the same for them. Never the less, a set of similar analyses with increased thermal loading showed that unless the thermal contact resistance is not extremely high, the temperature distribution maps in Fig. 5-18a remains comparable with Fig. 5-18b. The increased thermal loads were extracted from two magnetic analyses, when σ was assumed to be in its value at 80° and 100° introducing total losses of 4628.5 W to 4722.8 W on the bar respectively. The similarity may only be attributed to good conduction of heat into iron.

Figures 5-18c and 5-18d are the same as figures 5-18a and 5-18b respectively when the slot liner is assumed to be an insulator. As can be seen, the generated heat (energy) is localised in the bar and raises its temperature dramatically. For the sake of clarity, figures 5-18c and 5-18d are repeated in figures 5-18e and 5-18f respectively in a shorter time.

Compared to the distribution of current density in the bar with a uniform conductivity, a minor distortion is created by the non-uniform temperature distribution in the bar. To detect this effect, the per-unit value of heat generation, q''' in (5-18) in any element is compared to the per-unit value of $|J_t(x, y)|^2$ in the same element. Figures 5-19a and 5-19b show the actual distribution of current density in the bar and the result of this comparison. As can be

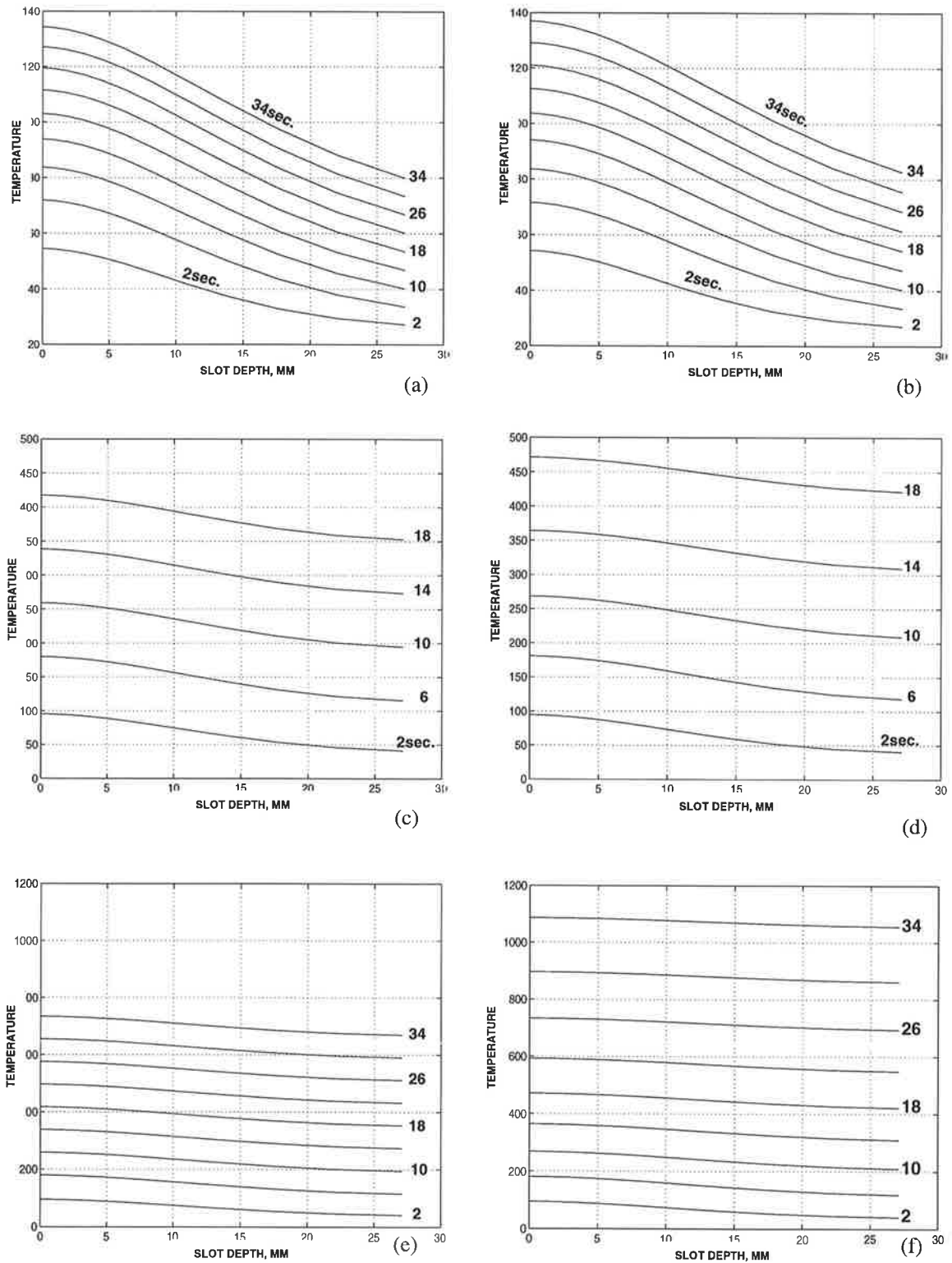


Fig. 5-18 Comparison of the temperature distribution in the bar:

a: Uniform conductivity, conducting slot liner;

c: Same as 'a' but with an insulator slot liner;

e: Same as 'c' but in 34 seconds.

b: Non-uniform conductivity, conducting slot liner;

d: Same as 'b' but with an insulator slot liner.

f: Same as 'd' but in 34 seconds.

seen, the current density deviates slightly more than 2% during a 32-second stall. It is noteworthy that all of the per-unit parameters are calculated on the base of their values at the top of slot. Therefore, comparing figures 5-19a and 5-19b, it can be recognised that the main deviation happens at the top of slot, where the temperature is maximum.

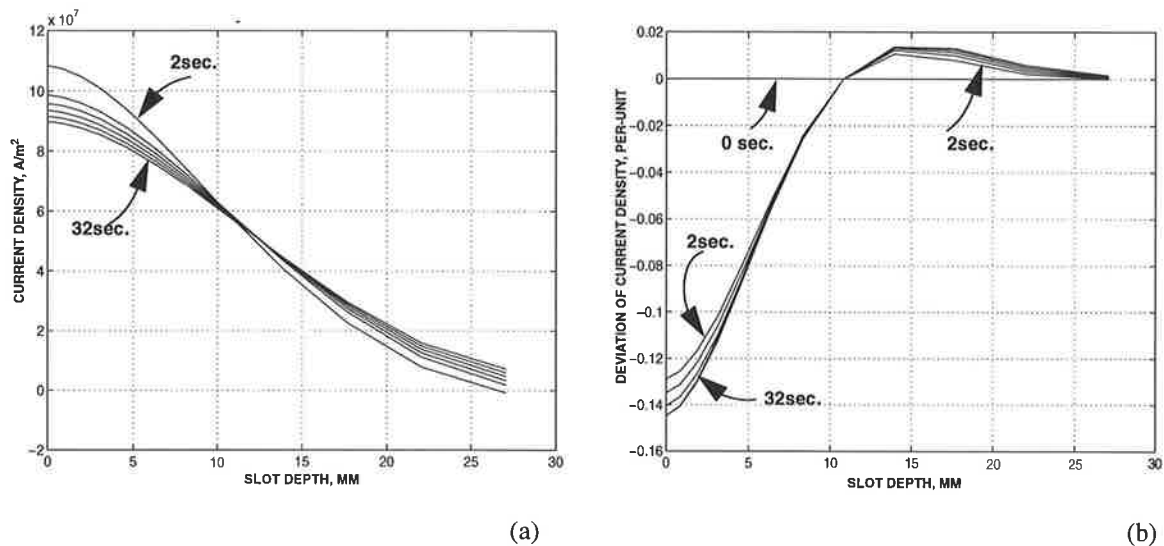


Fig. 5-19 a: The distribution of current density b: the deviation of current density from a uniform conductivity distribution, in the bar at the end of 2, 8, 14, 20, 26, 32 seconds.

Finally, from the results of this section, it can be concluded that taking the influence of temperature on the thermal conductivities and the current distribution is not necessary. This is involved in carrying out repeated finite element studies with variable materials properties and loss distribution where the extra computing effort may improve the accuracy by nearly 2% unless unrealistic conditions are imposed.

3.4.2 Sensitivity analysis of stator parts

Since the number of parameters are large in this part, to avoid numerous figures, the temperature of the hot point in each component is chosen as a measure of the evaluation. The parameters are varied in a reasonable range and the response of the model is recorded in each case.

The conductivity of copper across the conductors is dependant on the cross-sectional geometry of each conductor and the filling factor of the slot. The same parameter across the laminations of the iron core varies with many factors, including the pressure in which the

iron packet is manufactured (see section 4.0 on page 85 for details). The accuracy of the assembling and impregnation affects the overall conductivity of the interface between the stator winding and the stator core. All of the aforementioned conductivities were doubled in turn and the variation of the hot point temperatures in all components of the motor were extracted after 5 to 20 seconds in steps of 5 seconds. Table 5-6 shows the results of this

Table 5-6 Variation of the hot point temperature in different components as percentage of the hot point temperature at normal conditions at the same part individually.

	Conductivity in P.U.			time	Variation of hot point temperature in per-cent at:					
	k_x	k_y	k_z		RC	RB	RRN	SC	SB	SRN
SBAR1&2	2	2	1	5	0.0022	0.0022	0	0.0788	-1.0010	0.0440
				10	0.0031	0.0016	0.0015	0.1829	-2.4527	-0.0489
				15	0.0063	0.0050	0.0037	0.2879	-3.9468	-0.1932
				20	0.0145	0.0125	0.0105	0.4732	-6.5349	-0.4770
Iron core	1	1	2	5	-0.0087	-0.0086	-0.0064	-0.0038	0	0
				10	-0.0282	-0.0264	-0.0231	-0.0152	0	0
				15	-0.0429	-0.0413	-0.0397	-0.0257	0	0
				20	-0.0658	-0.0652	-0.0647	-0.0475	0	0
Slot liner	2	2	2	5	0.0066	0.0043	0.0021	0.6339	-0.1641	0
				10	0.0188	0.0124	0.0092	1.5641	-0.4951	-0.0035
				15	0.0391	0.0300	0.0211	2.5552	-0.8383	-0.0128
				20	0.0988	0.0825	0.0637	4.5659	-1.6061	-0.0640

analysis in percents. The result for each component is presented as a percentage of the variation of hot point temperature at the same component in normal conditions.

3.4.3 Sensitivity to convection film coefficients

The convected heat transfer between a solid and the fluid in contact with it is strongly dependant on the geometry of the interface and the physical situation of the surface. In addition, the convection film coefficient varies with the wall temperature. Therefore, one may expect a wide variation in the results caused by inaccurate values of convection coefficients. This is true for the steady state analysis when all of the heat generation in the system is eventually dissipated via convection. However, in a transient analysis, during the first few ten seconds of stall the major part of the generated heat is expected to be stored in the internal thermal capacitance of the system so that practically the dissipated heat from the system may not be significant. This seems to be more realistic if the motor is initially cool, at

the room temperature, so that the large thermal capacity of solid parts is capable of absorbing a large amount of heat before the temperature rise in different boundaries becomes large enough for considerable convection. Fig. 5-20 shows the variation of convected heat flux from certain interfaces of the model during first 76 seconds of stall when the motor was fed from a 287V source

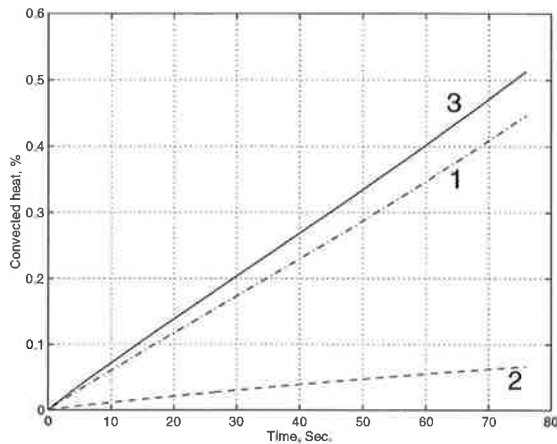


Fig. 5-20 The variation of convected heat as percentage of total power loss in the motor from:
Stator (curve 1);
Rotor (curve 2);
Entire motor (curve 3).

Nevertheless, some sensitivity analyses have been carried out to investigate the effect the convection coefficients, \bar{h} , on the convected heat from the following boundaries:

- (a) Stator end winding exposed to the end-cap, Copp-EC;
- (b) Rotor end winding exposed to the end-cap, Alum-EC;
- (c) Top parts of the iron core exposed to the end-cap, Core-EC.

These were examined by looking at the change in the instantaneous hot point temperature within each component at $t = 26$ seconds when \bar{h} was changed from 1.5 p.u. to 3.0 p.u. in steps of 0.5 p.u. at each boundary individually. Table 5-7 shows the result of this investigation on model one. The total instantaneous heat flux from the whole boundaries of the model¹ at the same time is also shown in this table. As can be seen in Table 5-7, the deviation of the hot point temperature in the components is not significant when \bar{h} is changed within a unrealistically wide margins.

1. This is 1/72 of the total heat flow from the motor.

Table 5-7 Variation of the hot point temperature at t=26 seconds within different components when the convection coefficient of the given boundary is changed.

boundary	h, P.U.	Variation of the hot point temperature in per-cent at:						Total convected heat flux [W]
		RC	RB	RRN	SC	SB	SRN	
All	1.0	0.0	0.0	0.0	0.0	0.0	-0.3879	14.00
Copp-EC	1.5	-0.0028	-0.0019	-0.0019	-0.1918	-0.6218	-0.3879	14.60
	2.0	-0.0047	-0.0038	-0.0028	-0.3681	-1.2306	-0.7698	18.00
	2.5	-0.0076	-0.0056	-0.0047	-0.5328	-1.8281	-1.1464	21.00
	3.0	-0.0095	-0.0066	-0.0056	-0.6839	-2.4134	-1.5169	23.70
Core-EC	1.5	-0.0114	-0.0103	-0.0121	-0.1608	-0.0009	0	11.00
	2.0	-0.0218	-0.0216	-0.0233	-0.3197	-0.0009	0	11.10
	2.5	-0.0323	-0.0329	-0.0345	-0.4766	-0.0009	0	11.20
	3.0	-0.0437	-0.0433	-0.0457	-0.6316	-0.0017	0	11.40
Alumi-EC	1.5	-0.4757	-0.5165	-0.6370	-0.2248	0	0	11.50
	2.0	-0.9457	-1.0263	-1.2349	-0.4476	0	0	12.10
	2.5	-1.4081	-1.5287	-1.7964	-0.6665	0	0	12.70
	3.0	-1.8648	-2.0245	-2.3504	-0.8835	-0.0009	0	13.30

On the other hand, although the increment in the total convected heat is significant individually but they are not still considerable compared to the total losses in the motor. The convected heat flow through all boundaries of the model as percentages of the total convected heat at normal conditions are shown in Table 5-8 This table also shows the variation of the total convected heat as a percentage of the total losses in the model.

Since the temperature rise at the boundary of the stator back iron to the surrounding is not significant, the distribution of temperature within the motor is not expected to be affected by any change in the \bar{h} of this boundary.

By looking at the results of this section, it can be concluded that even a substantial error in the estimation of the some parameters may reflect as a quite minute error on the analysis results. For example, in the worst case, an error of 50% introduces an error of less than 0.63% in the Copp-EC boundary model one.

The next chapter, includes the analysis results and also the test results based on the procedure which was discussed in this chapter.

Table 5-8 The convected heat from different boundaries of the motor at t = 26 seconds for

\bar{h} in P.U. at			Convected heat in percent ¹ at t = 26 seconds from the boundary of:						Tot. conv. heat tot. loss %
Copp-EC	Core-EC	Alum-EC	Alum-EC	RC-EC	SC-EC	Copp-EC	Frame	Total	
1	1	1	11.927	1.551	0.801	85.413	0.056	100.000	1.40 (Normal)
1.5	1	1	11.927	1.551	0.795	120.184	0.056	133.945	1.89
2.0	1	1	11.927	1.551	0.790	150.459	0.056	165.138	2.32
2.5	1	1	11.927	1.551	0.784	177.982	0.056	192.661	2.71
3.0	1	1	11.927	1.551	0.779	202.752	0.056	217.431	3.06
1	1.5	1	11.927	2.303	1.193	85.413	0.056	100.917	1.42
1	2.0	1	11.927	3.055	1.578	85.413	0.056	101.835	1.44
1	2.5	1	11.927	3.789	1.954	85.413	0.056	102.752	1.45
1	3.0	1	11.927	4.523	2.321	85.413	0.056	104.587	1.47
1	1	1.5	17.798	1.541	0.800	85.413	0.056	105.505	1.49
1	1	2.0	23.486	1.532	0.799	85.413	0.056	111.009	1.57
1	1	2.5	29.083	1.523	0.797	85.413	0.056	116.514	1.64
1	1	3.0	34.587	1.514	0.796	85.413	0.056	122.018	1.72

1. The base of these calculations is the total convected heat at normal conditions.

* * * * *

CHAPTER SIX

SIMULATION AND TEST RESULTS

Contents: Measurement of temperature, Sources of measurement errors, Specifications of the models, Test setup and verification of results for the models, Study of heat flow in the motor

1.0 INTRODUCTION

In this chapter, first the procedure for the experimental work, including the method of temperature measurement in a transient regime and the test setup for the machines is explained. Then, the analysis and the test results in strategically selected points are discussed. The nature of the results inevitably involves the presentation of numerous graphs. Therefore, for the sake of space saving and appearance, the presented figures are summarised and compressed while attempting to preserve clarity and emphasise the salient trends.

2.0 MEASUREMENT OF TEMPERATURE

The measurement of temperature under steady state conditions is almost a straight forward procedure. However, in transient conditions, some important considerations are necessary. In addition, the variation of temperature at all of the required points should be measured simultaneously where usage of a data logger or similar storing equipment becomes imperative. Since the Thermo-Couples (TC's) are usually attached to a conducting body, they may not be isolated electrically. Whence, any inter-connection of their terminals constructs extra loops resulting in disturbances due to circulating currents in the loops. Therefore, all of the inputs to the data logger are usually isolated from each other and they are read sequentially, rather than simultaneously, while all of the others are disconnected.

So, if the inputs are due to be scanned with a rate of 40 channels per second, there would be a (1/40)-sec time shift between the data read from any two consecutive channels. Therefore, a 1-second time shift will be accumulated between the data read from the first and the last channel if all 40 channels exist. This is probably the major disadvantage of such a measurement technique. The error may become significant in rapidly varying inputs while it can be partially compensated by application of appropriate offset time shifts on each set of results.

In this project, a “3530 D&F ORION delta” data logger was used. Up to 20 inputs per acquisition card may be recorded with this instrument. The input stage of the logger includes different signal conditioners, and allows application of different types of inputs, including any combination of variety of TC’s, DC and/or AC voltages. Separate transducers were used to convert voltage, current and power into DC voltages before application into the data-logger. All temperatures were measured by using T type (Copper-Constantan) TC’s attached to the measurement points. The instrument was fully controlled by a PC and the outputs were recorded as text files for further processing. More information about the measurement of temperature is given in Appendix D.

2.1 Sources of measurement errors

No measurement is free of error. The expected sources of some relevant errors in the measurement of temperature in this project are as follows:

1. Error caused by the thermal contact resistance between the TC and the test point surface;
2. Error caused by the data acquisition system including:
 - a. Non-simultaneous measurement of temperatures by different channels (sweep time);
 - b. The time delay of each channel individually,
3. Loading effect of the TC’s on the thermal system including:
 - a. The effect of each TC locally and individually,
 - b. The global effect on the entire thermal system.

Usage of epoxy glue was inevitable at some test points in order to fix the TC's in the correct position. This may also cause some measurement error since it modifies the local thermal properties of the model.

3.0 SPECIFICATIONS OF THE MODELS

In order to verify the validity of the proposed thermal model in general, rather than case-dependant form, two induction motors with wide differences were selected as the test motors. Some relevant specifications of the motors, referred as models one and two from this part on, are given in Table 6-1. The equivalent slot pitch of each motor which is used for the purpose

Table 6-1 Specification of the models

	Model 1	Model 2
Rated Power, kW	15	250
Rated Voltage, V	415	415
Rated Current, A	26.30	405.02
SC current (full voltage, cold)	93.94	2586.5 ¹
Connection	Delta	Delta
No. of poles	4	4
Winding step	1-7,9,11	1-15
Number of coils/pole	3	6
Wire diameter, mm	1	1.4
Number of wires in parallel	1	14
Number of turns per coil	50	5
Number of slots (stator)	36	72
Number of slots (rotor)	28	66
Number of poles in parallel	4	4
Insulation class	F	H
Radial air-gap, mm	0.48	1.5
Packet length, mm	190	580
Cooling	TEFC	TEFC
Winding	Concentric	Lap
Type of cage	Die-casted aluminium	Assembled copper

1. The mains voltage dropped from 420 to 317.05 under this current.

of modelling is shown in Fig. 6-1. Some major differences between two motors from the view point of thermal modelling may be high lighted as follows:

1. The rotor cage, including the bars, the end-rings and the fan blades, in model one is die-casted aluminium. The same part in model two is constructed by pre-fabricated copper bars, brazed to two end rings, making a complex and irregular geometry, being extremely non-homogenous in the end-ring region. This also provides a major difference for the thermal contact resistance between the rotor bars and the rotor cores in the selected models.
2. The cross sectional geometry of the rotor bars are quite different in the models (see Fig. 6-1), causing different patterns of loss density in the bars in each model.
3. The ratings of the motors are widely different.

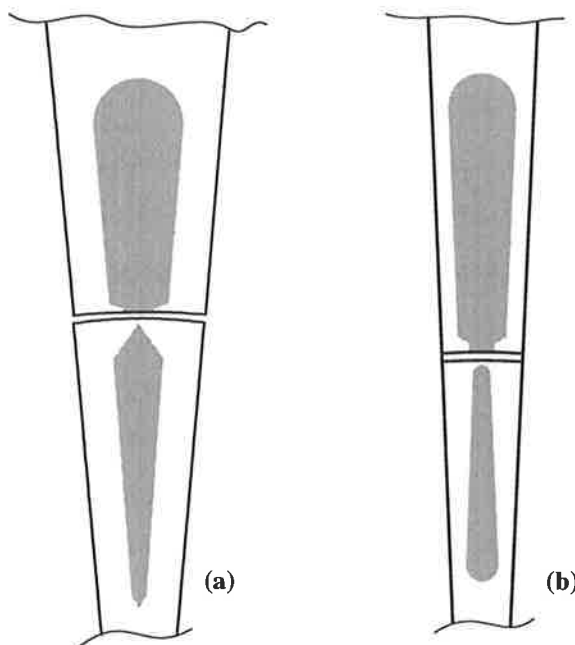


Fig. 6-1 Profile of the equivalent slot pitch of:
a: model one
b: model two

NOTE: Two figures do not share the same drawing scale.

4.0 VERIFICATION OF THE RESULTS

The validity of the analysis results were checked against a set of comprehensive tests on the aforementioned models. Although none of the designed models are case-dependent, for the sake of comparison the initial temperature in each analysis and the line voltage at the same analysis were adjusted to be equal to the corresponding parameters during the appropriate test. In fact, because of lack of enough data about the mains and the employed voltage regulator, an accurate setting of the line voltage under load could not be guaranteed in advance. The summary of the tests on each machine and the procedure of the verification are described in the following sections.

4.1 Test setup for model one

Since the test was due to be performed at standstill, as many as possible TC's, limited by the loading effect of the TC's, could be installed. Therefore, fourteen TC's were strategically distributed on the rotor as shown in Fig. 6-2 to monitor the variation of temperature along all three dimensions in the rotor. As can be seen, TC1 to TC7 are allocated to record the peripheral variation of temperature at the top of seven consecutive rotor bars around the cage at their mid-points. TC11 to TC13 and also TC1 are installed to detect the same parameter along the axial direction at the top of a rotor bar. This group of thermo couples, TC1 to TC7 and also TC11 to TC13, were located in similar radial positions in respect to the pertinent bar. Finally, TC8 to TC11 trace the variation of temperature along the radial direction in the rotor bar. In addition, TC14 was installed at the top of rotor end-ring for the same purpose. Unfortunately, during the test it was found that TC12 was not properly responding to the temperature and therefore its output was discarded.

Three other TC's were also installed to measure the variation of temperature on the stator parts: TC15 for the embedded stator winding, TC16 for stator end winding and TC17 for stator core at the tooth area. No TC was permanently installed on the stator outer surface because the variation of temperature at this surface was not expected to be considerable. However, it was confirmed during the test by employing an additional TC attached to this area.

The reliability of such transient tests with significant temperature gradients involves an accurate positioning of the TC's; any millimeter of error in the installation of TC's may cause a considerable error. Therefore, the location of the thermocouples and the corresponding points on the model were confirmed prior to any test.

Since the slot with the maximum heat generation in the rotor bar was modelled in the 3-D model it was essential to carry out the measurement on the corresponding bar on the rotor. Thus, the locking position of the rotor was so aligned that the slot equipped with the TC's become the same as the modelled bar, corresponding the position of 0° in Fig. 5-10. A trial and error method was used during a set of preliminary tests to fulfil this requirement. The motor was locked in a temporary position and fed from a reduced voltage for 20 to 30 seconds¹ and the variation of temperatures at TC1 to TC7 was recorded. This test was

repeated several times until the most suitable position was found for the permanent locking. In the meantime, to cancel out any error caused by the internal heat flow after each switch off, enough time was allowed prior to the following test.

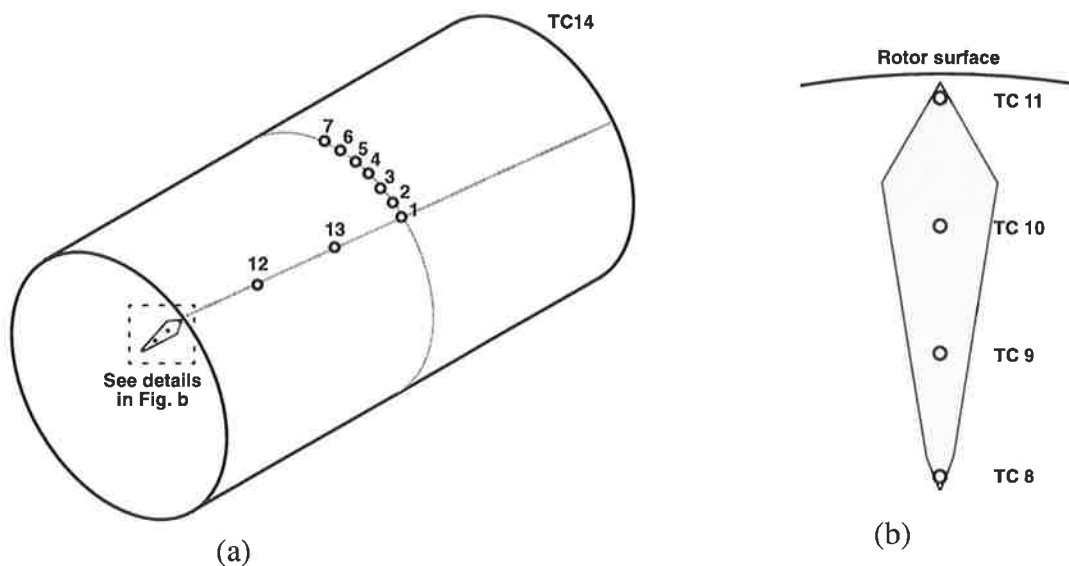


Fig. 6-2 Location of thermocouples on the rotor.

4.2 Verification of the results for model one

Two individual tests, with full voltage and reduced voltage, 419 and 289 volts respectively, were performed on the locked motor. The tests were carried out on two consecutive days in order to ensure a quite uniform initial temperature distribution within the motor parts. An induction regulator was used to adjust the test voltage; the no-load voltage was adjusted to 440 and 300 volts respectively for the tests, however, it dropped to the aforementioned values when the regulator was loaded.

Although uniform initial temperatures were read on all TC's before switching on at each test individually, the recorded results show slightly different initial temperatures. This was attributed to the time interval between any two consecutive readings, controlled by the frequency of scanning by the logger. This component of error was partially cancelled out by application of appropriate time shift on the measured temperatures. The initial (room)

1. This time should be long enough to be able to detect the variation of temperature accurately.

temperatures were not the same for both tests, so, the initial temperatures for each analysis was chosen accordingly.

In addition to the measurement of temperatures at the TC's, four channels of the data logger were dedicated to record the variation of line current, line voltage and three phase power by the two-wattmeter method. The duration of each test was limited by the maximum temperature within the motor, monitored by the output of data logger. The full voltage test allowed 26 seconds under load before a high temperature of order of 150°C was detected in the motor. The similar situation for the reduced voltage test occurred after 76 seconds. The picture of temperature distribution within the modelled part of the rotor cage and stator winding along with the meshing map and the locations of attached thermo couples to these parts are shown in Fig. 6-3.

A combination of the simulation and the test results with the rated voltage are classified in Fig. 6-4 to Fig. 6-7. The results of the study on the variation of temperature along the radial direction are grouped in Fig. 6-4. In this figure, "a" and "b" are extracted from the analysis on the 3-D model and represent the variation of the temperature along the nodes on the radial axis of the rotor bar with time and location respectively. As can be seen in Fig. 6-4a, the difference between the temperatures at the top and the bottom of the slot remains nearly constant from $t = 11$ seconds onward; this difference reaches one half of its final value within a time, as short as $t = 2.2$ seconds. In fact, during the early seconds of stall, the temperature rise at each point is related to the local heat generation only. Therefore, it is more significant at the surface regions of the slots compared to that in the bottom parts of the slot. However, after a while, the radial and axial thermal gradient become large enough to establish corresponding components of conductive heat flow at different parts of the motor. The radial heat flow from the top parts of each bar toward its bottom parts on the one hand and the axial flow from either end of toward its middle part on the other hand adds to the local heat generation at each point and modifies the trend of temperature rise. Semi-steady state conditions appear for the local heat flow in the radial direction of each bar after a certain time, 11 seconds in this case.

The semi-steady state condition may be recognised from the fixed thermal gradient along the depth of the bar in Fig. 6-4a. This can also be detected from Fig. 6-4b where the rate of

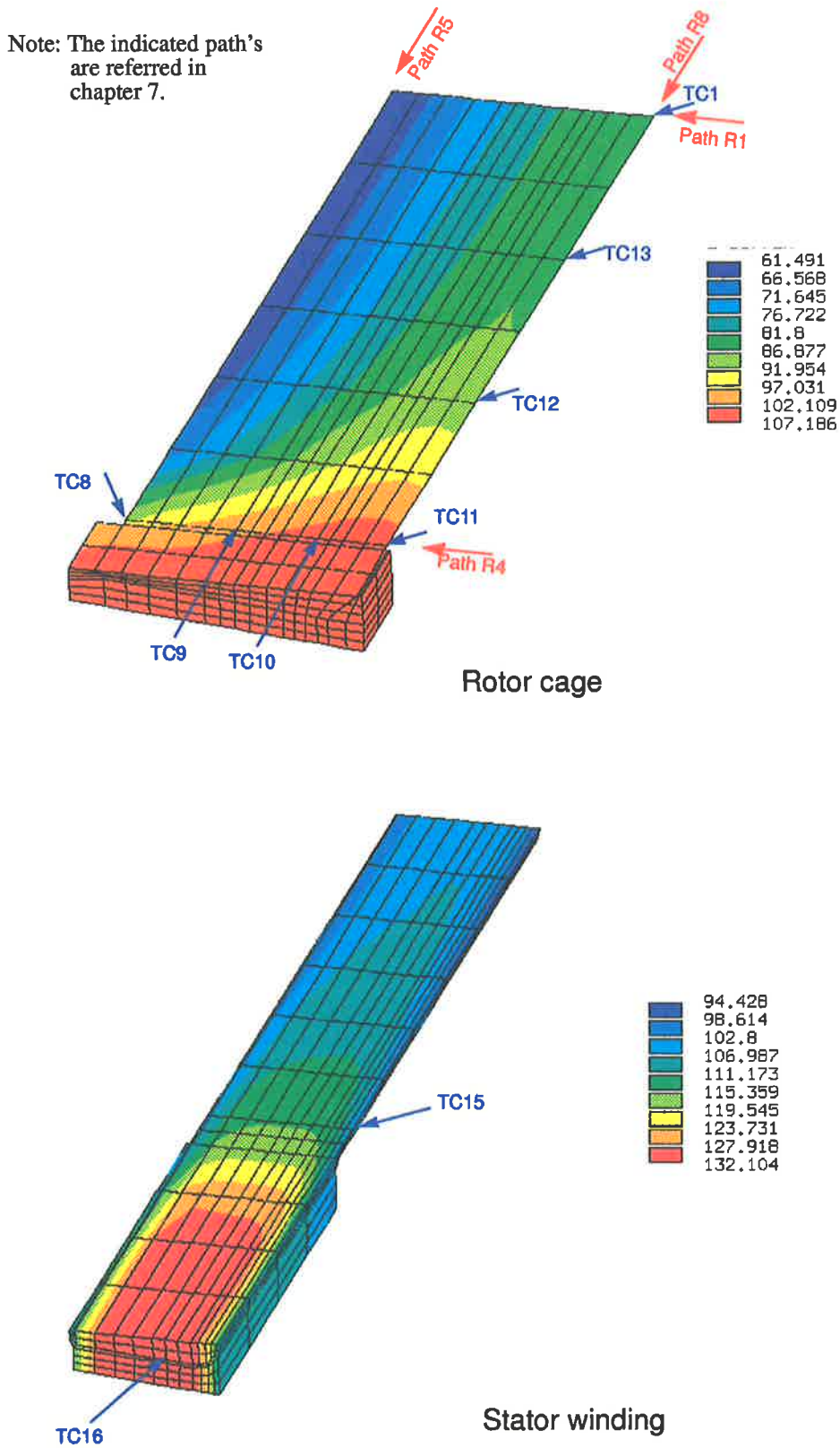


Fig. 6-3 The location of the TC's on the rotor and stator windings and along with the temperature distribution map of the modelled parts of the cage and stator winding after 26 seconds (full voltage)

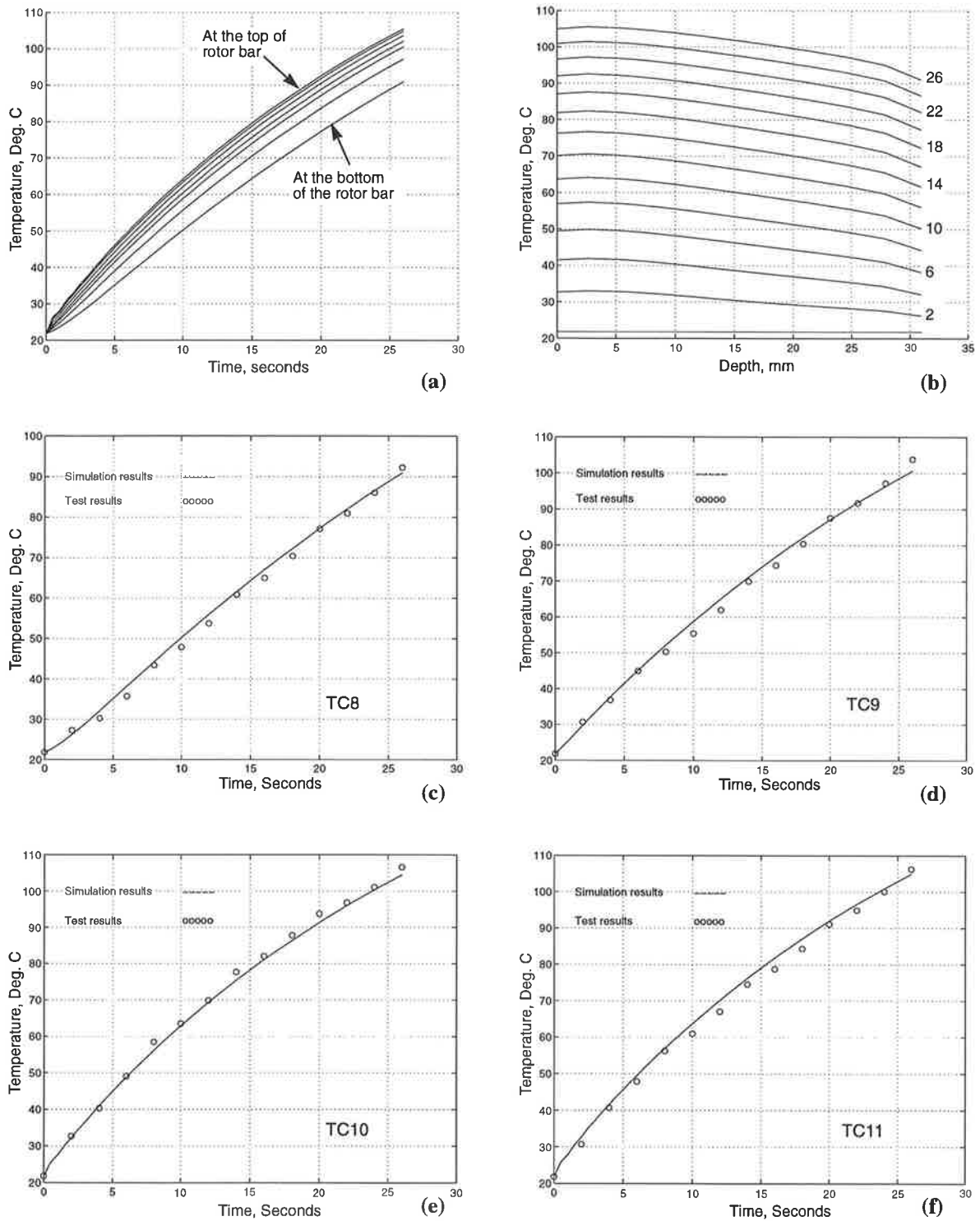


Fig. 6-4 Variation of temperature along the radial axis of rotor bar with time and location, full voltage (419 volts):

- a:** Variation of temperature at the nodes along the rotor radial axis with time, simulation results from the 3-D model;
- b:** Variation of temperature at the nodes along the rotor radial axis with location in different times, simulation results from the 3-D model;
- c to f:** Comparison of the simulation results with the test results at the location of TC8 to TC11.

temperature rise at all nodes becomes similar after nearly 11 seconds. Needless to say that the amount of the heat flow into the core may not be the same in different axial positions.

In addition to the displaced heat, which is mainly transferred from the region of high heat generation at the top of the bar toward the region of low heat generation at the bottom parts of the bar, the difference between the rates of local heat generation between the mentioned parts is partially counterbalanced by the modification in the distribution of current in the bar as the bar temperature rises. The rise in the bar temperature increases the electrical resistivity of the bar and consequently increases the effective skin depth in the bar. This results in a reduction in the current density at the top parts of the bar (see section 3.3.2 on page 113).

In Fig. 6-4c to Fig. 6-4f, the analysis results at four nodes along the same path, corresponding to the locations of TC8 to TC11 in Fig. 6-2 and Fig. 6-3, are compared to that of the test results. As can be seen, a good agreement exists between the two sets of results. The slight deviation may be attributed the uncertain status of thermal contact between the rotor bar and iron core, in addition to the inevitable errors as mentioned earlier in this chapter.

The axial temperature rise related results are shown in Fig. 6-5. In this group of figures, Fig. 6-5c is same as Fig. 6-4f and it is repeated for the sake of clarity of the comparison. Again, Fig. 6-5a and Fig. 6-5b are extracted from the simulation result, illustrating the variation of temperature at the nodes on the top of the bar along the axial direction with time and node location respectively. Unlike the radial direction, the rate of the temperature rise remains unsteady in different axial positions. This is not unexpected since in the latter case the axial heat transfer along the bar on the one hand, and the non-equally absorbed heat by the core in different axial positions on the other hand, play a dominant role in the configuration of these temperature patterns. It is noteworthy that the radial semi-steady state conditions at any axial position may establish independently while the axial flow is still changing!

Fig. 6-3a shows the pattern of temperature distribution within the modelled part of the rotor cage along with the meshing map and the locations of the TC1 and TC8 to TC13 (see Fig. 6-2).

A summary of the peripheral related results from the two dimensional model along with that of the test results at corresponding points on the actual motor, TC1 to TC7, are shown in Fig.

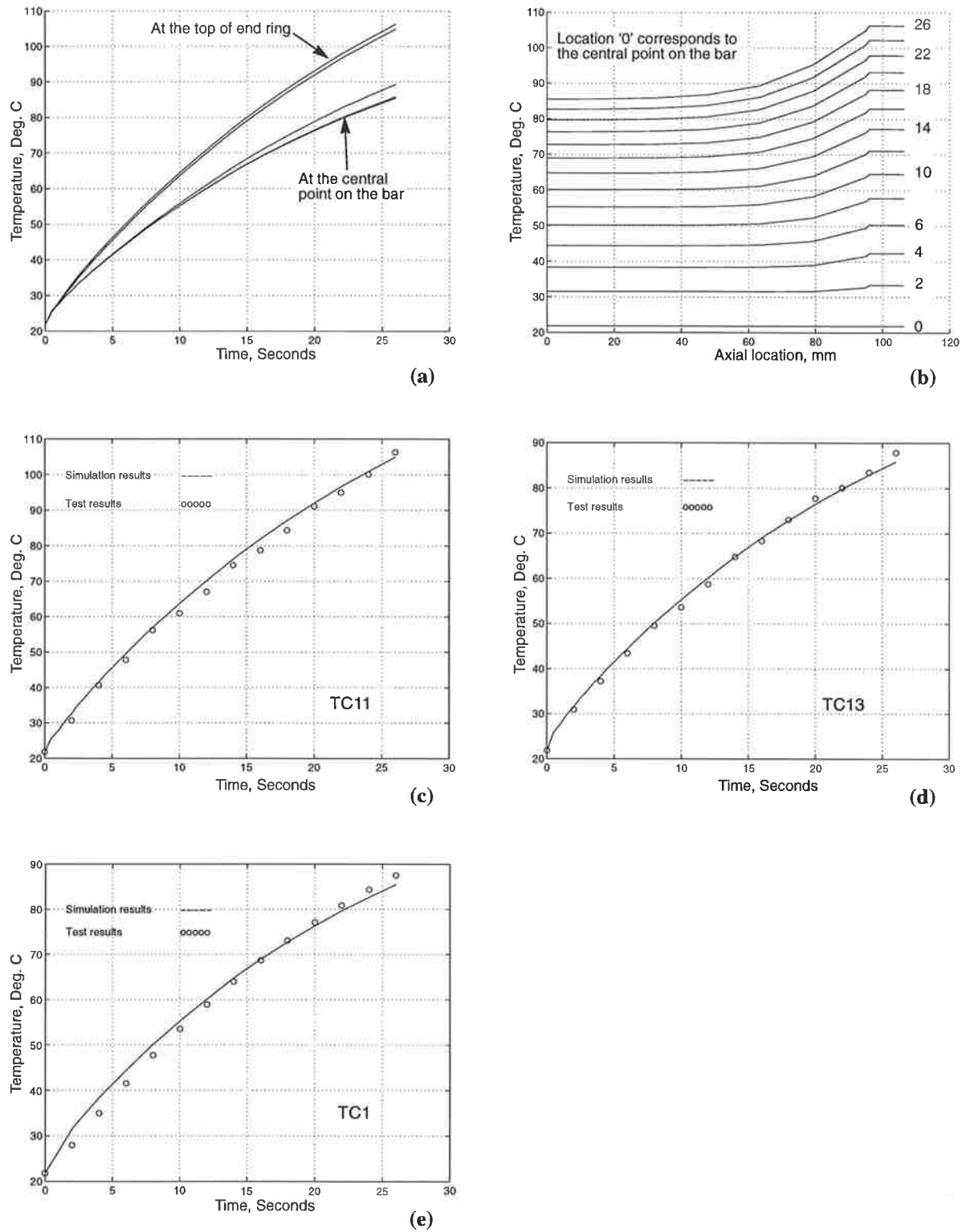


Fig. 6-5 Variation of temperature along the axial direction of the rotor, full voltage (419 volts):

- a:** Variation of temperature along the nodes located at the top of the rotor bar along the axial direction with time, simulation results from the 3-D model;
- b:** Variation of temperature along the nodes located at the top of the rotor bar along the axial direction with location in different times, simulation results from the 3-D model;
- c to e:** Comparison of the simulation results with the test results at the location of TC11 to TC13.

6-6. Fig. 6-6a, extracted from the analysis results, shows the variation of temperature at the tops of seven consecutive slots with time. In Fig. 6-6b the measured temperatures by TC1 to TC7 are shown as functions of the location. As explained earlier, the rate of temperature rise at each point is mainly governed by the local heat generation during the early seconds. This can be detected from the non-similar temperature at $t = 2$ seconds on both graphs. The internal heat flow alters this rate thereafter.

Compared to the displaced heat, the local ohmic losses at each slot are still the dominant component of heat generation. On this basis, a monotonic trend of relative temperature rises at all slots may be expected. This condition exists on the test results until $t = 20$ seconds, where the temperature difference between the locations of TC6 and TC7 levels off and changes its sign thereafter; it remains unchanged in the simulation results. This may be attributed to a possible modification in the thermal properties of the motor, in particular regarding the peripheral heat transfer. The non-uniform expansion of the aluminium bars in the slots during the heating process may be given as an example.

In general, the bars expand and shrink during each heating/cooling process of the aluminium (or a copper) cage, mainly along the bars, which may cause a non-uniform modification in the bar/core thermal contact in different bars¹. So, one may expect unequal rates of heat exchange through this interface in different slots, even in a die-casted aluminium cage. The non-equal axial and radial heat flow in individual bars may also alter this rate.

As can be seen, the difference between the temperatures of the hottest bar and the coolest one reaches to a maximum of about 5.9°C after 18 seconds and levels out thereafter. This is likely to be caused by the increased heat transfer into the core as a result of elevated temperature. This is much clearer in the test with reduced voltage where the results are available over a longer period (see Fig. C-12).

Finally, the simulation and the test results along the peripheral direction at $t = 26$ seconds are compared in Fig. 6-6c. Regarding the numerous potential sources of errors and uncertainties in a thermal analysis, the agreement of the results are acceptable.

1. This may also cause a mechanical imbalance in the motor.

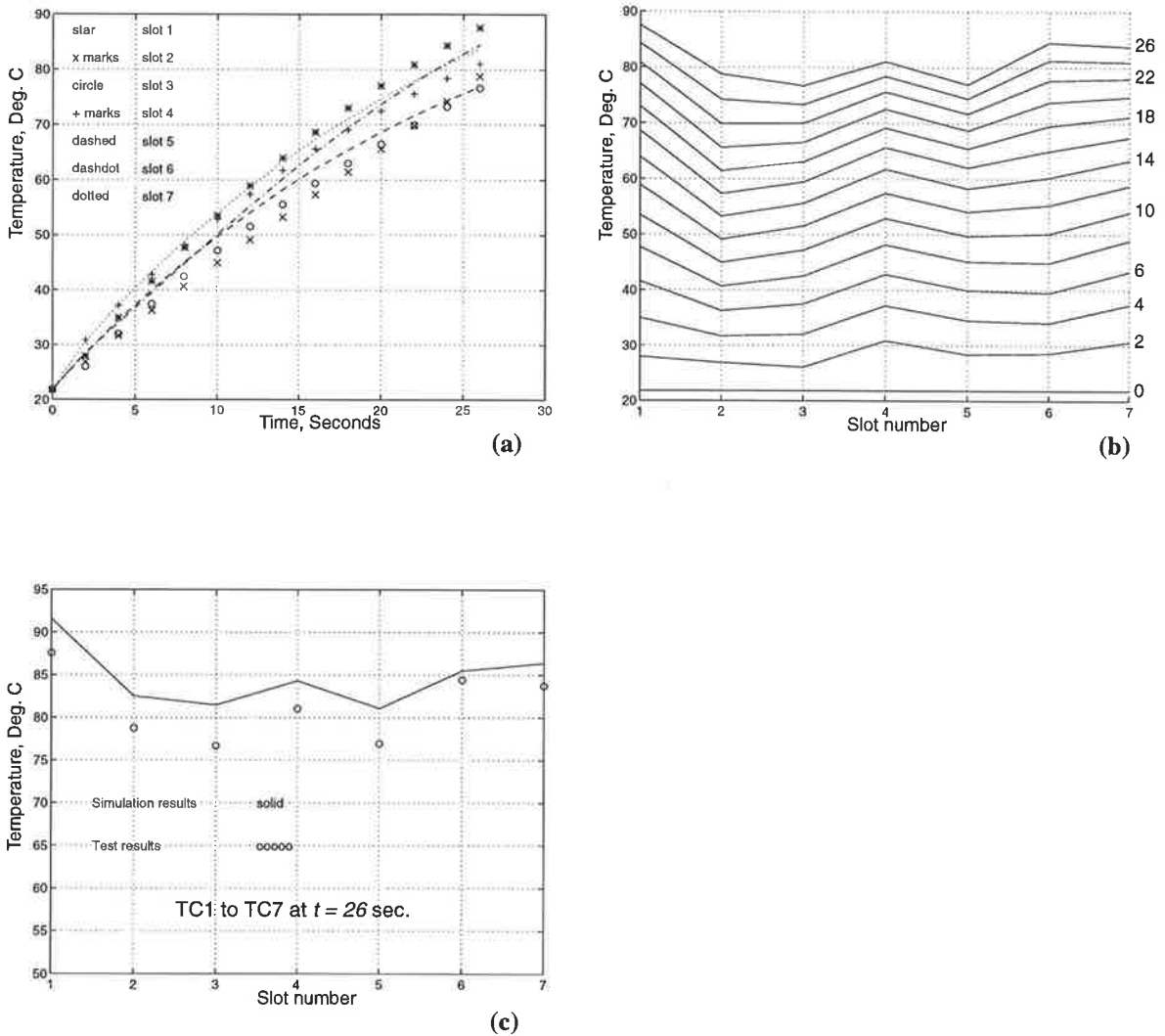


Fig. 6-6 Variation of temperature along the peripheral direction of the rotor with time and location, full voltage (419 volts):

- a:** Variation of temperature at the nodes located at the top of seven consecutive slots with time, simulation results from the 2-D model;
- b:** Variation of temperature at TC1 to TC7, (same as “a”), with location in different times, test results from the 2-D model;
- c:** Comparison of the simulation results and the test results at the last time step.

The rate of temperature rise at three points on the stator, stator end-winding, stator winding and a tooth was measured and compared to the analysis results at the same points in Fig. 6-7. As can be seen, the results are quite satisfactory.

In order to have a further check on the validity of the modelling, another test on the same machine, but with a reduced voltage was carried out and the results were compared to that of another analysis with corresponding conditions. The results of this investigation are grouped in the same way as the rated voltage in Fig. C-10 to Fig. C-13 on pages 205 to 208.

4.3 Test setup and verification of results for model two

The procedure used for model one was mainly followed for this model. Two individual tests, using different voltages were scheduled for this motor. However, because of the limitations of the voltage regulator under heavy loads, the minimum available voltage was not significantly different from that of the mains voltage. Therefore, only the results of the second test are reported here. The first locked rotor test was performed for 19 seconds under 297.80 to 301.56 volts while the second test was carried out for 26 seconds when the motor was directly fed from the line¹. The 415 volts line voltage dropped to 317.05 volts soon after the switch on and increased to 322.8 at the end of the test just prior to switch off. A line current of 2586.5A to 2530.5A was measured within the same period.

The variation of temperature with time was directly measured at 20 keypoints. Details of the location of the thermocouples are shown in Fig. 6-8. Thermocouples TC1 to TC9 were installed to detect the variation of temperature along the peripheral direction, at the top of 9 consecutive rotor bars around the rotor. TC10 to TC13 were allocated to record the variation of temperature along the axial direction on a rotor bar. However, TC10 failed to respond for some reason. The variations of temperature at the stator winding and the stator core were tracked via TC16 to TC20 as shown in the figure. The simulation and the test results are grouped according to the location and the physical direction in the motor.

The variation of measured temperatures at the test points on the axial points on the rotor bar with the maximum loss are shown in Fig. 6-9. Similar results but at two different point on the

1. Longer period of test under the larger voltage may seem strange for some readers. Since the locked rotor test under full or nearly full voltage is accompanied with a high risk of motor failure, the preliminary tests should be carried out more conservatively.

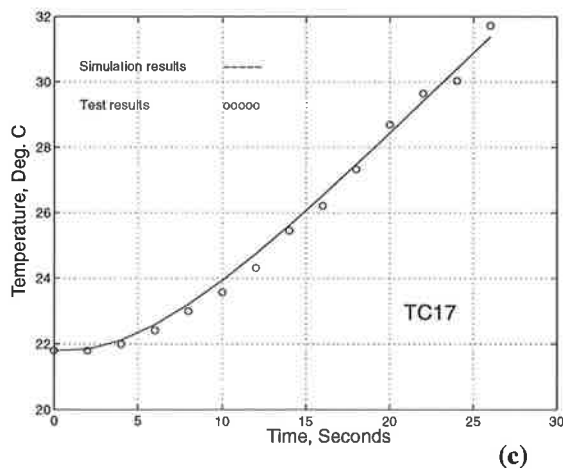
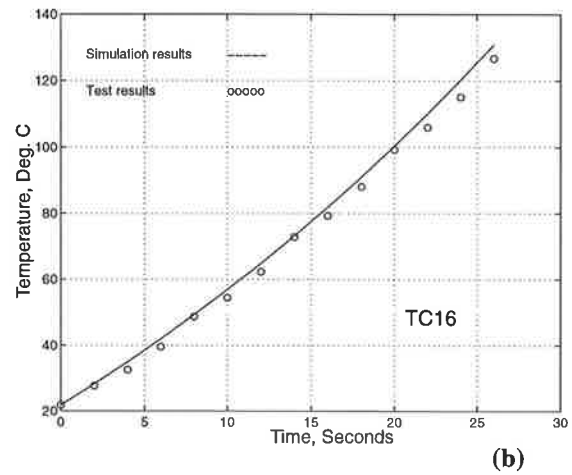
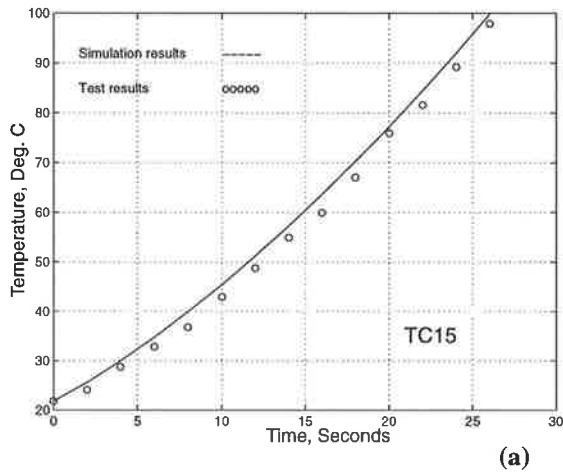
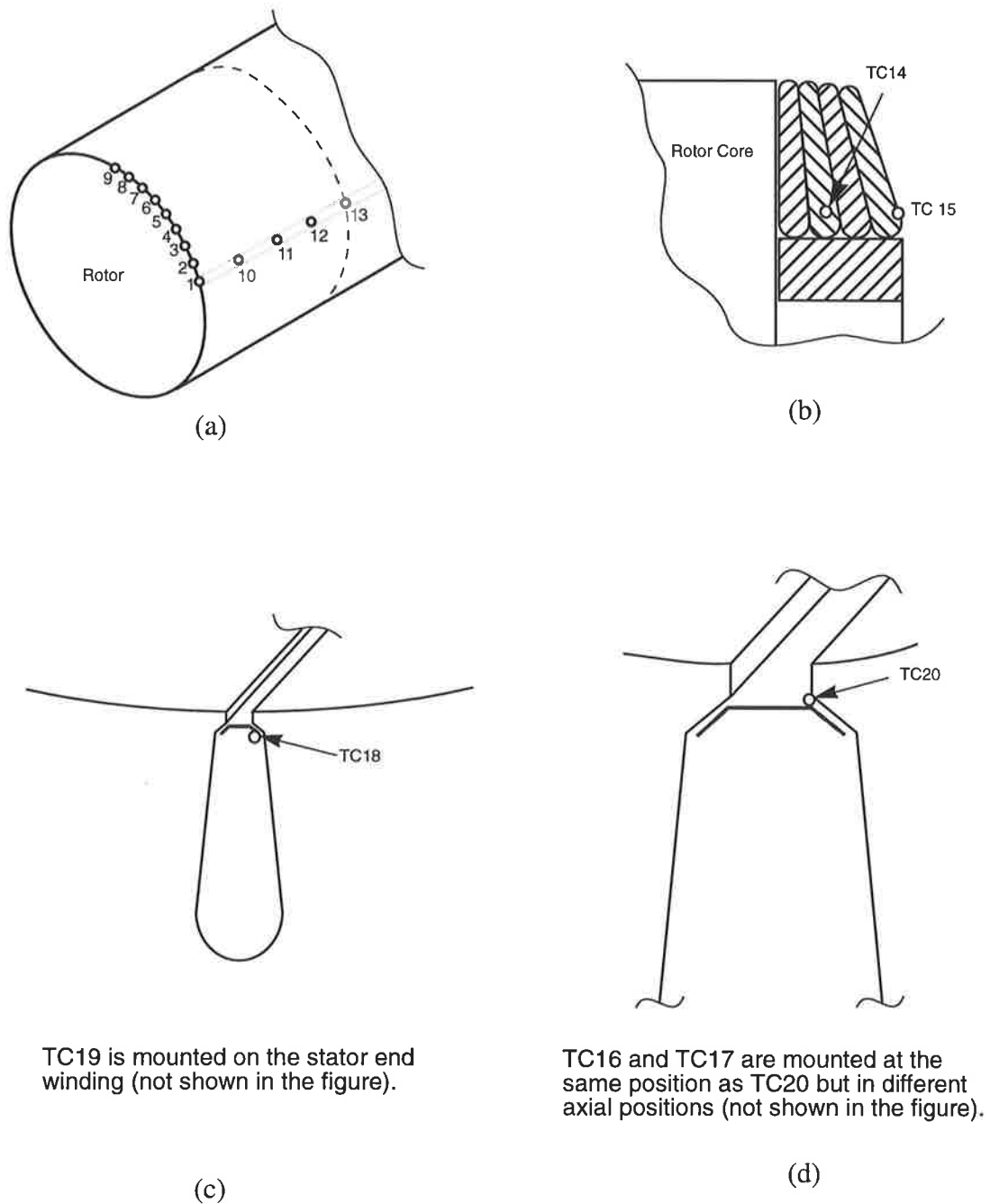


Fig. 6-7 Comparison of simulation results from the 3-D model with the test results at different locations in the stator, full voltage (419 volts):

a: Stator winding (TC15);

b: Stator end winding (TC16);

c: Stator core (TC17);



TC19 is mounted on the stator end winding (not shown in the figure).

TC16 and TC17 are mounted at the same position as TC20 but in different axial positions (not shown in the figure).

Fig. 6-8 Location of thermocouples on the rotor parts of model two:
a: peripheral and axial test points,
b: rotor end-rings,
c: Stator winding,
d: Stator core.

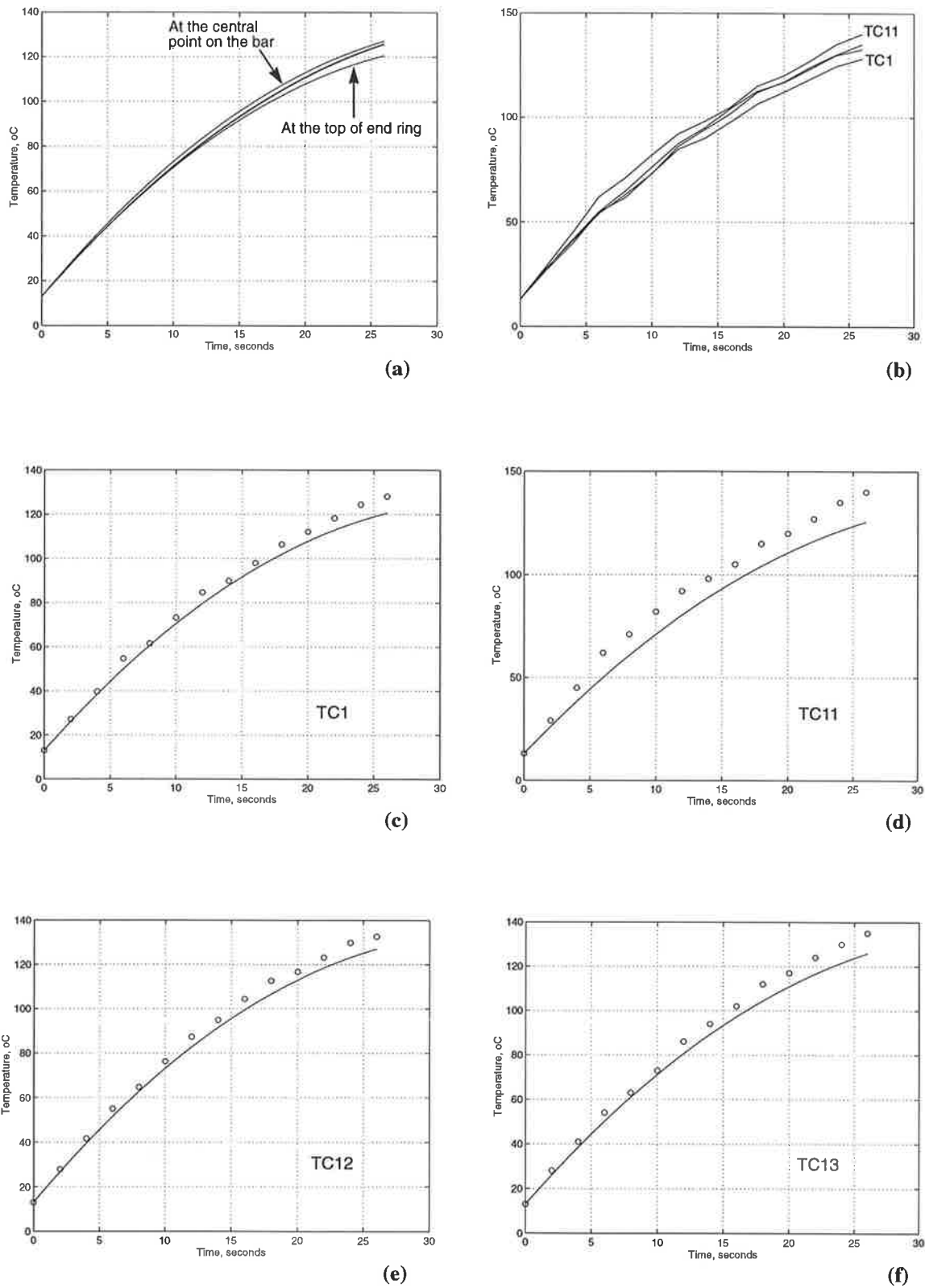


Fig. 6-9 Variation of temperature at the axial location on the rotor (model2):

- a:** Simulation results at locations 1, 11,12 and 13,
- b:** Test results at the same points as 'a',
- c to f:** Comparison of simulation and test results at the above points individually.

rotor end-ring are shown in Fig. 6-10. A comparison of the test and analysis results at this region shows a different trend of temperature rise within the first 2 seconds after power on. It is noteworthy that the simulation results were extracted every 0.2 seconds for the first 3 seconds, and every 2 seconds for the rest of analysis time. However, the sampling rate of the data logger did not allow this resolution, so there were no data recorded between zero and 2 seconds.

Fig. 6-11 demonstrates the trend of heat flow within the end-ring during the early seconds after switch on. For the sake of clarity in this figure, the vectors are scaled individually at each time. As can be seen, the major component of the initial heat flow occurs at the bar/ring interface area, pumping the heat from the end-ring toward the bar. During this period, some heat is also delivered into the rotor core via the ring/core interface. However, the flow into the bar diminishes within 1.2 seconds and changes its direction thereafter and remains as the major component of heat flow for the rest of the simulation period. This result is quite opposite to that of the previous model. This clearly highlights the governing effect of the rotor bar/core interface resistance. The cold and large thermal capacity of the rotor core in a die-casted cage absorbs a significant heat from the cage and establishes a ring to bar/core heat flow during the transient conditions (see Fig. 6-3a).

Another difference between the results of the two models, which is caused by the large interface thermal resistance is the increasing trend of temperature variation along the peripheral direction as shown in Fig. 6-12. This can be seen by the comparison of this figure with its counterparts in model one (Fig. 6-6 and Fig. C-12 on pages 143 and 207 respectively). In case of model one, the difference between the test points around the rotor decreases monotonically with time. This means the heat flow into the rotor core is large enough to damp down this variation. On the contrary, Fig. 6-12 shows an increasing trend of temperature in the same direction which may only be attributed to the poorer heat exchange between the fabricated copper cage and the core. Walker [73] carried out a similar test on a 425kW induction motor with different characteristics. The relevant test results are shown in Fig. 6-12d; as can be seen, the peripheral variation of temperature in his model is still higher than that of model two in this project. It is noteworthy that Walker assumed an adiabatic boundary around the rotor bars ignoring any heat transfer into the core. Table 6-2 shows some specifications of Walker's model.

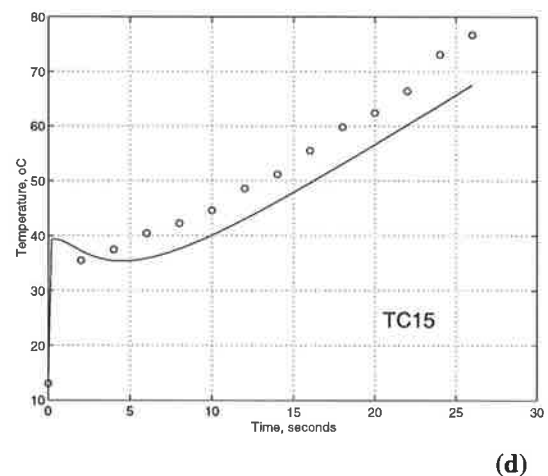
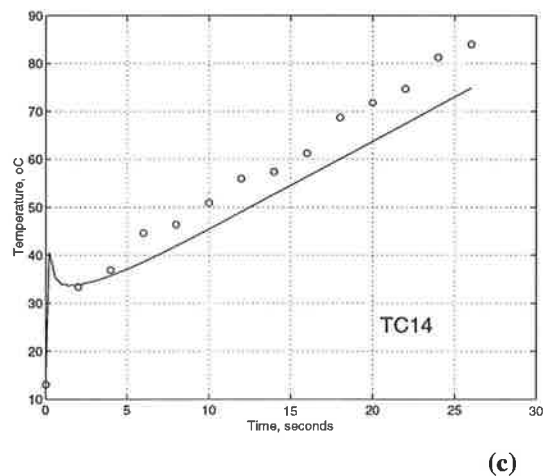
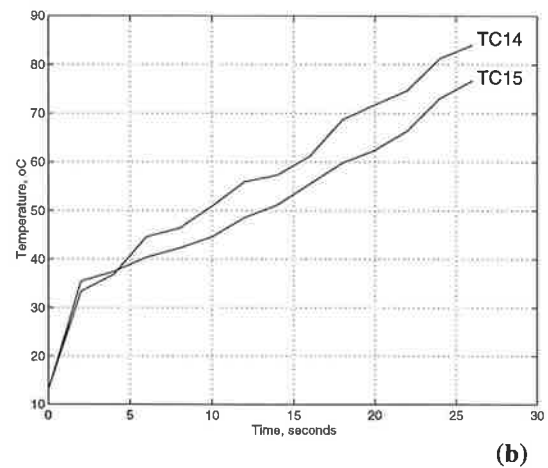
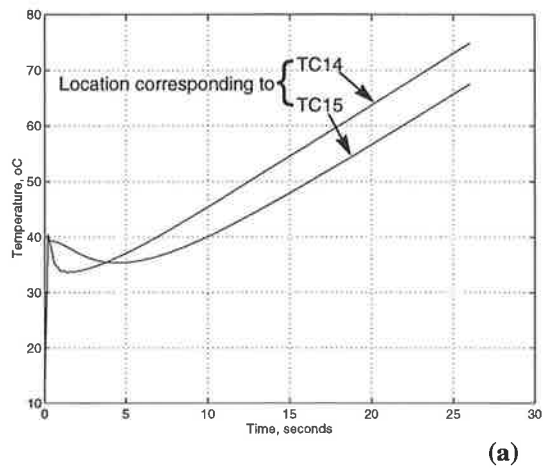


Fig. 6-10 Variation of temperature at the rotor end-ring (model2):

- a:** Simulation results at locations 14 and 15,
- b:** Test results at the same points as 'a',
- c and d:** Comparison of simulation and test results at the above points individually.

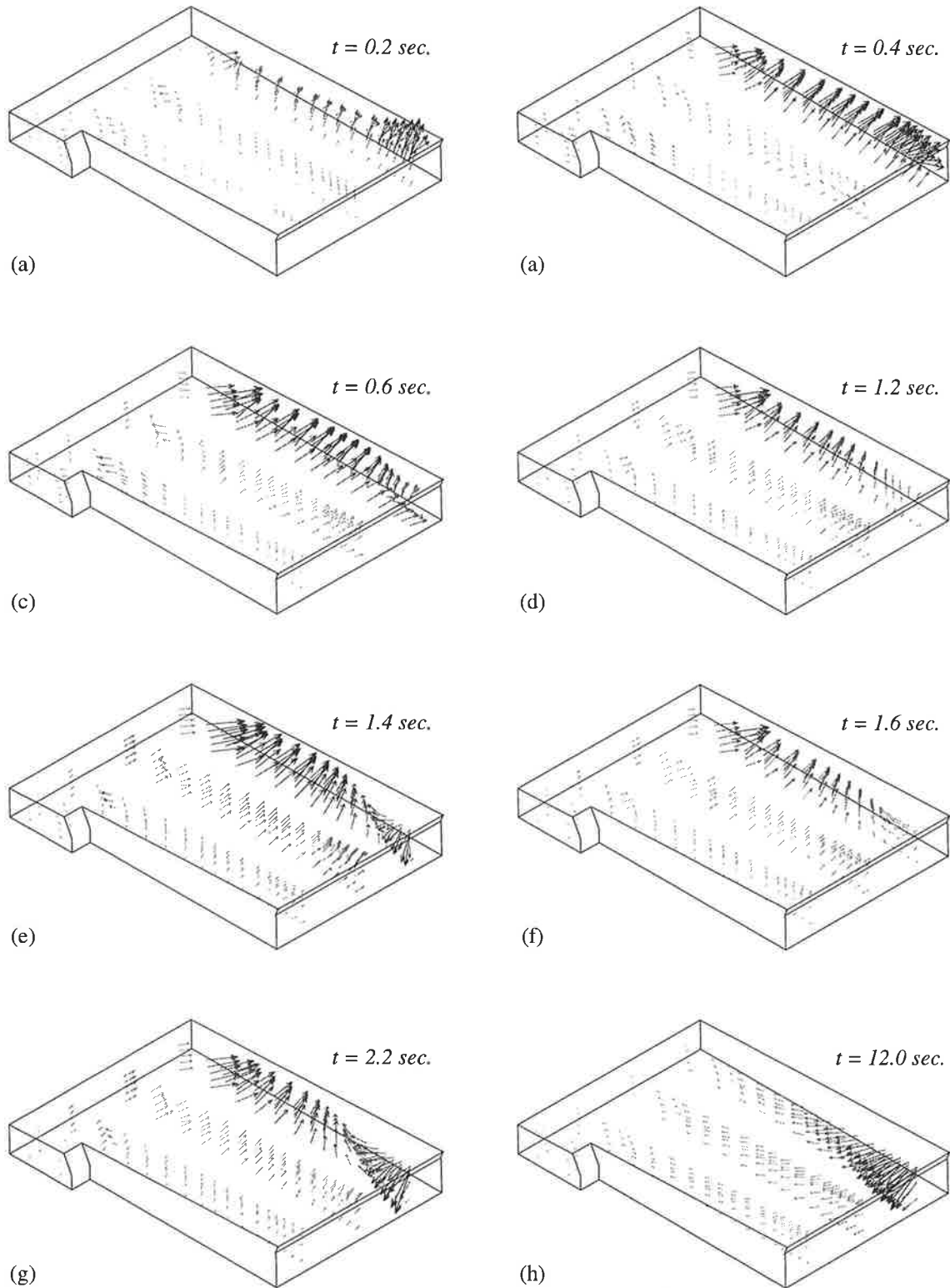


Fig. 6-11 Vector demonstration of the heat flow within the rotor end-ring at selected times as indicated.

Note 1. The physical orientation of these figures are similar to that of Fig. 6-15b,

Note 2. Each vector denotes the heat flow at its origin,

Note 3. The vectors are scaled in each figure individually.

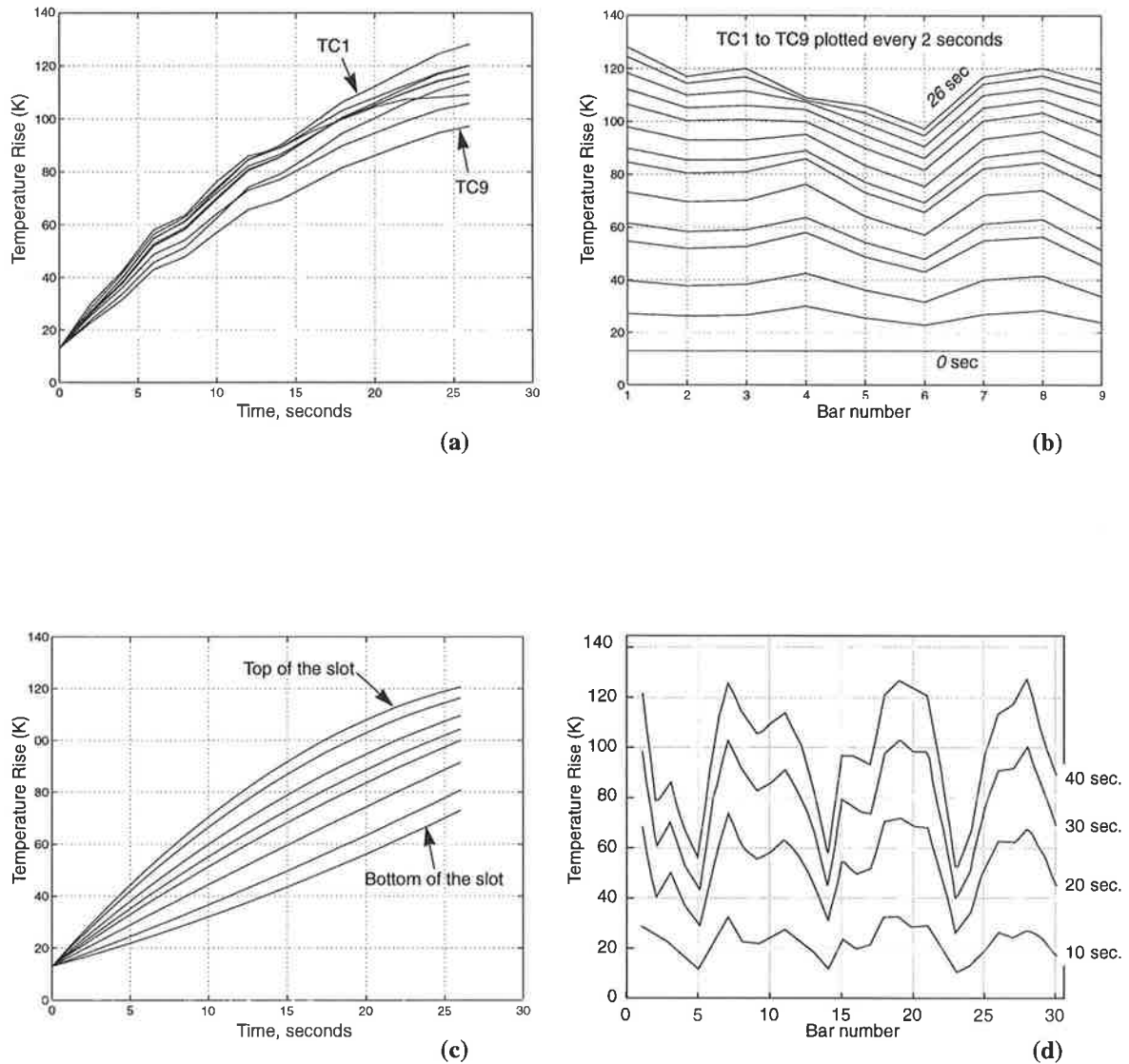


Fig. 6-12 Variation of temperature at the peripheral and radial locations on the rotor:

- a:** Variation of temperature with time along the peripheral direction (test results at locations 1 to 9),
- b:** Variation of temperature at different rotor bars at the given times (test results at locations 1 to 9),
- c:** Variation of temperature with time along the nodes at the central radial direction on the rotor bar (simulation results).
- d:** Similar to 'b' but on a 420 kW motor in Walker's [73] work (reproduced form of Fig. 5.19 in the reference).

Table 6-2 Specifications of Walker's [73] model

Power, kW	425
No. of poles	2
Line Voltage, volts	3300
No. of Rotor slots	56
No. of stator slots	48
Rotor bar type	Rectangular
Rotor slot opening	2.5
Rotor skew	0
Radial air-gap, mm	3

Comparison of simulation and the test results at corresponding points on the rotor bar area shows a good agreement in general. However, some discrepancy exists in the rotor end ring region. In this motor, the ring is fabricated by brazing the end parts of the bars, producing a non-uniform medium with possible trapped air. Consequently the temperature variation in the ring is not expected to vary smoothly with location. For the purpose of modelling, this part of the motor is substituted by uniform copper with equivalent material properties. Therefore, selection of physically similar points on the model and the actual motor may not represent similar status on them which may contribute to the aforementioned discrepancy.

The simulation and test results at three axially different location of the stator core are shown in Fig. 6-14a and Fig. 6-14b individually. The comparison of these results at each point, as shown in Fig. 6-14c to Fig. 6-14e indicates a satisfactory level of agreement with the maximum difference less than $1.2^{\circ}C$ at all times. Similar results at a certain point on the stator end winding and another point at the embedded part of the stator winding are given in Fig. 6-14. More information on each graph is given in the caption of each figure.

The picture of temperature distribution in the stator core at $t = 26$ seconds, as shown in Fig. 6-15a, demonstrates that the temperature at the stator core has not increased significantly, in particular, the outer surface of the stator is still at the room temperature. This was not unexpected and therefore no direct measurement was performed at the outer surface. However practical observation soon after switch off confirmed this fact. This means the convected heat from the relevant boundaries is quite minor and no extra error could occur if these boundaries were assumed as adiabatic for the sake of computing time saving. Fig. 6-15b shows the map of temperature distribution in the modelled parts of the stator winding and the rotor cage at the end of simulation period, $t = 26$ seconds.

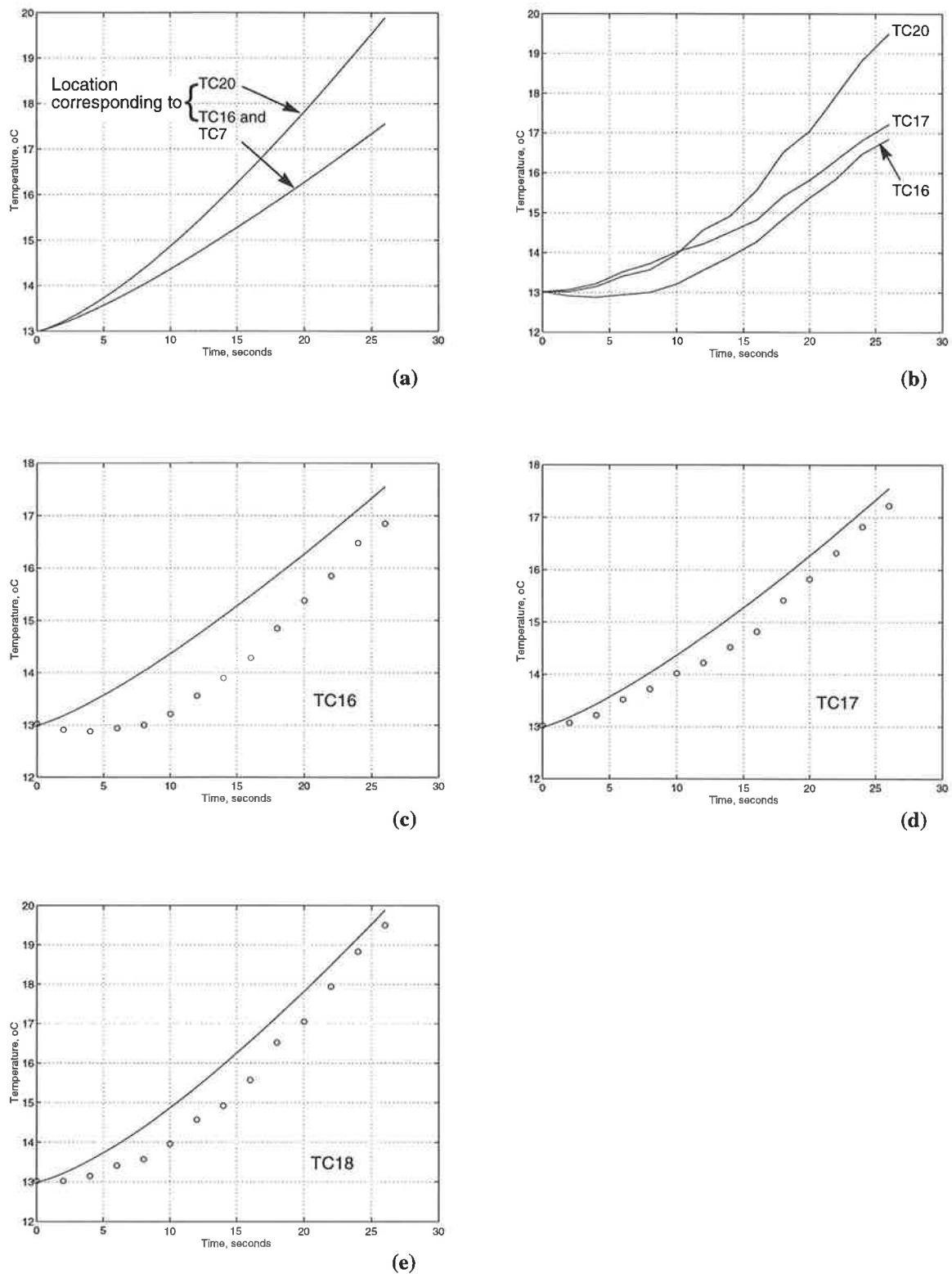


Fig. 6-13 Variation of temperature at the test points on the stator core (model2):

- a:** Simulation results at points corresponding to the location of TC16, TC17 and TC20,
- b:** Test results at TC16, TC17 and TC20,
- c to e:** Comparison of the simulation and test results at the above points individually.

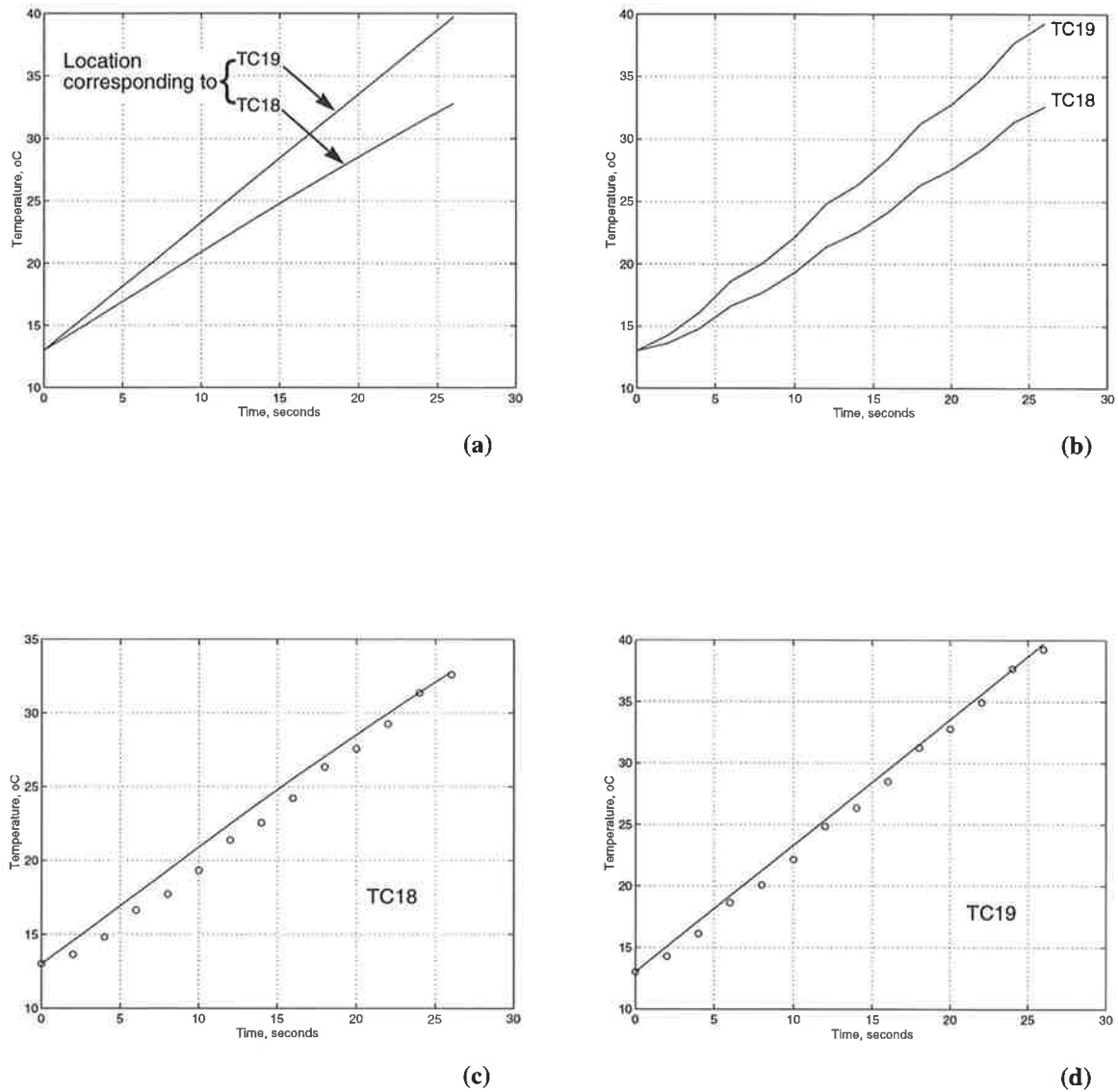


Fig. 6-14 Variation of temperature at the test points on the stator winding (model2):

- a:** Simulation results at points corresponding to the location of TC18 and TC19,
- b:** Test results at TC18 and TC19,
- c and d:** Comparison of the simulation and test results at the above points individually.

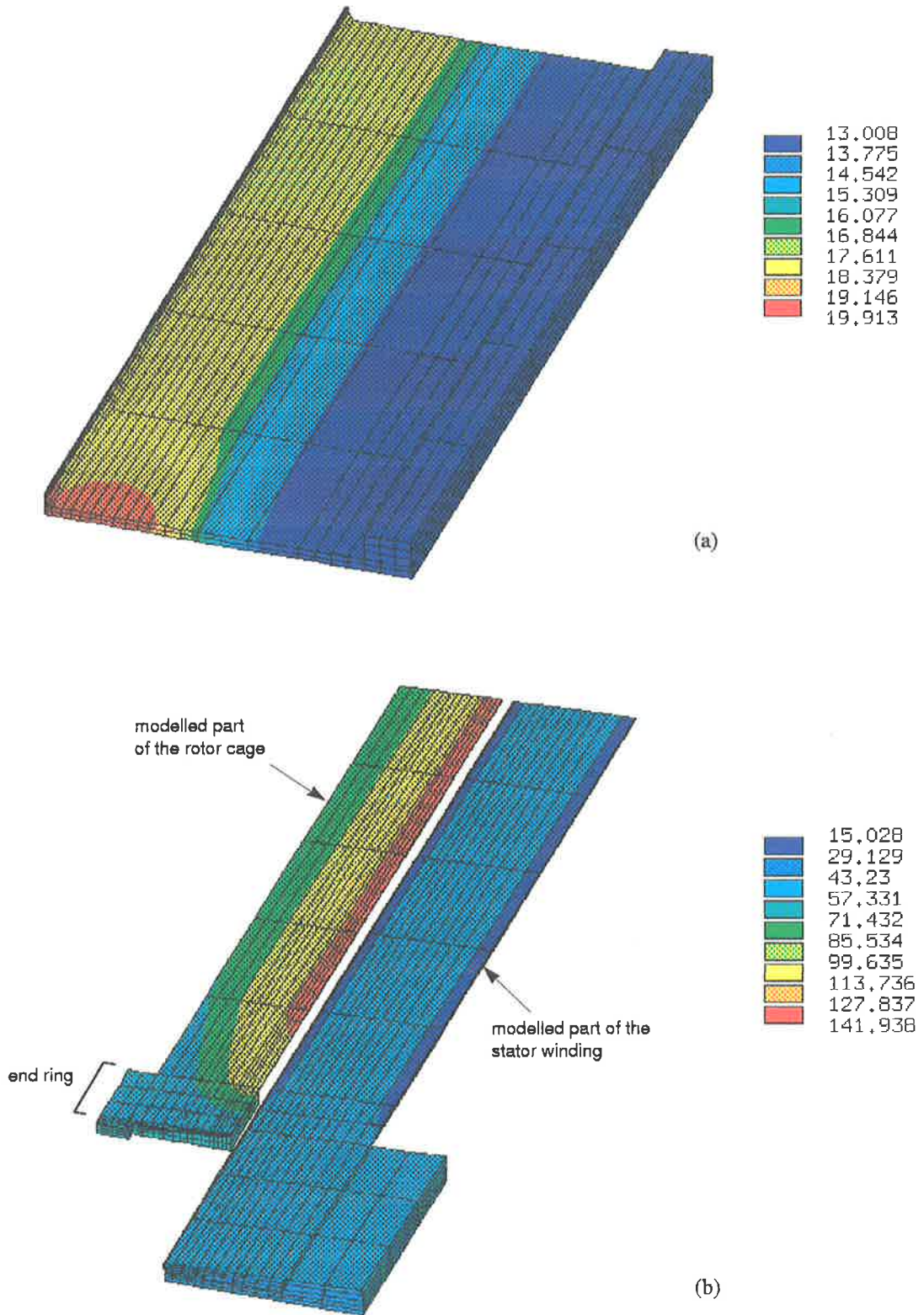


Fig. 6-15 Distribution of temperature at $t = 26$ sec. in the modelled parts (model 2):
a: stator core,
b: rotor cage and stator winding.

4.4 Some general comments on the results

A comparison of the overall results on the two models shows that:

- (a) The accuracy of the predicted temperatures, in particular in the rotor area, in model one is higher than that of model two. This may be attributed to the uncertain contact resistance at the rotor bar/core interface in a fabricated rotor and also the substitution of the complex material end-ring with its equivalent.
- (b) The duration of each locked rotor test was governed by the maximum permitted level of temperature at any point in the motors. In the case of model one, 15kW motor, the temperature at the stator winding reached to this level before any other point in the motor. On the contrary, the temperature rise at the similar part on the second model was still well below its rated level when the top parts of the rotor bar experienced the highest permitted temperature. The similarity in the duration of two individual tests on the two different machines, 26 seconds, was a coincidence and there were no pre-defined test periods for the motors.

5.0 STUDY OF HEAT FLOW IN THE MOTOR

Localised heat at any point in a motor may produce a hot point failure while other points in the motor are well below their locally rated temperatures. Therefore, prediction of the trend of heat flow within a motor can be as important as the distribution of temperatures in it. This prediction, at the design stage of course, allows modification of the thermal system to provide suitable heat channels to enhance this flow and eventually, increase the specific power of the motor. The heat exchange among the components of the motor may be easily extracted from the available results of the finite element analysis.

In this project, a finite element based lumped parameter model is introduced to demonstrate the trend of heat flow among the components of an induction motor. The motor is divided into a number of components and a weighted average temperature is calculated for each component. Then, the values of the circuit elements, the effective resistances, are extracted from the calculate heat flow among the components and their average temperatures.

This concept was applied on model one only and some additional interesting results were achieved. In order to set up the lumped parameter model, the entire motor was divided into seven individual components as follow:

1. On the rotor side: Rotor end-ring, Rotor bar and Rotor core;
2. On the stator side: stator core, the embedded part of the stator winding in the slots, the extension of stator winding before joining to the end winding, and the stator end-winding.

Then, considering the topology of the components, an equivalent circuit as shown in Fig. 6-16 was constructed. In this figure, R_{th1} to R_{th6} are a set of virtual resistances indicating the

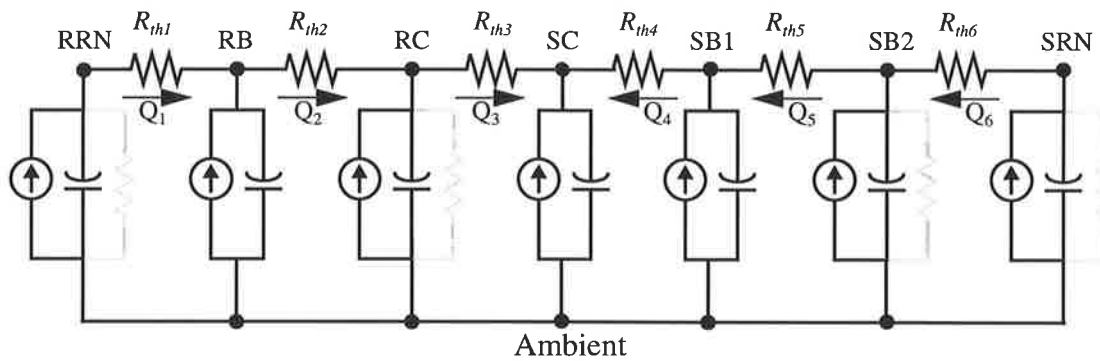


Fig. 6-16 The thermal equivalent circuit of a stalled induction motor

RRN: Rotor end-ring
RB: Rotor bar
RC: Rotor core
SC: Stator core
SB1: Embedded part of the stator winding

SB2: Extension of stator winding up to the end winding
SRN: Stator end-winding

equivalent thermal resistances between appropriate pairs of the components. The dashed resistors represent the path for convective heat transfer from each component into the ambient; the losses at each component are applied via a current source. The thermal capacitances of all components are also shown in the figure.

Since any component has potentially a non-uniform temperature distribution as well as an interface contact area with its adjacent components, an analytical calculation of the internal thermal resistances and the contact resistances is not possible. Therefore, a set of equivalent

thermal resistances is evaluated for each branch. In fact, these elements are virtual resistances evaluated after the finite element solution.

The weighted average temperature within each component on the basis of the finite element solution results, is defined as:

$$T_{avg}(t) = \frac{\sum(V_{el} \cdot T_{el}(t))}{\sum V_{el}} \quad (6-1)$$

With some manipulation on (6-1) a new definition is found for $T_{avg}(t)$ in a component with uniform ρ and c as follows:

$$T_{avg}(t) = \frac{(\rho \cdot c) \sum(V_{el} \cdot T_{el}(t))}{(\rho \cdot c) \sum V_{el}} \quad (6-2)$$

or:

$$T_{avg}(t) = \frac{\sum(\rho \cdot c \cdot V_{el} \cdot T_{el}(t))}{\sum(\rho \cdot c \cdot V_{el})} \quad (6-3)$$

In (6-3), the numerator is the total stored energy, enthalpy, within the component while the denominator represents the total thermal capacitance of the component. Therefore, $T_{avg}(t)$ is re-defined as:

$$T_{avg}(t) = \frac{\text{Stored energy in the component at time } t}{\text{Total thermal capacitance of the component}} \quad (6-4)$$

This means, $T_{avg}(t)$ is a temperature that will store the actual energy in the component if it is distributed uniformly within it.

The internal heat exchanges between the components, $q_{ij}(t)$, are also extracted from the finite element solution at any time step. Therefore, the effective thermal resistance between any pair of adjacent components i and j , represented by nodes n_i and n_j , at any time may be calculated from:

$$R_{ij, eff}(t) = \frac{T_{avg, i}(t) - T_{avg, j}(t)}{q_{ij}(t)} \quad (6-5)$$

In a steady state analysis of a single node lumped parameter model, the total power loss in the motor is the only component of the heat flow; and the temperature rise at the (single) node becomes the temperature difference between the node and the ambient. Therefore, equation (6-5) simplifies into:

$$R_{ij, eff} = \frac{\text{Temperature rise}}{\text{Power loss}} \quad (6-6)$$

Equation (6-6) was used by Boys [14] to evaluate the variation of steady state thermal resistance as a function of frequency in a single node LPM.

5.1 Results from the lumped parameter model

Fig. 6-17 and Fig. 6-18 show the time variation of thermal heat flow and the node temperatures in different branches and nodes of the equivalent circuit shown in Fig. 6-16. The variation of effective thermal resistances of Fig. 6-16 are also shown in Fig. 6-19. In order to assess the validity of the average temperatures, the ratios of the maximum temperature to the average temperature within each component were extracted from the finite element solution at any time step. In addition, the same ratios were extracted assuming entire rotor parts on the one hand and entire stator parts on the other hand as single components. The results are shown in Fig. 6-20. As can be seen in Fig. 6-19, the equivalent resistance between the rotor bar and rotor core, as expected, is quite small compared to other resistances. The equivalent resistance between the stator core and the embedded part of stator winding has the maximum resistance.

According to the basic formula of conducted heat flow ($\dot{q} = K \cdot A \cdot \Delta T / \Delta x$), a larger equivalent thermal resistance may be expected in a path as the temperature gradient increases for the same difference in the average temperatures. The very cold stator core is isolated from the hot stator winding, SB1, by a virtual resistance, R_{th4} . The extremely large value of this resistance is an example for this case. This was also confirmed by an investigation in a simple one-dimensional rectangular model.

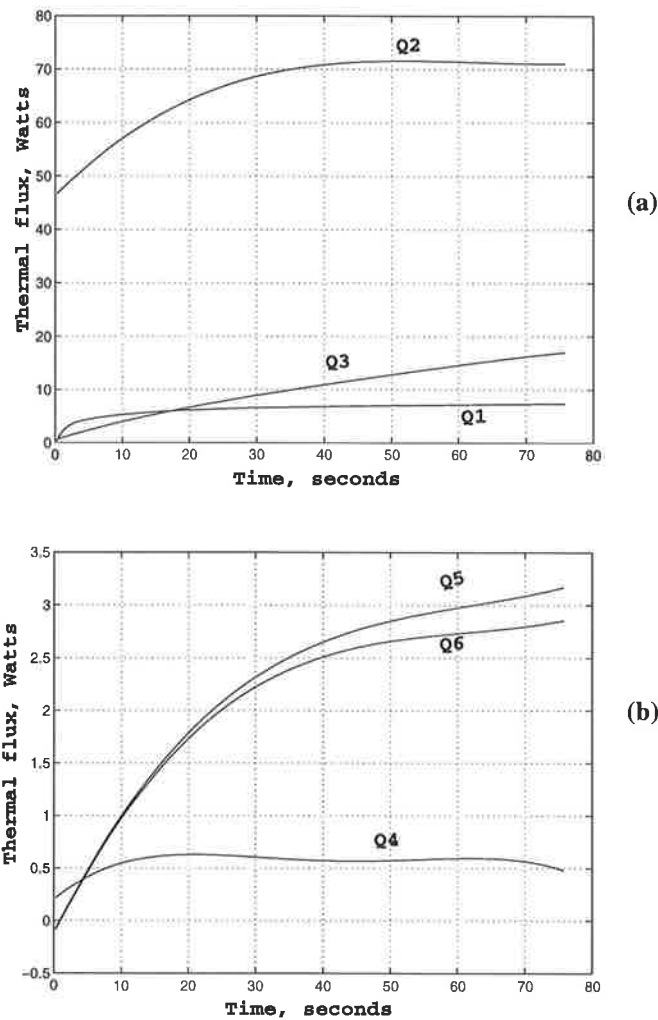


Fig. 6-17 The variation of thermal flux through different parts in the motor.

Fig. 6-20a shows that the rotor core has a dominant role in the average temperature in the entire rotor. However, assuming only the rotor bar or entire rotor as single components may introduce underestimation of the transient hot point temperature by 20% and 40% at each component respectively. The rate of underestimation in the entire stator is so high that the transient average temperature may not be valid in this component (see Fig. 6-20b); this may not be valid even in a steady state analysis because a high temperature difference may be expected between the stator core and the other parts of the stator. Assuming the stator winding as an individual component also may cause a considerable error of up to 25% in the estimation of transient hot point temperature (see Fig. 6-20c).

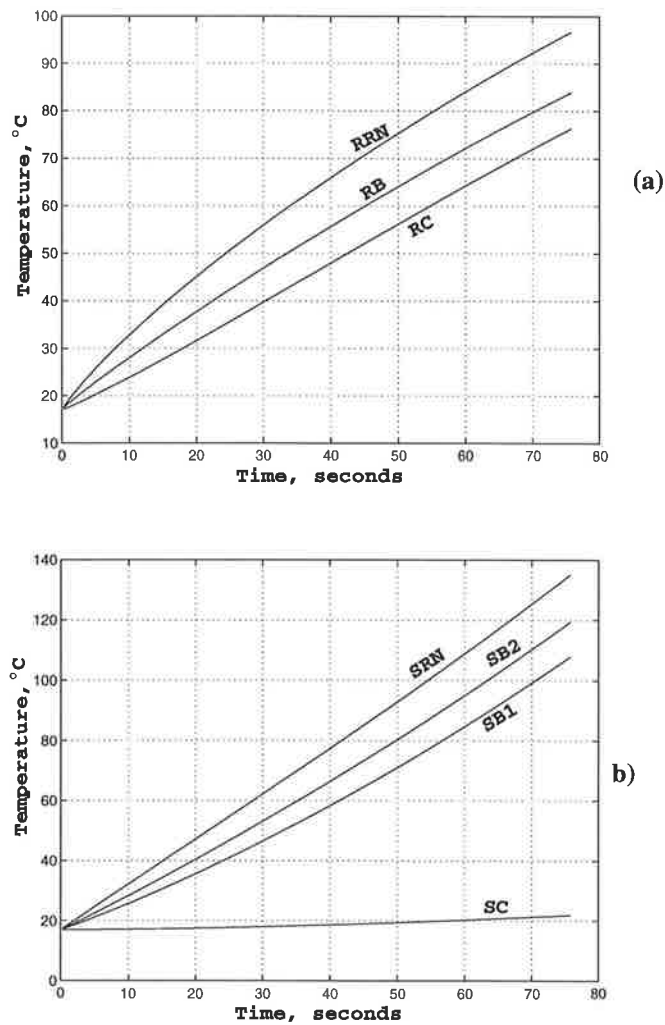


Fig. 6-18 The variation of average temperature in different nodes on the (a) rotor (b) stator

Since the properties of the constructional materials of the motor do not change significantly with temperature (within the working temperature margins), a linear correlation can be assumed between the average temperatures in the nodes, including the T_{max}/T_{min} ratios, and the motor loading. Theoretically, this is only valid if the heat convected to the surroundings is ignored since it varies with the temperature at the boundaries. However, the convected heat from different boundaries of a motor during the early seconds of stall is not considerable unless non-realistically large convection film coefficients are applied. Fig. 5-20 shows the convected heat from the 15kW test motor during its stall for the case of this study. As can be seen, the total convected heat from the entire motor is less than 0.52% of the ohmic losses.

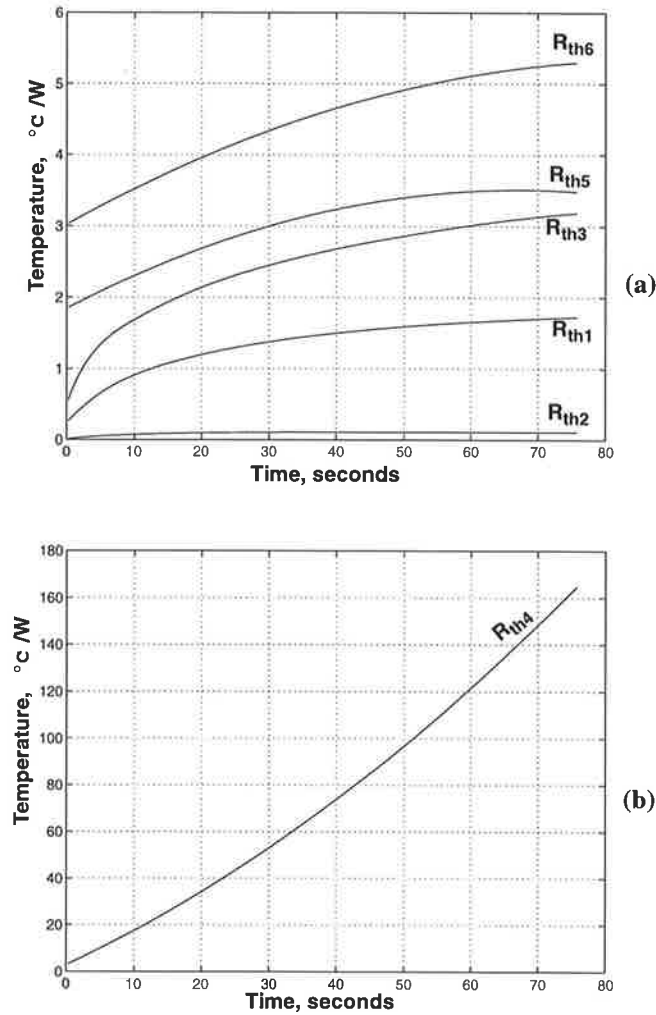


Fig. 6-19 Variation of the effective thermal resistances:

5.2 Some comments on the results of current topic

1. The air-gap is assumed as a good thermal barrier in most published LPM work [11, 14, 21, 87]. Although this may result in correct results, the main concept seems to be non-realistic. In fact, the large interface area between the rotor and stator surfaces in an induction motor along with its usually short air-gap annuls the effect of poor thermal conductivity of the air, so that the thermal resistance of this component becomes reasonably comparable with that of other components. However, the low difference between the average temperatures of the rotor and the stator surfaces in a steady state

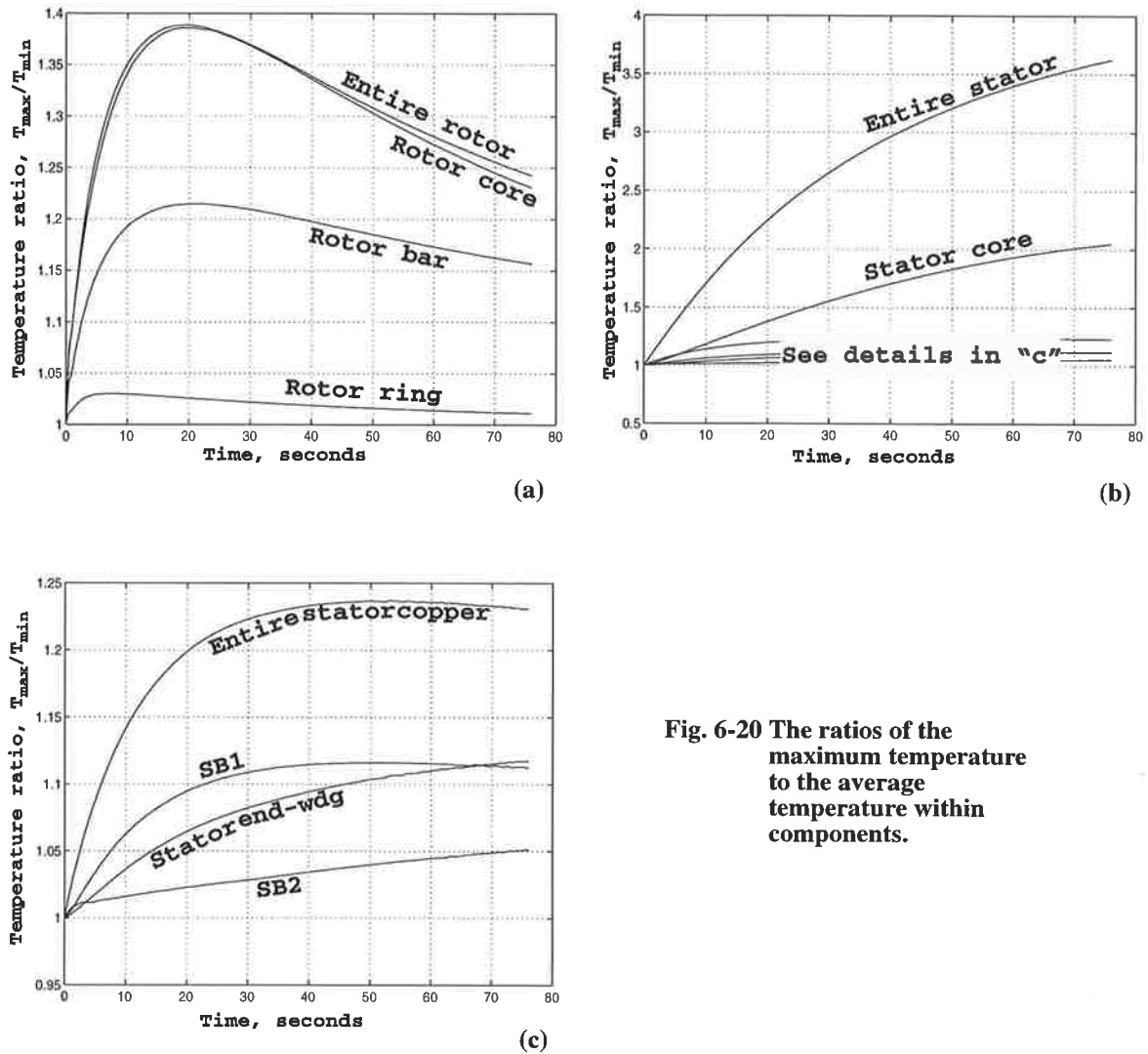


Fig. 6-20 The ratios of the maximum temperature to the average temperature within components.

analysis of a running motor weakens the sensitivity of the solution to the changes in this thermal resistance and consequently the non-realistic assumption does not introduce any significant error.

On the other hand, in the transient analysis of a motor, when a large change occurs in the currents, such as starting the motor, the temperature rise at the surface of the rotor is much larger than that of the stator before the steady state conditions are established, therefore the heat transfer through the air-gap becomes considerable. This is more significant in the case of this study. The rate of heat flow through the air-gap and the average values of temperature at the rotor and stator cores can be seen in Fig. 6-17 and Fig. 6-18 respectively.

2. Obviously, the values of the virtual thermal resistances are configuration dependant; any change in the definition of the components or their configuration is expected to affect the values of the extracted thermal resistances. The less number of nodes, the more variation in the R_{th} 's and also the T_{max}/T_{av} ratio in each component is expected. This is true in the case of normal LPM's too.
3. An investigation in the temperature rise curves in Fig. 6-20a to Fig. 6-20c shows some different time constants within the components. Obviously, approaching the T_{max}/T_{av} ratio to unity within each component is a measure of uniform distribution of temperature in it. The ratio become maximum within 20 seconds in the rotor bar and rotor core while it takes some different and longer time in case of stator winding parts. The similar time for the stator core is expected to be considerably longer than that of other parts.
4. The non-uniform distribution of temperature within any or both of the two adjacent components is mainly responsible for the time variation of the assigned virtual resistance between them. The value of this resistance is also significantly affected by the difference between the heating time constants of the components. For example, Fig. 6-17b shows a nearly uniform heat flow from the stator bar SB1 into the stator core SC (Q4) while the difference between the average temperatures at the relevant nodes is increasing with time (see Fig. 6-18b). Consequently, a time-variant virtual resistance is headed between these nodes. This may seem unrealistic compared to the thermal resistance of the slot liner only, which may be nearly constant. However, it should be emphasised that, the calculated virtual resistance includes the effect of non-uniform distribution of temperature within the entire bodies in either sides of this resistance, rather than assuming uniform temperatures for each body with zero internal resistances as in a traditional lumped parameter model. Similar conditions exist for R_{th3} where the time constants of the rotor and stator cores are considerably different.

* * * * *

CHAPTER SEVEN

TRANSIENT THERMAL ANALYSIS DURING STARTING

Contents: Procedure of the modelling, Dynamic equivalent circuit of the motor, Determination of equivalent circuit parameters, Test setup and Verifications

1.0 INTRODUCTION

Modelling of an induction motor within the period of starting, from the instant of switch on to establishment of the preliminary steady state¹ conditions in the motor, is a case-dependant procedure which is very strongly affected by the method of starting, the mechanical characteristics of the motor and the attached load. Any deviation from the pre-assumed conditions, such as the rms value of the applied voltage and/or its waveform, modifies the predicted results. Therefore, the thermal analysis of a motor within this period relies upon comprehensive data about the mechanical and electrical conditions of the system including the motor and the load. An accurate analysis under these conditions is well beyond the topic of this thesis. So, only the milestones of this work are discussed in this chapter.

During each start of a large induction motor, a vast energy is injected into both windings of the motor, in particular the rotor cage. Consequently, for a frequently started motor, the generated heat in different parts of the motor is not dissipated between any two subsequent critical conditions. Similar conditions may be expected in motors:

1. The preliminary steady state conditions is assigned to a situation when the motor reaches its operating point associated with the torque-speed characteristics of the load soon after the start up. This point is subject to change later on because of the variation of motor parameters with temperature before the thermal steady state conditions are established.

- (a) driving high inertia loads, including that of the actual load and any intermediate accessories, such as gear boxes and couplings,
- (b) working with high slip, or having frequent over-loadings,
- (c) started under load from a reduced voltage such as Y/Δ method or by an autotransformer;
- (d) driving loads with either flat $T(n)$ characteristics or with large starting torque, such as lifts, cranes, compressors, ball mills, etc.

Thus, if it is not controlled by suitable protection devices, the temperature rises continuously until a thermal failure occurs. In the case of an aluminium cage, when the metal expands and pushes on the rotor bridge, it may even melt [19]; this phenomenon is more likely in deep bar rotors. The sequence could happen several times before the iron at the rotor slot bridge cracks and the melted aluminium sprays into the air gap [19]. In addition, before a complete failure, some side effects such as variation of the bar geometry during each heating/cooling process and/or losing the mechanical balance may occur which causes some alteration in the motor behaviour.

According to the existing standards, any induction motor should withstand its rated voltage against a locked rotor for a specific time (see the Australian Standard for the TEFC motors in Fig. 1-1 as an example). In small motors, the duration of starting is very short. Therefore, if the motor fulfils the appropriate standard requirement, one may hardly expect the temperature rise in any specific point in the motor at the end of starting to exceed the locally permitted values. On the contrary, this is not necessarily true in large motors despite the current decreasing during acceleration. Therefore, prediction of the transient temperature distribution within the critical points of such motor during start up may be categorised as a substantial design step.

2.0 PROCEDURE OF THE MODELLING

Except for some special cases, the main stages of the modelling during start up is similar to that of the locked rotor. The 3-D half-slot thermal model is used for this analysis. The distribution of thermal load at any time step is extracted from the solution of the 2-D finite element magnetic model. However, the magnetic model should be loaded appropriately for

any predicted speed corresponding to the time step. A modified equivalent circuit of the motor, so called “dynamic equivalent circuit” is used to find the stator and the rotor currents at different speeds. However, prediction of the variation of the currents with time involves the knowledge of $\omega_m(t)$ characteristics of the mechanical system. In practice, this is a function of the electrical and mechanical characteristics of the motor as well as the mechanical characteristics of the load and may be predicted as explained below. Details of the dynamic equivalent circuit along with the procedure of its construction are described in the following section.

The time average of the developed torque in an induction motor in terms of the Thevenin equivalent circuit parameters is:

$$T_m = \frac{1}{\omega_s} \cdot \frac{q_1 V_{1a}^2 (r_2/s)}{(r_{e1} + r_2/s)^2 + (x_{e1} + x_2)^2} \quad (7-1)$$

where:

$$V_{1a} = V_1 \frac{jx_\phi}{r_1 + j(x_1 + x_\phi)}$$

$$r_{e1} + x_{e1} = (r_1 + x_1) \text{ in parallel to } x_\phi$$

$$V_{1a} = \text{the Thevenin equivalent source voltage}$$

$$\omega_s = \text{the angular synchronous speed}$$

$$s = \text{slip}$$

The classic equivalent circuit of an induction motor and its Thevenin equivalent are shown in Fig. 7-1.

The acceleration torque T_{acc} is the difference between the developed torque and the load torque including the mechanical losses, T_l as follows:

$$T_{acc} = T_m(\omega_m) - T_l(\omega_m) \quad (7-2)$$

Thus, the instantaneous speed of the motor may be calculated from:

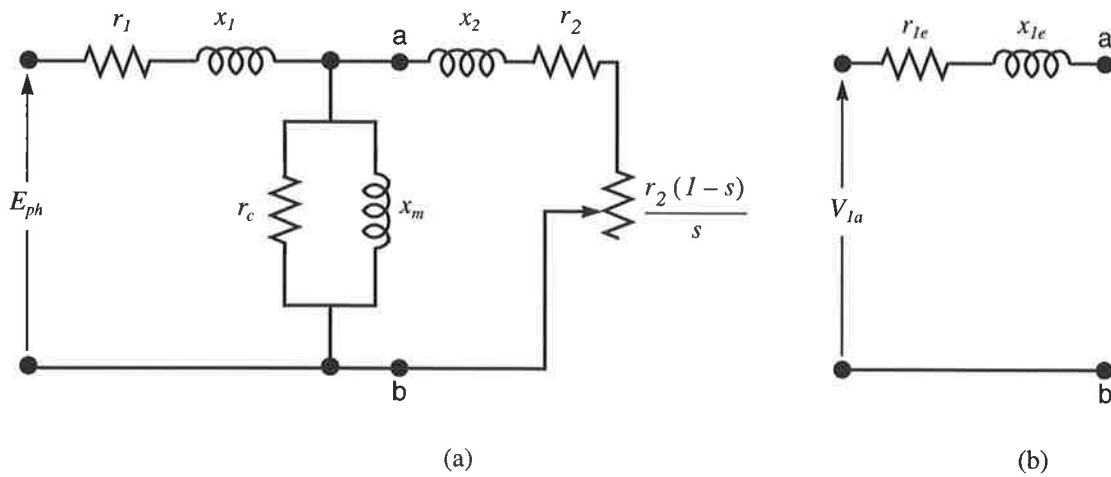


Fig. 7-1 The equivalent circuit of an induction motor:
a: The classic equivalent circuit,
b: The Thevenin equivalent circuit to the left of ab.

$$T_m(\omega_m) - T_l(\omega_m) = J \left(\frac{d\omega_m}{dt} \right) \tag{7-3}$$

J is the polar moment of inertia of the entire rotating parts. Usage of the time average value of the developed torque in the mechanical dynamic equations (7-1) to (7-3) implies that the electrical and the magnetic time constants of the motor are assumed to be much shorter than that of the mechanical system. This also means that the electrical and the magnetic circuits are assumed to be in a semi-steady state conditions at any time during the starting.

The $T_m(\omega_m)$ characteristics of the motor may be extracted by some modifications from the existing form of (7-1). Having the mechanical characteristics of the load and also J , the variation of ω_m with time, $\omega_m(t)$, can be obtained from (7-3). Since the variation of the motor parameters with temperature and also the convected heat from different areas are ignored, all of the calculated data become speed-dependant rather than time dependant. Therefore, they may be used in the analysis of the motor under any given load on condition that the characteristics of speed vs. time is available.

2.1 Dynamic equivalent circuit of the motor

The parameters of the classic equivalent circuit of induction motor, as shown in Fig. 7-1a are usually obtained from a blocked rotor test and a light running test. Therefore, usage of this circuit eventually involves some error under any speed, in particular, when the motor is due to be analysed within a wide range of speed from standstill to full speed. Some of the relevant errors are as follows:

- (a) r_c is calculated from a light running test at nearly (and not exactly) synchronous speed where the ohmic losses in the stator and rotor are ignored. In a physical motor, the stator ohmic losses at no load may be considerable, in particular in the motors with long air-gaps.
- (b) r_c includes the effect of the friction and windage losses at the test speed as an error. Theoretically, this power should be deducted from the developed mechanical power on the rotor side,
- (c) Iron losses in the rotor core vary with speed. A fixed value of r_c can not represent this effect,
- (d) The values of the rotor equivalent resistance, r_2 , and the reactance x_2 are extracted from the locked rotor test whence both parameters, in particular r_2 , reduces with speed. This effect becomes more severe in a deep bar rotor.

Consequently, this equivalent circuit may not be valid to represent a motor during acceleration unless its parameters are modified to generate a “dynamic equivalent circuit”.

Most likely, the rotor resistance is the main variable component in the motor during the start up. In simple-geometry rotor bars, such as a rectangular bar, the variation of the bar resistance and also its reactance may be easily extracted from Alger's [1] method, or the transmission line equivalent circuit procedure [8,9,39]¹. Using this method, Smith [69] studied the behaviour of a deep-bar motor during acceleration under a compressor load. He

1. Alger's method and also the transmission line (or ladder equivalent circuit) method are applicable on the open-slot rotors only.

proposed a ladder equivalent circuit for the rotor bar and determined the relevant parameters by fitting the circuit on the manufacturer's data at standstill and under full load. In a similar attempt, Rogers [61] extracted the rotor ac resistance at standstill using the ratio of available values for starting torque and the full load torque. The iron losses, or the variation of this component of losses was ignored in all of the aforementioned works.

2.2 Determination of equivalent circuit parameters

The values of x_1 and r_1 are assumed to be constant as speed and/or voltage varies. Therefore, they are obtained from a locked rotor test as used in the classic tests. This analysis is based on the following additional assumptions:

- (a) The effect of saturation of the rotor bar bridges is neglected during the preliminary magnetic analyses to determine x_1 , r_2 , and x_2 . Otherwise, a prohibitively large amount of analyst effort along with computer resources are required.
- (b) The variation of r_1 and r_2 with temperature during the starting is ignored. This assumption is made for the sake of time limit only. It is quite possible to update the values of the resistances at the end of each time step of the thermal analysis. This effect was thoroughly studied by the author [23] and it was shown that the introduced error is acceptable.

Determination of r_2 and x_2 . The values of the rotor resistance and leakage reactance at different speeds (and consequently frequencies) are attained from a combination of magnetic analysis and test results at 50 Hz as follows:

- (a) Running a set of preliminary magnetic analyses, the frequency of the rotor current is varied from zero to 50 Hz and the map of the distribution of current density¹, the effective resistance, and also the leakage inductance of the rotor are calculated as P.U. quantities,

1. This will be used in the application of thermal loads on the rotor bars.

- (b) Using the available values of the effective resistance and the leakage inductance of the rotor from the test results at 50 Hz, corresponding to the stand still conditions, the ohmic values of the same parameters in other frequencies are calculated from the available P.U. quantities.

Theoretically, the saturation level of the iron core also modifies the rotor resistance and it may be easily taken into account by using the process as explained on page 36 (chapter 2). Considering the accuracy of the available data and lengthiness of the procedure, this was not justified for the case of preliminary magnetic analyses.

Measurement of r_c and x_m . The value of r_c should be measured by isolating the iron losses from any other components of losses such as friction and windage losses as also the rotor ohmic losses. The value of this parameter at synchronous speed represents the iron losses in the stator core only, since the rotor core losses and ohmic losses are automatically absent. So, it can be easily determined by the measurement of the electrical input power to the motor and having r_1 in hand, when the motor is driven at synchronous speed by another mechanical source. However, at any other speed, r_c includes the effect of the stator core losses at the supply frequency along with that of the rotor core at slip frequency. To eliminate the effect of rotor ohmic losses at non-synchronous speeds, the rotor winding/cage should be open circuited which is only applicable on a wound rotor. Nevertheless, if another packet of rotor core with no cage is available, the same procedure may be applied on a cage rotor as well. In both cases, the motor should be driven in a wide range of speed and the iron losses in the induction motor should be extracted from the supplied power into the motor at any stator voltage. This method also allows obtaining the variation of the rotor iron losses with speed and voltage.

The corresponding values of x_m under any condition is similarly extracted by looking at the reactive power at that condition.

3.0 PROCEDURE OF THE PRELIMINARY TESTS

Using the corresponding values of equivalent circuit parameters at any speed, the currents in the stator and rotor are calculated for the same speed. Then, a 2-D magnetic analysis is performed to find the distribution of flux density in the iron core and also the distribution of

current density in the winding areas taking the effect of saturation into account. These data are then used to obtain the distribution of thermal load in the motor.

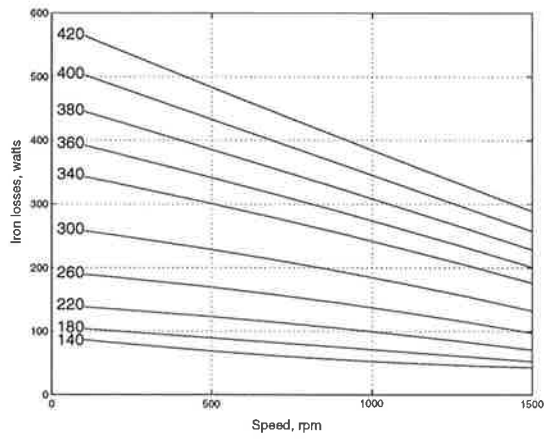
The method is applied on the 15kW TEFC induction motor, used as model one in this project. The iron losses are measured by using a variable speed DC machine as drive. The total input power $P_{in, tot}$ into the set, including the power from the DC source $P_{in, dc}$ and that of AC source $P_{in, ac}$ were measured when different AC voltages, including zero volts, were applied on the induction motor. The iron losses at any voltage V and speed n were extracted from:

$$P_{iron}|_{V, n} = P_{in, tot}|_{V, n} - P_{in, tot}|_{(V=0), n} - \text{stator ohmic losses}|_{V, n} \quad (7-4)$$

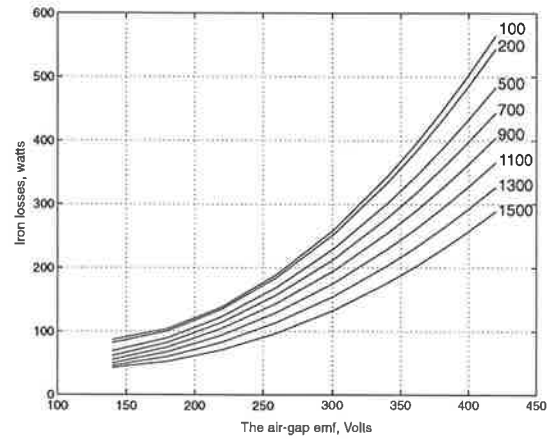
Unsurprisingly, at the large applied AC voltages, the developed torque by the eddy currents in the rotor core and hysteresis losses (hysteresis torque) in the same part of the induction motor was enough to drive the set with a maximum speed of 550rpm where the input power into the DC machine became negative.

Some of the preliminary test results on the cage-less motor are grouped in Fig. 7-2. In this figure, 'a' and 'b' show the direct measurement results for the iron losses in the motor as functions of phase voltage and speed. Under the test conditions on the cage-less motor, the voltage drop across the stator impedance is quite negligible. Therefore, the air-gap emf is assumed to be same as the input voltage. In many circumstances, e.g. under load or in particular during the stall or starting, the voltage drop across the stator winding is essential. So, in order to combine the two sets of the test results from the locked rotor and open circuit tests, the air-gap emf is used as the interface.

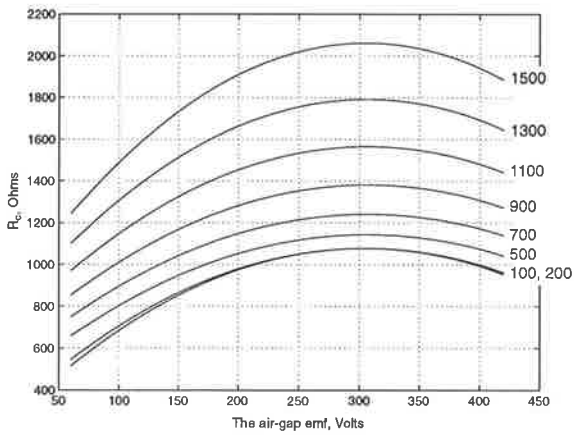
The variation of the extracted values for R_c and X_m with air-gap emf are shown in figures 'c' and 'd'. As expected, the variation of R_c with speed, representing the variation of iron losses with this variable, is considerable. On the contrary, X_m remains nearly constant as speed varies. The resultant variation of X_m with speed in Fig. 7-2d is not significant, especially in view of the potential error in the procedure. For this reason, this figure does not distinguish between individual speeds.



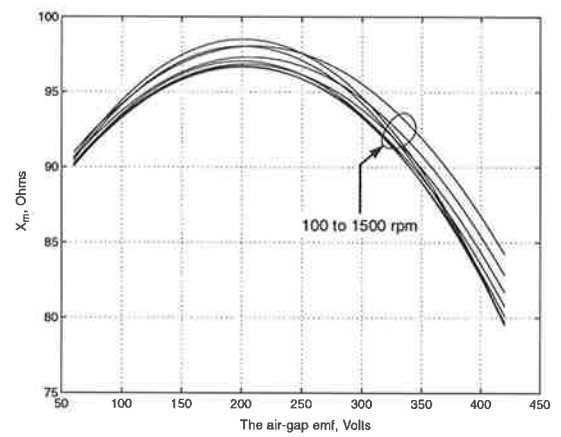
(a)



(b)



(c)



(d)

Fig. 7-2 Test results from the test on the cage-less motor:
a: Variation of iron losses with phase voltage,
b: Variation of iron losses with shaft speed,
c: Variation of R_c with air-gap voltage,
d: Variation of X_m with air-gap voltage.

The measured values for R_c and X_m at the synchronous speed in Fig. 7-2c and 'd' are slightly different from that of the direct test using the normal rotor (see Fig. 5-6 on page 100). This can be attributed to the accumulation of errors in the present method as the number of measurements is much more than that of the direct measurement. In addition, the possible difference in radii of the two rotors may add to the error.

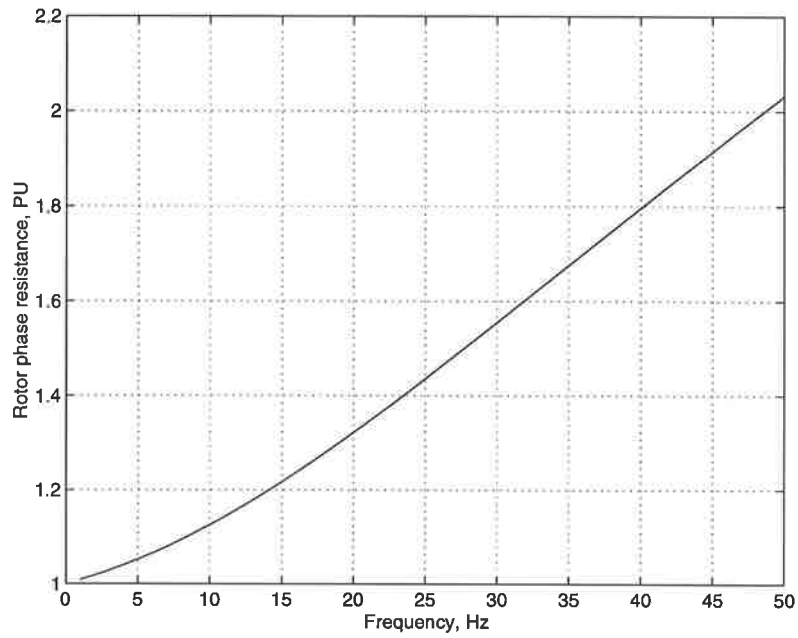
The variation of the rotor resistance and rotor leakage inductance as P.U. quantities are shown in Fig. 7-3. These results are combined with the corresponding voltages at synchronous speed (see Fig. 5-6 on page 100) to achieve the variation of each parameter with speed and voltage.

Having the parameters of the equivalent circuit in hand, the stator current I_1 and the rotor current I_2' are calculated at different speeds, from standstill to the synchronous speed. Fig. 7-4a shows the variation of these currents with speed when the motor is fed by the rated voltage. This figure also shows the variation of the same parameters when the deep bar effect is ignored. The associated error in this case is shown in Fig. 7-4b. As can be seen, ignoring the deep bar effect may introduce a major error in the estimation of motor currents during the start/operation.

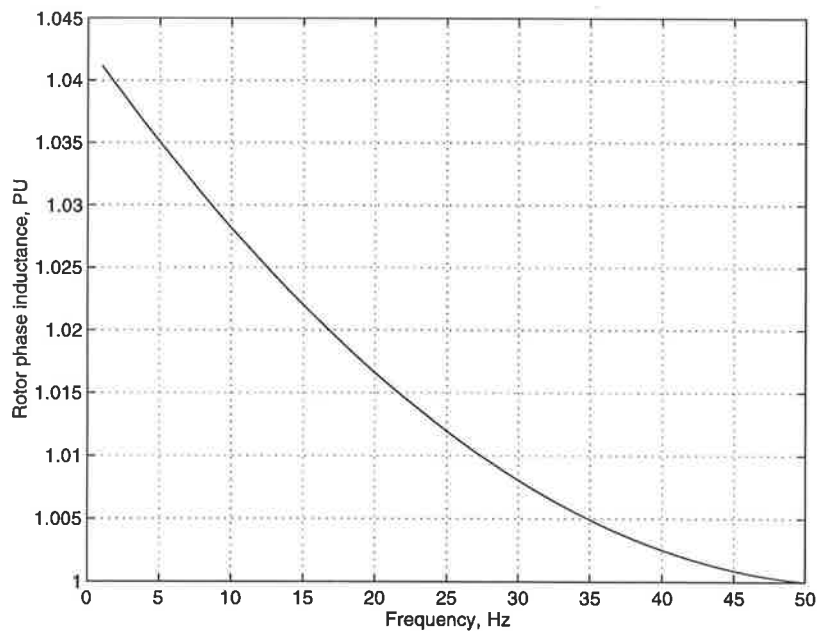
4.0 TEST SETUP AND VERIFICATIONS

In order to verify the proposed method, a start-up test was performed on the 15kW motor, used as model one in this project. The output of each installed TC on the rotor was fed into the data-logger via a pair of slip-rings. However, practical limitations allowed installation of only 8 pairs of slip-rings where the outputs of TC1 to TC6 and also TC11 and TC13 were selected out of the 14 installed TC's to be monitored¹. The outputs of TC15 to TC17 on the stator were also fed into the data-logger. In addition, to temperatures, the variation of speed, phase current, line voltage, and power were recorded by using appropriate transducers. The location of the TC's is shown in Fig. 6-2 on page 136.

1. During the process of the results it was found that TC4 and TC17 had not responded appropriately. Therefore, the recorded data by these TC's were discarded.



(a)



(b)

Fig. 7-3 Variation of rotor resistance and inductance with frequency

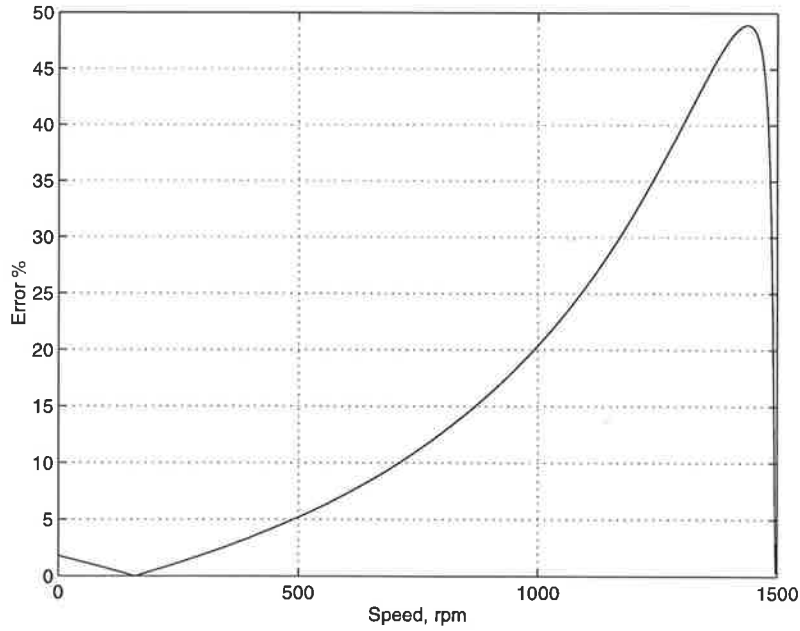
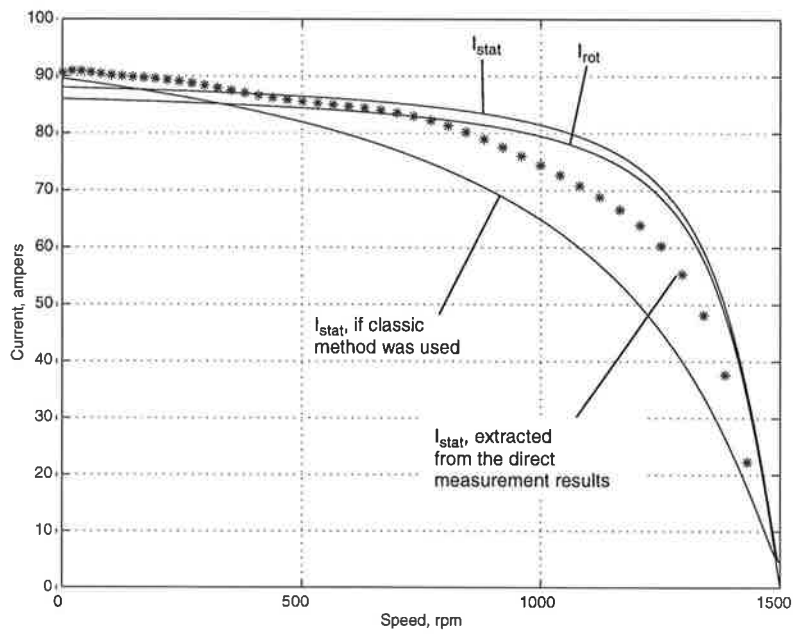


Fig. 7-4 Motor currents in different conditions and the associated error:

a: Variation of I_1 and I'_2 with speed when the motor is fed from the rated voltage,

b: Percentage of error if the classic test method is used

The motor was attached to a partially braked 420kW dynamometer as a high inertia load started with rated voltage. The variation of the measured current, voltage, and speed with time, and also the variation of current with speed are shown in Fig. 7-5. The sampling rate of

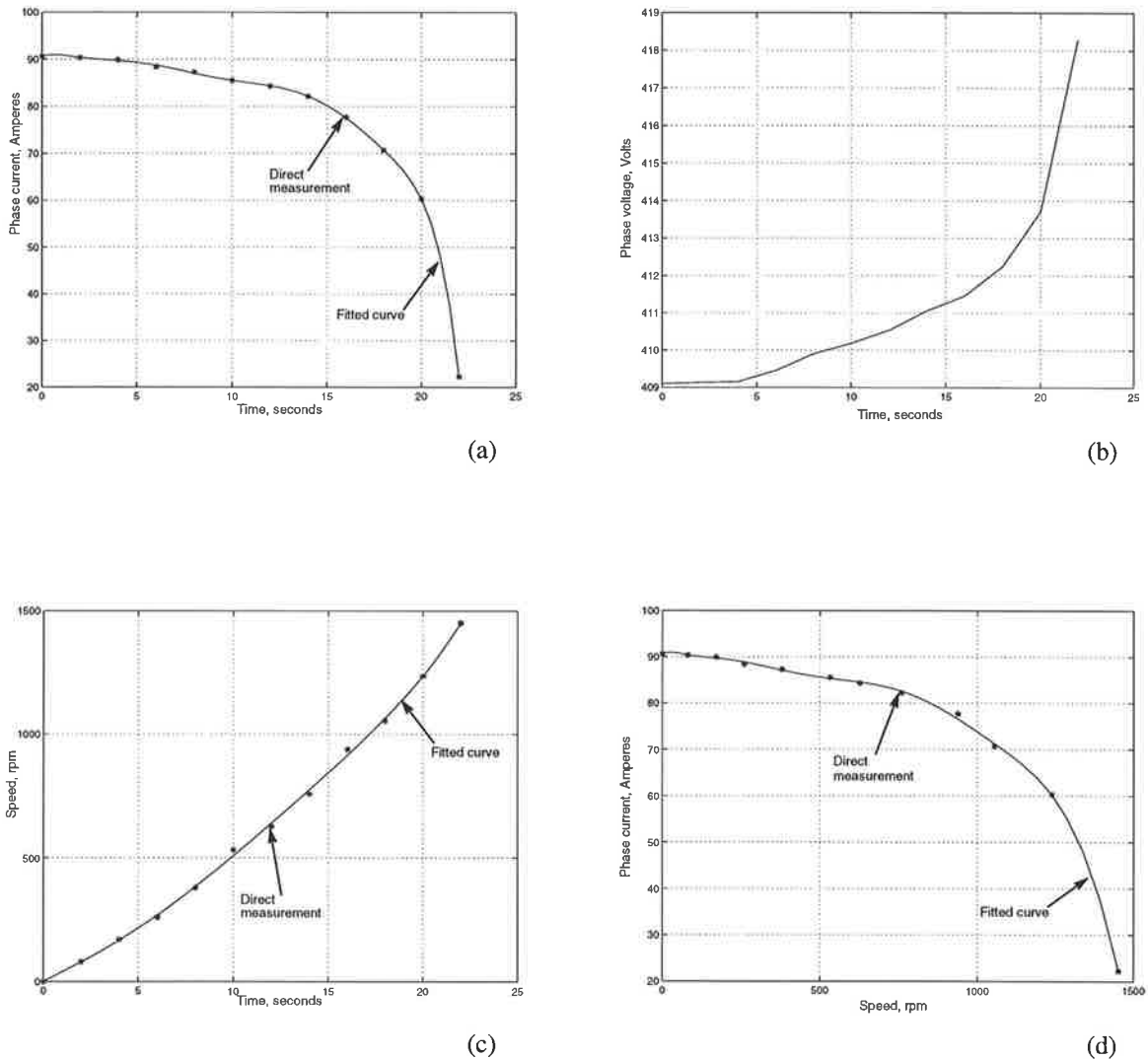


Fig. 7-5 Measurement results from the run-up test:

- a to c:** The variation of current, voltage, and speed with time respectively,
- d:** The variation of current with speed (extracted from the test results).

the data-logger was set to 2 seconds. However, since the variation of the speed with time was due to be used as an initial data for the analysis this parameter was fitted to an appropriate curve in order to obtain any necessary data with a higher resolution. In Fig. 7-5, the asterisks demonstrate the actual measurement results while the fitted curves are plotted as solid lines.

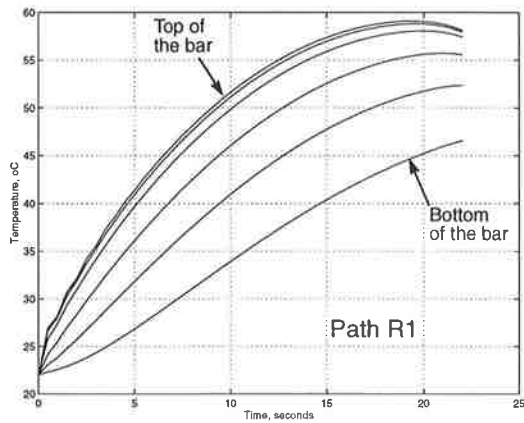
Compared to normal test/simulation procedures, a higher error may be expected in all parts of this work. This is involved in numerous tests, and more important, usage of two different rotors in the acquisition of data for the analysis. Therefore, any non-similarity of the rotors may contribute the error of the final results. In addition, the variation of the rotor and stator resistances with temperature during the start up is not included in the prediction of the currents.

The fitted form of Fig. 7-5d is repeated in Fig. 7-4a (shown as asterisks) for the sake of comparison. As can be seen, the actual measured current reduces faster than the estimated value which may be a consequence of the aforementioned errors.

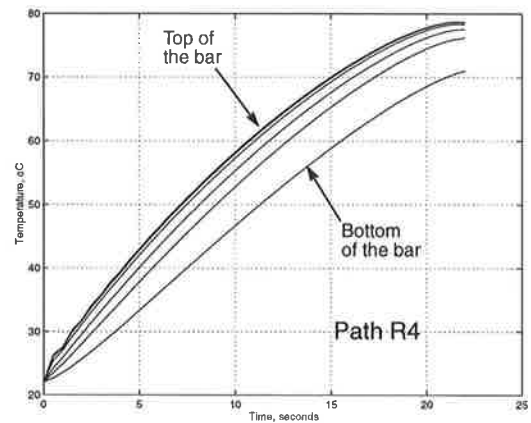
The time variation of the temperatures at a number of nodes along different paths on the rotor cage, extracted from the analysis results, are shown in Fig. 7-6. Paths R1 and R4 include the nodes along the radial axis of the bar at the middle and the top of the bar respectively. The nodes along the axial direction of the bar at the bottom and top of the bar are grouped as paths R5 and R8 respectively. The location of these paths is schematically shown in Fig. 6-3.

As can be seen in Fig. 7-6d (and also Fig. 7-7b and 'd'), the thermal gradient along the axial direction is larger than that of the corresponding locked rotor case (see Fig. 6-9b, 'c', and 'd' on page 147). Since the mid-point of the bar receives no heat from the other parts of the bar, temperature rise in this region levels off faster than the other parts as the current reduces with time. This gives rise to the ratio of the axial to radial heat flow which results in a larger axial thermal gradient. This was confirmed on the computer model by a step by step observation of the heat flow vectors in the rotor bar.

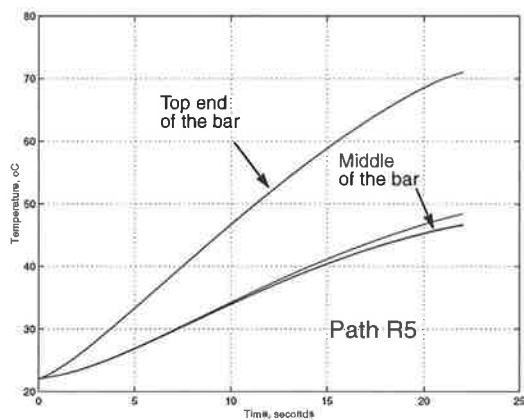
And finally, the experimental and analysis results at the selected TC's are shown in Fig. 7-7. All of the measured temperatures on the rotor are grouped on figure 'a'. As expected, the peripheral variation of temperature, monitored by TC1 to TC6, is much less than the case of locked rotor. The variation of measured temperature at TC1, TC11 and TC13 are compared to that of analysis results at the corresponding points of the 3-D model in figures 'b' to 'd' respectively. Figures 'e' and 'f' demonstrate similar comparison but for TC15 and TC16 on the stator bar and end-winding respectively.



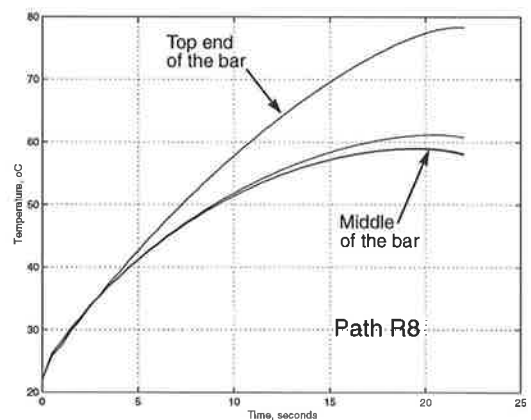
(a)



(b)



(c)

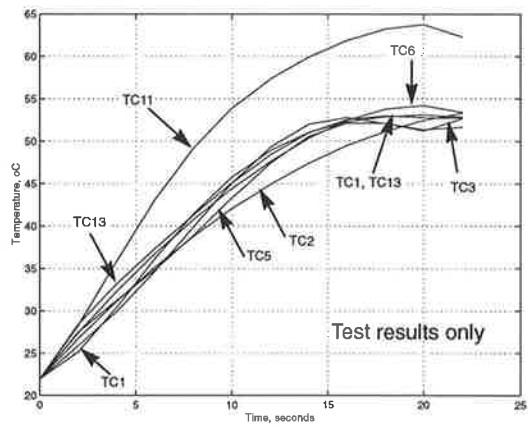


(d)

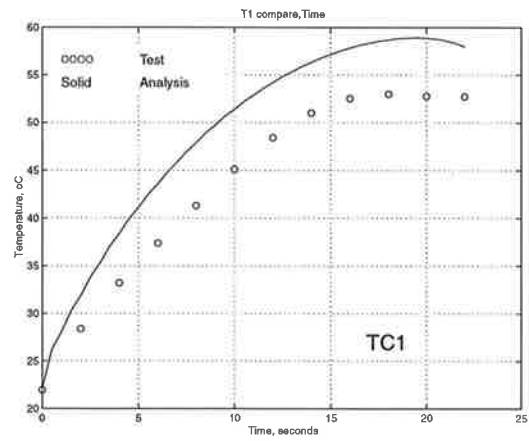
Fig. 7-6 Variation of temperature along the indicated paths in the rotor cage

The agreement of the test and simulation results is above the expected level. Although this may be an approval of the modelling, never the less, additional tests with different acceleration times on the same model, or preferably on a different motor should be performed for further verification.

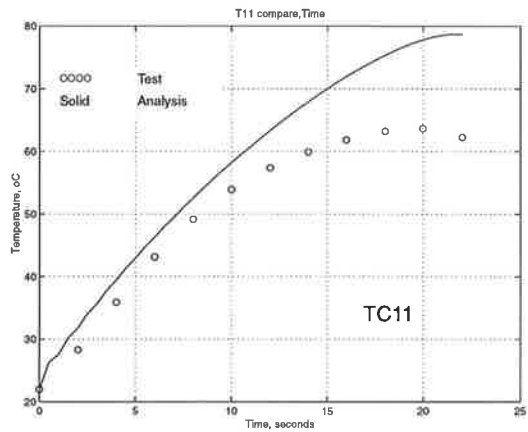
The effect of the convected heat from different boundaries is not included accurately in the present work as it is a complicated speed and temperature-dependent procedure, being far from the current subject. Consequently, one may expect the accuracy of the current model



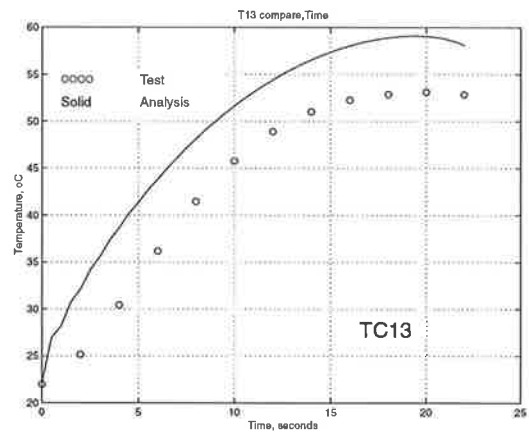
(a)



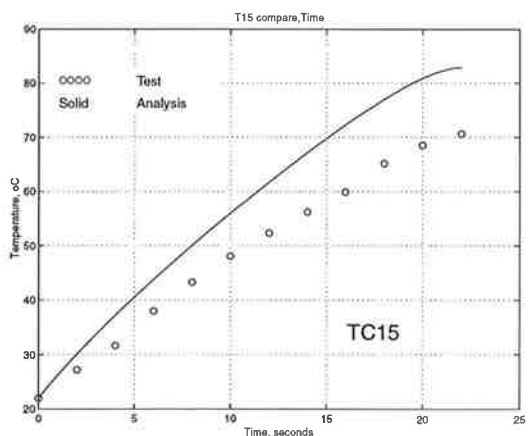
(b)



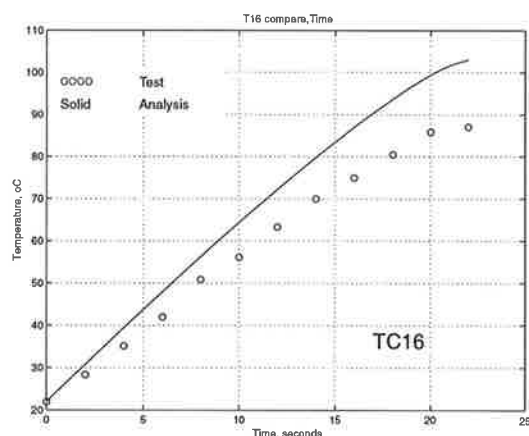
(c)



(d)



(e)



(f)

Fig. 7-7 The measurement results and comparison with the analysis results at the indicated points.

deteriorate as the duration of the acceleration prolongs. However, it is notable that the thermal capacity of the solid parts in the motor, in particular the stator winding, the rotor core and rotor cage play a ruling role during the early seconds, or probably the first few minutes, after switch on. In fact, as long as the above capacitances are capable to absorb heat, the internal conduction within the motor is the dominant component of heat transfer in the thermal system and the convected heat, even via a forced convection may be still negligible.

In brief, as long as the convection is negligible, the proposed model may be used in the simulation of induction motors under any transient conditions, including starting with variable voltage and/or its frequency, with any error in estimation of temperature being slightly on the side conservative side.

* * * * *

CHAPTER EIGHT

CONCLUSION

Unlike many other areas of electric machines, there are still no reliable initial data, and well defined formulation for the estimation of temperature distribution within an induction motor; therefore, thermal modelling of this type of motor is still a challenging area. The history of work is very scattered and more important, most of the contributions in the area of thermal analysis are concentrated on the study of the motor under steady state conditions.

The main purpose of this work is development of a systematic method for the prediction of temperature distribution in induction motors with more concentration on the deep-bar motors at stall. However, the status of an induction motor during start-up under a high inertia load was also overviewed as a complementary study for the motor under the transient conditions; the results of study were evaluated by a relevant test on the 15kW motor, used as model one.

The work was carried out in two major sections, magnetic analysis and thermal analysis. Because of the complexity of the model, in particular for the purpose of transient thermal analysis, finite element method was found to be the most appropriate tool to cope with both disciplines at the same time. The magnetic and the corresponding thermal models were meshed with matching element shapes which enabled accurate interchange of data between the models.

An extensive study was carried out on the magnetic analysis of induction motors. In this study, the procedure to predict the parameters of the classic equivalent circuit of the motor by finite element method was carried out. A harmonic finite element magnetic analysis was used in order to take the effect of rotor bar current displacement into account. However, this

conflicted with the direct inclusion of the non-linear magnetic behaviour of the iron core. This problem was overcome by using the so called “effective reluctivity method” in the analysis of model one. However, this method was found to be very lengthy when the magnetic circuit is highly saturated. Later on, a shorter method using simultaneous static and harmonic analysis method, was developed by the author. This method was used in the analysis of model two.

A two dimensional magnetic model was constructed and the distribution of current density in the rotor bars and also flux density in the iron core was attained. The elemental losses in the bar area were directly obtained from the local current density at the same element. Similar losses distribution within the iron parts were achieved by the interpolation of calculated local flux densities, $B(x, y)$ in the $P_{loss}(B)$ characteristics of the iron core. As expected, the ohmic losses were the dominant component of losses in each motor (individually) at stall.

During an overview, different possible approaches for the thermal analysis were studied and the advantages and disadvantages of each method were pointed out. Various loading and boundary conditions, in particular for an induction motor were examined. The outcome of this study showed that by using a three dimensional thermal model, representing one half of the slot or its equivalent, and a complementary two dimensional cross-sectional thermal model, all of the thermal behaviour of a motor under transient conditions may be tracked. This not only saves a vast computing time in comparison to the full three dimensional model, but saves an enormous programming effort and model generation time. The 2-D model is used to take the influence of the variation of rotor bar currents in the slots as a result of stator mmf spatial harmonics. The rate of variation was studied separately and used to modify the applied thermal loads on the rotor bars in the 2-D model.

Lack of reliable initial data on the properties of the constructional materials and also on the boundaries brought out the need for some sensitivity analyses. Therefore, the influence of some pre-assumed initial data on the accuracy of the final results was investigated. Using a simple shaped rectangular model, the influence of various parameters were examined and conclusively shown that the role of the heat transfer from the bar to the rotor core is crucial significance in limiting the temperature rise from the instant of switch-on. Also, the conduction within the bar considerably damps down the temperature gradient along the radial direction in the bar, again within a relatively short time after energizing.

Composite materials such as the stranded stator copper winding, or the laminated iron were substituted by equivalent materials with orthotropic thermal conductivities. The equivalent values of the thermal properties were extracted by keeping the elemental thermal capacities intact while their thermal conductivities were calculated by looking at the alignment of the copper wires or iron laminations, the amount of filling materials, including the trapped air within the composite.

To include the effect the temperature on the electric conductivity of the bar and also on the thermal conductivity of all parts in the model, a set of consecutive thermal and magnetic analysis were carried out and the values of the aforementioned parameters were updated each time step. This analysis showed a maximum of 2% deviation from the corresponding case with constant conductivities, unless significantly unrealistic boundary conditions were imposed. This means the accuracy of the analysis may be improved up to 2% in some parts for the expense of an enormously longer computing time. This is not justified in the thermal analysis where the accuracy of the available data is much lower than this level.

The validity of the proposed method of modelling was verified by direct test results on a 15kW induction motor with a die-cast aluminium cage and a 250kW motor having a fabricated copper cage. Two individual tests with 419V and 289V were carried out on the 15kW motor and the predicted results from the analysis of the of the variation of temperature in 17 points spread in all three directions in the rotor and some parts of stator was confirmed. Similar tests were carried out on model two, measuring the temperature at 20 strategic points. The test results showed a better agreement with the analysis results in model one, compared to the corresponding results on model two. This was justified to be related to the poorer accuracy of the available data for model two.

In both cases, it was found that the temperature rises rapidly in the top parts of the rotor bar soon after the switch on whilst very little change occurs in the lower parts. During this period, the eddy current losses generate nearly adiabatic temperature rise in the region. After a short period, (0 to 3 sec) the temperature between the top and lower parts becomes large enough to drive the heat downwards by the thermal gradient.

The behaviour of two machines, with die-cast aluminium cage and with fabricated copper cage, was quite different for the axial heat flow. The major part of the generated heat,

including that of the end-rings, in the die-cast cage finds its way into the thermal ocean of rotor core via the low thermal resistance bar/core interface. Therefore, as long as the temperature rise in the core is not comparable to that of the end-rings, the temperature is higher than other parts of the cage in this region. In contrast, the temperature rise in the middle parts of the rotor cage becomes significant, compared to the other parts of the cage, shortly after switch on and establishes a bar to end-ring heat flow in the cage as it hardly can flow across the thermal barrier between the fabricated bar and the core. The thermal resistance of this interface may vary from one bar to the other, and also in different parts on any single bar.

Using the confirmed results of FE analysis, a “finite element based lumped parameter model” was constructed for the 15kW motor. Using this model, the internal heat flow in the thermal system was studied and also the validity of LPM with fixed parameters in transient condition was discussed.

Finally, the thermal behaviour of the motor during start-up from cold conditions was overviewed. The classic equivalent circuit was found to be invalid when the motor, in particular with a deep-bar cage, is due to be analysed within a wide range of speed and therefore a dynamic equivalent circuit was defined and constructed for this purpose. Unexpectedly, in comparison to the case of corresponding locked rotor test, a larger thermal gradient was spotted along the axial direction which was justified to be related to the thermal response of the bar at different locations from the mid-point to the end of each bar.

In general, the proposed model was found to be accurate enough when the motor is locked. However, the agreement of the test and simulation results is slightly on the conservative side when the convection is not accurately included. Better results may be expected if more accurate data were available for the convective boundaries.

* * * * *

APPENDIX A

MMF OF A DISTRIBUTED WINDINGS

1.0 MMF OF A SINGLE PHASE WINDING

The idealized mmf pattern of a uniformly distributed winding, considered as a uniform current sheet of spread σ , has a trapezoidal shape as shown in Fig. A-1a. With a N -turn

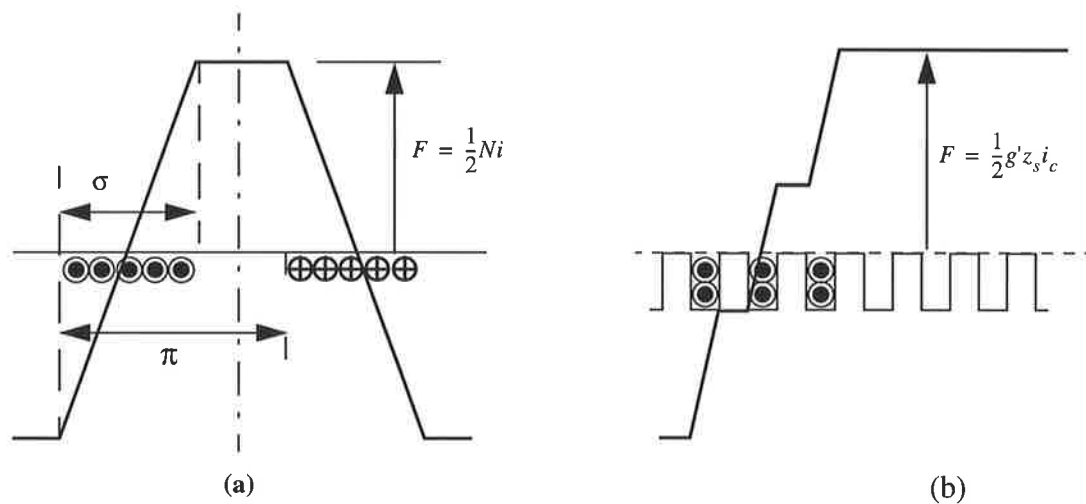


Fig. A-1 a: MMF of a uniformly distributed phase winding b: MMF of a winding distributed in limited number of slots

phase band per pole, carrying i amps, the mmf per pole is $\frac{1}{2}Ni$. A Fourier analysis of this pattern yields a series of harmonic sinusoids of order $n=1, 3, 5, \dots$ in terms of spatial angle x around the air-gap measured in electrical units, each term having the form of [65]:

$$F_n = \frac{1}{2}Ni \frac{4}{n\pi} \frac{\sin \frac{1}{2}(n\sigma)}{\frac{1}{2}(n\sigma)} = i \frac{2}{n\pi} (k_{dn}N) \sin(nx) \quad (\text{A-1})$$

where k_{dn} is the distribution factor defined as:

$$k_{dn} = \frac{\sin \frac{n\sigma}{2}}{g' \sin \frac{n\sigma}{2g'}} \quad (\text{A-2})$$

$g' = S/2pm$ is the number of slots per pole and per phase where S and p are the number of slots on a uniformly slotted armature, and the number of pole pairs respectively.

If the span of a coil is not a full pole-pitch, but is chorded to cover $\pi \pm \epsilon$ electrical radians, a new factor, so called as *coil-span factor* is applied on $k_{dn}N$ in (A-1) to give:

$$k_{dn}k_{cn}N = k_{wn}N \quad (\text{A-3})$$

for the effective turns of the phase band. $k_{wn} = k_{dn}k_{cn}$ is called winding factor for n th harmonic. k_{cn} is the coil-span factor (or chording factor) for n th harmonic defined as:

$$k_{cn} = \cos\left(\frac{1}{2}n\epsilon\right) \quad (\text{A-4})$$

With a sinusoidal phase current of $i = i_m \cos \omega t$, each term of the Fourier series becomes:

$$F_n = i_m \cos \omega t \cdot \frac{2}{\pi} k_{wn} N \sin nx \quad (\text{A-5})$$

This produces a stationary magnetic field which can be resolved into a couple of sinusoidally distributed mmf's named as forward and backward components, travelling in either direction at synchronous speed.

In an actual machine, the winding is embedded in a limited number of slots and the distribution of air-gap mmf will be as in Fig. A-1b. This has a minor effect on the

fundamental and low order space harmonics, but the slot harmonic become predominant in integral-slot windings [65].

2.0 TRAVELLING WAVE MMF OF A POLY-PHASE WINDING

A sinusoidally distributed symmetrical q -phase winding, with $q = 2, 3, 4, \dots$ has its phase axes displaced successively around the air-gap by an electrical angle of $2\pi/q$, and is fed from a balanced set of q -phase currents. In a symmetrical q -phase winding, only the forward travelling wave component is present, since the backward components cancel out each other. So, the resultant mmf of a symmetrical q -phase winding has a constant amplitude and travels at synchronous speed. However, if the winding is distributed in a limited number of slots, the space harmonics would be present and affect the distribution of the field.

A three phase winding is a very common case of poly-phase windings. MMF of a practical three phase winding (distributed in limited number of slots) using (A-5), becomes:

$$F = \frac{q}{2} \cdot \frac{4}{\pi} \cdot \frac{Ni_m}{2} \left(k_{w1} \sin(x - \omega t) + \frac{k_{w5}}{5} \cdot \sin(5x - \omega t) - \frac{k_{w7}}{7} \sin(7x - \omega t) + \frac{k_{w11}}{11} \sin(11x - \omega t) + \dots \right) \quad (\text{A-6})$$

In (A-6), it is assumed that the phase windings are fed with the set of three phase sinusoidal currents as:

$$i_a = i_m \cos \omega t$$

$$i_b = i_m \cos(\omega t - 2\pi/3)$$

$$i_c = i_m \cos(\omega t - 4\pi/3)$$

where, i_m is the amplitude of sinusoidal phase current. The MMF wave includes the fundamental harmonic as well as the higher order harmonics of 5, 7, 11, 13, ... or $6a \pm 1$, where a is any positive integer, all multiples of 3 are absent in this waveform. The fundamental MMF wave moves at a speed corresponding to ω , while that of higher order harmonics rotate with speeds proportional to the reciprocal of their order, in the same direction as the fundamental for $n = 6a + 1$, and opposite for $n = 6a - 1$ harmonics. The

spatial harmonics of mmf of model one, when only the stator winding is excited sinusoidally, are shown in Fig. C-1.

3.0 EQUIVALENT WINDINGS

The behaviour of an electric machine is evaluated by the interaction between the generated mmf's by the rotor and stator windings individually. Therefore, it may be expected to substitute any of the windings with its equivalent winding. The equivalent winding may have different geometry and design but it should produce the same mmf distribution in the air-gap. In general, two poly-phase windings, 1 and 2 are equivalent when:

$$k_{w1}N_{ph1}I_{c1} = k_{w2}N_{ph2}I_{c2} \quad (\text{A-7})$$

k_{w1} and k_{w2} refer to the fundamental winding factors the windings.

This fact is essential in the substitution of a cage with a wound rotor or with another cage having different number of slots. The substitution is usually used when the number of rotor (or stator) slots in a specific fraction of the motor is not a whole number while the modelling of same fraction of the motor [79] is desired.

If the number of phases, q , in a q -phase winding is large and the phase currents are all of equal rms magnitude I_c with the phase displacement of $2\pi/q$ successively, the winding is approximated with a sinusoidally distributed current sheet. Then the resultant mmf of the winding according to (A-6) becomes:

$$F_a = \sqrt{2} \left(\frac{q}{\pi} \right) k_{w1} N_{ph} I_c \quad (\text{A-8})$$

For example, a uniform cage winding with an adequate number of bars approximates closely to this condition. A cage with S slots (and therefore S/p slots per pole-pair) can be considered as an m -phase winding $m = \frac{S}{2p}$ where all of the phase windings are single-turn coils. The winding factor $k_{w1} = k_{d1}k_{c1}$ is clearly unity. The fundamental of the MMF becomes:

$$F_a = \frac{1}{\sqrt{2\pi p}} SI_c \quad (\text{A-9})$$

Harmonics of orders other than those of $n = S / (2p)$ will normally be very small [65].

* * * * *

APPENDIX B

MEASUREMENT OF THERMAL CONDUCTIVITY OF SOLIDS

Depending on the availability of experimental facilities, the margins of the conductivity, the temperature range and the expected accuracy, different techniques may be employed to measure the conductivity of a solid. The usual methods for the measurement of this parameter may be categorized as static and dynamic [11] methods. The first method requires a knowledge of the heat flow density and temperature gradient in a direction normal to isothermal surfaces. Then the conductivities may be extracted from the solution of the well known Fourier's law of conduction. In contrast, the dynamic method involves the solution of diffusion equations to determine the diffusivity of the material; it requires the measurement of time in which a thermal disturbance propagates a known distance. Then, the thermal conductivity is calculated from (3-18); therefore, the specific heat and also the density of the material should be known in this method. In this section, a sample of each technique is briefly outlined.

1.0 RADIAL HEAT FLOW METHOD

This is a static measurement method in which a cylindrical shape of the material [57] is constructed as the test specimen and a hot wire is used as the heat source inside the cylinder. Fig. B-1 shows the specimen and the details of testing configuration. Fourier's law in a one dimensional cylindrical thermal system is [33]:

$$q_r = k_r \cdot (2\pi rL) \frac{dT}{dr} \quad (\text{B-1})$$

Application of (B-1) on the thermal system of Fig. B-1 in a steady state results in:

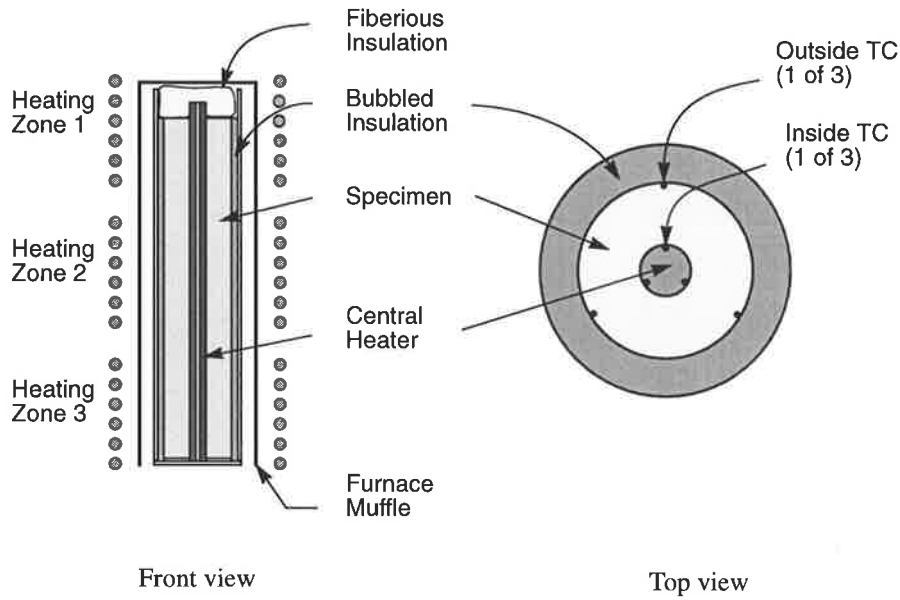


Fig. B-1 Schematic diagram of a radial thermal conductivity measurement apparatus.

$$\int_{r_i}^{r_o} \frac{1}{r} dr = -\frac{2\pi r z L \cdot k_r}{q_r} \int_{T_i}^{T_o} dT \quad (\text{B-2})$$

Then

$$k_r = \frac{q_r \ln(r_o/r_i)}{2\pi L (T_i - T_o)} \quad (\text{B-3})$$

The values of physical dimensions and also temperatures are measured directly by appropriate instruments. q_r is evaluated by the measurement of electric power loss in the hot wire by means of voltage drop and current measurement as:

$$q_r = V \cdot I \quad (\text{B-4})$$

where, V and I are the voltage drop and electric current in the wire.

2.0 HOT WIRE METHOD

Hot wire method is a dynamic measurement technique and it is mainly used in the measurement of the conductivity of gases and liquids (e.g. transformer oil). However, it has

been adapted for solids as well. The heat source in this technique is a platinum or nichrom¹ wire which is heated by a dc or sinusoidal ac electric current. The specimen is made in two equal sizes and is heated by the hot wire as shown in Fig. B-2. Usage of the larger sizes of the

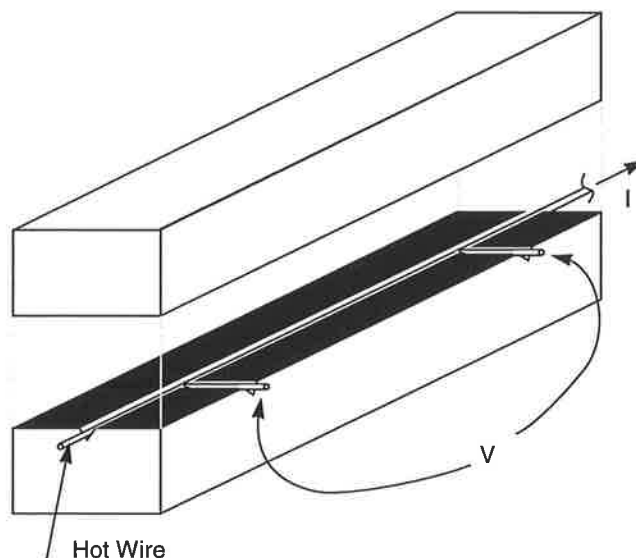


Fig. B-2 Schematic diagram of a hot-wire thermal conductivity test.

specimen result in a higher accuracy of measurement.

Theoretically, the line source establishes a uniform radial heat transfer within the infinite solid.

The fundamental heat transfer equation in cylindrical coordinates is [33]:

$$\frac{\partial T}{\partial t} = \alpha \left[\frac{\partial^2 T}{\partial r^2} + \frac{1}{r} \frac{\partial T}{\partial r} \right] \quad (\text{B-5})$$

where r is the radial distance from the centre axis of the wire. The initial temperature at all parts of the body is assumed to be T_0 at time zero. After sometime t , at a infinite distance from the centre, it is still T_0 . Therefore, at any point within the model at $r > r_w$, a steady state heat transfer occurs so that:

1. The resistivity versus temperature is well defined for these materials.

$$T(r, 0) = T_0 \quad (\text{B-6})$$

$$\lim_{r \rightarrow \infty} T(r, t) = T_0 \quad (\text{B-7})$$

$$\left[-2\pi k \frac{\partial T}{\partial r} \right]_{r=r_w} = q_r(t) \quad (\text{B-8})$$

Using the initial and boundary conditions of (B-6), (B-7) and (B-8) the solution of (B-1) for small values of r at a long time, results in:

$$T(r, t) - T_0 = \frac{q_r}{4\pi k} \cdot \ln\left(\frac{4\alpha t}{r^2 c}\right) \quad (\text{B-9})$$

where:

$c = \ln(\gamma)$, γ is Euler's constant (= 0.5772).

In practice, the temperature in the volume of hot wire including its outer surface is assumed to be uniform. Then, $T(r, t)$ is extracted at the surface of the hot wire as a function of time.

This can be done either by using thermocouples or usually by measurement of the electrical resistivity of the hot wire. q_t is calculated by electric measurements of the current and voltage drop in the wire. Since the physical dimensions of the specimen are limited, the temperature at the external surface of the specimen will not remain constant for long time in particular for good heat conductors. Therefore, the accepted upper limit of thermal conductivity measurement by this method is on the order of $2 \text{ W}/(\text{m}^\circ\text{C})$ which is not suitable for iron or copper conductors. A modified form of this method was used by [58] to obtain the two orthogonal conductivities of laminated iron simultaneously.

* * * * *

APPENDIX C

ADDITIONAL GRAPHS

In this appendix, some additional graphs related to different parts of the thesis are given. The figures are referenced within the chapters as follows:

Fig. C-1 to Fig. C-4	referenced on section 2.3 on page 92
Fig. C-5 and Fig. C-6	referenced on section 2.4 on page 94
Fig. C-7 and Fig. C-9	referenced on section 3.3.1 on page 110
Fig. C-10 to Fig. C-13	referenced on section 4.2 on page 136

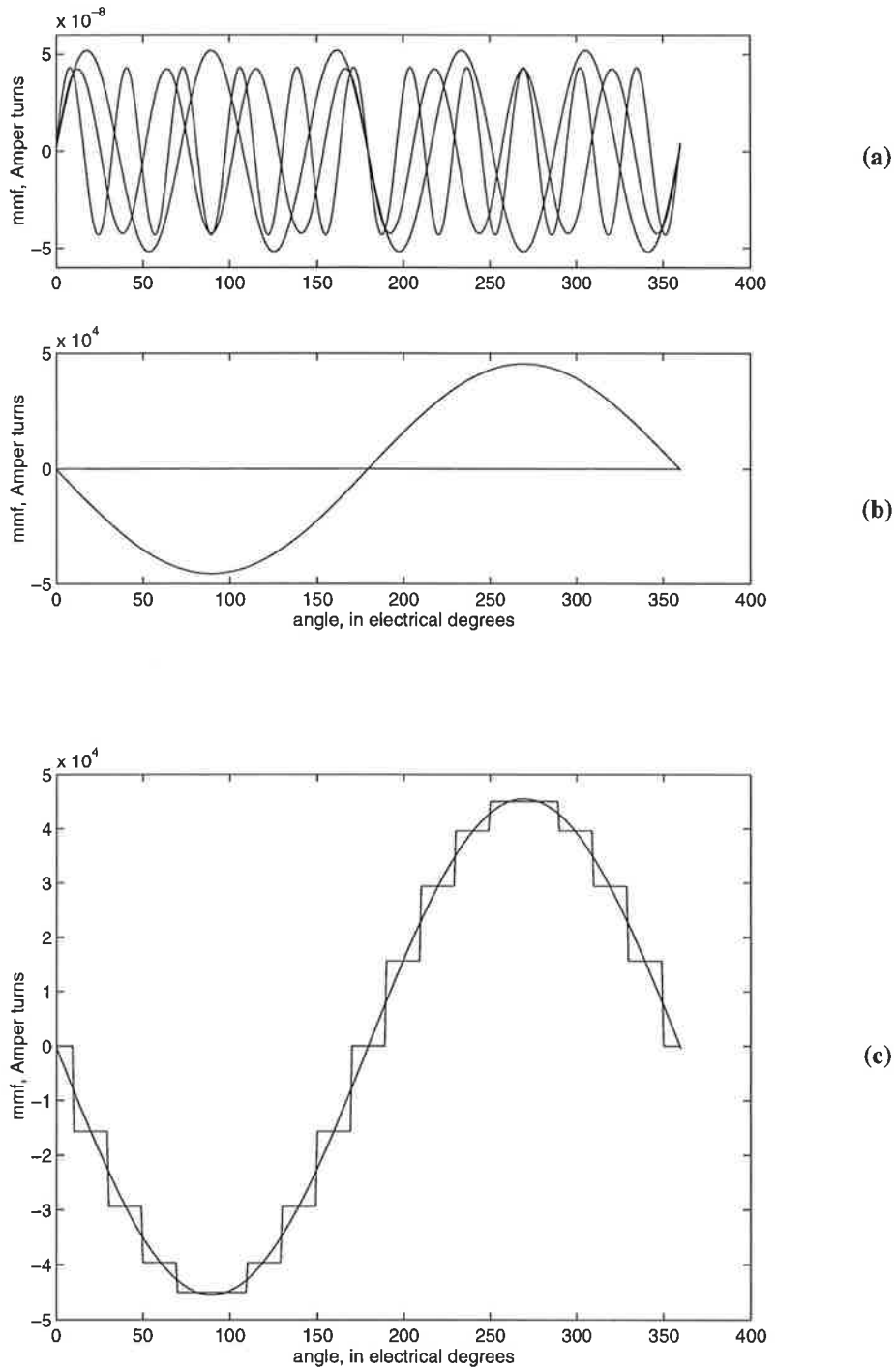


Fig. C-1 Distribution of field mmf when the stator winding only is sinusoidally excited:
a: Distribution of 5th, 7th and 11th space harmonics
b: Distribution of 5th, 7th and 11th space harmonics along with the fundamental harmonic (the amplitude of higher harmonics are very small)
c: Actual field mmf along with the fundamental and the evaluated mmf distribution

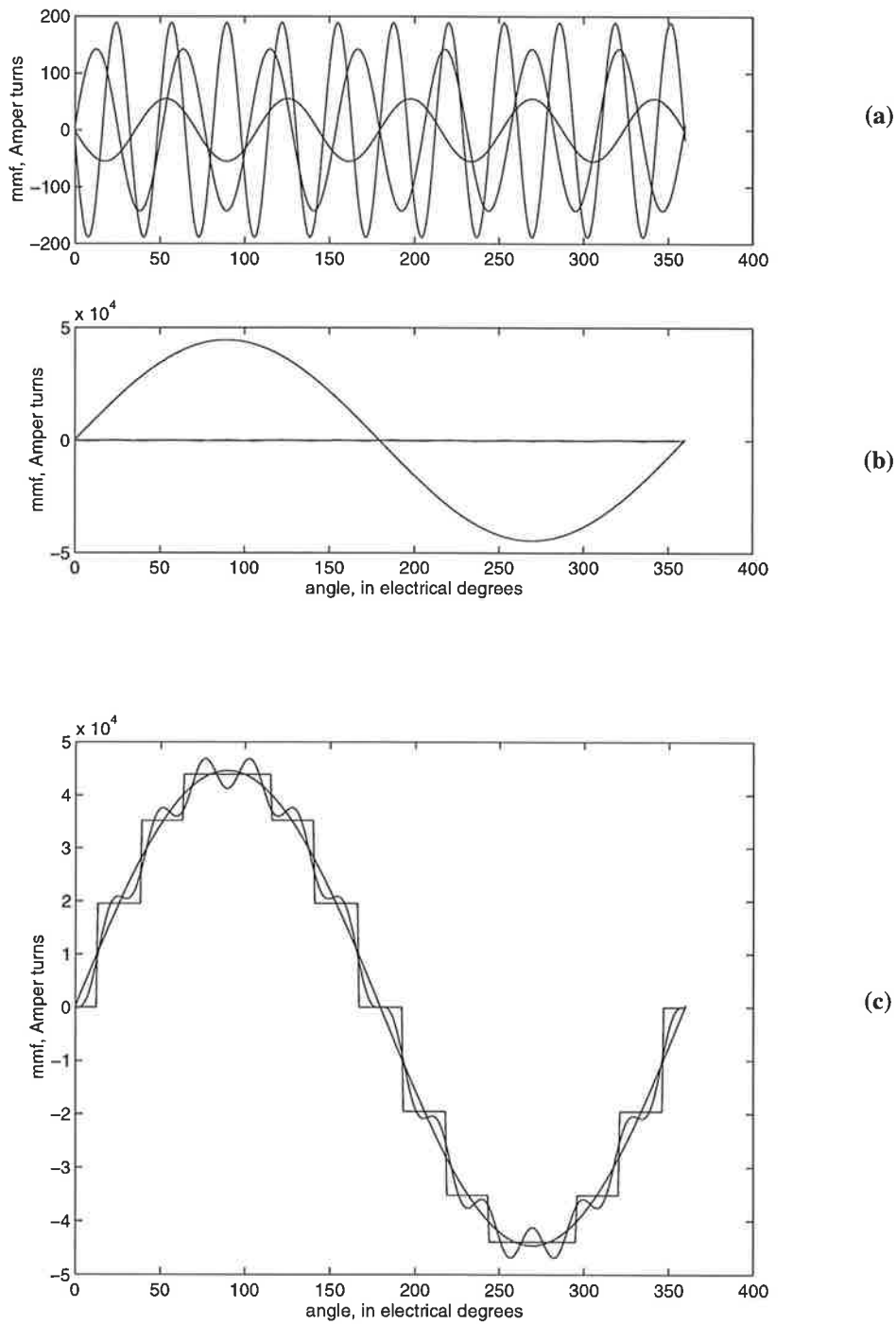


Fig. C-2 Distribution of field mmf when the rotor bars only are sinusoidally excited:

a: Distribution of 5th, 7th and 11th space harmonics

b: Distribution of 5th, 7th and 11th space harmonics along with the fundamental harmonic (the amplitude of higher harmonics are very small)

c: Actual field mmf along with the fundamental and the evaluated mmf distribution

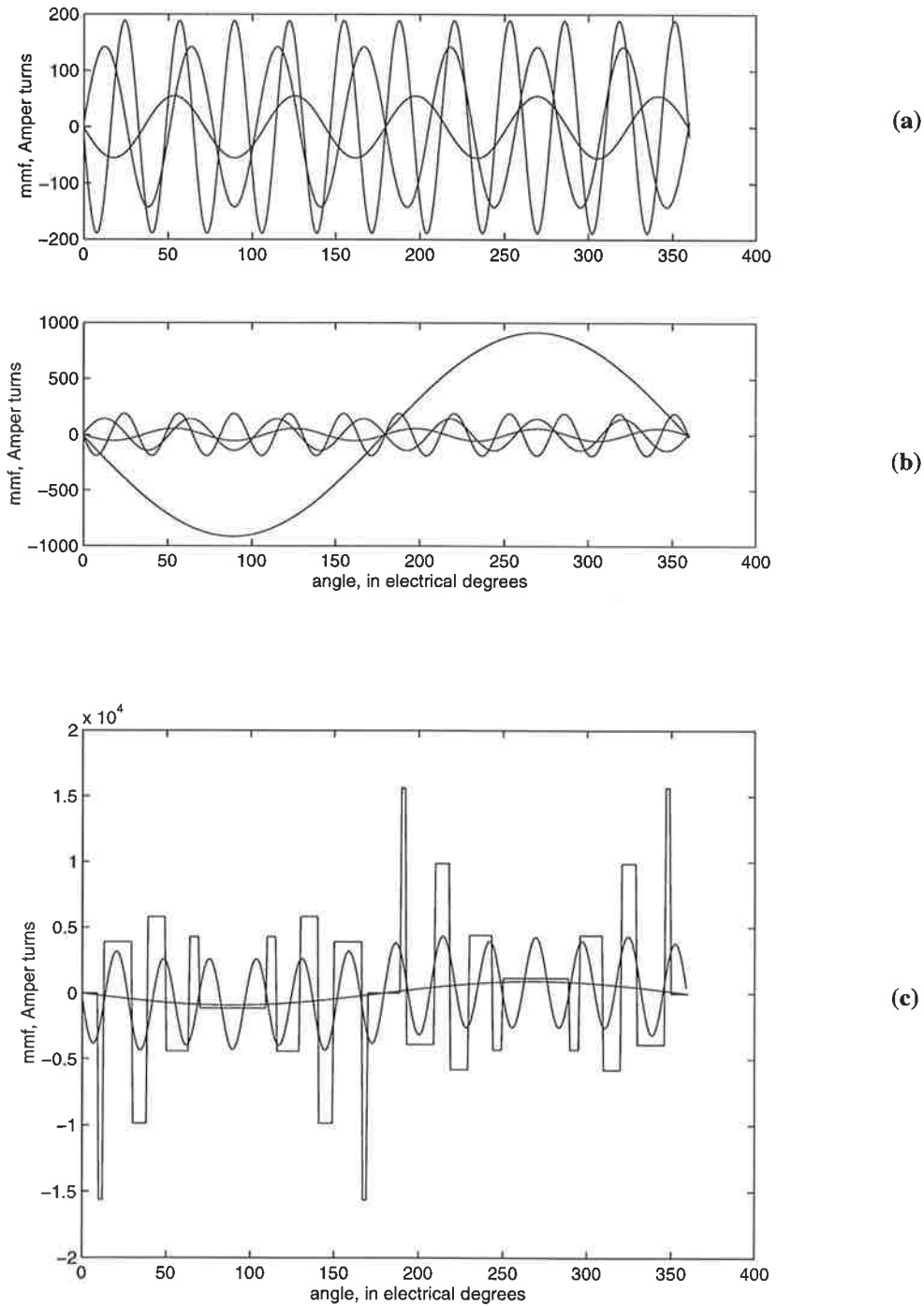


Fig. C-3 Distribution of field mmf when both of the rotor cage and stator winding are sinusoidally excited:

- a:** Distribution of 5th, 7th and 11th space harmonics
- b:** Distribution of 5th, 7th and 11th space harmonics along with the fundamental harmonic
- c:** Actual field mmf along with the fundamental and the evaluated mmf distribution

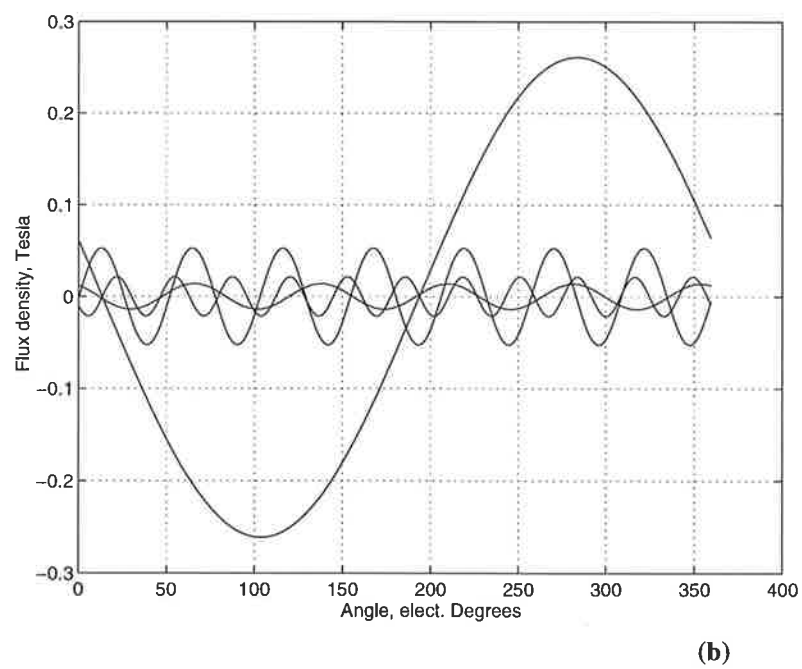
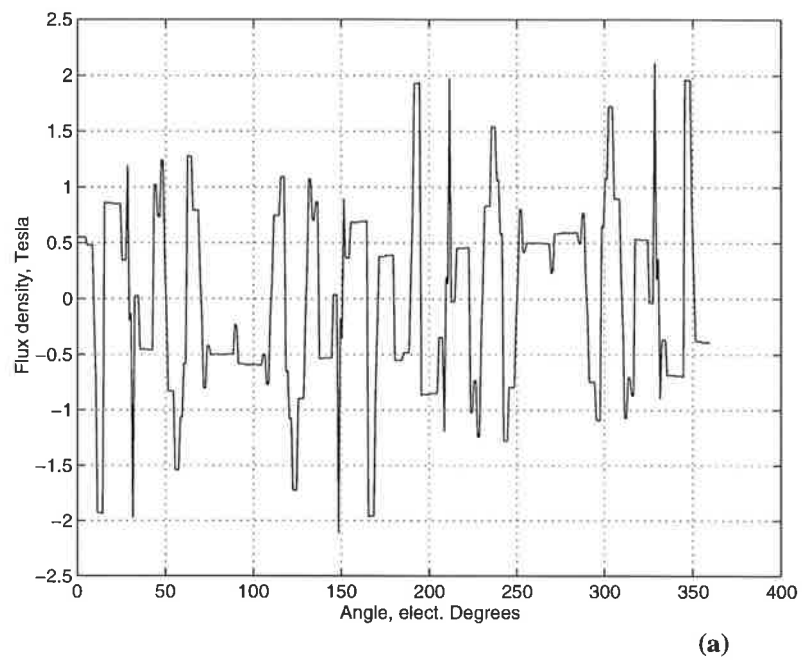


Fig. C-4 Distribution of the real component of magnetic flux density in the air-gap:

a: Actual distribution,

b: The fundamental harmonic, 5th, 7th and 11th harmonic

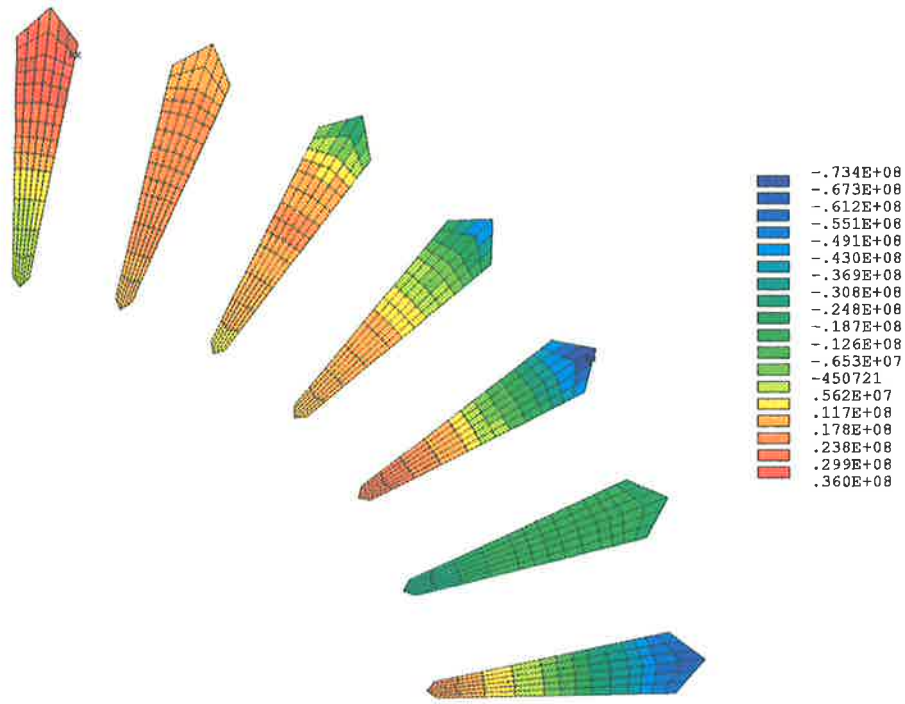


Fig. C-5 The distribution of the real component of current density at the rotor bars of the 2-dimensional model, when the motor was supplied by the rated voltage.

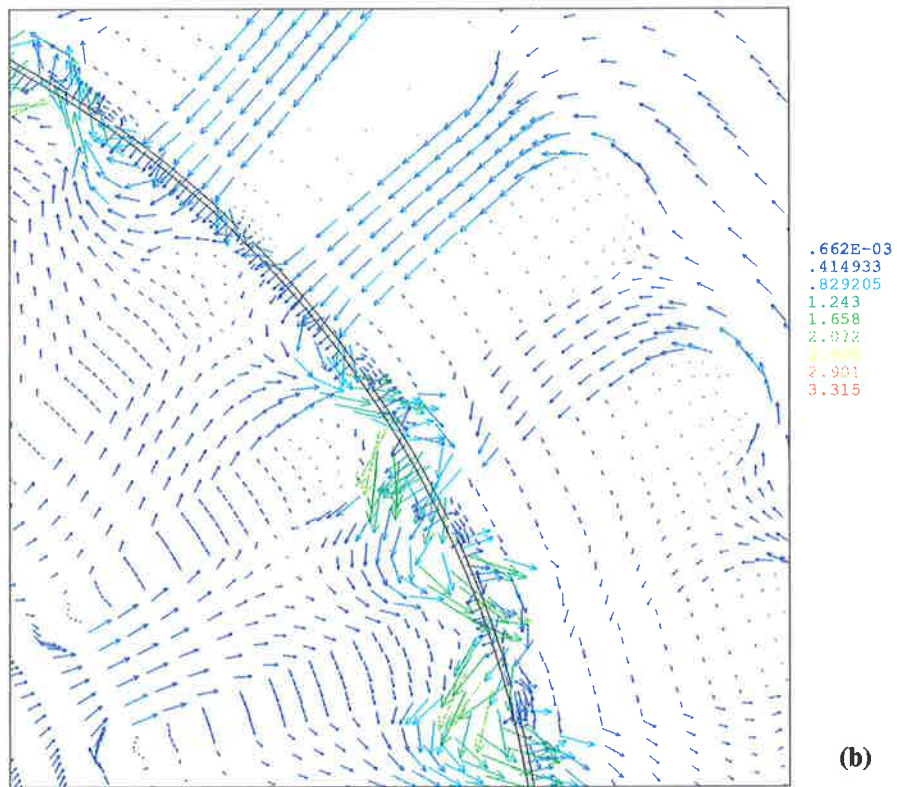
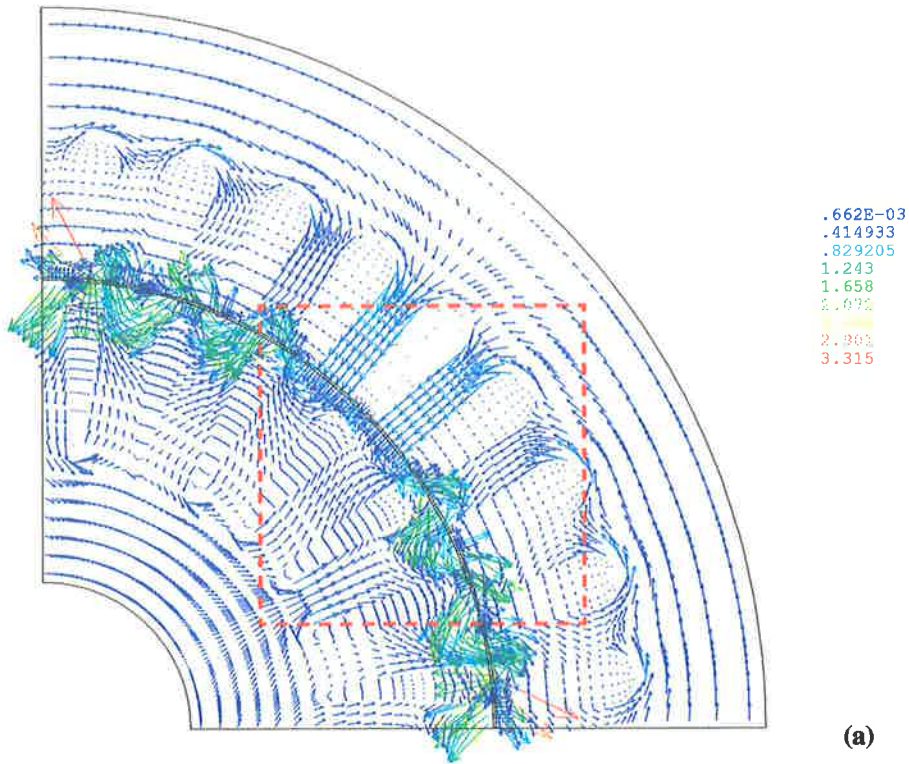
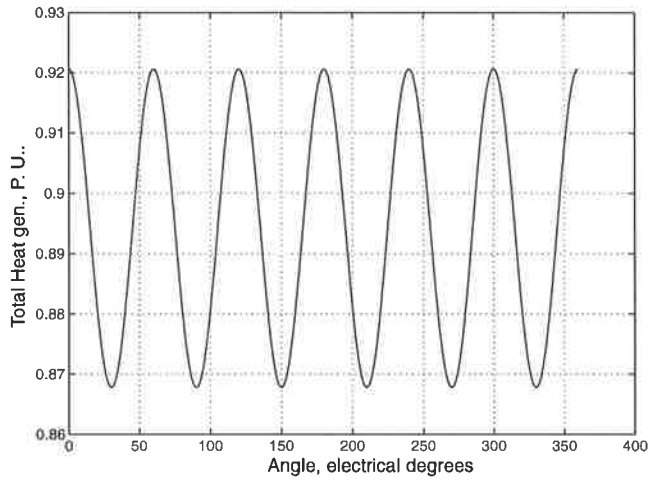
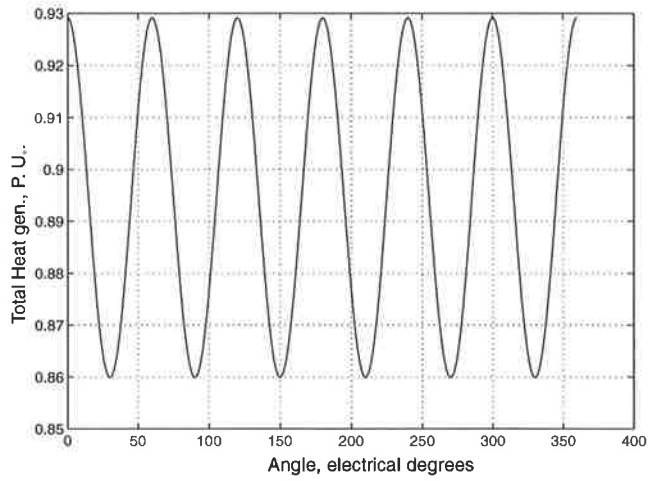


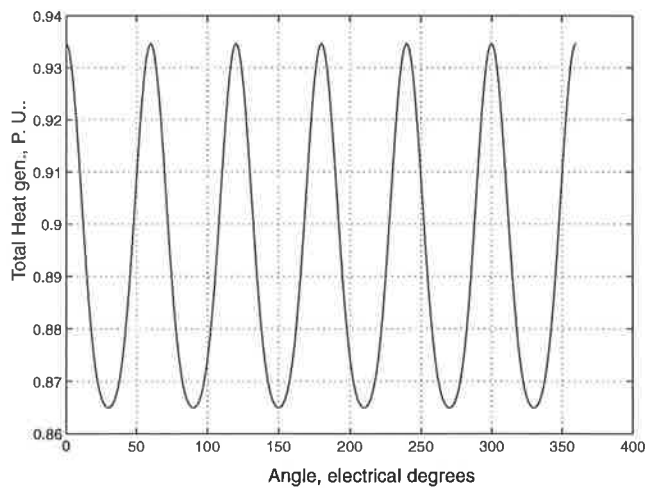
Fig. C-6 The distribution of the real component of flux density in the 2-dimensional model, when the motor was supplied by the rated voltage:
a: in entire modelled part (one pole area),
b: the details of the selected part in 'a'.



a: Total heat generation when the fundamental and 5th harmonics are taken into account.

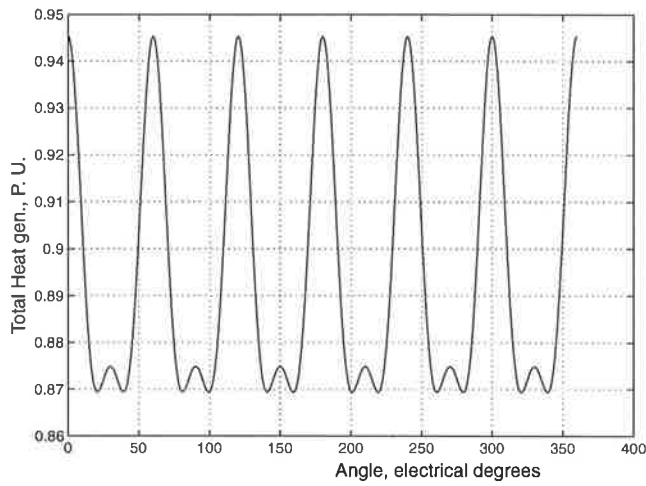


b: Total heat generation when the fundamental, 5th and 7th harmonics are taken into account.

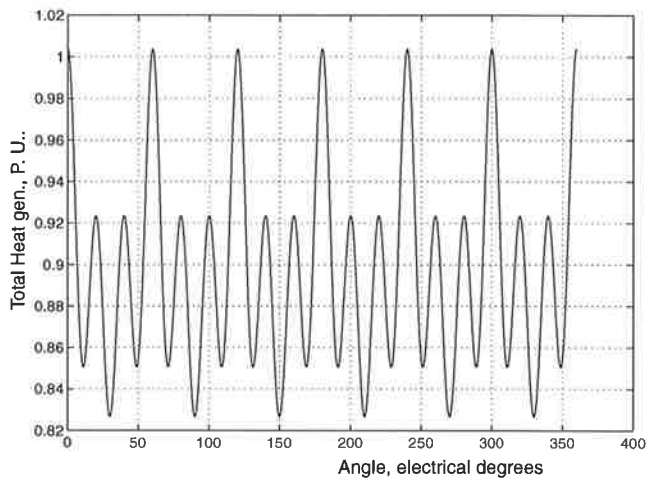


c: Total heat generation when the fundamental, 5th, 7th and 11th harmonics are taken into account.

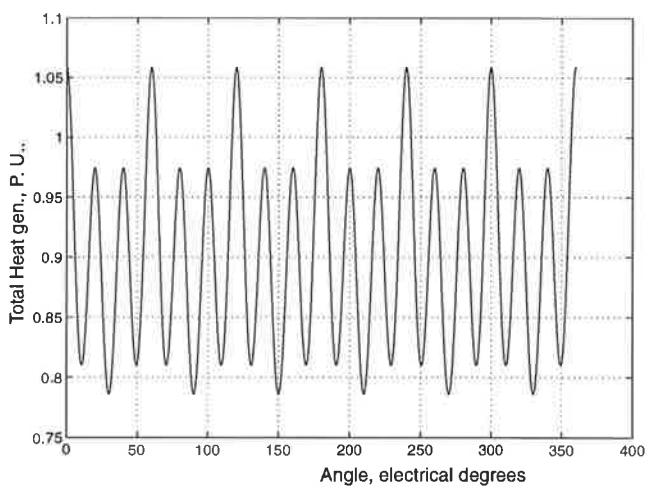
Fig. C-7 Distribution of heat generation in a rotor bar as a function of its relative spatial position to the stator mmf



a: Total heat generation when the fundamental, 5th, and 13th harmonics are taken into account.

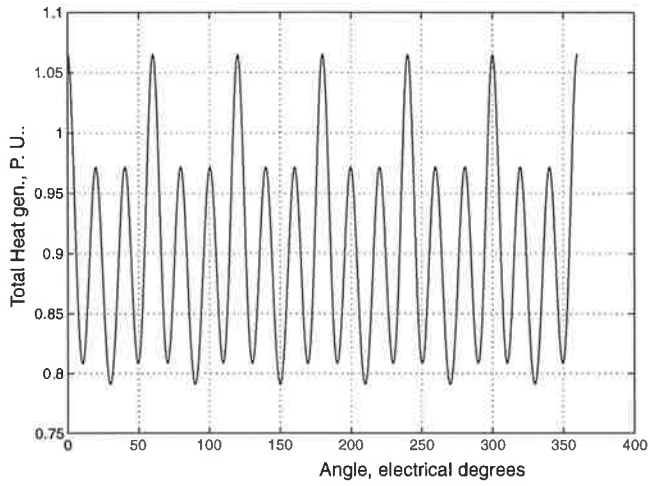


b: Total heat generation when the fundamental, 5th, and 17th harmonics are taken into account.

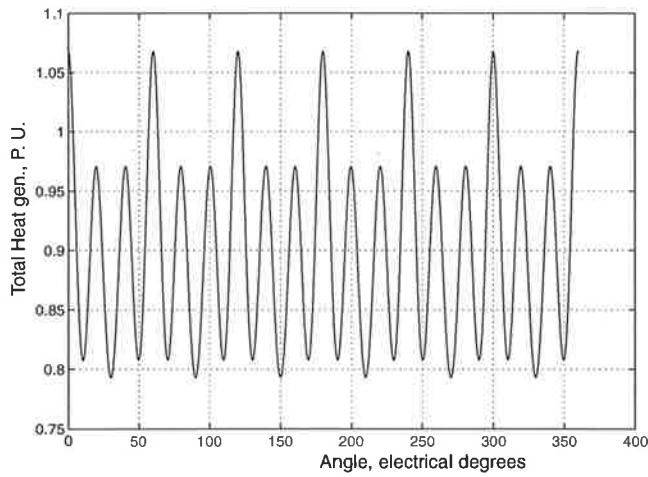


c: Total heat generation when the fundamental, 5th, and 19th harmonics are taken into account.

Fig. C-8 Distribution of heat generation in a rotor bar as a function of its relative spatial position to the stator mmf



a: Total heat generation when the fundamental, 5th, and 23th harmonics are taken into account.



b: Total heat generation when the fundamental, 5th, and 25th harmonics are taken into account.

Fig. C-9 Distribution of heat generation in a rotor bar as a function of its relative spatial position to the stator mmf

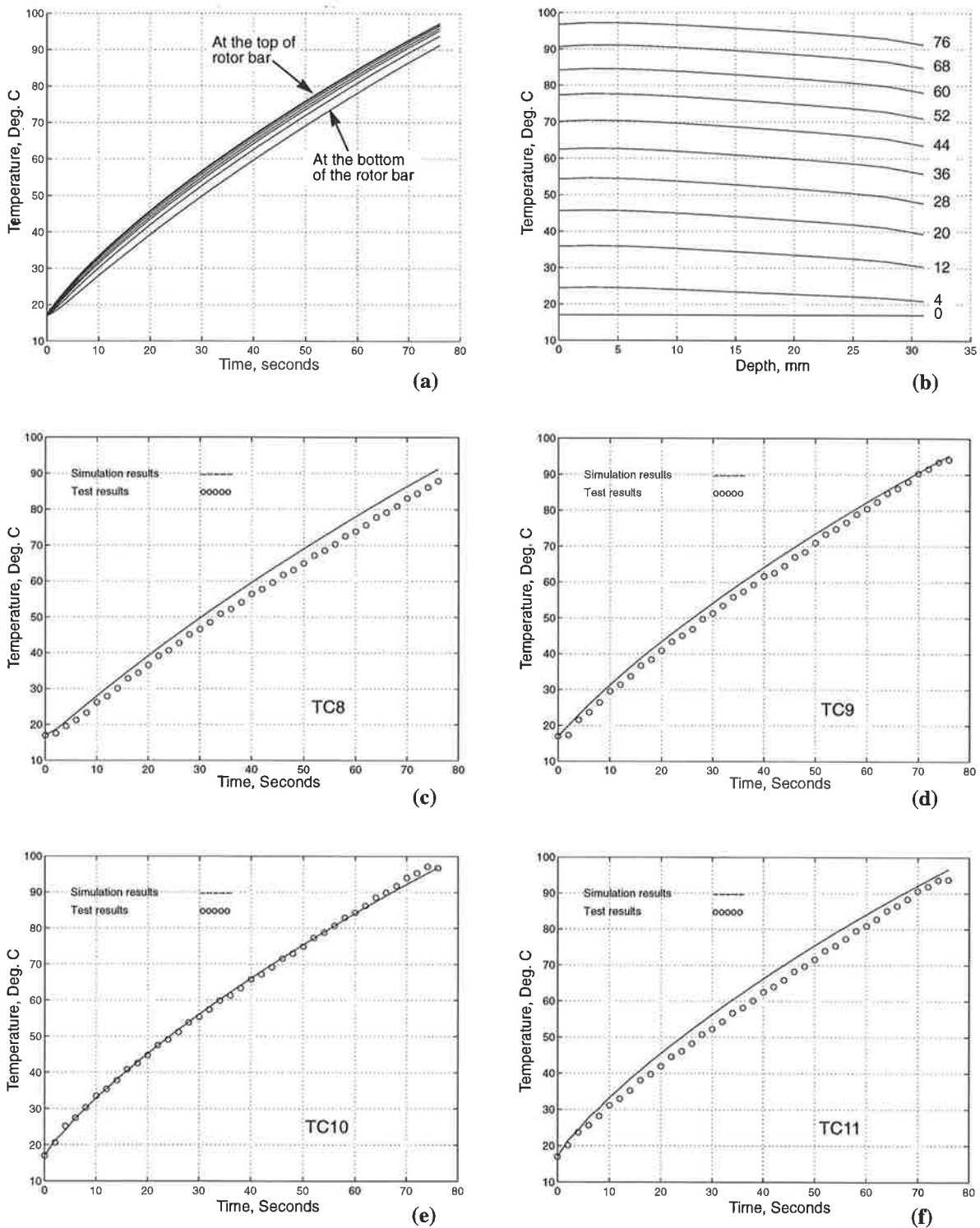


Fig. C-10 Variation of temperature along the radial axis of rotor with time and location, reduced voltage (289 volts):

- a: Variation of temperature at the nodes along the rotor radial axis with time, simulation results from the 3-D model;
- b: Variation of temperature at the nodes along the rotor radial axis with location in different times, simulation results from the 3-D model;
- c to f: Comparison of the simulation results with the test results at the location of TC8 to TC11.

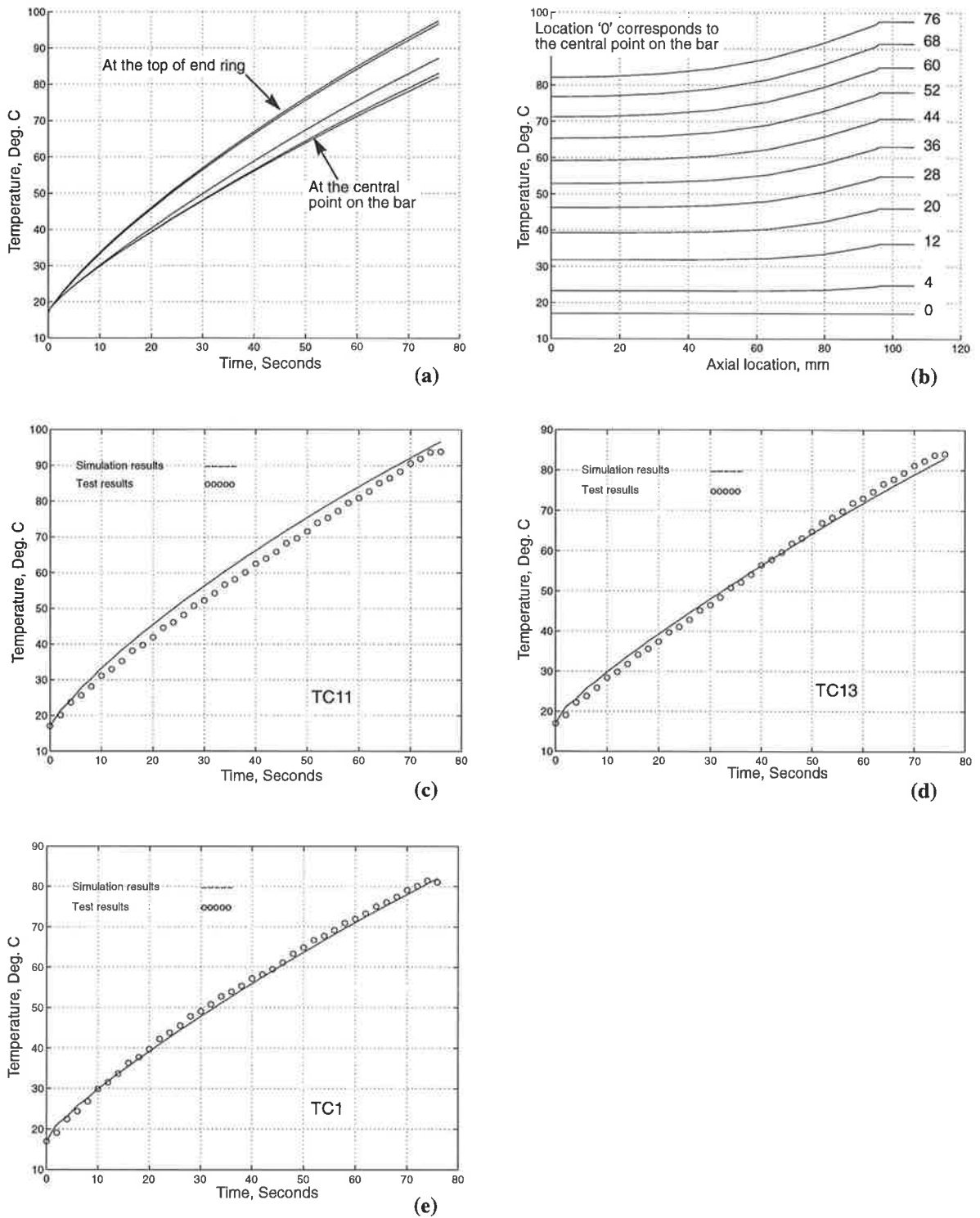


Fig. C-11 Simulation and test results with reduced voltage (289 volts):

- a to d:** Comparison of simulation results from the 3-D model with the test results at the locations of TC 8 to TC 11 respectively;
- e to f:** Comparison of simulation results from the 3-D model with the test results at the locations of TC 13 and TC 1 respectively;

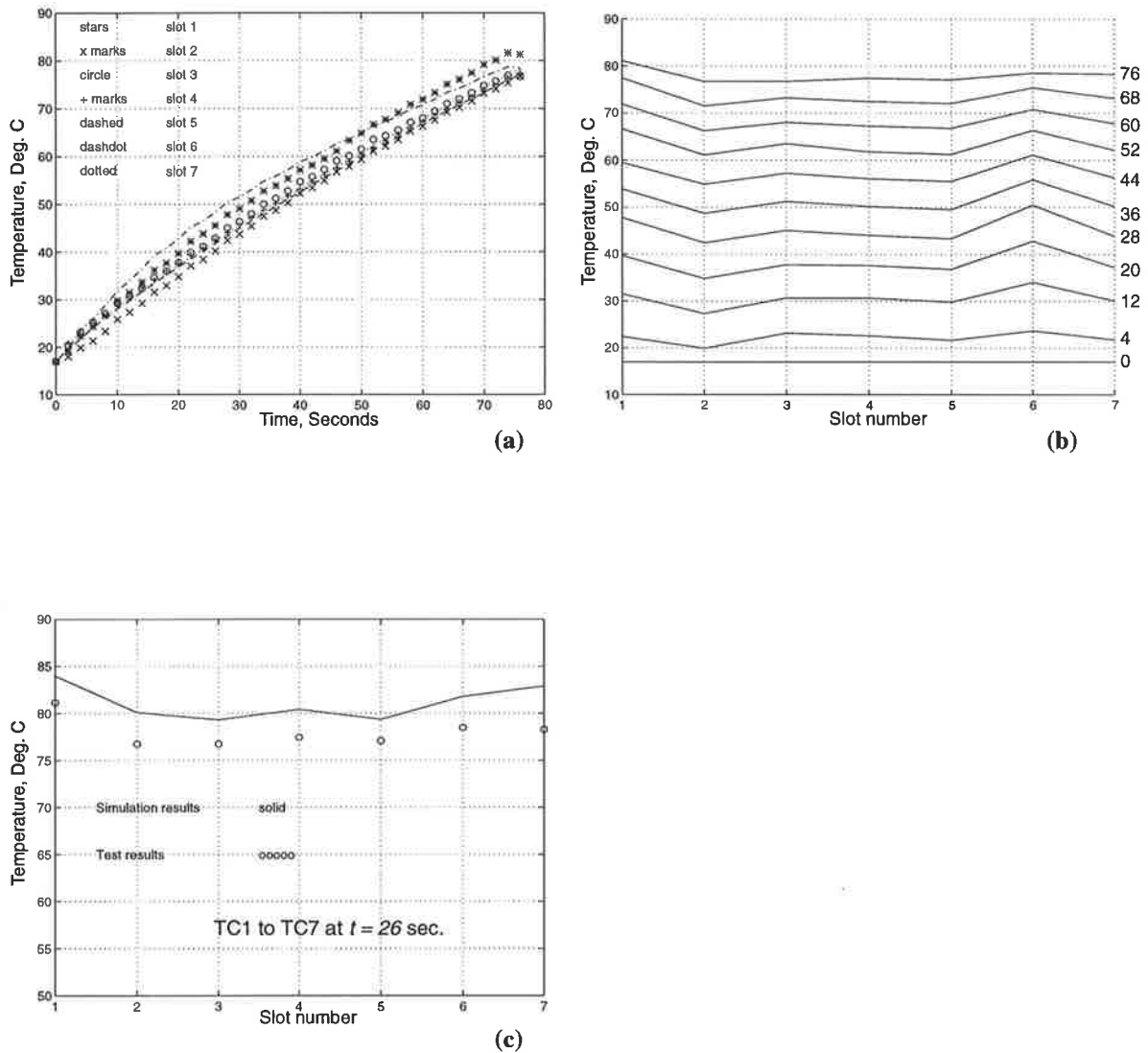


Fig. C-12 Simulation and test results with reduced voltage (289 volts):

- a to d:** Comparison of simulation results from the 3-D model with the test results at the locations of TC 8 to TC 11 respectively;
- e to f:** Comparison of simulation results from the 3-D model with the test results at the locations of TC 13 and TC 1 respectively;

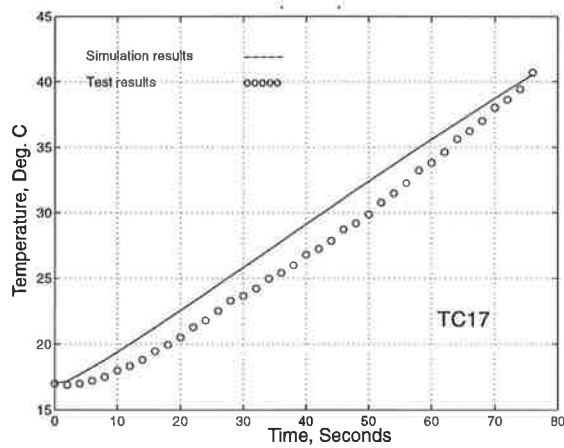
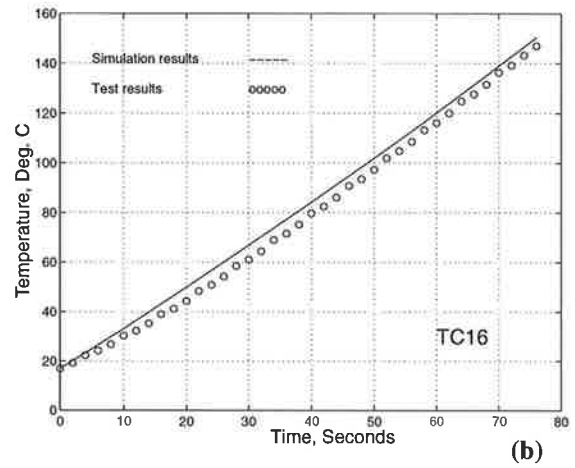
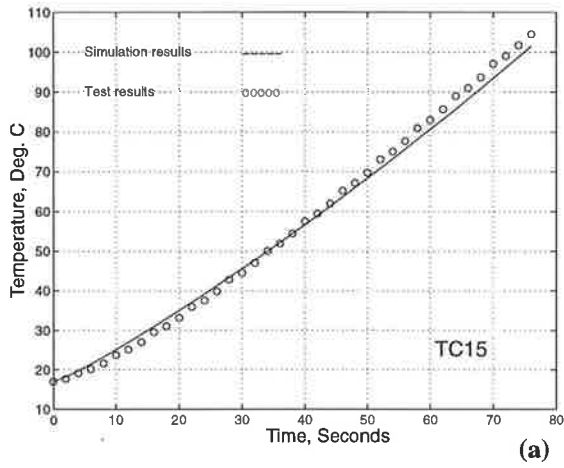


Fig. C-13 Simulation and test results with reduced voltage (289 volts):

- a to d:** Comparison of simulation results from the 3-D model with the test results at the locations of TC 8 to TC 11 respectively;
- e to f:** Comparison of simulation results from the 3-D model with the test results at the locations of TC 13 and TC 1 respectively;

APPENDIX D

TEMPERATURE MEASUREMENT WITH THERMOCOUPLES

1.0 INTRODUCTION¹

One of the most frequently used temperature transducers is the thermocouple. Thermocouples are very rugged and inexpensive and can operate over a wide temperature range. A thermocouple is created whenever two dissimilar metals touch and the contact point produces a small open-circuit voltage as a function of temperature. This thermoelectric voltage is known as the Seebeck voltage, named after Thomas Seebeck, who discovered it in 1821. The voltage is non-linear with respect to temperature. However, for small changes in temperature, the voltage is approximately linear, or

$$\delta V = S_E \cdot \delta T \quad (\text{D-1})$$

where δV is the change in voltage, S_E is the Seebeck coefficient, and δT is the change in temperature. Fig. D-1 shows a basic method of temperature measurement by thermocouple.

S_E varies with changes in temperature, however, causing the output voltages of thermocouples to be non-linear over their operating ranges. Several types of thermocouples are available; these thermocouples are designated by capital letters that indicate their composition according to American National Standards Institute (ANSI) conventions. For example, a J-type thermocouple has one iron lead and one constantan (a copper-nickel alloy) lead.

1. Most parts of this appendix are extracted from Instrupedia CD-ROM supplied by "National Instruments", USA.

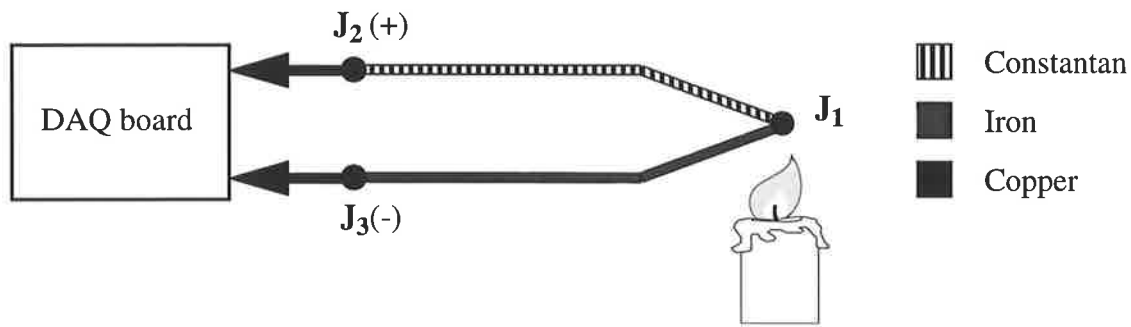


Fig. D-1 Schematic diagram of a J-Type Thermocouple

2.0 THERMOCOUPLE CIRCUITS

2.1 General Case

To measure a thermocouple Seebeck voltage, the thermocouple cannot simply be connected to a voltmeter or other measurement system, because connecting the thermocouple leads to the measurement system creates additional thermoelectric circuits.

In Fig. D-1 a J-type thermocouple is used to measure the temperature of a candle flame. The two thermocouple wires are connected to the copper leads of a Data Acquisition (DAQ) board. It is noteworthy that the circuit contains three dissimilar metal junctions, J1, J2, and J3. J1, the thermocouple junction, generates a Seebeck voltage proportional to the temperature of the candle flame. J2 and J3 each have their own Seebeck coefficient and generate their own thermoelectric voltage proportional to the temperature at the DAQ terminals. To determine the voltage contribution from J1, the temperatures of junctions J2 and J3 as well as the voltage-to-temperature relationships for these junctions should be known; then the contributions of the parasitic thermocouples at J2 and J3 should be subtracted from the measured voltage.

2.2 Cold-Junction Compensation

Thermocouples require some form of temperature reference to compensate for aforementioned unwanted parasitic thermocouples. The term “*cold junction*” comes from the traditional practice of holding this reference junction at 0°C in an ice bath. The National

Institute of Standards and Technology (NIST) thermocouple reference tables are created with this setup, illustrated in Fig. D-2.

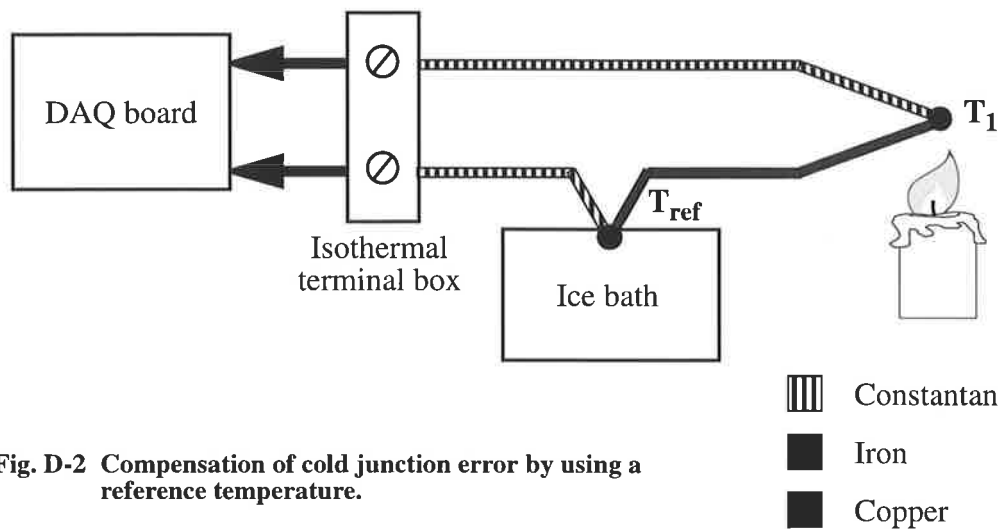


Fig. D-2 Compensation of cold junction error by using a reference temperature.

In Fig. D-2, the measured voltage depends on the difference in temperatures T_1 and T_{ref} ; in case of using ice bath as the reference temperature, T_{ref} is 0 C° . Since the voltmeter lead connections are the same temperature, the voltages generated at these two points are equal and opposing. Therefore, the net voltage error added by these connections is zero.

Under these conditions, if the measurement temperature is above 0 C° , a thermocouple has a positive output; if below 0 C° , the output is negative. When the reference junction and the measurement junction are the same temperature, the net voltage is zero.

Although an ice bath reference is accurate, it is not always practical. A more practical approach is to measure the temperature of the reference junction with a direct-reading temperature sensor and subtract the parasitic thermocouple thermoelectric voltage contributions. This process is called cold-junction compensation. The cold-junction effect can be compensated by taking advantage of some thermocouple characteristics.

Using the Thermocouple Law of Intermediate Metals and making some simple assumptions, the input voltage to the DAQ board in Fig. D-1 becomes only a function of the thermocouple type, the thermocouple voltage, and the cold-junction temperature. Then the measured

voltage is in fact independent of the composition of the measurement leads and the cold junctions, J2 and J3.

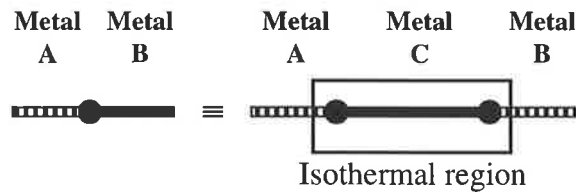


Fig. D-3 Illustration of thermocouple law of Intermediate Metals

According to the Thermocouple Law of Intermediate Metals, illustrated in Fig. D-3, inserting any type of wire into a thermocouple circuit has no effect on the output as long as both ends of that wire are the same temperature, or isothermal.

Fig. D-2 is similar to the previously described circuit in Fig. D-1 but a short length of

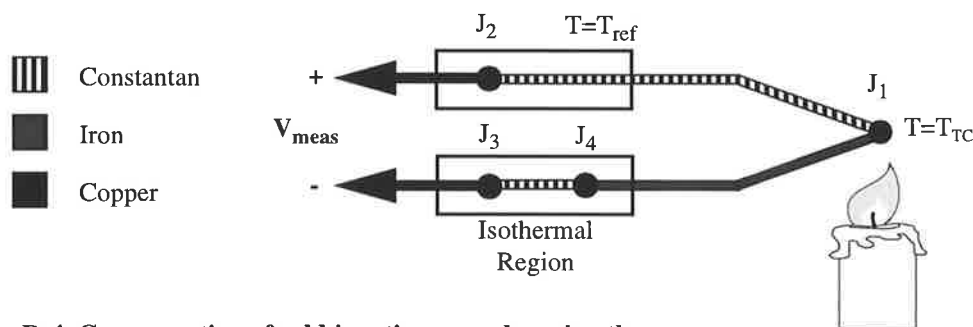


Fig. D-4 Compensation of cold junction error by using the thermocouple law of intermediate metals.

constantan wire has been inserted just before junction J3 and the junctions are assumed to be held at identical temperatures. Assuming that junctions J3 and J4 are at the same temperature, the Thermocouple Law of Intermediate Metals indicates that the circuit in Fig. D-2 is electrically equivalent to the circuit in Fig. D-1. Consequently, any result taken from the circuit in Fig. D-2 also applies to the circuit illustrated in Fig. D-1.

In Fig. D-2, junctions J3 and J4 are the same type (copper-constantan) and are located in an isothermal region. Since the junctions occur in opposite directions, their total contribution to the measured voltage is zero. Both junctions of J1 and J2 are the same type (iron-constantan

in this figure); they are usually at different temperatures and their voltages are in opposite directions. Therefore, junctions J_1 and J_2 are the only two junctions with outputs that may have any effect on the total voltage measured. Considering the polarity of generated voltages in the junctions, V_{meas} in Fig. D-2 can be calculated as:

$$V_{meas} = V_{TC} - V_{T_{ref}} \quad (D-2)$$

where:

V_{meas} = The voltage to be measured at DAQ;

V_{TC} = The generated voltage at the measurement point

$V_{T_{ref}}$ = The generated voltage at the reference point

Therefore, by measuring V_{meas} and T_{ref} , and knowing the voltage-to-temperature relationship of the thermocouple, the temperature of the thermocouple can be determined.

There are two techniques for implementing cold-junction compensation: hardware compensation and software compensation. Both techniques require that the temperature at the reference junction be known or measured with a direct-reading sensor. A direct-reading sensor has an output that depends only on the temperature of the measurement point. Semiconductor sensors or thermistors are the most common devices used to measure the reference-junction temperature.

With hardware compensation, a variable voltage source is inserted into the circuit to cancel the parasitic thermoelectric voltages. The variable voltage source generates a compensation voltage according to the ambient temperature, and thus adds the correct voltage to cancel the unwanted thermoelectric signals.

Alternatively, in a software compensating method, a sensor measures the reference-junction temperature. Then, an appropriate voltage is added to the measured voltage on the main thermocouple junction, V_{meas} .

2.3 Linearizing the Data

Thermocouple output voltages are highly nonlinear. The Seebeck coefficient can vary by a factor of three or more over the operating temperature range of some thermocouples. Therefore, the thermocouple output voltage is usually approximate by using complex polynomials. Alternatively, the voltage-temperature curve is matched against a look-up table. Table D-1 shows a list of the NIST polynomial coefficients for several popular thermocouple types fitted on a general form of polynomial as:

$$T = a_0 + a_1x + a_2x^2 + \dots + a_nx^n \quad (\text{D-3})$$

where x is the thermocouple voltage in volts, T is the temperature in degrees Celsius, and a_0 through a_n are coefficients that are specific to each thermocouple type.

Table D-1 NIST Polynomial Coefficients

Thermocouple Type	E	J	K	R	S	T
Temp. Range	-100 to 1000	0 to 760	0 to 1370	0 to 1000	0 to 1750	-160 to 400
a_0	0.104967248	-0.048868252	0.226584602	0.263632917	0.927763167	0.100860910
a_1	17,189.45282	19,873.14503	24,125.10900	179,075.491	169,526.5150	25,727.94369
a_2	-282,639.0850	-218,614.5353	67,233.4248	-48,840,341.37	-31,568,363.94	-7,673,345.829
a_3	12,695,339.5	11,569,199.78	2,210,340.682	1.90002E +10	8,990,730,663	78,025,595.81
a_4	-448,703,084.6	-264,917,531.4	-860,963,914.9	-4.82704E +12	-1.63565E +12	-9,247,486,589
a_5	1.10866E -10	2,018,441,314	4.83506E +10	7.62091E +14	1.88027E +14	6.97688 E+11
a_6	-1.76807E +11		-1.18452E +12	-7.20026E +16	-1.37241E +16	-2.66192E +13
a_7	1.71842E +12		1.38690E +13	3.71496E +18	6.17501E +17	3.94078E +14
a_8	-9.19278E +12		-6.33708E +13	-8.03104E +19	-1.56105E +19	
a_9	2.06132E +13				1.69535E +20	

* * * * *

BIBLIOGRAPHY

- [1] Alger, P. L.: "The Nature of Induction Machines, Gordon and Breach" (book), New York, 1965.
- [2] Agarwal, Paul D.; Alger, P. L.: "Saturation Factors for Leakage Reactance of Induction Motors", February 1961.
- [3] Andria, G; Dell Aquila, A; Salvatore, L.; Savino, M.: "Improvement in Modelling and Testing of Induction Motors", IEEE, Vol. EC-2, No. 2, June 1987
- [4] Arkkio, A.: "Finite Element Analysis of Cage Induction Motors Fed by Static Frequency Converters", IEEE, Vol. 26, No. 2, March 1990.
- [5] Armor, A. F.; Chari, M. V. K.: "Heat Flow in the Stator Core of Large Turbine-generators, by the Method of Three Dimensional Finite Element", IEEE Trans., PAS-95, pp1657-1662, 1976.
- [6] Armor, A. F.: "Transient, Three Dimensional, Finite Element Analysis of Heat Flow in Turbine-generator Rotors", IEEE Trans. PAS-99, pp934-946, 1980.
- [7] ASTM C201-86: "Standard Test Method for Thermal Conductivity of Refractories", Annual Book of ASTM Standards, American Society for Testing and Materials, Philadelphia, PA.
- [8] Babb, D. S.; Williams, J. E.: "Circuit Analysis Method for Determination of A-C Impedances of Machine Conductors", Trans. AIEE, vol. 70, pp 661-666, 1951.
- [9] Babb, D.S.; Williams, J. E.: "Network Analysis of A-C Machine Conductors" Trans. AIEE, vol. 70, pp 2001-2005, 1951.
- [10] Boglietti, A.; Ferraris, P.; Lazzari, M.; Profumo, F.: "Induction motor equivalent circuit

- parameters determination from standard tests made with inverter supply” Sixth International Conference on Electrical Machines and Drives (Conf. Publ. No.376), p. xvii+651, 271-6, UK, 1993.
- [11] Bousbaine, A.; McCormick, M.; Low, W.F.: “In-situ determination of thermal coefficients for electrical machines”, IEEE Transactions on Energy Conversion, vol. 10, no.3, pp 385-391, 1995.
- [12] Bousbaine, A.; Low, W.F.; McCormick, M., Benamrouche, N.: “Finite Element Analysis of Temperature Distribution in an Induction Motor”, Electrical & Magnetic Fields from Numerical Models to Industrial Applications, Proc. 2nd International workshop, pp 123-126, 1995.
- [13] Bousbaine, A.; McCormick, M.; Low, W.F.: “Thermal Modelling of Induction Motors Based on Accurate Loss Density Measurements”, International conference on Electrical Machines, vol.3, pp953-957, Sept. 1992.
- [14] Boys J. T.; Miles, M. J.: “Empirical Thermal Model for inverter Driven Cage Induction Machines”, IEE Proc. Electr. Power Appl., Vol. 141, No. 6, pp360-372, Nov. 1994.
- [15] Brocci, R. A.: “Analysis of Axisymmetric Linear Heat Conduction Problems by finite Element Methods”, ASME Winter Annual Meeting, Nov. 1969.
- [16] Bruges, W.E.: “Evaluation and Application of Certain Ladder-Type Networks”, Proc. Roy. Soc. Edinb. A,62 (Pt. 2), pp 175-186, 1946.
- [17] Cannistra, G.; Sylos Labini, M.: “Thermal analysis induction motor using network and finite element method” Proc. IEE, the Fifth International conference on Electrical Machines and Drives, pp 300-304, Sept. 1991.
- [18] Chan, C. C., Yan L., Wang, P., Chau K.T.: “Analysis of Electrical and Thermal Fields for Induction Motors During Starting”, IEEE Trans. pp53-60, EC-9, No.1, 1994
- [19] Dymond, J.H.; Findlay, R.D.: “Some Commentary on the Choice of Rotor Bar Material For Induction Motors”, IEEE Transactions on Energy Conversion, vol.10, no.3, pp425-430, 1995.
- [20] Edmund, O.; Schweitzer, III; Antenor A. Z.: “Thermal Protection of Motors Enhanced by Interactive Electrical and Thermal Models”, IEEE Trans., pp1749-1755, PAS-103, No. 7, 1984.

-
- [21] Eltom, A. H.; Moharari, N. S.: "Motor Temperature Estimation Incorporating Dynamic Rotor Impedance", IEEE Trans. EC-6, No. 1, pp107-113, 1991.
- [22] Feyzi, M. R.; Parker, A. M.: "A New Method of Finite Element Analysis for Non-Linear Magnetic Fields Including Skin Effect Areas", Australian universities power engineering conference (AUPEC'95), vol. 1, pp 144-150, Perth 1995.
- [23] Feyzi, M. R.; Parker, A. M.: "Heating in Deep-Bar Cages", IEE proceedings, Electr. Power Appl., Vol. 144, No.4, pp 271-276, July 1997.
- [24] Feyzi, M. R.; Parker, A. M.: "Transmission Line Equivalent Circuit for Open-Slot Cage Rotor Bar of Induction Motor" Proc. 4th Iranian Conference on Elect. Engineering, Power section, pp 327-334, Tehran, May 1996.
- [25] Fudeh, H.R.; Ong, C. M.: "Modelling and analysis of induction machines containing space harmonics", IEEE, Vol. PAS-102, No. 8 August 1983.
- [26] Gascoigne, A. E.; Gol, O.; Kearney, D.: "Stress Analysis in the Cage Induction Motor Under D.O.L. Starting Conditions (and reply)", Journal of Electrical and Electronics Engineering, Australia, vol.15, no.2, p. 215-17, June 1995.
- [27] Gerlando, A. D.; Vistoli, I.: "Improved thermal modelling of induction motor for design purposes" sixth international IEE Conference on Electrical Machines and Drives (Conf. Publ. No.376), pp381-6, Sept. 1993.
- [28] Gilbert, A. J.: "A method of measuring loss distribution in electrical machines", Proc. IEE, Vol. 108 A, pp239-244, 1961.
- [29] Gol, O.; FIEAust; Kearney, D.: "Stress Analysis in the Cage Induction Motor Under D.O.L. Starting Conditions", Journal of Electrical and Electronics Engineering, Australia, vol.13, no.2, pp81-87, June 1993.
- [30] Griffith, J. W.; McCoy, R. M.; Sharma D. K.: "Induction Motor Squirrel Cage Rotor Winding Thermal Analysis", IEEE Trans. pp22-25, EC-1, No. 3, 1986.
- [31] Gryglewicz-Kacerka, W; Mukosie, J.: "Thermal Analysis of Induction Motor with Axial and Radial Cooling Ducts", Proc. of Int. Conf. on Electr. Machines, pp971-975, Vol. 3, Manchester, Sept. 1992.
- [32] Guenov, S. Y.; Florov P. I.; Ibeh, C. C.: "Steady State Thermal Analysis of Induction Motors by Finite Element Method" Proc. of Int. Conf. on Electr. Machines, pp948-952,

- Vol. 3, Manchester, Sept. 1992.
- [33] Holman, Jack Philip: "Heat transfer", (Book), McGraw-Hill, Sydney, 1989.
- [34] Hwang, Chang-Chou; Pan, Ching-Tsai: "Thermal Analysis of Induction Motors Using Three-dimensional Finite Element Method", Journal of Chinese Institute of Engineers, vol. 12, No. 5, pp 599-610, 1989.
- [35] Ingot Product Bulletin, "High Conductivity Aluminium Rotor Alloys", 1-37-1A/ Revision 1, August 1972.
- [36] Ito, M., Fujimoto, N., Okuda, H.; Takahashi, N.: "Analytical Model for Magnetic Field Analysis of Induction Motor Performance", IEEE Trans., Pas-100, No.11, November 1981.
- [37] Jordan, Howard E.: "Analysis of Induction Machines in Dynamic Systems", New York, January 31-February 5, 1965.
- [38] Kreith, F.: "Principles of Heat Transfer" (book), Intext Educational Publishers, 3rd Edition, New York, 1973.
- [39] Klingshirn, E.A.; Jordan H.E. "Simulation of Polyphase Induction Motors With Deep Rotors Bars", IEEE Trans. PAS -89, no 6, pp 1038-1043, 1970.
- [40] Konrad, A.: "The Numerical Solution of Steady-state Skin Effect Problems, an Integrodifferential Approach", IEEE Tran. MAG-17, No. 1, January 1981.
- [41] Kotrba, Ing. Vit: "Temperature Field in the Ribbed Frame of the Induction Motor Type T.E.F.C.", Proc. of Int. Conf. on Electr. Machines, pp968-975, Vol. 3, Manchester, Sept. 1992.
- [42] Kylander, G.: "Temperature simulation of a 15-kW induction machine operating at variable speed", Proc. International Conference on Electrical Machines, p. 3 vol. xvi+1308, 943-7 vol.3 Sept. 1992.
- [43] Kylander, G.: "Thermal Modelling of Small Induction Motors", Technical report No. 265, (partial PhD thesis), School of Elect. and Computer Engineering, Chalmers University of Technology, Sweden, 1995.
- [44] Levi, W.; Landy, C.F.: "Improved Models for the Simulation of Deep Bar Induction Motors". Trans. IEEE, EC-5, No. 2, pp 393-400, 1990.
- [45] Luomi, J.; Niemenmaa, A.: "On the Use of Effective Reluctivities in Magnetic Field

- Analysis of Induction Motors Fed from a Sinusoidal Voltage Source”, International Conference on Electrical Machines, Munich, 1986.
- [46] McCulloch, M. D., Landy, C. F.: “Evaluation of the Short Circuit Current in Induction Motors with Deep Bar”, Proc. IEE, the sixth International conference on Electrical Machines and Drives, pp 15-19, Sept. 1993.
- [47] Mellor, P. H.; Roberts D.; Turner D. R.: “Lumped parameter thermal model for electrical machines of TEFC design”, IEE proc.-B, pp205-218, Vol. 138, No. 5, Sept. 1991.
- [48] Mukhopadhyay, S. C.; Bose S.; Pal, S. K.: “Determination of harmonic equivalent circuit parameters of a cage rotor induction motor”, Journal of the Institution of Engineers (India) Electrical Engineering Division, vol.75, p. 159-63, Feb. 1995.
- [49] Namburi, N. R.; Barton, T. H.: “Thermal Modelling of Induction Motor”, IEEE Trans., PAS-102, No. 8, pp2636-2639, 1983.
- [50] Oberretl, K.: “Dependence of rotor bar currents from rotor position in squirrel cage motors”, Int. Conf. Elect. Machines, pp 1761-1767, Athens, Greece, Sept. 1980.
- [51] Ohishi, H., Sakabe S., Yamashita K.: “Analysis of Temperature Distribution in Coil-Strands of Electric Machines with One Turn Coil”, IEEE Trans. pp432-438, EC-2, No. 3, 1987.
- [52] Parkin, T. S., Preston, T. W.: “Induction Motor Analysis Using Finite Elements”, Proc. IEE, the sixth International conference on Electrical Machines and Drives, pp 20-24, Sept. 1993.
- [53] Preston, T. W.: “Induction Motor Analysis by Time Stepping Techniques”, IEEE Trans., MAG-24, No. 1, pp. 471-474, Jan. 1988.
- [54] Puchstein, A. F.: “Calculation of Slot Constants”, AIEE Trans., vol. 66, pp 1315-1323, 1947.
- [55] Ralph, J. W.; Williamson, S.: “Solution of Two-Dimensional Nonlinear Field Problems with Sinusoidal Excitation Sources Using First Order Elements”, IEEE Trans., MAG-19, pp 2433-2436, 1983.
- [56] Rajagopal, M. S.; Seetharamu, K. N.: “Transient Thermal Analysis Of Induction Motors”, Proc. of IEEE International conf., Vol. 2, New Delhi, Jan. 1996.

-
- [57] Robert, F. Speyer: "Thermal Analysis of Materials", (Book), Marcel Dekker, Inc., New York, 1994.
- [58] Roberts, T. J.: "Determination of the Thermal Constants of the Heat Equations of Electrical Machines", Proc. Instn Mech. Engrs., Vol. 184, Pt 3E, pp84-92, 1969-70.
- [59] Robinson, M. J.: "Finite Element calculation of Equivalent Circuit Parameters for Induction Motors", PhD Thesis, University of London, Nov. 1988.
- [60] Roger, J.; Jimenez, G.: "The Finite Element Method Application to the Study of the Temperature Distribution Inside Electric Rotating Machines", Proceedings Int. Conf. on Electrical Machines, pp976-980, 1992.
- [61] Rogers, G. J.; Shirmohammadi, B.: "Induction Machine Modelling for Electromagnetic Transient Program", IEEE Trans., EC-2, No. 4, pp622-628, December 1987.
- [62] Rybicki Edmund, F.; Hopper, Allen T.: "Higher Order Finite Element Method for Transient Temperature Analysis of Inhomogenous Materials", ASME Winter Annual Meeting, Nov. 1969.
- [63] Sarker, P. K., Mukherjee; S. K. Sen.: "Use of Three Dimensional Finite Element for Computation of Temperature Distribution in the Stator of an Induction Motor", Proc. IEE, Vol. 138, pp 75-86, 1991.
- [64] Saunders, R.M.: "Electromechanical Energy Conversion in Double Cylindrical Structures", October 1963.
- [65] Say, M.G.: "Alternating Current Machines", 4th edition, Pitman Publishing Cooperation, 1978.
- [66] Silvester, P.; Cabayan, H. S.: "Efficient Techniques for Finite Element Analysis of Electrical Machines", IEEE Trans., PAS-92, pp 1274-1281, 1973.
- [67] Silvester, P.; Madabushi, V.K. Chari: "Finite Element Solution of Saturable Magnetic Field Problems", IEEE Trans., PAS-89, No. 7, pp 1642-1651, Sept./Oct. 1970.
- [68] Siyambalapitiya, D. J. T.; McLaren, P. G.; Tavner P. J.: "Transient Thermal Characteristics of Induction Machine Rotor Cage", IEEE Tran., EC-3(4), pp849-854, Dec. 1988.
- [69] Smith, R.F.; Nichols, J.O.: "Analysis of a deep bar induction motor and compressor load during start-up", New York, January 29-February 3, 1978.

-
- [70] Standard Association of Australia: "Electrical Equipments for Explosive Atmospheres-Explosion-Protection Techniques", Part6 (Increased Safety), 1988.
- [71] Steinmetz, C.P.: "The Alternative Current Induction Motor", AIEE Trans., Vol. 14, pp185-2177, 1897.
- [72] Vickers, H., "Induction Motor, the Theory, Design and Application" (book), 2nd Edition, Sir Isaac Pitman and Sons Publication, London, 1953.
- [73] Walker, J. D.: "Cage Rotor Heating at Stall", PhD Thesis, The university of Cambridge, Oct. 1991.
- [74] Williams, A.: "Heat flow Across Stacks of Steel Laminations", Journal Mech. Eng. Science, Vol. 13, No. 3, pp. 217-223, 1971.
- [75] Williamson, S.; Begg, M. C.: "Calculation of the Bar Resistance and Slot Reactance of Cage Rotors with Closed Slots", IEE Proc. B, vol. 132, No.3, pp. 125-132, 1985.
- [76] Williamson, S, Flack, T. J.: "Effect of Radial Rotor Ventilation Ducts on caGe Motor Equivalent Circuit Parameters", IEE Proc. Electr. Power Appli, Vol. 141, No. 3, pp155-162, May 1994.
- [77] Williamson, S., Lim, L. H.; Smith, A.C.: "Transient Analysis of Cage-Induction Motors Using Finite-Elements", IEEE, Vol. 26, No. 2, March 1990.
- [78] Williamson, S.; Lloyd, M. R.: "Cage Rotor Heating at Standstill", IEE Proceedings, Vol. 134, Pt. B, No. 6, pp 325-332, Nov. 1987.
- [79] Williamson, S.; Ralph, J. W.: "Finite Element analysis of an Induction Motor Fed from a Constant-voltage Source", IEE Proc. B, vol. 130, No. 1, Jan. 1983.
- [80] Williamson, S.; Robinson M. J.: "Calculation of Bar Resistance and Leakage Reactance of Cage Rotors", 3rd Int. Conf. Electr. Mach. and Drives, IEE, London, Nov., pp 122-126, 1987.
- [81] Williamson, S., Robinson M. J.: "Calculation of cage induction motor equivalent circuit parameters using finite elements", IEE Proc. B, Vol. 138, No. 5, pp264-276, September 1991.
- [82] Williamson, S., Robinson, M. J.: "Finite Element Calculation of Equivalent Circuit Parameters for Induction Motor", PhD thesis, Imperial college of Science and technology, London, 1988.

-
- [83] Williamson, S. Walker, J. D.: "Calculation of Stall Bar Temperature Rise", Fifth Int. Conf. on Electr. Machines, pp 271-275, Sept. 1991.
- [84] Williamson, S. Walker, J. D.: "Rotor Cage Current Distribution at Stall", Int. Conf. on Electr. Machines, pp 952-962, Boston, U S A 1990.
- [85] Wislow, A. M.: "Magnetic field calculation in an irregular triangular mesh". Lawrence Radiation Laboratory, Livermore, California, UCRL-7784-T, Rev. 1, 1965.
- [86] Zhu, J. G.; Ramsden, V. S.; Watterson P. A.: "Finite Element Calculation of Core Losses in Motors With Non-Sinusoidal Fields", Proc. of Int. Conf. on Electr. Machines, pp1182-1186, Vol. 3, Manchester, Sept. 1992.
- [87] Zocholl Stanley, E.; Schweitzer, III.; Edmund, O.; Aliaga-Zegarra, A.: "Thermal Protection of Motors Enhanced by Interactive Electrical and Thermal Models", IEEE Trans., pp1749-1755, PAS-103, No. 7, 1984.